

Mathematical models for collective cell spreading

Katrina K Treloar

BAppSc (Hons)

under the supervision of

Professor Matthew Simpson
and

Associate Professor Scott McCue

Mathematical Sciences

Faculty of Science and Engineering

Tissue Repair and Regeneration Program
Institute of Health and Biomedical Innovation

Queensland University of Technology

August 2015



SUBMITTED IN FULFILLMENT OF THE REQUIREMENTS OF THE DEGREE OF
DOCTOR OF PHILOSOPHY

Abstract

Collective cell spreading is frequently observed in development, tissue repair and disease progression. Mathematical modelling used in conjunction with experimental investigation can provide key insights into the mechanisms driving the spread of cell populations. The principle aim of this thesis is to apply mathematical modelling frameworks to new experimental data to identify and quantify several key features underlying collective cell spreading. This work is presented as a thesis by published papers and consists of five related works which may either be read as a whole or as separate entities.

We begin by describing a set of experiments to investigate the unique roles of cell motility and cell proliferation in driving an initially confined fibroblast cell population. To interpret our experimental observations we use a combination of lattice-based discrete simulations and a related continuum partial differential equation model. We obtain independent estimates of the cell diffusivity, D , by extracting information about the location of the leading edge from experiments where cell proliferation has been suppressed in the spreading population. Independent estimates of the cell proliferation rate, λ are obtained using cell density information from experiments where cell proliferation is not inhibited in the spreading population. Previous work suggests that cell populations with a high λ/D ratio will be characterised by steep fronts, whereas systems with a low λ/D will lead to shallow diffusive fronts and we confirm this here. Our results provide evidence that standard mathematical models, based on the Fisher–Kolmogorov equation, are appropriate to interpret and predict such experimental observations.

We extend our investigation to quantify the mechanisms driving the collective spread of melanoma cell populations. In addition to cell motility and cell proliferation mechanisms, cell-to-cell adhesion is thought to be a crucial mechanism involved in melanoma cell population spreading. Standard mathematical models often neglect cell-to-cell adhesion and it is unclear how estimates of the strength of cell-to-cell adhesion in a cell population can be extracted from experimental data. In this work, we show that multiple types of data must be integrated to independently quantify each of the three mechanisms present in the spreading melanoma cell populations. In addition, we provide a method of quantifying the strength of cell-to-cell adhesion by extracting information about the location of isolated cells in the spreading population.

Our experimental and mathematical modelling investigation to quantify the mechanisms driving the spread of fibroblast and melanoma cell populations raises several additional questions which we examine in the final sections of the thesis. Firstly, we examine whether the location of the leading edge, which is often used to parameterise mathematical models, is sensitive to the choice of image analysis tools. We show that a standard measure of cell migration can vary by as much as 25%. In addition, we use a mathematical model to provide a physical interpretation of the location of the leading edge and find that varying the image threshold parameter is equivalent to varying the location of the leading edge in the range of approximately 1–5% of the maximum cell density. Our results suggest that it is impossible to meaningful compare previously published measures of cell migration since previously results have been obtained using different image analysis tools and the details of these tools are often not reported.

Secondly, we explore the role of *in vitro* assay geometry by performing experiments in two distinct geometries. The first geometry describes a tumour-like geometry where a cell population spreads outwards into an open space. The second geometry describes a wound-like geometry where a cell population spreads inwards to close a void. Applying the same techniques to independently quantify D and λ , we find that *in vitro* assay geometry does affect these estimates. Our work suggests that estimates of the cell diffusivity vary by up to 50% while estimates of the cell proliferation rate vary by up to 30%.

Finally, we test whether standard mathematical models, which assume that there is no spatial structure such as cell clustering present in the system, are appropriate to describe the spread of the melanoma cell populations considered in this work. We analyse discrete simulation using pair correlation functions to show that spatial structure can form in a spreading population of cells either through sufficiently strong cell-to-cell adhesion or sufficiently rapid cell proliferation. We use the same pair correlation functions to analyse experimental images and find that the strength of cell-to-cell adhesion is sufficiently weak and rate of cell proliferation is sufficiently slow, so as not to induce any spatial structure in the spreading populations.

We conclude by discussing the potential to apply the experimental and modelling approaches presented here to understand other aspects underlying collective cell spreading.

Declaration

I hereby declare that this submission is my own work and to the best of my knowledge it contains no material previously published or written by another person, nor material which to a substantial extent has been accepted for the award of any other degree or diploma at QUT or any other educational institution, except where due acknowledgement is made in the thesis. Any contribution made to the research by colleagues, with whom I have worked at QUT or elsewhere, during my candidature, is fully acknowledged.

I also declare that the intellectual content of this thesis is the product of my own work, except to the extent that assistance from others in the project's design and conception or in style, presentation and linguistic expression is acknowledged.

Signature _____ Date _____

Acknowledgements

First and foremost, this thesis would not have existed without the support of Prof Mat Simpson. I am grateful for your guidance throughout my PhD and the generous time that you have always committed to further my education. Many thanks for the opportunity to combine mathematical modelling with experimental data, I appreciate and have thoroughly enjoyed this aspect of my research.

Throughout my PhD, I have had the opportunity to collaborate with several researchers and I would like to acknowledge their contribution to this work. In particular, I am sincerely thankful to E Prof Sean McElwain for his enthusiasm and guidance on all aspects of this work. Thanks must also go to A Prof Ruth Baker and Dr Ben Binder for their helpful comments and advice as we were publishing this work. To our experimental collaborators, A Prof David Leavesley and Dr Kerry Manton, for their input on the biology of the problem. Lastly, many thanks must go to Ms Parvathi Haridas for performing the experiments in this work and for her patience, among other things, in answering all of my questions relating to the experiments in this work.

I would like to acknowledge the financial support of an Australian Postgraduate Award and additional funding provided throughout my candidature by the School of Mathematical Sciences, Institute of Health and Biomedical Innovation and my principal supervisor.

Thank you to my fellow PhD students and my friends outside the academic world for their support and advice during my PhD. I am wholeheartedly grateful for my family, especially my Mum, Dad, Natalie, Joyce and Tony, your continual love and support means the world to me. Finally to Anna, this work is for you.

Contents

Abstract	i
Declaration	iii
Acknowledgements	v
Chapter 1 Introduction	1
1.1 Overview	1
1.2 Research questions	3
1.3 Aims and outcomes of this thesis	6
1.4 Structure of this thesis	8
1.5 Statements of joint authorship	9
Chapter 2 Quantifying the roles of cell motility and cell proliferation in a circular barrier assay	15
2.1 Background	16
2.2 Experimental methods	17
2.2.1 Cell culture	17
2.2.2 Barrier assay	17
2.2.3 Cell staining	18
2.2.4 Image analysis	18
2.3 Modelling methods	19
2.3.1 Discrete model	19
2.3.2 Continuum model	19
2.4 Results	20
2.4.1 Carrying capacity density estimate	20
2.4.2 Cell motility estimates	20
2.4.3 Cell proliferation estimates	22
2.4.4 Position of the leading edge	24
2.4.5 Shape of the leading-edge	28
2.5 Discussion	29
Chapter 3 Multiple types of data are required to identify the mechanisms influencing the spatial expansion of melanoma cell colonies	33
3.1 Background	34
3.2 Experimental methods	35
3.2.1 Cell culture	35
3.2.2 Circular barrier assay	36
3.2.3 Detection of motility and cell-to-cell adhesion proteins in MM127 cells using immunofluorescence and western blotting	36
3.2.4 Image acquisition and analysis	36
3.3 Results	37

3.3.1	Identifying the mechanisms controlling the expansion of melanoma cell colonies	37
3.3.2	Modelling the spatial expansion of a melanoma cell colony	38
3.3.3	Estimating the rate of cell motility and strength of cell-to-cell adhesion	41
3.3.4	Estimating the rate of proliferation	49
3.3.5	Predicting the spatial expansion of a melanoma cell colony	51
3.4	Discussion	54
Chapter 4 Sensitivity of edge detection methods for quantifying cell migration as says		59
4.1	Background	60
4.2	Experimental methods	61
4.2.1	Cell culture	61
4.2.2	Circular barrier assay	61
4.2.3	Edge detection methods	62
4.3	Modelling methods	63
4.4	Results	64
4.4.1	Locating the leading edge	64
4.4.2	Comparing edge detection techniques	65
4.4.3	A physical interpretation of the leading edge	70
4.5	Discussion	72
Chapter 5 Are <i>in vitro</i> estimates of cell diffusivity and cell proliferation rate sensitive to assay geometry?		75
5.1	Background	76
5.2	Experimental methods	78
5.2.1	Circular barrier assay	78
5.2.2	Image acquisition and analysis	78
5.3	Modelling methods	80
5.3.1	Discrete model	80
5.3.2	Continuum model	81
5.3.3	Standard measure of spatial spreading	82
5.4	Results	82
5.4.1	Cell diffusivity estimates	82
5.4.2	Cell proliferation estimates	85
5.4.3	Predicting the behaviour of spreading cell populations in different geometries	88
5.4.4	Comparing estimates of D and λ in different geometries	92
5.5	Discussion	94
Chapter 6 Assessing the role of spatial correlations in collective cell spreading		99
6.1	Background	100
6.2	Methods	101
6.2.1	Cell culture	101
6.2.2	Circular barrier assay	102
6.2.3	Image acquisition and analysis	102
6.2.4	Pair correlation function	102
6.3	Results	104
6.3.1	Visual inspection of spreading MM127 melanoma cell populations does not provide insights into possible spatial correlations	104

6.3.2	Discrete simulations of the experimental process provide insight into possible mechanisms inducing spatial correlations	105
6.3.3	Spatial correlations are not present in spreading MM127 melanoma cell populations	110
6.4	Discussion	112
Chapter 7 Conclusions		113
7.1	Summary	113
7.2	Future work	116
7.3	Final remarks	119
Appendix A Supplementary material for Chapter 2: ‘Quantifying the role of cell motility and cell proliferation in a circular barrier assay’		121
A.1	Estimates of the cell diameter	121
A.2	Image analysis using the MATLAB image processing toolbox	122
A.3	Experimental edge detection of the population-scale images (crystal violet stained images)	124
A.4	Numerical solutions of the partial differential equation models	124
A.5	Estimating the random motility coefficient	124
A.6	Position of the leading edge with Mitomycin-C pretreatment	126
A.7	Proliferation rate estimates	127
A.8	Locating the leading edge using the solution of a partial differential equation	130
A.9	Leading edge position after 24 and 48 hours	130
Appendix B Supplementary material for Chapter 3: ‘Multiple types of data are required to identify the mechanisms influencing the spatial expansion of melanoma cell colonies’		133
B.1	Estimating the diameter of the cell nucleus	133
B.2	Data type 1: Location of the leading edge	134
B.3	Data type 2: Cell density profiles	135
B.4	Data type 3: Degree of cell clustering	136
B.5	Data type 4: Cell density counts	137
B.6	Predicting the spatial expansion of a MM127 melanoma cell colony	139
B.7	Image acquisition and analysis	141
Appendix C Supplementary material for Chapter 5: ‘Are <i>in vitro</i> estimates of cell diffusivity and cell proliferation rate sensitive to assay geometry?’		143
C.1	Cell culture	143
C.2	Measurements of the cell diameter	143
C.3	Image acquisition and analysis	143
C.3.1	Population-scale image acquisition and analysis	143
C.3.2	Individual-scale image acquisition and analysis	145
C.4	Leading edge data	145
C.5	Effective cell diffusivity estimates	146
C.6	Cell proliferation rate data	147
C.7	Alternative effective cell proliferation rate estimates	147
C.8	Effective cell proliferation rate estimates with Mitomycin-C pretreatment	150
C.9	Locating the leading edge using the solution of a partial differential equation	151
C.10	Calculating the variation in the parameter estimates	151

Appendix D Supplementary material for Chapter 6: ‘Assessing the role of spatial correlations during collective cell spreading’	153
D.1 Estimating the total area occupied by individual MM127 melanoma cells .	153
D.2 Computing average pair correlation functions	155
D.3 Average pair correlation signals for experiments with different initial cell densities	157
D.4 Pair correlation signals in subregions located across the spreading cell population	158
D.5 Insensitivity of pair correlation signal to δ	160
D.6 Average pair correlation function in the w direction	161
Bibliography	162

CHAPTER 1

Introduction

1.1 Overview

Collective cell spreading¹ is essential for development [159], tissue repair [85, 86, 89] and disease progression [132, 153]. During these processes, cohorts of individual cells may migrate, proliferate and/or adhere to other cells, resulting in the spatial spread of a cell population [85, 86, 132, 159]. For example, development relies on the ability of cell populations to be transported to new locations [159], while during wound-healing, fronts of cells invade the wounded area as part of the repair process [85, 86]. Less desirably, abnormalities in collective cell spreading may lead to malignant spreading and slowed wound-repair [89, 132, 153]. Consequently, mathematical models to describe collective cell spreading have been a recent subject of great interest since they have the potential to provide insights into the mechanisms driving collective cell spreading [85, 86, 116, 132, 133].

Mathematical modelling approaches to describe collective cell spreading generally take one of two forms [3, 9, 38, 85, 97, 116, 132]. The first approach describes the spread of the entire cell population at the population-level using a continuum description, such as a partial differential equation [20, 85, 86, 97, 113, 116, 132]. The second approach characterises the behaviour of individual cells within the spreading cell population, using a discrete description [3, 9, 38, 52, 57, 146]. Mathematical models are traditionally continuum-based and the standard continuum mathematical model used to describe how a population of motile and proliferative cells spread in two dimensions is related to the Fisher–Kolmogorov equation, which is given by

$$\frac{\partial \bar{c}}{\partial t} = D \nabla^2 \bar{c} + \lambda \bar{c} \left(1 - \frac{\bar{c}}{K}\right), \quad (1.1)$$

where $\bar{c}(x, y, t)$ [cells/L²] is the dimensional cell density, D [L²/T] is the cell diffusivity (random motility coefficient), λ [/T] is the cell proliferation rate and K [cells/L²] is the carrying-capacity density [20, 85, 86, 97, 113, 116, 132]. In one-dimensional Cartesian geometry, Equation (1.1) simplifies to the Fisher–Kolmogorov equation [42] which has constant shape travelling wave solutions, $C(z) = \bar{c}(x - st)$, moving at constant speed s [85, 86, 97]. The front speed approaches $s = \sqrt{4D\lambda}$ as $t \rightarrow \infty$ for initial conditions with compact support [97]. Variations of the Fisher–Kolmogorov equation, incorporating

¹In this work, the term *collective cell spreading* refers to the spatial movement of an entire cell population due to combinations of motility (migration), proliferation and/or cell-to-cell adhesion mechanisms.

directed motility [104] or nonlinear diffusion [20, 155], have also been used to describe collective cell spreading. These variations also have travelling wave solutions and different relationships between the wave speed and the model parameters can be derived for these generalisations [20, 104, 155].

An alternative modelling approach to describe collective cell spreading involves simulating the behaviour of individual cells in a population using a discrete, or individual-based, modelling framework [3, 9, 38, 52, 57, 146]. There are several discrete tools that can be used to simulate this behaviour including lattice-based random walk models, cellular Potts models and off-lattice cell-based models [3, 9, 38, 52, 57, 146]. Each discrete model tracks and updates individual cells according to a set of rules which are typically based on observations of the biophysical behaviour [3, 9, 38, 52, 57, 146]. Discrete models have the benefit that they produce data, such as snapshots and movies, that are more compatible with experimental data compared to partial differential equation models [125]. Furthermore, discrete models can be designed to incorporate realistic cell behaviours which can be more difficult using a partial differential equation description [125]. However, individual-based models are computationally expensive and many realisations are required to obtain reliable statistics, meaning that it is often difficult to simulate realistic biological systems [88]. Continuum models are more amenable to analytical exploration and hence can be advantageous over individual-based models [88, 127].

Experimental observations of collective cell spreading often involve both individual-level and population level observations, and it is important to understand how behaviours at the individual-level may affect the behaviour of the entire cell population [53]. Likewise, understanding how information at the population-level may influence behaviours at the individual-level is equally as important [53]. For example, time-lapse imaging often provides detailed information about how a single cell interacts and responds to its environment, and observations can be easily incorporated in a discrete model [159]. Additionally, population-level measurements, such as the front speed can be compared to population-level information from either the discrete or continuum model [85, 86]. Consequently, a multi-scale approach may provide a better alternative to traditional continuum modelling since discrete-to-continuum models can easily capture individual-level behaviours while still having the same advantages of continuum modelling [120].

Mathematical modelling can provide insights into the mechanisms driving collective cell spreading [20, 85, 86, 116, 132, 133]. Recent modelling approaches have used tandem experimental studies to quantify various aspects of collective cell spreading. Maini *et al.* [85, 86] illustrated that a very simple wound-healing assay gives rise to constant speed travelling waves as predicted by Fisher's equation. Sengers *et al.* [113] characterised the migration and proliferation of two skeletal cell types by extracting detailed information about the cell density profile across the spreading cell populations illustrating that the standard continuum model (Equation 1.1) could accurately describe one of the cell populations, while an alternative continuum model was needed to characterise the other cell population [113].

Combined modelling and experimental studies have also accounted for possible cell-to-cell adhesion mechanisms in the cell population. Khain *et al.* [72, 74] developed a discrete mathematical model to describe the expansion of a motile and proliferative cell colony in which the cell motility is reduced by cell-to-cell adhesion. In their model, they represented simulated cells on a two-dimensional lattice, and they allowed the simulated cells to both move and proliferate. Cell-to-cell adhesion was introduced by including a mechanism where the simulated cells could adhere to nearest neighbour simulated cells, effectively reducing their motility. Khain *et al.* [72, 74] applied this model to investigate the behaviour of glioma cells in a two-dimensional scratch assay, predicting the location and speed of the leading edge of the expanding glioma cell colony. In another study, Simpson *et al.* [121] extended Khain’s model to investigate the migration of MCF-7 breast cancer cells in a three-dimensional Transwell apparatus [121].

The tandem use of experimental investigation and mathematical modelling provides an abundance of opportunities to identify and quantify the mechanisms driving collective cell spreading. In the following section, we will identify and discuss five aspects related to mathematical models for collective cell spreading that we will address in this thesis.

1.2 Research questions

In this work, we will utilise combined mathematical modelling tools and experimental investigation to identify and quantify several features underlying collective cell spreading. In particular, we propose to answer the following five questions:

(1) How can we separately quantify the roles of cell motility and cell proliferation in a spreading cell population?

Cell motility and cell proliferation are thought to play major roles in driving the spread of cell populations [85, 89, 116, 132, 153]. Identifying and isolating the contribution of each of these mechanisms, may provide an opportunity to understand how these mechanisms control the spread of a cell population. Swanson *et al.* [132] suggests that cell populations with a high ratio of cell proliferation to cell motility will be characterised by steep fronts, whereas systems with a low ratio of cell proliferation to cell motility will lead to shallow fronts. This is important when surgically removing tumours, since the boundary between the tumour tissue and normal tissue is increasingly difficult to detect as the front becomes more diffuse [132].

Cell-based assays are commonly-used to quantify the capacity of cell populations to spread in an *in vitro* environment [7, 30, 69, 70, 78, 144]. Several types of assays have been developed to investigate collective cell population spreading in two and three dimensions including Transwell, scratch, exclusion zone and spheroid assays [7, 30, 78, 144]. Recently, two-dimensional circular barrier assays have become a popular alternative to scratch assays since they do not damage the cell monolayer, or the substrate, and are therefore thought to be more reproducible than scratch assays [145]. Circular barrier assays can be conducted by initially placing cells

either inside or outside the barrier, which is then lifted to initiate the cell spreading [7, 78, 125, 138, 145].

Consequently, if we considered the spread of a cell population in *in vitro* environment, how do we use experimental and modelling techniques to independently quantify the roles of cell motility and cell proliferation. Maini et al. [85, 86] illustrated that there are many choices of λ and D in the standard continuum model which can be used to match the experimental front speed. An alternative approach to identify parameters is to fit solutions of the mathematical model to experimental density profiles [113]. The disadvantage of fitting the solution of mathematical models to cell density information alone is that this does not necessarily ensure that the parameterised model can make independent predictions. One way to overcome this may be to collect different types of experimental data so that the process of model calibration can be separated from the process of model prediction.

(2) What are the mechanisms underlying the spread of melanoma cell populations and how do we independently quantify the contribution of each mechanism?

Collective cell spreading is driven by several mechanisms including cell motility, cell-to-cell adhesion and cell proliferation [85, 132, 153]. Typical mathematical modelling approaches to describe the movement of such fronts use partial differential equations which only incorporate descriptions of cell motility and cell proliferation [85, 97, 113, 116, 125, 132], and often neglect cell-to-cell adhesion [33, 75, 121]. Several experimental studies have observed that the loss of cell-to-cell adhesion between individual melanoma cells is associated with increased spatial spreading [29, 65, 79, 87, 93, 108], suggesting that cell-to-cell adhesion plays an important role in spreading melanoma cell populations.

There are currently no widely accepted protocols for designing experiments that allow us to independently quantify the contributions of cell motility, cell-to-cell adhesion and cell proliferation in spreading cell populations [72, 74–76, 121]. In addition, there is no standard method to assess the degree of the cell-to-cell adhesion in a cell population. We hypothesise that collecting and analysing several sets of experimental data describing the same experimental procedure may be required in order for us to independently quantify the role of these mechanisms in spreading melanoma cell populations.

(3) Does the location of the leading edge of a spreading cell population depend on the details of the image analysis tools?

An essential element of interpreting and quantifying cell migration assays is to locate the position of the leading edge of the spreading population so that the rate at which the cell population spreads across the substrate can be calculated. A common approach to quantify the cell migration rate in an assay is to calculate the

initial area occupied by a population of cells and measure the percentage change in area with time [7, 56, 94, 145, 161]. This can be expressed as

$$M(t) = \frac{A(t) - A(0)}{A(0)} \times 100, \quad (1.2)$$

where $A(0)$ is the initial area enclosed by the population of cells at $t = 0$, $A(t)$ is the area enclosed by the population of cells at time t , and $M(t)$ is the percentage change in area as a function of time t .

Estimates of cell migration rates using Equation (1.2) are often obtained by manually tracing the area enclosing the spreading cell population [55, 160]. Unfortunately, manually tracing the area enclosed by the leading edge of a spreading cell population is very subjective [135]. To overcome this limitation, automated image analysis software, including ImageJ [66] and MATLAB's Image Processing Toolbox [90], have been used as an alternative to manual tracing [69, 164]. These software tools use edge detection and segmentation algorithms to determine the location of the leading edge of the spreading cell population. This data can then be used to quantify the cell migration rate in terms of the percent change in area using Equation (4.1). In addition to using automatic edge detection algorithms, it is also possible to implement manual edge detection options in MATLAB's Image Processing Toolbox [90] so that the user has complete control over the image detection thresholds. However, it is unclear whether the details of the image analysis method affects the location of the detected leading edge, or whether we are able to provide a physical interpretation of the leading edge.

(4) Does *in vitro* assay geometry affect estimates of the rate of cell motility and rate of cell proliferation?

Wound-healing and tumour progression are often studied in the same context since the mechanisms that drive these processes are thought to be similar [22, 28, 44, 115, 153]. Despite their similarities, these processes have distinct geometries: (i) during wound-healing, cell populations spread inwards to close the wound void, and (ii) during tumour progression, cell populations spread outwards causing the tumour to expand [7, 153]. Recent work using microfabrication methods focused on creating various-sized channels through which cells could migrate, with the observation that the speed of the leading edge of the cell population depends on the channel width [148]. Therefore, it seems reasonable to assume that assay geometry could play a role in determining the rate at which cell populations spread.

If we consider a population of otherwise identical cells, it is unclear whether they will exhibit different rates of spreading in different *in vitro* assay geometries. The standard continuum model, based on the Fisher–Kolmogorov equation, used to estimate D and λ from experimental observations has an additional implicit assumption that estimates obtained in one geometry could be relevant when considering the same population spreading in a different geometry. However, from a biological point of

view, it seems reasonable to anticipate that cell populations could respond differently under different circumstances. This means that our estimates of D and λ using the standard continuum model might be different when calibrating this model under different experimental geometries.

(5) **How do we diagnose spatial structure in a spreading cell population?**

Standard continuum models, such as Fisher's equation, invoke a mean-field assumption implying that there is no underlying spatial structure, such as cell clustering, present in the system [80, 127]. It is well known that strong cell-to-cell adhesion or sufficiently rapid cell proliferation can lead an initially uniform population of cells to become clustered over time [2, 127]. Previous work has compared averaged discrete simulation data with predictions from standard mean-field descriptions of these discrete simulations for systems where either strong adhesion [67] or rapid proliferation is present [12, 126]. These previous comparisons have confirmed that standard mean-field models fail to accurately predict the averaged behaviour of the discrete model which implies that the usual mean-field assumption is inappropriate where either strong cell-to-cell adhesion or rapid proliferation is present [12, 67, 126, 127].

For a given context, it is not always clear which modelling framework is appropriate without first testing the underlying model assumptions. For example, spreading populations of 3T3 fibroblast cells do not generally exhibit visible cell clustering, whereas populations of MDA MB 231 breast cancer cells appear to be highly clustered [125, 127]. At first glance, it may appear reasonable to use a mean-field model to describe the spreading of a population of 3T3 cells and an alternative model to describe the spreading of a population of MDA MB 231 cells. However, recent work has indicated that the presence or absence of spatial correlations can be difficult to detect visually and so our use of a mean-field model for 3T3 cell population spreading may, in fact, be inappropriate [2]. Consequently, applying diagnostic tools which are capable of identifying spatial structure in a given cell population may provide insights into which modelling frameworks are suitable for exploring a particular system.

This thesis will address these five unanswered questions. In the next section we outline the principle aims of this thesis.

1.3 Aims and outcomes of this thesis

The principle aim of this thesis is to use mathematical modelling in conjunction with experimental investigation to identify and quantify several key features underlying collective cell spreading.

The thesis consists of the five following principal aims:

- Apply multiscale models of collective cell spreading to new experimental data with the aim of independently quantifying the rate of cell motility and rate of cell proliferation in a spreading cell population,

- Identify multiple types of data to distinguish between the roles of cell motility, cell proliferation and cell-to-cell adhesion in spreading melanoma cell populations,
- Quantify the variability in detecting the leading edge of cell migration assays using image analysis techniques, and in turn use mathematical modelling to provide a physical interpretation of the leading edge,
- Investigate the affect of *in vitro* assay geometry on estimates of the rate of cell motility and rate of cell proliferation, and
- Use modelling tools to diagnose the presence of spatial correlations in spreading melanoma cell populations.

This thesis is presented by publication and consists of five papers which have been published in peer-reviewed journals. The PhD candidate has contributed significantly to all five papers and is the primary author of four out of the five papers. The work presented in this thesis fulfils the Queensland University of Technology requirements for the award of thesis by published papers.

This thesis comprises the following publications:

- Simpson, M.J., **Treloar, K.K.**, Binder, B.J., Haridas, P., Manton, K.J., Leavesley, D.I., McElwain, D.L.S. & Baker, R.E. Quantifying the roles of cell motility and cell proliferation in a circular barrier assay. *J. R. Soc. Interface.* **10**, 2013007 (2013). (Chapter 2.)
- **Treloar, K.K.**, Simpson, M.J., Haridas, P., Manton, K.J., Leavesley, D.I., McElwain, D.L.S. & Baker, R.E. Multiple types of data are required to identify the mechanisms influencing the spatial expansion of melanoma cell colonies. *BMC Syst. Biol.* **7**, 137 (2013). (Chapter 3.)
- **Treloar, K.K.** & Simpson, M.J. Sensitivity of edge detection methods for quantifying cell migration assays. *PLoS ONE.* **8**, e67389 (2013). (Chapter 4.)
- **Treloar, K.K.**, Simpson, M.J., McElwain, D.L.S. & Baker, R.E. Are *in vitro* estimates of cell diffusivity and cell proliferation rate sensitive to assay geometry? *J. Theor. Biol.* **356**, 71–84 (2014). (Chapter 5.)
- **Treloar, K.K.**, Simpson, M.J., Binder, B.J., McElwain, D.L.S. & Baker, R.E. Assessing the role of spatial correlations during collective cell spreading *Sci. Rep.* **4**, 5713 (2014). (Chapter 6.)

Each chapter of this thesis constitutes a paper, meaning that each chapter can either be read individually or alternatively the chapters can be read as a whole. While the style and layout of each paper has been standardised throughout, the contents of each chapter have been reproduced in this work exactly as they were published. Consequently, this means that there is a cross-over in ideas and there is some overlap between chapters in the details of the experimental and modelling frameworks. The structure of each chapter is comprised of a background section outlining the relevant literature, a methods section detailing the experimental and modelling methods applied in the associated chapter, results and a discussion of the results.

In the next section, we outline the structure of the thesis and in the process outline the novel contributions for each paper.

1.4 Structure of this thesis

The structure of this thesis is as follows. In this chapter, we provided a review of experimental and mathematical modelling studies for collective cell spreading, stated the proposed research questions and outlined the aims of this thesis.

In Chapter 2, we begin by describing a set of experiments to investigate the roles of cell motility and cell proliferation in driving an initially confined fibroblast cell population. We perform two sets of experiments to distinguish between these two mechanisms by suppressing cell proliferation in the first set of experiments and then repeating the experiments with cell proliferation. The experimental data is analysed using two mathematical models; a lattice-based discrete random walk model and a related partial differential equation model. We are able to obtain independent estimates of the cell diffusivity, D , and cell proliferation rate, λ , and confirm that these estimates lead to accurate modelling predictions of the spatial and temporal position of the leading edge of the spreading cell population, as well as the cell density profiles.

Chapter 3 extends the experimental and modelling approach discussed in Chapter 2 to investigate the spread of melanoma cell populations. Cell-to-cell adhesion is thought to be a crucial aspect involved in melanoma cell population spreading and hence we account for this by using a discrete random walk model that incorporates both cell motility, cell proliferation and cell-to-cell adhesion mechanisms. We use multiple types of data to identify the cell diffusivity, D , strength of cell-to-cell adhesion, q , and cell proliferation rate, λ . Our systematic approach indicates that standard types of data, such as the area enclosed by the leading edge, do not provide sufficient information to uniquely identify D , q and λ . In addition, we propose a method to independently quantify the degree of cell-to-cell adhesion in a spreading population.

Throughout Chapters 2 and 3, we estimate the cell diffusivity using information about the position of the leading edge of the spreading cell populations. In each case, we use image analysis tools and make implicit choices about the details of the image analysis methods, such as the threshold applied. Chapter 4 investigates how the detected position of the leading edge varies depending on the choice of threshold in the image analysis algorithm. Our results indicate that the observed spreading rates are very sensitive to the choice of image analysis tools and we show that a standard measure of cell migration can vary by as much as 25% for the same experimental images depending on the details of the image analysis tools. In addition, we obtain a physical interpretation of our edge detection results using a mathematical model. Our modelling indicates that variations in the image threshold parameter correspond to a consistent variation in the local cell density. This means that varying the threshold parameter is equivalent to varying the location of the leading edge in the range of approximately 1–5% of the maximum cell density.

The work presented in Chapters 2 to 4 considers the spread of cell populations in one particular geometry. In Chapter 5 we examine whether the geometry of the *in vitro* assay affects estimates of the cell diffusivity and cell proliferation rate for a population of fibroblast cells. We perform experiments in two distinct geometries: (i) a tumour-like geometry where a cell population spreads outwards into an open space and (ii) a wound-like geometry where a cell population spreads inwards to close a void. Applying the same experimental and modelling approach presented in Chapter 2 and 3, we find that estimates of D and λ are affected by the choice of *in vitro* assay geometry.

In Chapter 6, we explore whether a standard continuum model, which assumes that there is no spatial structure present in the cell population, can be used to describe the spread of melanoma cell populations. We use a combination of discrete simulations and pair correlation functions to illustrate that spatial structure can form in a spreading population of cells either through sufficiently strong cell-to-cell adhesion or sufficiently rapid cell proliferation. We analyse experimental images of the melanoma cell populations using the same pair correlation functions. Our results indicate that the spreading melanoma cell populations remain very close to spatially uniform, suggesting that the strength of cell-to-cell adhesion and the rate of cell proliferation are both sufficiently small so as not to induce any spatial patterning in the spreading populations. Our analysis of the role of spatial correlations in the melanoma cell population suggests that a mean-field model is appropriate to describe the collective spreading of this particular cell line.

Chapter 7 summarises the main findings of this study, and suggests potential avenues of future investigation. Additional details of the research conducted including experimental datasets and some details of the numerical scheme are given in the appendices.

1.5 Statements of joint authorship

In this section, we outline the contributions of the PhD candidate and the co-authors to each paper. All co-authors have consented to the presentation of this material in this thesis.

Chapter 2: Quantifying the roles of cell motility and cell proliferation in a circular barrier assay

For this chapter, the associated published reference is:

Simpson, M.J., **Treloar, K.K.**, Binder, B.J., Haridas, P., Manton, K.J., Leavesley, D.I., McElwain, D.L.S. & Baker, R.E. Quantifying the roles of cell motility and cell proliferation in a circular barrier assay. *J. R. Soc. Interface*. **10**, 2013007 (2013).

Abstract

Moving fronts of cells are essential features of embryonic development, wound repair and cancer metastasis. This paper describes a set of experiments to investigate the roles of random motility and proliferation in driving the spread of an initially-confined cell population. The experiments include an analysis of cell spreading when proliferation was inhibited. Our data have been analysed using two mathematical models: a lattice-based

discrete model and a related continuum partial differential equation model. We obtain independent estimates of the random motility parameter, D , and the intrinsic proliferation rate, λ , and we confirm that these estimates lead to accurate modelling predictions of the position of the leading edge of the moving front as well as the evolution of the cell density profiles. Previous work suggests that systems with a high λ/D ratio will be characterised by steep fronts, whereas systems with a low λ/D ratio will lead to shallow diffuse fronts and this is confirmed in the present study. Our results provide evidence that continuum models, based on the Fisher–Kolmogorov equation, are a reliable platform upon which we can interpret and predict such experimental observations.

Statement of joint authorship

The work was divided as follows:

- Simpson, M.J. initiated the concept for the manuscript, oversaw and directed the research, wrote the manuscript, oversaw drafting and redrafting of several manuscripts, wrote the cover and revision letter, critically reviewed and revised the manuscript, and acted as corresponding author.
- **Treloar, K.K. (Candidate)** implemented the modelling framework, extracted the experimental data, performed all data analysis, composed all figures and supplementary material, and critically reviewed and revised the manuscript.
- Binder, B.J. provided technical assistance, assisted with the interpretation of results and critically reviewed the manuscript.
- Haridas, P. performed the experiments.
- Manton, K.J. and Leavesley, D.I. provided assistance with the experiments and offered biological interpretations.
- McElwain, D.L.S. and Baker, R.E. provided assistance with the interpretation of results and critically reviewed the manuscript.

Chapter 3. Multiple types of data are required to identify the mechanisms influencing the spatial expansion of melanoma cell colonies

For this chapter, the associated published reference is:

Treloar, K.K., Simpson, M.J., Haridas, P., Manton, K.J., Leavesley, D.I., McElwain, D.L.S. & Baker, R.E. Multiple types of data are required to identify the mechanisms influencing the spatial expansion of melanoma cell colonies. *BMC Syst. Biol.* **7**, 137 (2013).

Abstract

The expansion of cell colonies is driven by a delicate balance of several mechanisms including cell motility, cell-to-cell adhesion and cell proliferation. New approaches that can be used to independently identify and quantify the role of each mechanism will help us understand how each mechanism contributes to the expansion process. Standard mathematical modelling approaches to describe such cell colony expansion typically neglect cell-to-cell adhesion, despite the fact that cell-to-cell adhesion is thought to play an important role. We use a combined experimental and mathematical modelling approach to determine the

cell diffusivity, D , cell-to-cell adhesion strength, q , and cell proliferation rate, λ , in an expanding colony of MM127 melanoma cells. Using a circular barrier assay, we extract several types of experimental data and use a mathematical model to independently estimate D , q and λ . In our first set of experiments, we suppress cell proliferation and analyse three different types of data to estimate D and q . We find that standard types of data, such as the area enclosed by the leading edge of the expanding colony and more detailed cell density profiles throughout the expanding colony, does not provide sufficient information to uniquely identify D and q . We find that additional data relating to the degree of cell-to-cell clustering is required to provide independent estimates of q , and in turn D . In our second set of experiments, where proliferation is not suppressed, we use data describing temporal changes in cell density to determine the cell proliferation rate. In summary, we find that our experiments are best described using the range $D = 161 - 243 \mu\text{m}^2/\text{hour}$, $q = 0.3 - 0.5$ (low to moderate strength) and $\lambda = 0.0305 - 0.0398 / \text{hour}$, and with these parameters we can accurately predict the temporal variations in the spatial extent and cell density profile throughout the expanding melanoma cell colony. Our systematic approach to identify the cell diffusivity, cell-to-cell adhesion strength and cell proliferation rate highlights the importance of integrating multiple types of data to accurately quantify the factors influencing the spatial expansion of melanoma cell colonies.

Statement of joint authorship

The work was divided as follows:

- **Treloar, K.K. (candidate)** implemented the methodology, extracted the experimental data, performed all data analysis, wrote the manuscript and supplementary material, composed all figures, critically reviewed and revised the manuscript.
- Simpson, M.J. initiated the concept for the manuscript, oversaw and directed the research, contributed to the writing of the manuscript, oversaw drafting and redrafting of several manuscripts, wrote the cover and revision letter, critically reviewed and revised the manuscript, and acted as corresponding author.
- Haridas, P. performed the experiments.
- Manton, K.J. and Leavesley, D.I. provided assistance with the experiments and offered biological interpretations.
- McElwain, D.L.S. and Baker, R.E. provided assistance with the interpretation of results and critically reviewed the manuscript.

Chapter 4. Sensitivity of edge detection methods for quantifying cell migration assays

For this chapter, the associated published reference is:

Treloar, K.K. & Simpson, M.J. Sensitivity of edge detection methods for quantifying cell migration assays. *PLoS ONE*. **8**, e67389 (2013).

Abstract

Quantitative imaging methods to analyse cell migration assays are not standardised. Here we present a suite of two-dimensional barrier assays describing the collective spreading

of an initially-confined population of 3T3 fibroblast cells. To quantify the motility rate we apply two different automatic image detection methods to locate the position of the leading edge of the spreading population after 24, 48 and 72 hours. These results are compared with a manual edge detection method where we systematically vary the detection threshold. Our results indicate that the observed spreading rates are very sensitive to the choice of image analysis tools and we show that a standard measure of cell migration can vary by as much as 25% for the same experimental images depending on the details of the image analysis tools. Our results imply that it is very difficult, if not impossible, to meaningfully compare previously published measures of cell migration since previous results have been obtained using different image analysis techniques and the details of these techniques are not always reported. Using a mathematical model, we provide a physical interpretation of our edge detection results. The physical interpretation is important since edge detection algorithms alone do not specify any physical measure, or physical definition, of the leading edge of the spreading population. Our modelling indicates that variations in the image threshold parameter correspond to a consistent variation in the local cell density. This means that varying the threshold parameter is equivalent to varying the location of the leading edge in the range of approximately 1–5% of the maximum cell density.

Statement of joint authorship

The work was divided as follows:

- **Treloar, K.K. (candidate)** implemented the methodology, extracted the experimental data, performed all data analysis, composed all figures, wrote the manuscript, composed all figures, critically reviewed and revised the manuscript.
- Simpson, M.J. initiated the concept for the manuscript, oversaw and directed the research, contributed to the writing of the manuscript, oversaw drafting and redrafting of several manuscripts, wrote the cover and revision letter, critically reviewed and revised the manuscript, and acted as corresponding author.

Chapter 5. Are *in vitro* estimates of cell diffusivity and cell proliferation rate sensitive to assay geometry?

For this chapter, the associated published reference is:

Treloar, K.K., Simpson, M.J., McElwain, D.L.S. & Baker, R.E. Are *in vitro* estimates of cell diffusivity and cell proliferation rate sensitive to assay geometry? *J. Theor. Biol.* **356**, 71–84 (2014).

Abstract

Cells respond to various biochemical and physical cues during wound-healing and tumour progression. *In vitro* assays used to study these processes are typically conducted in one particular geometry and it is unclear how the assay geometry affects the capacity of cell populations to spread, or whether the relevant mechanisms, such as cell motility and cell proliferation, are somehow sensitive to the geometry of the assay. In this work we use a circular barrier assay to characterise the spreading of cell populations in two

different geometries. Assay 1 describes a tumour-like geometry where a cell population spreads outwards into an open space. Assay 2 describes a wound-like geometry where a cell population spreads inwards to close a void. We use a combination of discrete and continuum mathematical models and automated image processing methods to obtain independent estimates of the effective cell diffusivity, D , and the effective cell proliferation rate, λ . Using our parameterised mathematical model we confirm that our estimates of D and λ accurately predict the time-evolution of the location of the leading edge and the cell density profiles for both assay 1 and assay 2. Our work suggests that the effective cell diffusivity is up to 50% lower for assay 2 compared to assay 1, whereas the effective cell proliferation rate is up to 30% lower for assay 2 compared to assay 1.

Statement of joint authorship

The work was divided as follows:

- **Treloar, K.K. (candidate)** implemented the methodology, performed all data analysis, wrote the manuscript and supplementary material, composed all figures, contributed to the writing of the revision letter, critically reviewed and revised the manuscript.
- Simpson, M.J. initiated the concept for the manuscript, oversaw and directed the research, oversaw drafting and redrafting of several manuscripts, wrote the cover and revision letter, critically reviewed and revised the manuscript, and acted as corresponding author.
- McElwain, D.L.S. and Baker, R.E. provided assistance with the interpretation of results and critically reviewed the manuscript.

Chapter 6. Assessing the role of spatial correlations during collective cell spreading

For this chapter, the associated published reference is:

Treloar, K.K., Simpson, M.J., Binder, B.J., McElwain, D.L.S. & Baker, R.E. Assessing the role of spatial correlations during collective cell spreading *Sci. Rep.* **4**, 5713 (2014).

Abstract

Spreading cell fronts are essential features of development, repair and disease processes. Many mathematical models used to describe the motion of cell fronts, such as Fisher's equation, invoke a mean-field assumption which implies that there is no spatial structure, such as cell clustering, present. Here, we examine the presence of spatial structure using a combination of *in vitro* circular barrier assays, discrete random walk simulations and pair correlation functions. In particular, we analyse discrete simulation data using pair correlation functions to show that spatial structure can form in a spreading population of cells either through sufficiently strong cell-to-cell adhesion or sufficiently rapid cell proliferation. We analyse images from a circular barrier assay describing the spreading of a population of MM127 melanoma cells using the same pair correlation functions. Our results indicate that the spreading melanoma cell populations remain very close to spatially uniform, suggesting that the strength of cell-to-cell adhesion and the rate of cell

proliferation are both sufficiently small so as not to induce any spatial patterning in the spreading populations.

Statement of joint authorship

The work was divided as follows:

- **Treloar, K.K.** implemented the methodology, performed all data analysis, wrote the manuscript, supplementary material, cover letter and revision letter, composed all figures, revised the manuscript and acted as corresponding author under the guidance of Simpson, M.J.
- Simpson, M.J initiated the concept for the manuscript, oversaw and directed the research, oversaw drafting and redrafting of several manuscripts, critically reviewed and revised the manuscript.
- Binder, B.J., McElwain, D.L.S. and Baker, R.E. provided assistance with the interpretation of results and critically reviewed the manuscript.

CHAPTER 2

Quantifying the roles of cell motility and cell proliferation in a circular barrier assay

A paper published in the *Journal of the Royal Society Interface*.

Simpson, M.J., Treloar, K.K., Binder, B.J., Haridas, P., Manton, K.J., Leavesley, D.I., McElwain, D.L.S. & Baker, R.E. Quantifying the roles of cell motility and cell proliferation in a circular barrier assay. *J. R. Soc. Interface*. **10**, 2013007 (2013).

Abstract

Moving fronts of cells are essential features of embryonic development, wound repair and cancer metastasis. This paper describes a set of experiments to investigate the roles of random motility and proliferation in driving the spread of an initially-confined cell population. The experiments include an analysis of cell spreading when proliferation was inhibited. Our data have been analysed using two mathematical models: a lattice-based discrete model and a related continuum partial differential equation model. We obtain independent estimates of the random motility parameter, D , and the intrinsic proliferation rate, λ , and we confirm that these estimates lead to accurate modelling predictions of the position of the leading edge of the moving front as well as the evolution of the cell density profiles. Previous work suggests that systems with a high λ/D ratio will be characterised by steep fronts, whereas systems with a low λ/D ratio will lead to shallow diffuse fronts and this is confirmed in the present study. Our results provide evidence that continuum models, based on the Fisher–Kolmogorov equation, are a reliable platform upon which we can interpret and predict such experimental observations.

2.1 Background

Spatial spreading of cell populations, characterised by moving fronts, is essential for development [159], tissue repair [85, 86] and disease progression [132]. Many kinds of experimental observations can be made to characterise cell spreading, including measuring front speed [85, 86], recording time-lapse observations [159], or measuring properties of various subpopulations [98, 118].

The formation of moving cell fronts can be thought of as an emergent population-level outcome driven by individual-level properties of cells within the population [53]. For such a system it is relevant to ask whether we can predict how differences in cell behaviour, such as a change in the relative frequency of motility and proliferation events, affects the emergent properties. This is important if we consider designing intervention strategies aimed at manipulating the front speed [30]. To design such interventions, we must first be able to identify, and quantify, the various components of cell behaviour that lead to moving fronts so that we can begin to understand how to manipulate these components to obtain a particular outcome.

The standard continuum model used to represent cell spreading is

$$\frac{\partial \bar{c}}{\partial t} = D \nabla^2 \bar{c} + \lambda \bar{c} \left(1 - \frac{\bar{c}}{K}\right), \quad (2.1)$$

where $\bar{c}(r, t)$ is the cell density, D is the cell diffusivity (random motility coefficient), λ is the intrinsic proliferation rate and K is the carrying-capacity density [97, 116]. In one-dimensional Cartesian geometry, Equation (2.1) simplifies to the Fisher–Kolmogorov equation [42] which has constant shape travelling wave solutions, $C(z) = \bar{c}(x - st)$, moving at constant speed s [85, 86, 97]. The front speed approaches $s = \sqrt{4D\lambda}$ as $t \rightarrow \infty$ for initial conditions with compact support [97]. Variations of the Fisher–Kolmogorov equation, incorporating directed motility [104] or nonlinear diffusion [20, 155], also have travelling wave solutions and different relationships between the wave speed and the model parameters can be derived for these generalisations. Other options for modelling cell spreading processes include using discrete approaches that are related to Equation (2.1) in an appropriate limit [120]. Discrete models have the advantage that they produce discrete stochastic data that are similar to experimental images and movies [27], as well as having a formal mathematical relationship with continuum models, such as Equation (2.1) [21, 33, 120].

Many choices of λ and D in the Fisher–Kolmogorov equation give the same asymptotic front speed, $s = \sqrt{4D\lambda}$. This property was demonstrated by Maini and coworkers [85, 86], who measured the front speed in a scrape assay and showed that several reasonable choices of λ and D could be used to match the front speed. Other approaches to identifying parameters have used measurements of the cell density profile, $\bar{c}(r, t)$. For example, Sengers and coworkers [113, 114] fitted the solution of a reaction–diffusion equation to experimental density profiles to match the experimental data [113, 114]. Similarly, Sherratt and Murray [116] studied a wound healing experiment and chose the parameters in two

different reaction–diffusion equations so that both models predicted the observed closure rates. The disadvantage of fitting the solution of mathematical models to cell density information alone is that this does not necessarily ensure that the parameterised model can make independent predictions. One way to overcome this is to collect different types of experimental data so that the process of model calibration can be separated from the process of model prediction.

In addition to making experimental observations of the position of a moving front of cells, here we study the shape of the moving front to understand how the relative roles of cell motility and cell proliferation affect these details. We study the details of the leading edge since the shape of the moving front is thought to have clinical implications. For example, in the context of glioma invasion, Swanson [132] discusses the difference between shallow-fronted tumours (low λ/D ratio) and sharp-fronted tumours (high λ/D ratio) [132]. These differences are relevant when considering surgical removal since the boundary between the tumour tissue and normal tissue is increasingly difficult to detect as the front becomes more diffuse [96,132]. The shape of the leading edge is also of interest in the context of melanoma progression where visual inspection of the invading cancer, including the details of the leading edge, is thought to provide important information about the aggressiveness of the tumour [59].

In this work we investigate how cell motility and proliferation controls the position and shape of the leading edge of a two-dimensional cell spreading system. Using a circular *barrier assay*, we perform experiments that provide independent estimates of D and λ . We then make separate modelling predictions with regard to the position and shape of the leading edge. We investigate how the relative roles of motility and proliferation affects the spreading by performing two parallel sets of experiments. In the first we consider cell spreading driven by motility without proliferation, whereas in the second consider cell spreading driven by combined motility and proliferation. All experimental observations are repeated at three different initial cell densities.

2.2 Experimental methods

2.2.1 Cell culture

Murine fibroblast cells (3T3 cells) were cultured in Dulbecco’s modified Eagle medium (Invitrogen, Australia) with 5% fetal calf serum (FCS) (Hyclone, New Zealand), 2 mM L-glutamine (Invitrogen) and 1% v/v Penicillin/Streptomycin (Invitrogen) in 5% CO₂ at 37°C. Monolayers of 3T3 cells were cultured in T175 cm² tissue culture flasks (Nunc, Thermo Scientific, Denmark).

2.2.2 Barrier assay

We use a barrier assay since several studies claim that they are more reproducible than a scrape assay [69, 145]. Metal–silicone barriers, 6000 μm in diameter (Aix Scientifics, Germany), were cleaned, sterilised, dried and placed in the centre a 24-well tissue culture plate with 500 μL culture medium. Each well in the tissue culture plate has a diameter

of 15,600 μm . The plate was placed at 37°C in a humidified incubator at 5% CO₂ for one hour to allow the barriers to attach to the surface of the tissue culture plate. Cells were lifted just prior to confluence using 0.05% trypsin (Invitrogen, Australia). Viable cells were counted using a Trypan blue exclusion test and a haemocytometer.

Three different densities of cell suspension were used: 5,000, 10,000 and 30,000 cells/100 μL . The cell suspension was carefully introduced in the barrier so that the cells were approximately evenly distributed. Once seeded, the tissue culture plate was placed in an incubator. Mitomycin-C (Sigma Aldrich, Australia), an inhibitor of cell proliferation, 10 $\mu\text{g}/\text{mL}$, was added to some cell solutions for four hours. After allowing the cells to attach for one hour, the barriers were removed and the cell layer was washed with serum free medium (SFM; culture medium without FCS) and replaced with 0.5 mL of culture medium. The attachment time was varied, we found one hour was sufficient to prevent cells washing off the plate when the cell layer was washed with SFM. Plates were incubated at 37°C, 5% CO₂, for four different times, $t = 0, 24, 48$ and 72 hours. Each assay, for each initial density, was repeated three times ($n = 3$).

2.2.3 Cell staining

Two staining techniques were used to analyse these experiments:

- (i) Population-scale images were obtained by fixing the cells with 10% formalin, followed by 0.01% crystal violet (Sigma–Aldrich, Australia). The stain was rinsed with phosphate-buffered saline (Invitrogen, Australia) and the plates were air-dried. Images were taken on a stereo microscope with a Nikon digital camera (DXM1200C).
- (ii) Individual-scale images were obtained by fixing the cells with 10% formalin, then made permeable using ice-cold 70% ethanol and the nucleus stained with propidium iodide (PI), 1 mg/ml (Invitrogen, Australia). Images were taken using a Laborlux fluorescence microscope with a Nikon digital camera (DXM1200C) at 100x magnification. Overlapping images were taken to reconstruct both horizontal and vertical transects through the spreading population.

2.2.4 Image analysis

The average cell diameter, Δ , was estimated using Leica LAS AF Lite software (Appendix A). All other image analysis was performed using customised software written with MATLAB's Image Processing Toolbox (v7.12) [90] (Appendix A). In summary, to estimate the location of the leading edge of the spreading populations, edge detection and image segmentation algorithms were used to identify and isolate the entire cell population from the background of the image. To count cell numbers in the PI-stained images, we assumed that each cell corresponds to a distinct identifiable region in the image. Each cell was automatically identified. For some images, at high cell density, we found that a relatively small number of cells had to be manually identified and counted.

2.3 Modelling methods

2.3.1 Discrete model

An interacting random walk model with proliferation is used to simulate the experiments. The model is interacting in the sense that it permits only one agent to occupy each lattice site so that the model incorporates volume exclusion and finite size effects [21, 33, 120, 123]. We take the most straightforward modelling approach by implementing the discrete model on a two-dimensional square lattice with spacing Δ . We could use a more sophisticated lattice-based [9, 15] or lattice-free [19, 27, 105] modelling approach; however, given that this is the first time that a mathematical model has been used to separately quantify the parameters governing cell migration and cell proliferation in a barrier assay, it is reasonable to take a parsimonious modelling approach. In our discrete simulations each site is indexed (i, j) , where $i, j \in \mathbb{Z}^+$, and each site has position $(x, y) = (i\Delta, j\Delta)$. A random sequential update method [24] is used to perform the simulations using a von Neumann neighbourhood [71]. If there are $N(t)$ agents at time t , during the next time step of duration τ , $N(t)$ agents are selected at random and given the opportunity move with probability $P_m \in [0, 1]$. The random sequential update method means that not all the $N(t)$ agents are always selected in every step, and sometimes a particular agent will be selected more than once per time step. Our experiments indicate that the initially-circular region maintains a circular shape (Section 2.4), therefore we implement an unbiased mechanism where an agent at (x, y) attempts to step to $(x \pm \Delta, y)$ or $(x, y \pm \Delta)$ with equal probability. Once the $N(t)$ potential motility events have been assessed, another $N(t)$ agents are selected at random and given the opportunity to proliferate with probability $P_p \in [0, 1]$. We model proliferation with an unbiased mechanism whereby a proliferative agent at (x, y) attempts to deposit a daughter agent at $(x \pm \Delta, y)$ or $(x, y \pm \Delta)$, with each target site chosen with equal probability. Potential motility and proliferation events that would place an agent on an occupied site are aborted [21, 33, 120]. We note that there are no differences in the averaged behaviour for simulations in which $N(t)$ agents are selected at random during the time step of duration τ , or whether all $N(t)$ agents are selected at random [120].

2.3.2 Continuum model

In the k^{th} identically-prepared realisation the occupancy of site (i, j) is denoted $C_{i,j}^k$, with $C_{i,j}^k = 1$ for an occupied site, and $C_{i,j}^k = 0$ for a vacant site. If the average occupancy of site (i, j) , evaluated for M identically-prepared realisations, is $\langle C_{i,j} \rangle = (1/M) \sum_{k=1}^M C_{i,j}^k$, the corresponding continuous density, $\bar{c}(r, t)$, is governed by Equation (2.1) [120] with $K = 1$, where $\lambda = \lim_{\Delta, \tau \rightarrow 0} (P_p/\tau)$ and $D = \lim_{\Delta, \tau \rightarrow 0} (P_m \Delta^2 / 4\tau)$ [120]. Here, $\langle C_{i,j} \rangle \in [0, 1]$, is equivalent to $\bar{c}(r, t)$ as M becomes sufficiently large, provided that the ratio P_p/P_m is sufficiently small. This mathematical relationship allows us to use the averaged data from the discrete model and the solution of Equation (2.1) interchangeably, provided that

P_p/P_m is sufficiently small. We do not discuss this equivalence here since it has been analysed, in detail, previously [120].

To interpret our experimental data using Equation (2.1), we obtain numerical solutions (Appendix A) of

$$\frac{\partial c}{\partial t} = D \left(\frac{\partial^2 c}{\partial r^2} + \frac{1}{r} \frac{\partial c}{\partial r} \right) + \lambda c (1 - c), \quad (2.2)$$

which is equivalent to Equation (2.1) in an axisymmetric geometry where the dimensional cell density, $\bar{c}(r, t)$, has been scaled relative to the carrying capacity density, $c(r, t) = \bar{c}(r, t)/K$, with $c(r, t) \in [0, 1]$. Numerical solutions are obtained on $0 \leq r \leq 7,800 \mu\text{m}$, with zero flux boundary conditions at $r = 0 \mu\text{m}$ and at $r = 7,800 \mu\text{m}$. The initial condition for all numerical solutions is given by

$$c(r, 0) = \begin{cases} c_0, & 0 \leq r < 3,000 \mu\text{m}, \\ 0, & 3,000 \leq r \leq 7,800 \mu\text{m}, \end{cases} \quad (2.3)$$

where c_0 is the initial density of cells inside the barrier.

2.4 Results

2.4.1 Carrying capacity density estimate

Images of individual cells were acquired, and Leica software was used to obtain measurements of the cell diameter of cells ($n = 15$), giving $\Delta \simeq 25 \mu\text{m}$ (Appendix A). We estimated the carrying capacity density, K , by calculating the maximum packing density of circular disk-like cells on a two-dimensional square lattice. Since, $\Delta \simeq 25 \mu\text{m}$, we have $K = 1/25^2 \approx 1.6 \times 10^{-3} \text{ cells}/\mu\text{m}^2$.

2.4.2 Cell motility estimates

In our initial analysis we assume that there is no proliferation. Assays were conducted using three different initial cell densities by placing 5,000, 10,000 or 30,000 cells inside the barriers after Mitomycin-C pretreatment. Each experiment, at each initial density, was repeated three times ($n = 3$). Snapshots in Figure 2.1 show that the spreading population maintains an approximately circular shape. We used image analysis software (Section 2.2, Appendix A) to quantify the increase in size of the region enclosed by the leading edge of the spreading population. The location of the leading edge, determined by our image analysis software, is superimposed in Figure 2.1 (a)–(d). We converted the area estimates into an equivalent circular diameter, d , giving $d = 6,080, 6,600, 7,060$ and $7,540 \mu\text{m}$ after $t = 0, 24, 48$ and 72 hours, respectively. Equivalent results for the experiments where 5,000 and 30,000 cells were placed in the barriers are given in Appendix A.

To model this spreading behaviour we used the discrete model with $\Delta = 25 \mu\text{m}$, $P_p = 0$ and $P_m = 1$. Simulations were performed on a lattice of size 624×624 , whose dimensions were chosen so that the width of the lattice was equal to the $15,600 \mu\text{m}$ diameter of well in the 24-well plate, $15,600/25 = 624$. To initialise the simulations, agents were placed uniformly inside a circle of diameter $6,000 \mu\text{m}$. The centre of the circle was placed at

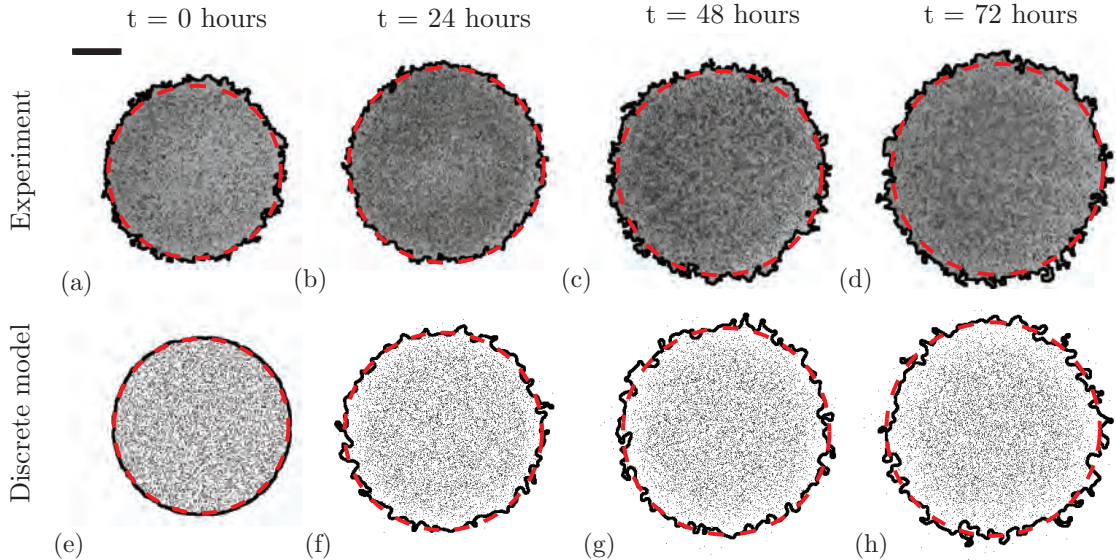


Figure 2.1: Experimental images in (a)–(d) show a barrier assay where 10,000 cells were initially placed uniformly within the barrier after pretreatment with Mitomycin-C. Images in (a)–(d) correspond to $t = 0, 24, 48$ and 72 hours, respectively. The black (solid) line indicates the position of the leading edge detected by the image analysis software. The area enclosed by the leading edge was converted to an equivalent circular diameter giving $d = 6,060, 6,600, 7,060$ and $7,540\ \mu\text{m}$ in (a)–(d), respectively. Images in (e)–(h) correspond to snapshots from the discrete model on a 624×624 lattice with $\Delta = 25\ \mu\text{m}$. Simulations were performed by initially placing 10,000 agents uniformly inside a circular region of diameter $6,000\ \mu\text{m}$, and the system evolved with $P_m = 1$, $P_p = 0.0$ and $\tau = 0.09191$ hours. The leading edge of the simulated spreading population is shown by the black (solid) line. Here, D was chosen so that the area enclosed by the leading edge of the simulated population is, on average, equal to the area enclosed by the leading edge of the population in the corresponding experimental images. The red curves (dashed) in (a)–(h) correspond to the $c(r,t) = 0.017$ contour of the numerical solution of Equation (2.2) with $\lambda = 0$ and $D = 1,700\ \mu\text{m}^2/\text{hour}$. The scale bar corresponds to $1,500\ \mu\text{m}$.

the centre of the lattice, which is equivalent to placing the $6,000\ \mu\text{m}$ barrier in the centre of the $15,600\ \mu\text{m}$ well. The circular region representing the barrier has a diameter of $6,000/25 = 240$ lattice sites, containing $\pi(240)^2/4 \approx 45,239$ lattice sites. To model the three different initial cell densities, simulations were initiated by placing either 5,000, 10,000 or 30,000 agents uniformly, at random, across these 45,239 lattice sites. Zero flux boundary conditions were imposed, and the model was used to perform simulations until $t = 0, 24, 48$ and 72 hours.

To calibrate the discrete model we performed simulations of each experiment with $P_m = 1$ which gives, on average, an isolated agent an opportunity to undergo a motility event during each time step. We systematically varied the duration of the time step τ [121], which is equivalent to varying D . For 25 different values of D in the range $D \in [100, 5000]\ \mu\text{m}^2/\text{hour}$, each experiment was simulated three times ($n = 3$) and the image analysis software was used to locate the position of the leading edge in the discrete snapshots in exactly the same way that the leading edge was located in the experimental images. This gave us an estimate of the area enclosed by the leading edge for the simulated spreading populations at $t = 24, 48$ and 72 hours allowing us to find an optimal value of D to match the experiments (Appendix A). Results in Figure 2.1 (e)–(h) show snapshots from a single realisation of the calibrated discrete model together with the leading edge. Similar results

were obtained for the experiments with 5,000 and 30,000 cells (Appendix A). In summary, we found estimates of the diffusivity to be $D = 1,500, 1,700$ and $2,900 \mu\text{m}^2/\text{hour}$ for the 5,000, 10,000 and 30,000 cell experiments, respectively.

We also quantitatively model the spreading behaviour in Figure 2.1 using Equation (2.2). One way to do this is to solve Equation (2.2), using our estimates of D with $\lambda = 0$, and choose a particular contour of the solution, $c(r, t) = c^*$, that matches the average spreading observed in the experiments. Choosing $c^* = 0.017$ matches the experimental measurements (Appendix A). To demonstrate the efficacy of our approach, we superimpose the $c^* = 0.017$ contour of the solutions of Equation (2.2) on the images in Figure 2.1. Equivalent results for the 5,000 and 30,000 experiments are summarised in Appendix A.

Our approach to estimate D used the image analysis software to calibrate the discrete model. Using our estimates of D , we chose the contour of the solution of Equation (2.2), with $\lambda = 0$, so that the position of the leading edge, determined by the image analysis software, matched the solution of Equation (2.2). Without the image analysis software, it is not obvious how to interpret the image data in Figure 2.1 using the solution of Equation (2.2) since we do not know in advance which contour of the solution corresponds to the leading edge of the spreading populations. Here, we overcome this by applying the same image analysis technique to both the experimental images and the discrete snapshots.

2.4.3 Cell proliferation estimates

Previously, we assumed that Mitomycin-C pretreatment prevents cell proliferation [112, 133] and we now test this by quantifying the observed proliferation rate in the experiments. Assays were performed in triplicate ($n = 3$) for each initial cell density of 5,000, 10,000 and 30,000 cells. We used PI staining and higher magnification images to identify the nucleus of individual cells allowing us to estimate the temporal changes in the cell density in the central region of the assay. In each experimental replicate we recorded snapshots of four square subregions of dimension $400 \mu\text{m} \times 400 \mu\text{m}$. This means we analysed 16 square subregions for each initial density. The approximate location of the subregions is shown in Figure 2.2 (a), confirming that they were located away from the leading edge so that the cells were approximately uniformly distributed within each subregion.

Images in Figure 2.2 (d)–(g) show snapshots of the cells in a central subregion after Mitomycin-C pretreatment indicating that the number of cells does not change significantly with time. These images indicate that the diameter of the cell nucleus appears to increase with time, on average over $t = 72$ hours, from approximately $16\mu\text{m}^2$ to $25\mu\text{m}^2$. However it is unclear whether the size of the cells also increases with time as the PI staining highlights the cell nucleus rather than the cell cytoplasm. Images in Figure 2.2 (h)–(k) show an identically-prepared experiment without Mitomycin-C pretreatment where the number of cells increases dramatically with time, and there is no obvious change in the size of the cell nucleus.

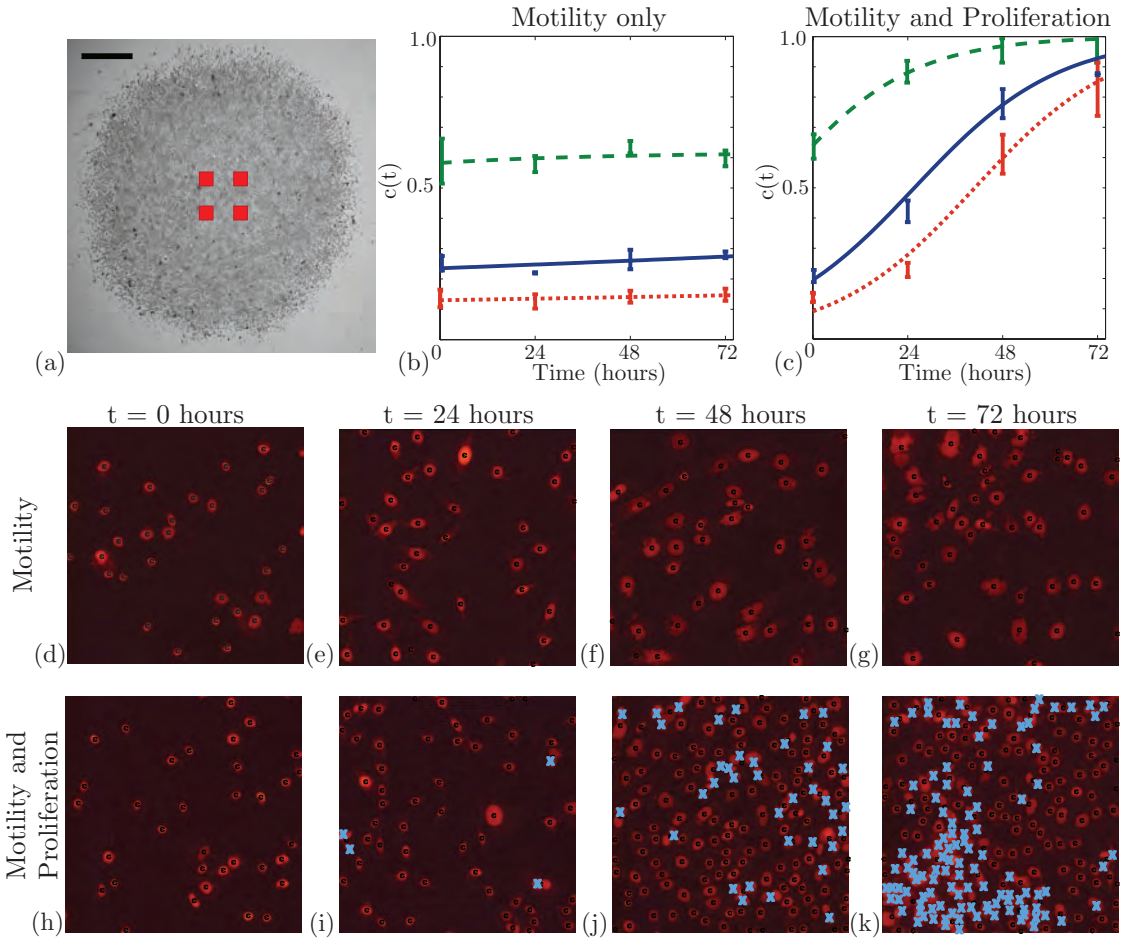


Figure 2.2: Proliferation in the barrier assay was quantified by counting the number of cells in four different subregions in each experimental replicate. The relative size and approximate location of the subregions are shown in (a), where the scale bar corresponds to 1,500 μm . The number of cells in the subregions were counted, and the corresponding time evolution of the mean scaled cell density is shown in (b)–(c), with error bars indicating one standard deviation from the mean. Red (dotted), blue (solid) and green (dashed) curves in (b)–(c) correspond to appropriately-parameterised logistic growth curves for the experiments where 5,000, 10,000 and 30,000 cells were placed initially in the barrier, respectively. Images in (d)–(g) show four subregions, of dimensions 400 $\mu\text{m} \times 400 \mu\text{m}$, for the experiment where 5,000 cells were initially placed inside the barrier after pretreatment with Mitomycin–C. The images in (d)–(g) correspond to $t = 0, 24, 48$ and 72 hours, respectively. The PI-staining shows the cells in red. Black dots indicate cells that were automatically identified using the image analysis software. Results in (h)–(k) show equivalent images from an experiment without Mitomycin–C pretreatment. The blue crosses in (i)–(k) indicate cells that were manually counted.

To quantify the differences between Figure 2.2 (d)–(g) and Figure 2.2 (h)–(k), we plot the nondimensional cell density in Figures 2.2 (b)–(c). We observe that the cell density in the experiments without Mitomycin–C pretreatment increased rapidly over time. To quantify the growth, we note that Equation (2.2) can be simplified when the cell density, $c(r, t)$, is spatially uniform so that locally we have $c(r, t) = c(t)$. Under these conditions Equation (2.2) simplifies to the logistic equation:

$$\frac{dc}{dt} = \lambda c(1 - c), \quad (2.4)$$

which has the solution

$$c(t) = \frac{c(0)e^{\lambda t}}{1 + c(0)(e^{\lambda t} - 1)}, \quad (2.5)$$

where $c(t) \in [0, 1]$. We used a line search to choose the optimal value of λ that minimised the least-squares error between our measurements, in Figure 2.2 (b)–(c), and the solution of the logistic equation (Appendix A). This gave $\lambda = 0.0561$ /hour for the experiment with 5,000 cells without Mitomycin–C pretreatment and $\lambda = 0.0016$ /hour for the equivalent experiment with Mitomycin–C pretreatment, confirming that Mitomycin–C pretreatment prevented proliferation and justifies our modelling assumption in Figure 2.1 where we set $P_p = 0$. Equivalent measurements were repeated for the experiments with 10,000 and 30,000 cells, and the relevant logistic growth curves are superimposed in Figure 2.2 (b)–(c). For these experiments we found $\lambda = 0.0552$ /hour for the 10,000 cell experiment without Mitomycin–C pretreatment, and $\lambda = 0.0021$ /hour for the equivalent experiment with Mitomycin–C pretreatment. Similarly, our results indicate $\lambda = 0.0594$ /hour for the 30,000 cell experiment without Mitomycin–C pretreatment, and $\lambda = 0.0026$ /hour for the 30,000 cell experiment with Mitomycin–C pretreatment.

2.4.4 Position of the leading edge

We now test whether our estimates of D and λ lead to accurate predictions of the time evolution of the position of the leading edge of the spreading populations. Experimental images in Figure 2.3 show the distribution of cells at $t = 0$, and compare the distribution after 72 hours both with, and without, Mitomycin–C pretreatment. The extent of the spreading is significantly larger in the proliferative populations. To quantify these differences, we make predictions using Equation (2.2) and Equation (5.6), with c_0 chosen to approximate the different initial cell densities. For the experiments with 5,000 cells initially we have $c_0 = 5,000/45,239 \approx 0.11$; similarly for 10,000 and 30,000 cells initially we have $c_0 \approx 0.22$ and $c_0 \approx 0.66$, respectively. Using these initial conditions, and our estimates of D , we solved Equation (2.2) with $\lambda = 0$ to match the experiments where proliferation was suppressed, and we superimpose the $c(r, t) = 0.017$ contour of the solution at $t = 72$ hours onto the images in the second column in Figure 2.3. For the same initial conditions, we used the previously-determined values of D and λ to solve Equation (2.2) and the relevant contours are superimposed in the third column of Figure 2.3. A visual comparison of the experimental images and the numerical solutions of Equation (2.2) in Figure 2.3 indicates that the modelling prediction of the position of the leading edge accurately captures the observed spreading. The comparison of the modelling and experimental results in Figure 2.3 involved no calibration, indicating that our modelling framework can make reasonably accurate predictions of the experimental observations.

We analysed the remaining images at $t = 0, 24$ and 48 hours, using the same procedure, to produce equivalent results shown in the fourth column of Figure 2.3. For each experiment we superimpose the predicted diameter of the spreading population using the $c(r, t) = 0.017$ contour of the relevant solution of Equation (2.2). Comparing the partial differential equation solution with the experimental results illustrates that the modelling framework reliably predicts the observed spreading patterns. The match between the modelling

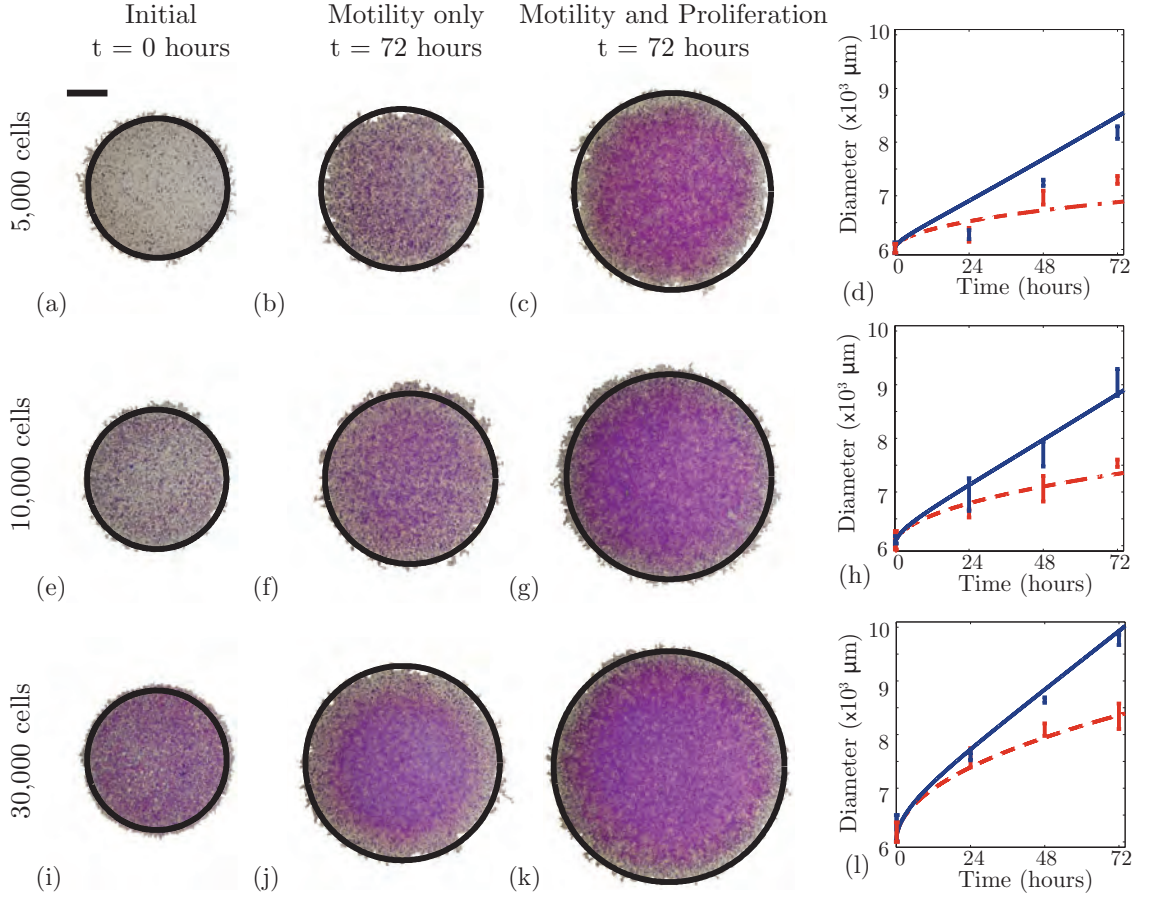


Figure 2.3: The position of the leading edge was determined by analysing experimental images for the experiments with 5,000, (a)–(d), 10,000, (e)–(h) and 30,000, (i)–(l) cells initially. Images are shown at $t = 0$ (first column), at $t = 72$ hours for the experiments with Mitomycin-C pretreatment (second column) and at $t = 72$ hours for the experiments without Mitomycin-C pretreatment (third column). In each image the $c(r, t) = 0.017$ contour of the relevant solution of Equation (2.2) is superimposed in black (solid) on the spreading population and the scale bar represents 1,500 μm . Results in (d), (h) and (l) show the mean diameter ($n = 3$) calculated from experimental images at $t = 0, 24, 48$ and 72 hours, with the error bars representing one standard deviation from the mean. The curves in (d), (h) and (l) represent the time evolution of the position of the $c(r, t) = 0.017$ contour of the relevant solution of Equation (2.2). The blue (solid) curves correspond to spreading driven by combined motility and proliferation whereas the red (dashed) curves correspond to spreading by motility only. The numerical solution of Equation (2.2) correspond to $\delta r = 1.0 \mu\text{m}$, $\delta t = 0.005$ hours and $\epsilon = 1 \times 10^{-6}$.

prediction and the experimental measurements improves as the initial numbers of cells increases which could indicate that our parameter estimates are more reliable for the experiments with larger numbers of cells present.

For all experimental conditions in Figure 2.3, we observe that cell spreading driven by combined motility and proliferation occurs faster than in the equivalent experiment without proliferation. We observe a separation of timescales in the data as the difference between the diameter for the experiments with combined motility and proliferation, and the experiments without proliferation, are minimal at relatively short times, $t < 24$ hours. Over longer timescales, the influence of proliferation is more pronounced. For example, with 30,000 cells initially, the diameter of the proliferative spreading population is very similar to the diameter of the nonproliferative spreading population at $t = 24$ hours. Conversely,

the diameter of the experiment with proliferation is approximately $1,500 \mu\text{m}$ larger than the diameter of the equivalent experiment without proliferation after $t = 72$ hours. These differences indicate that cell migration takes place over a relatively short timescale whereas proliferation takes place over much longer timescales. With our estimates of D and λ , the corresponding ratio P_p/P_m in the discrete model is $P_p/P_m \approx 2 \times 10^{-3}$ indicating that, on average, an isolated uncrowded cell will undergo approximately 500 motility events for each proliferation event. Since $P_p/P_m \ll 1$, the effects of proliferation in the discrete simulations, or equivalent solutions of Equation (2.2), will be insignificant over relatively short timescales.

Our estimates of D and λ allow us to predict the long term front speed for the proliferative populations. Formally, Equation (2.2) does not support travelling wave solutions [97, 156]. However, the asymptotic result for the Fisher–Kolmogorov equation is approximately valid in an axisymmetric radial geometry for sufficiently large r [97]. For our parameter estimates, the mean front speed predicted by the Fisher–Kolmogorov equation, $s = \sqrt{4\lambda D}$, is $s = 18.3$ (16.3–24.6), 19.4 (13.8–22.1) and 26.2 (23.0–31.7) $\mu\text{m}/\text{hour}$, for the results with 5,000, 10,000 and 30,000 cells placed initially in the barrier. Here, the uncertainty in the prediction of s was estimated using our estimates of the uncertainty in D and λ (Appendix A). To test this prediction, we fit a straight line to the mean data in Figure 2.3 (d), (h) and (l), describing the time evolution of the diameter of the spreading proliferative populations, giving $s = 15.7$ (15.0–16.5), 20.1 (18.7–21.6) and 23.6 (23.0–24.1) $\mu\text{m}/\text{hour}$ for the results with 5,000, 10,000 and 30,000 cells placed initially in the barrier, respectively. The uncertainty in s was calculated by fitting straight lines to the mean data at $t = 0$ and the upper and lower bound, defined by the error bars in Figure 2.3 (d), (h) and (l), at $t > 0$. Given that our experiments are made over relatively short timescales in an axisymmetric radial geometry, it is remarkable that the Fisher–Kolmogorov prediction is relatively accurate. We also note that front speed measurements can depart from the Fisher–Kolmogorov result due to the effects of stochastic fluctuations [61, 62], which we have not quantified, but could be measured in future experimental investigations.

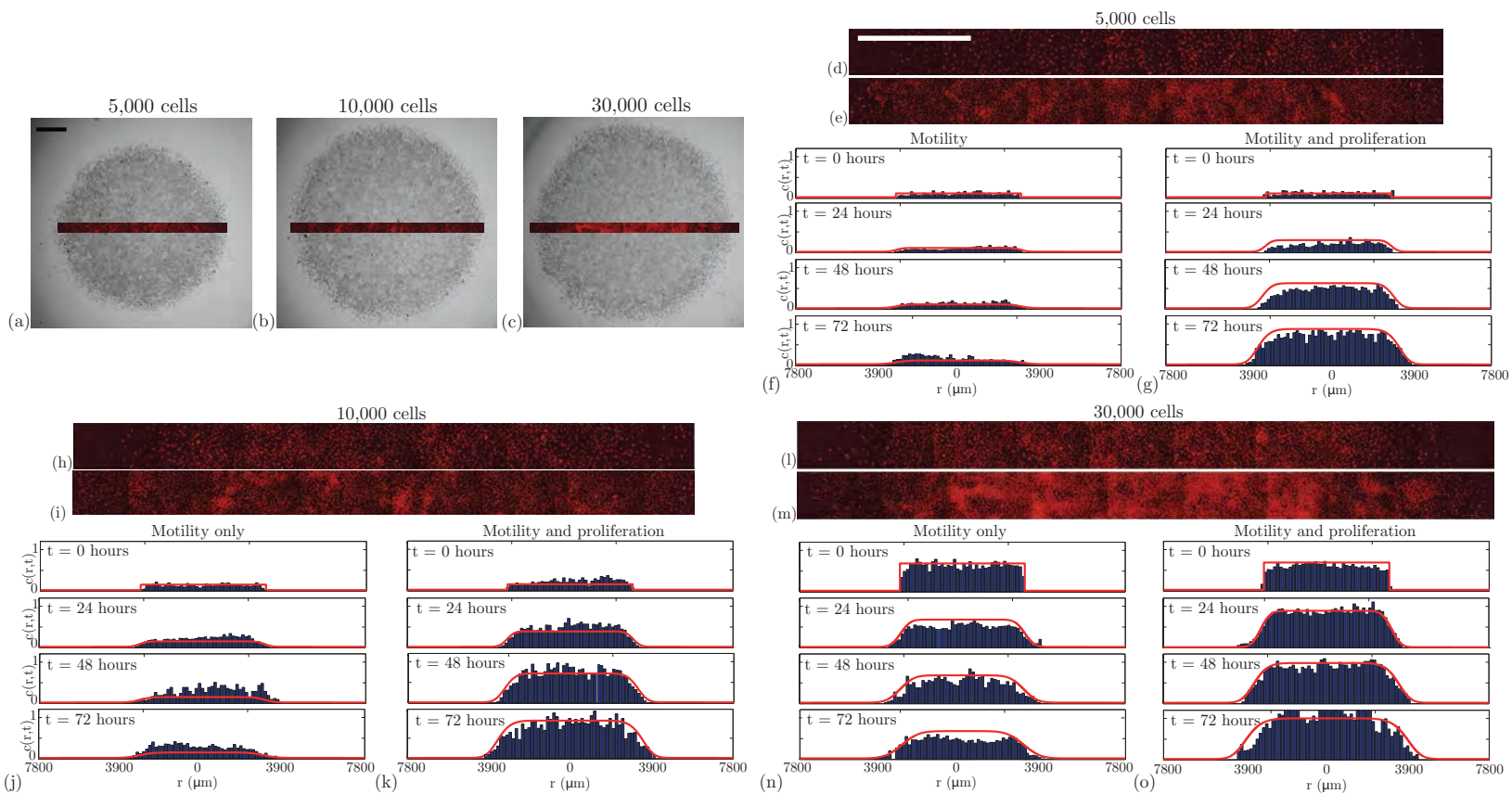


Figure 2.4: (a)–(c) Snapshots of the crystal violet stained image (gray scale) are compared with the corresponding PI-stained transect after 72 hours without Mitomycin-C pretreatment for experiments with 5,000, 10,000 and 30,000 cells initially placed in the barrier, respectively. The scale bar represents 1,500 μm . Images in (d)–(e), (h)–(i) and (l)–(m) show pairs of PI-stained transects after 72 hours for experiments with 5,000, 10,000 and 30,000 cells, respectively. The scale bar in (d) represents 1,500 μm and all images in (d)–(e), (h)–(i) and (l)–(m) are taken at the same scale. Images in (d), (h) and (l) correspond to Mitomycin-C pretreated experiments, and images in (e), (i) and (m) correspond to experiments without Mitomycin-C pretreatment. Histograms in (f)–(g), (j)–(k) and (n)–(o) show the time evolution of the cell density across the transect for the experiments with 5,000, 10,000 and 30,000 cells, respectively. Histograms are shown at $t = 0, 24, 48$ and 72 hours, as indicated. The solid curves in (f)–(g), (j)–(k) and (n)–(o) correspond to the relevant solutions of Equation (2.2). The initial condition is given by Equation (5.6), and results in (f)–(g), (j)–(k) and (n)–(o) correspond to $c_0 = 0.11, 0.22$ and 0.66 , respectively. The numerical solution of Equation (2.2) corresponds to $\delta r = 1.0 \mu\text{m}$, $\delta t = 0.005$ hours and $\epsilon = 1 \times 10^{-6}$.

2.4.5 Shape of the leading-edge

We now present measurements and modelling of the cell density profiles across a transect of the spreading population. Snapshots in Figure 2.4 (a)–(c) show the population-scale crystal violet stained images superimposed with a PI-stained transect to illustrate how the transect data corresponds to the images in Figure 2.3.

To quantify the spatial distribution of cells, we divided each transect into 40–60 equidistant sections, each of length $150 \mu\text{m}$, along the transect axis. The image analysis software was used to count the number of cells in each section, and this was converted into a nondimensional cell density, $c(r, t)$, which was used to construct the histograms of cell density in Figure 2.4. The histogram data at $t = 0$ confirms that the initial cell density is approximately uniform, which supports our previous modelling assumptions. The histogram data in Figure 2.4 for $t > 0$ allows us to compare the time evolution of the cell density in those experiments where proliferation is suppressed from those where proliferation was present. This data confirms that proliferation has a relatively small influence before $t = 24$ hours, but a far more pronounced effect by $t = 72$ hours. These differences are most obvious in Figure 2.4 (f)–(g), for the lowest initial density experiments. Here, we observe that the density profiles for the experiment where proliferation is suppressed remains relatively low for all time, whereas the density profiles for the corresponding proliferative experiments almost reaches carrying capacity density after 72 hours.

The relevant solution of Equation (2.2) is superimposed on each histogram in Figure 2.4. These solutions reflect the key differences between the six sets of experiments thereby confirming that the key features of these experiments can be captured, relatively accurately, by our modelling framework. The histogram data in Figure 2.4 enables us to compare how the balance of motility and proliferation controls the shape of the leading edge. Previous results in Figure 2.3 (d) indicate that the presence of proliferation in the 5,000 cell experiment drives the position of the leading edge approximately $1,500 \mu\text{m}$ further by $t = 72$ hours than the equivalent experiment where proliferation is suppressed. The histograms in Figure 2.4 (f)–(g) confirm this and highlights a major difference in the shape of the leading edge. To emphasise the difference in shape, we re-scaled this histogram data, focussing on the details of the shape of the leading edge, over a distance of approximately $1,650 \mu\text{m}$, in Figure 2.5 (a)–(b). The re-scaled images confirms that cell spreading driven by combined motility and proliferation leads to relatively steep fronts, whereas cell spreading in the absence of proliferation leads to relatively shallow fronts [132]. The relevant solutions of Equation (2.2) confirms that the experimental observations are consistent with differences predicted by our modelling framework. Additional results in Figure 2.5 (c)–(d) and Figure 2.5 (e)–(f) compare the shape of the leading edge at $t = 72$ hours for the experiments initialised with 10,000 and 30,000 cells, respectively. These results also confirm that proliferative fronts are relatively steep while fronts without proliferation are relatively shallow.

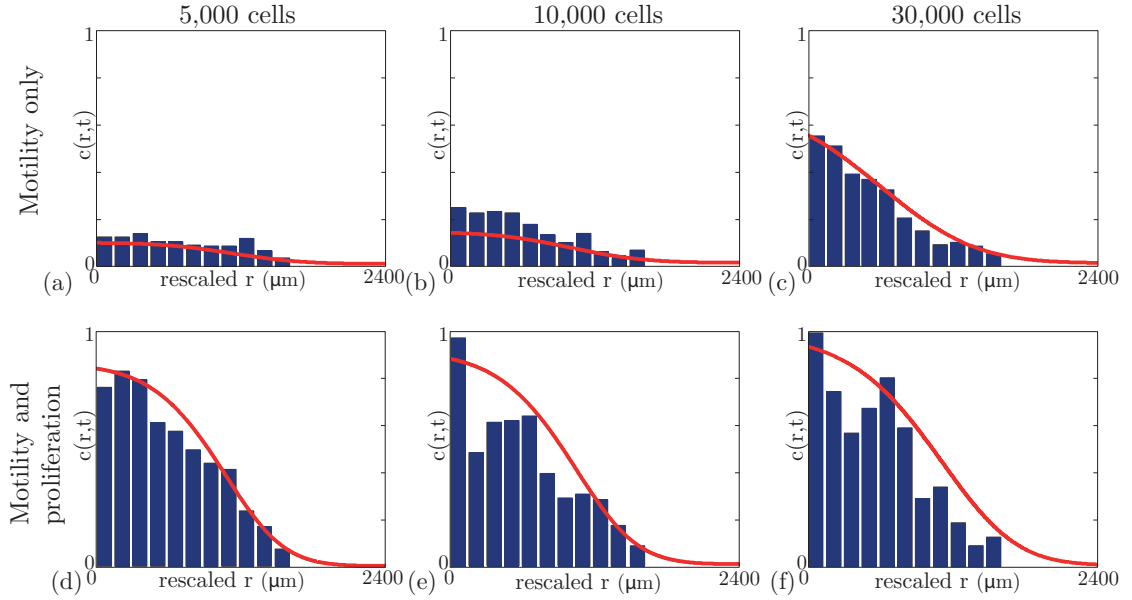


Figure 2.5: The shape of the leading edge is compared where the spreading is driven by motility alone (first row) and combined motility and proliferation (second row). To facilitate the comparison, in each case we shifted the radial coordinate to compare the density profiles over a distance of approximately 1,650 μm behind leading edge. The experimental data corresponds to a barrier assay with 5,000, (a),(d), 10,000, (e),(f) and 30,000, (c),(f), cells placed into the barrier initially. All data corresponds to 72 hours after the barrier was lifted. The solid curves are the numerical solutions of Equation (2.2), with the appropriate parameter values, previously described. The numerical solution of Equation (2.2) corresponds to $\delta r = 1.0 \mu\text{m}$, $\delta t = 0.005$ hours and $\epsilon = 1 \times 10^{-6}$.

2.5 Discussion

Quantifying the mechanisms driving cell spreading will improve our understanding of several processes including development [159], repair [85, 86] and certain diseases [132]. Previous experimental studies have focused on measuring the front speed [85, 86]. One of limitations of measuring the front speed alone is that there are many choices of D and λ that give the same front speed according to the Fisher–Kolmogorov equation [85, 86]. To address this, others have chosen model parameters to ensure that the solution of the model matches the density observations [113, 114, 116]. Using this kind of parameter fitting approach alone may not allow for any independent assessment of the predictive capability of the model unless separate experimental measurements are obtained so that the calibrated model can be independently tested. One way to overcome these limitations is to intentionally alter the details of the experiment so that we can separately identify the roles of cell motility and cell proliferation. Here, we use a combination of experimental and modelling techniques to isolate the roles of motility and proliferation in a two-dimensional circular barrier assay. We characterise D and λ separately, and then make independent modelling predictions about other aspects of the experiment.

Our experiments were designed to study the differences between cell spreading driven combined motility and proliferation, from an equivalent set of experiments where proliferation was suppressed [112]. By quantifying the differences between these experiments, we showed that Mitomycin–C pretreatment caused the cell density in the central region

of the assay to remain approximately constant over 72 hours, whereas equivalent cells in the central region without Mitomycin–C pretreatment proliferated significantly over the same time period. Using image analysis software, we showed that cell spreading is enhanced by the presence of cell proliferation.

High-magnification images of transects through the spreading population were used to reconstruct cell density profiles during each experiment. These density profiles confirmed that the proliferative experiments led to faster spreading than when proliferation was suppressed. The cell density profiles showed that the shape of the leading edge can be very different depending on whether or not cell proliferation is present. When proliferation was suppressed, we observed the formation of shallow fronts, whereas proliferative fronts relatively steep. We also used our parameterised modelling framework to make quantitative predictions of the shape of the leading edge in each experiment and found that our modelling provided reasonable predictions. Understanding the differences between cell spreading with and without proliferation, and confirming that our modelling framework can predict these differences, is important since the shape of the leading edge of a spreading cell population is thought to have important clinical implications [59, 132].

Our results highlight the need to consider the role of initial cell numbers since our estimates of D indicate a weak density dependence as we observe $D = 1,500, 1,700$ and $2,900 \mu\text{m}^2/\text{hour}$ for the experiments initialised with 5,000, 10,000 and 30,000 cells, respectively. From a practical point of view, given that estimates of cell diffusivity in the literature can vary over one or two orders of magnitude [85, 86, 113, 134], our observed variation is relatively small. Nonetheless, we do observe a consistent density-dependent mechanism for which there are several plausible explanations such as the possibility that cells produce a chemical signal (or signals) enhancing migration, or the possibility that cells modify the substrate as they migrate. For both these putative mechanisms, it is reasonable to assume that placing more cells in the barrier initially leads to enhanced migration. Although our current experimental platform was not designed to resolve these details, our results illustrate the importance of repeating barrier assays with different initial numbers of cells so that these effects can be observed and quantified.

The experimental observations reported here are relevant to current theoretical developments where there has been active debate regarding appropriate techniques to model collective cell motility. Some observations favour models based on linear diffusion, while others favour nonlinear diffusion [85, 86, 113, 116]. Recent theoretical developments have even suggested it is possible to accurately model the same discrete interacting motility mechanism either invoking a linear or a nonlinear diffusion equation. These differences depend on the details of how the continuum-limit is constructed [13].

Our combined modelling and experimental study illustrates how to separately quantify the effects of cell motility and cell proliferation in a barrier assay to help understand how each component contributes to cell spreading. We anticipate that designing more detailed experimental programs will be necessary when modelling cell spreading involving cell-to-cell adhesion [33, 121] or an epithelial-to-mesenchymal transition (EMT) [153]. For both

these extensions we must quantify how the cell motility is affected by cell-to-cell adhesion and how the EMT contributes to the net spreading of the population. Incorporating such details will be the subject of future research.

CHAPTER 3

Multiple types of data are required to identify the mechanisms influencing the spatial expansion of melanoma cell colonies

A paper published in *BMC Systems Biology*.

Treloar, K.K., Simpson, M.J., Haridas, P., Manton, K.J., Leavesley, D.I., McElwain, D.L.S. & Baker, R.E. Multiple types of data are required to identify the mechanisms influencing the spatial expansion of melanoma cell colonies. *BMC Syst. Biol.* **7**, 137 (2013).

Abstract

The expansion of cell colonies is driven by a delicate balance of several mechanisms including cell motility, cell-to-cell adhesion and cell proliferation. New approaches that can be used to independently identify and quantify the role of each mechanism will help us understand how each mechanism contributes to the expansion process. Standard mathematical modelling approaches to describe such cell colony expansion typically neglect cell-to-cell adhesion, despite the fact that cell-to-cell adhesion is thought to play an important role. We use a combined experimental and mathematical modelling approach to determine the cell diffusivity, D , cell-to-cell adhesion strength, q , and cell proliferation rate, λ , in an expanding colony of MM127 melanoma cells. Using a circular barrier assay, we extract several types of experimental data and use a mathematical model to independently estimate D , q and λ . In our first set of experiments, we suppress cell proliferation and analyse three different types of data to estimate D and q . We find that standard types of data, such as the area enclosed by the leading edge of the expanding colony and more detailed cell density profiles throughout the expanding colony, does not provide sufficient information to uniquely identify D and q . We find that additional data relating to the degree of cell-to-cell clustering is required to provide independent estimates of q , and in turn D . In our second set of experiments, where proliferation is not suppressed, we use data describing temporal changes in cell density to determine the cell proliferation rate. In summary, we find that our experiments are best described using the range $D = 161 - 243 \mu\text{m}^2/\text{hour}$, $q = 0.3 - 0.5$ (low to moderate strength) and $\lambda = 0.0305 - 0.0398 / \text{hour}$, and with these parameters we can accurately predict the temporal variations in the spatial extent and cell density profile throughout the expanding melanoma cell colony. Our systematic approach to identify the cell diffusivity, cell-to-cell adhesion strength and cell proliferation

rate highlights the importance of integrating multiple types of data to accurately quantify the factors influencing the spatial expansion of melanoma cell colonies.

3.1 Background

Cell colony expansion is driven by several mechanisms including cell motility, cell-to-cell adhesion and cell proliferation [85, 132, 153]. Methods that can be used to quantify the role of these various mechanisms driving *in vitro* colony expansion will assist in improving our understanding of them [25, 43, 53, 125, 132]. In this work, we propose a systematic approach to identify and quantify the mechanisms driving the expansion of melanoma cell colonies *in vitro*.

We choose to study melanoma cells since melanoma is the most dangerous form of skin cancer, which can spread rapidly and cause serious illness and death [16, 48, 131]. Approximately 75% of all skin cancer deaths are due to melanoma, and each year 132,000 new cases are diagnosed globally, with more than 12,500 of these reported in Australia [10]. While the five-year survival rate in patients with non-metastatic melanoma can be as high as 95%, the five-year survival rate for patients with metastatic melanoma is less than 15% [11]. The precise details of the mechanisms that drive melanoma cell colony expansion are unclear, and using a systematic approach which can independently identify and quantify the role of each individual mechanism may provide practical insights into how colonies of melanoma cells expand [23, 25, 39, 129].

Expanding colonies of cells are characterised by moving cell fronts [85, 116], and typical mathematical modelling approaches to describe the movement of such fronts use partial differential equations that incorporate descriptions of cell motility and cell proliferation [85, 97, 113, 116, 125, 132]. In most cases, the terms describing cell motility and cell proliferation in the partial differential equation are chosen without explicitly considering the details of the underlying biological process [85, 123, 136], and often neglect cell-to-cell adhesion [33, 75, 121]. However, several experimental studies have observed that the loss of cell-to-cell adhesion between individual melanoma cells is associated with increased spatial expansion [29, 65, 79, 87, 93, 108], suggesting that cell-to-cell adhesion plays an important role in the spatial expansion of melanoma cell colonies.

An alternative modelling approach to describe the expansion of cell colonies involves simulating the behaviour of individual cells in a colony in a discrete modelling framework [3, 5, 9, 38, 41, 52, 57, 109, 130, 146]. Discrete models have the benefit that they produce data, such as snapshots and movies, that are more compatible with experimental data compared to partial differential equation models [125]. Furthermore, discrete models can be designed to incorporate realistic cell behaviours which can be more difficult using a partial differential equation description [125]. A recent view of discrete cell-based modelling approaches can be found in [32, 109, 150]. Khain *et al.* [72, 74] developed a discrete mathematical model to describe the expansion of a motile and proliferative cell colony in which the cell motility is reduced by cell-to-cell adhesion. In their model, they represented simulated cells on a two-dimensional lattice, and they allowed the simulated

cells to both move and proliferate. Cell-to-cell adhesion was introduced by including a mechanism where the simulated cells could adhere to nearest neighbour simulated cells, effectively reducing their motility. Khain *et al.* [72, 74] applied this model to investigate the behaviour of glioma cells in a two-dimensional scratch assay, predicting the location and speed of the leading edge of the expanding glioma cell colony. In another study, Simpson *et al.* [121] extended Khain’s model to investigate the migration of MCF-7 breast cancer cells in a three-dimensional Transwell® apparatus [121]. Although both these recent modelling studies incorporated a cell-to-cell adhesion mechanism, there is no widely accepted protocol for designing experiments that allow us to independently quantify the contributions of cell motility, cell-to-cell adhesion and cell proliferation in expanding cell colonies [72, 74–76, 121]. We hypothesise that collecting and analysing several sets of experimental data describing the same experimental procedure may be required in order for us to independently quantify the role of these mechanisms.

In this work we use a circular barrier assay [69, 145] to investigate the interplay between cell motility, cell-to-cell adhesion and cell proliferation mechanisms in expanding colonies of MM127 melanoma cells. We take a systematic approach that uses multiple types of data to identify each of these mechanisms separately by performing two sets of experiments. In our first set of experiments, we use Mitomycin-C to suppress cell proliferation so that we can separate the roles of cell motility and cell-to-cell adhesion from the role of cell proliferation. We attempt to quantify the roles of cell motility and cell-to-cell adhesion by extracting information about the location of the leading edge of the expanding colony and detailed cell density profiles throughout the entire cell colony. We find that these approaches do not provide sufficient information to identify the rate of cell motility and strength of cell-to-cell adhesion, and that additional data, including a measurement of the degree of cell-to-cell clustering, is required. Once we have obtained estimates of the cell motility rate and cell-to-cell adhesion strength we use a second set of experiments, in which proliferation is not suppressed, to estimate the rate of cell proliferation. Finally, given our independent estimates of the cell motility rate, strength of cell-to-cell adhesion and the cell proliferation rate, we confirm that our estimates allow us to accurately predict the observed spatial expansion in the experiments by comparing the predicted location of the leading edge and the predicted cell density profiles from our parameterised mathematical model to our experimental measurements.

3.2 Experimental methods

3.2.1 Cell culture

Human malignant melanoma cells (MM127, [102, 107, 154]), a gift from Mitchell Stark (Queensland Institute of Medical Research), were cultured in RPMI-1640 with 2mM L-Glutamine, 23mM HEPES (Invitrogen, Australia) with 10% foetal calf serum (FCS; Hyclone, New Zealand) and 1% v/v penicillin/streptomycin (Invitrogen, Australia) in 5% CO₂ at 37 °C and 95% air atmosphere. Cells were harvested just prior to confluence using 0.05% trypsin-EDTA(1×) (Invitrogen, Australia). Cell viability was determined using a trypan blue exclusion test and cell number determined using a haemocytometer.

3.2.2 Circular barrier assay

Metal–silicone barriers, 6,000 μm in diameter (Aix Scientifics, Germany), were cleaned, sterilised using 70% Ethanol, dried and placed in the centre of each well of a 24-well tissue culture plate. Each well has a diameter of 15,600 μm . Experiments were performed using two different cell densities: 20,000 or 30,000 cells per well. To suppress cell proliferation, 10 $\mu\text{g}/\text{mL}$ Mitomycin–C (Sigma Aldrich, Australia) was added to half of all cell solutions for one hour at 37 °C prior to transfer to the wells [112]. 100 μL of cell suspension was carefully inserted into the barrier to ensure that the cells were approximately evenly distributed. Cells were allowed to settle and attach for four hours in a humidified incubator at 37 °C, 5% CO₂ and 95% air atmosphere. Assays commenced with the removal of the barrier and the cell layer was washed with warm serum free medium (SFM; culture medium without FCS) and replaced with 0.5 mL of culture medium. Cultures were incubated at 37 °C in 5% CO₂ and 95% air atmosphere for $t = 0$, 24 and 48 hours. Each assay, for each time point, was repeated three times.

3.2.3 Detection of motility and cell-to-cell adhesion proteins in MM127 cells using immunofluorescence and western blotting

The presence of mesenchymal-associated proteins including vimentin, N–cadherin and the epithelial-associated protein E–cadherin were demonstrated with immunofluorescence. Circular barrier assays were repeated on coverslips with 30,000 cells, for $t = 48$ hours, without Mityomycin–C pretreatment. Cells were fixed with 10% neutral buffered formalin, permeabilised with 0.1% Triton X–100 in PBS for 10 minutes, blocked with 0.5% BSA in PBS for 10 minutes and incubated with a primary antibody for 90 minutes. The secondary antibody was then added to the cells for 60 minutes. Between each stage, cells were washed three times with 0.5% BSA and five times after the addition of the secondary antibody. Images were acquired using a Leica SP5 confocal microscope fitted with a Nikon digital camera. The primary antibodies were as follows; Vimentin (Monoclonal, rabbit anti–human; clone SP20, Thermo Fisher LabVision, Australia), N–cadherin (Monoclonal, Mouse anti–human, clone 32, BD Transduction Laboratories, Australia) and E–cadherin (Monoclonal, mouse anti–human, clone HECD–1, Abcam, Australia). The secondary antibodies were as follows; Vimentin (Goat anti–rabbit, Alexa Fluor–568, Invitrogen, Australia) and for both N–cadherin and E–cadherin (Goat anti–mouse, Alexa Fluor–488, Invitrogen, Australia). Western blot was also performed to confirm that E–cadherin is not expressed in MM127 cells. The same primary antibody was used as in the immunofluorescence testing, while the secondary antibody used was (goat anti–mouse, Horseradish Peroxidase Conjugate, Invitrogen, Australia). Highly adhesive breast cancer cells (MCF–7, ATCC, Manassas, VA) were used as a positive control for E–cadherin immunoreactivity [46].

3.2.4 Image acquisition and analysis

Colony–scale images to show the spatial expansion of the cell colonies were obtained by fixing cells with 10% neutral buffered formalin, followed by 0.01% crystal violet (Sigma-

Aldrich, Australia) in 0.1 M borate buffer. The stain was rinsed with phosphate-buffered saline (Invitrogen, Australia) and samples air-dried. Images were acquired using a stereo microscope fitted with a Nikon digital camera. Images were analysed using customised software written with MATLAB's Image Processing Toolbox (v7.12) [90]. Edge detection and segmentation algorithms were applied to the colony-scale images to identify and isolate the entire cell colony from the background of the image, resulting in an estimate of the location of the leading edge (Appendix B) [125, 137].

Individual-scale images detailing the number and location of the cells in the colony were acquired by destaining the crystal violet stained samples with 70% ice-cold ethanol and staining the nuclei with 1 mg /ml Propidium Iodide (Invitrogen, Australia) in PBS. Images were acquired using a Nikon Eclipse Ti inverted microscope fitted with a Nikon digital camera. Overlapping adjacent images were used to reconstruct horizontal and vertical transects through the entire colony. Images were analysed using customised software written with MATLAB's Image Processing Toolbox (v7.12) [90]. Segmentation algorithms were used to automatically count the number of cells in the Propidium Iodide stained images [125]. For some images, we found that a number of cells had to be manually identified and counted. In all cases, a visual check was performed to validate that all cells had been identified correctly using the software, or through manual counting (Appendix B).

3.3 Results

3.3.1 Identifying the mechanisms controlling the expansion of melanoma cell colonies

The spatial expansion of melanoma cell colonies is a complex process that is influenced by various mechanisms including cell motility, cell proliferation and cell-to-cell adhesion [58, 82]. Although all three mechanisms are thought to play a critical role [58, 82], it is unclear how the contributions of each of these three mechanisms can be identified and measured in a quantitative framework [125]. In this work, we use a combined experimental and mathematical modelling approach to distinguish between, and to quantify the role of, each mechanism.

To observe the spatial expansion of melanoma cell colonies, we performed several experiments using a circular barrier assay [69, 145]. Figure 3.1 illustrates a schematic of the barrier assay. Human malignant melanoma cells (MM127, [102, 107, 154]) were placed inside the barrier at $t = 0$ hours. The barrier was then lifted, allowing the cell colony to expand outwards. The spatial expansion of the colony was measured at $t = 24$ and $t = 48$ hours by calculating the radius, R , of the expanding circular colony. In our work, we placed either 20,000 or 30,000 cells inside the barrier initially. To confirm the presence of cell motility and cell-to-cell adhesion proteins in the cell colony, we used immunofluorescence to examine the expression of E-cadherin, N-cadherin and vimentin [34, 68, 82, 153, 163]. E-cadherin, a cell-to-cell adhesion protein that is uniquely expressed by epithelial cells [68], was not detected (Figure 3.2 (a)). Western blot analysis (Figure 3.2 (a) inset) confirmed the absence of E-cadherin [68]. In contrast, N-cadherin

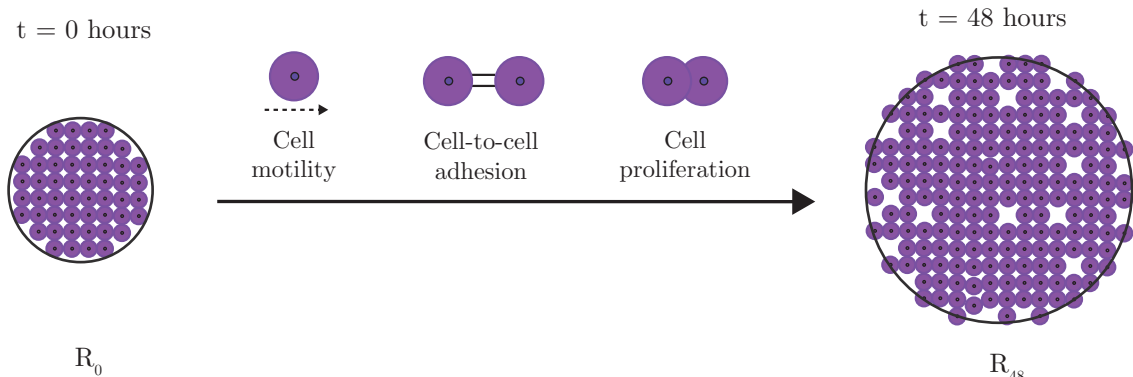


Figure 3.1: Cell motility, cell-to-cell adhesion and cell proliferation mechanisms drive cell colony expansion. Schematic representation of the circular barrier assay illustrating the mechanisms influencing the expansion of a two-dimensional cell colony. Cells are placed inside the barrier which is lifted at $t = 0$ hours allowing the colony of cells to expand outwards until $t = 48$ hours. The degree of expansion can be quantified by measuring and comparing the radius of the colony, R_0 and R_{48} .

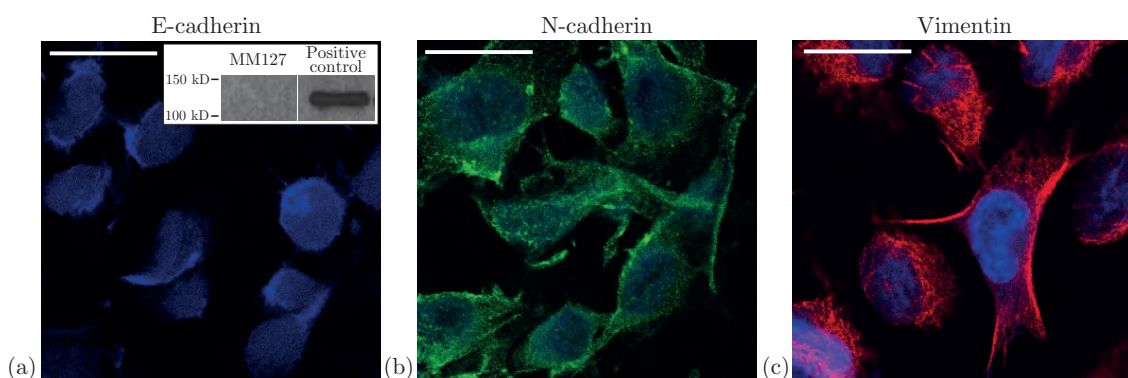


Figure 3.2: MM127 melanoma cells express mesenchymal markers. Immunofluorescence was used to examine expression of E-cadherin, a cell-to-cell adhesion protein uniquely expressed by epithelial cells (a), N-cadherin, a cell-to-cell adhesion protein uniquely expressed by mesenchymal cells (b), and vimentin, a protein that is uniquely expressed by mesenchymal cells (c) in MM127 cells. The scale bar corresponds to 25 μ m. MM127 melanoma cells were cultured in a circular barrier assay for $t = 48$ hours on glass coverslips in 500 μ L cell medium. All sections were stained with DAPI (blue) to identify the cell nucleus. N-cadherin and vimentin expression are indicated by the green and red staining, respectively. Western blot was used to examine the expression of E-cadherin protein in MM127 cells (Inset in (a)).

and vimentin, proteins that are uniquely expressed by mesenchymal cells, were detected (Figure 3.2 (b)–(c)). The expression of N-cadherin suggests that cell-to-cell adhesion plays a role in this system, while the presence of vimentin is consistent with our initial assumption that the cells are motile [68, 82, 153, 163]. In addition to the immunofluorescence results, we also visually identified that significant proliferation occurred during the barrier assays which we confirm during our later analysis (See section 3.3.4).

3.3.2 Modelling the spatial expansion of a melanoma cell colony

To interpret our experimental observations we used a discrete random walk model to simulate the expansion of the melanoma cell colonies [72–74, 121]. The random walk model describes how a simulated cell can undergo specific events in a sequence of random steps [27]. These events include adhesive motility and proliferation, and we note that all of

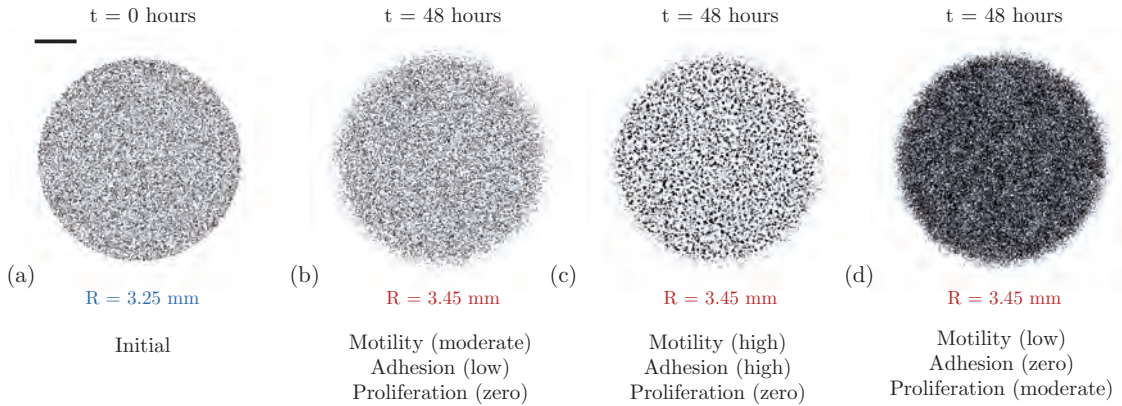


Figure 3.3: Multiple combinations of D , q and λ result in the same extent of spatial expansion. A circular barrier assay initialised with 20,000 cells was simulated using the mathematical model. The initial distribution of 20,000 simulated cells at $t = 0$ hours is shown in (a). The scale bar corresponds to 1,500 μm . Simulation snapshots shown in (b)–(d) illustrate three different combinations of the cell motility rate, cell-to-cell adhesion strength and cell proliferation rate used to replicate the experiments over $t = 48$ hours. All three simulations result in a similar extent of spatial expansion from $R = 3,250 \mu\text{m}$ at $t = 0$ hours to $R = 3,450 \mu\text{m}$ at $t = 48$ hours. Simulations were performed with (b) moderate motility, low cell-to-cell adhesion strength and zero proliferation; $D = 405 \mu\text{m}^2/\text{hour}$, $q = 0.1$, $\lambda = 0 / \text{hour}$, (c) high motility, high cell-to-cell adhesion strength and zero proliferation; $D = 810 \mu\text{m}^2/\text{hour}$, $q = 0.8$, $\lambda = 0 / \text{hour}$, and (d) low motility, zero cell-to-cell adhesion and moderate proliferation; $D = 162 \mu\text{m}^2/\text{hour}$, $q = 0$, $\lambda = 0.035 / \text{hour}$.

these mechanisms are simulated within a framework that incorporates realistic crowding effects [72–74, 121]. We simulate these mechanisms on a two-dimensional square lattice with lattice spacing Δ . We estimate Δ by measuring the diameter of the cell nucleus using ImageJ [66], giving $\Delta = 18 \mu\text{m}$. We choose to use the diameter of the cell nucleus as the estimate for Δ as this appears to be a realistic measurement for the equivalent circular space that each individual cell occupies on the tissue culture plate (Appendix B). Simulations of the experiments were performed on a lattice of size 867×867 , whose dimensions correspond to the $15,600 \mu\text{m}$ diameter of well in a 24-well plate ($15,600/18 \approx 867$). The simulations were initialised by placing either 20,000 or 30,000 simulated cells inside a circle located at the centre of the lattice. The radius of the initial circle was $3,250 \mu\text{m}$, which corresponds to the average initial radius of the cell colony for both initial densities (Appendix B). To reflect the way that the experiments were initiated, simulated cells were placed uniformly at random inside the circle so that the initial distribution of simulated cells matched the initial conditions in the experiments as accurately as possible. For example, if the initial radius of the circle is $3,250 \mu\text{m}$, we represent this using a circle whose diameter corresponds to 180 lattice sites since $180 \approx 3,250/18$. Hence, the total number of lattice sites inside that circle is $\pi 180^2 \approx 101736$ and we randomly occupy 19.65% of these sites to mimic an experiment initialised with 20,000 cells since $19.65\% = 100 \times (20,000/101736)$. Similarly, we randomly occupy 29.49% of these sites to mimic an experiment initialised with 30,000 cells since $29.49\% = 100 \times (30,000/101736)$. Figure 3.3 (a) illustrates the initial distribution for a simulation initialised with 20,000 simulated cells.

The model incorporates crowding effects by permitting each lattice site to be occupied by, at most, one simulated cell [33, 74, 121]. A random sequential update algorithm was used to perform the simulations [24] using the following algorithm. If there are $N(t)$ simulated cells at time t , during the next time step of duration τ , $N(t)$ simulated cells are selected at random, one at a time, and given the opportunity to move with probability $P_m(1 - q)^a$. The random sequential update methods means that not all $N(t)$ simulated cells are always selected during every time step; sometimes a particular simulated cell will be selected more than once per time step [24]. Here, $0 \leq P_m \leq 1$ is the probability that an isolated simulated cell moves a distance of one cell diameter, Δ , during a time interval of duration τ . The strength of adhesion is governed by the parameter $0 \leq q \leq 1$, and $0 \leq a \leq 4$ is the number of occupied nearest-neighbour lattice sites surrounding the simulated cell in question. When $q = 0$, there is no cell-to-cell adhesion and nearest neighbour cells do not adhere to each other. As q increases, the strength of cell-to-cell adhesion increases, and nearest-neighbour cells adhere more tightly to each other. If the opportunity to move is successful and the target site is vacant, a simulated cell at position (x, y) steps to $(x \pm \Delta, y)$ or $(x, y \pm \Delta)$ with each target site chosen with equal probability of $1/4$. Once the $N(t)$ potential motility events have been assessed, another $N(t)$ simulated cells are selected at random, one at a time, and given the opportunity to proliferate with probability $0 \leq P_p \leq 1$. If the opportunity to proliferate is successful, the proliferative simulated cell attempts to deposit a daughter simulated cell at $(x \pm \Delta, y)$ or $(x, y \pm \Delta)$ with each target site chosen with equal probability of $1/4$.

In this work, we interpret the parameters describing cell motility and cell proliferation in our model using standard measures. The cell motility rate is quantified in terms of the cell diffusivity, D [97], which is related to the parameters in our model by $D = (P_m \Delta^2)/(4\tau)$ [27, 125]. Similarly, the rate of cell proliferation is given by $\lambda = P_p/\tau$ [121, 125]. Values of D are often reported to be of the order, $D = 1000 \mu\text{m}^2/\text{hour}$ [97, 132]; however, typical estimates of D , calculated primarily from *in vitro* cell populations, are known to vary by as much as to two orders of magnitude [85, 121, 125, 132]. To the best of our knowledge, there are no known estimates of D for MM127 melanoma cells. A typical doubling time, $t_d = \log_e(2)/\lambda$, for melanoma cells is thought to be approximately 34 hours [128]. We note that while values of D and λ are sometimes reported in the literature, there are no such estimates of the strength of cell-to-cell adhesion, q [121].

In our analysis, we measure and quantify the dimensional cell density, $c^*(r, t)$, where r describes the radial position (μm) and t is time (hours). To measure the dimensional cell density, we consider a region of area A . In each region, we count the total number of cells, N , and divide through by the area to give $c(r, t) = N/A \text{ cells } / \mu\text{m}^2$. In all cases, we convert the dimensional cell density into an equivalent non-dimensional cell density, $c(r, t)$, by scaling with the carrying capacity density K . This gives $c(r, t) = c^*(r, t)/K$. We approximate the carrying capacity as the maximum packing density of circular-disk-like cells with diameter $18 \mu\text{m}$ on a two-dimensional square lattice, giving $K = 1/\Delta^2 \approx 3 \times 10^{-3} \text{ cells } / \mu\text{m}^2$ [125]. In some regions where the cell density is approximately spatially uniform, we will refer to the non-dimensional cell density as a function of time only,

$c(t)$ [125]. This is particularly useful when we estimate the proliferation rate since we focus on regions in the middle of the colony where the spatial distribution of cells is relatively uniform so that locally we have $c(r, t) \approx c(t)$ [125].

Initially, we used the mathematical model to investigate whether a simple visual comparison of the simulated circular barrier assays for typical choices of D , q and λ could provide any insight into the factors affecting the spatial expansion of the experimental melanoma cell colony. Simulations in Figure 3.3 (b)–(d) show three different realistic parameter combinations of D , q and λ . For these simulations we measure the extent of the spatial expansion of the colony by measuring the radius of the colony, R . Results in Figure 3.3 (b)–(d) show that the spatial expansion after $t = 48$ hours is equivalent for these different choices of D , q and λ . This observation suggests that there are multiple combinations of cell motility, cell-to-cell adhesion and cell proliferation parameters which could replicate the experiment results and therefore a simple visual inspection of the population is insufficient to identify the mechanisms influencing the expansion of the cell colony. To overcome this important limitation, we identified multiple types of data that could be extracted from the experiments. We will now describe each of these types of data and assess whether they are able to identify a unique set of D , q and λ parameters.

3.3.3 Estimating the rate of cell motility and strength of cell-to-cell adhesion

To distinguish between the roles of cell motility and cell-to-cell adhesion, we considered experiments where cell proliferation was suppressed by performing the barrier assays with Mitomycin-C pretreated cells [112, 125]. For each experiment we estimated the position of the leading edge of the expanding colony, the cell density profile along a transect throughout the entire expanding colony as well as measuring the degree of cell-to-cell clustering within the colony.

Data type 1: Location of the leading edge

The area enclosed by the leading edge of an expanding cell colony is a standard tool used to quantify the rate of cell colony expansion [94, 125, 137]. To determine the location of the leading edge we used image analysis software to analyse the experimental images showing the entire colony (Appendix B) [137]. Images in Figure 3.4 (a)–(b) show the position of the leading edge detected at $t = 0$ and $t = 48$ hours, respectively. In both cases, the image analysis software accurately detects the position of the leading edge. For each experimental image we calculated the area enclosed by the detected leading edge, A , and converted the estimate of A into an estimate of the radius of the expanding colony, R , by assuming that the cell colony maintained a circular shape, giving $R = \sqrt{A/\pi}$, [125, 137]. The estimates of the radius of the expanding colony are shown by the equivalent circular areas superimposed in Figure 3.4 (a)–(b). The excellent match between the detected leading edge and the corresponding equivalent circular area confirms that the cell colony maintains an approximately circular shape during the experiments. We repeated the leading edge detection procedure for all experimental images at $t = 0$, 24 and 48 hours for both initial cell densities. Results in Figure 3.4 (c)–(d) show how the estimates of R vary

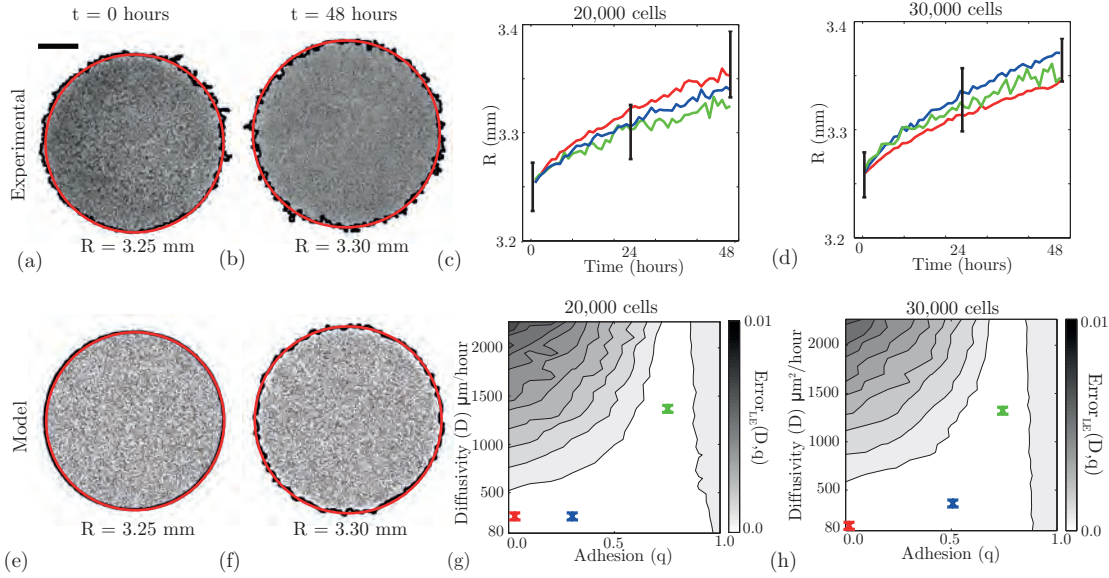


Figure 3.4: The radius of the colony does not allow us to uniquely estimate D and q . All results correspond to experiments where the cells were pretreated with Mitomycin-C to prevent cell proliferation. Images in (a)–(b), show the entire cell colony for experiments initialised with 30,000 cells at $t = 0$ and $t = 48$ hours, respectively. The scale bar corresponds to 1,500 μm . An equivalent model simulation is shown in (e)–(f), using $D = 243 \mu\text{m}^2/\text{hour}$, $q = 0$ and $\lambda = 0/\text{hour}$. For all images in (a)–(d), the detected location of the leading edge using the image analysis software is shown in black, while the red circle corresponds to the equivalent circle with the same area as enclosed by the leading edge. Results in (c) and (d) show the time evolution of the average radius of the expanding colony detected in the experiments. The error bars correspond to one standard deviation from the mean (black). Corresponding model simulations which match the experimental results are superimposed (colour lines). Simulation results were averaged over three identically-prepared realisations using three different combinations of parameters which are shown by the coloured crosses on the error surfaces in (g) and (h). The model simulations in (c)–(d) were generated using $D = 162 \mu\text{m}^2/\text{hour}$ and $q = 0$ (red), $D = 162 \mu\text{m}^2/\text{hour}$ and $q = 0.3$ (blue) and $D = 1215 \mu\text{m}^2/\text{hour}$ and $q = 0.8$ (green), while solutions in (d), were generated using $D = 81 \mu\text{m}^2/\text{hour}$ and $q = 0$ (red), $D = 243 \mu\text{m}^2/\text{hour}$ and $q = 0.5$ (blue), and $D = 1215 \mu\text{m}^2/\text{hour}$ and $q = 0.8$ (green), respectively. The error surfaces in (g) and (h) show $\text{Error}_{LE}(D, q)$, given by Equation 3.1, for various values of D and q . The error surfaces were by averaging the radius estimates from three experimental replicates and three identically-prepared model realisations.

with time, indicating that the average radius of the expanding colony in the absence of proliferation increases gradually over $t = 48$ hours. For the experiments initialised with 20,000 cells, the average radius increased from 3,250 μm to 3,300 μm , while the average radius of the expanding colony in the experiments initialised with 30,000 cells increased from 3,250 μm to 3,360 μm .

To investigate whether information about the radius of the expanding colony is sufficient to parameterise the cell diffusivity and strength of cell-to-cell adhesion, we used the mathematical model to perform several simulations to replicate the experiments where we varied the values of D and q . We initially considered a range of D values, approximately within the interval $0 < D \leq 3000 \mu\text{m}^2/\text{hour}$. We chose this range since typical reported values of the cell diffusivity are of the order $1000 \mu\text{m}^2/\text{hour}$ [97,132] which means that our initial range of possible cell diffusivity values would encompass such values. To determine the appropriate values of D , we restricted our estimates so that each potential value of D corresponded to an integer number of simulation time steps, $b = T/\tau$, where $T = 48$ hours

is the total duration of the simulation. For example, $D = 81 \mu\text{m}^2/\text{hour}$ corresponds to a simulation where we chose $P_m = 1$ and $\tau = 1$ hour, giving $b = 48/1 = 48$ simulation steps. Similarly, $D = 810 \mu\text{m}^2/\text{hour}$ corresponds to a simulation where we chose $P_m = 1$ and $\tau = 1/10 = 0.1$ hour, giving $b = 48/0.1 = 480$ simulation steps. After some initial parameter investigations (not shown), we simulated the experiments by focussing on 30 equally-spaced values of D between 81 and $2430 \mu\text{m}^2/\text{hour}$. Since values of q are unknown, we choose to simulate the model using 11 equally spaced values of q between 0 and 1 to account for the full possible range of values of the cell-to-cell adhesion strength.

For each different parameter combination, we simulated the experiments and averaged the results using three identically-prepared realisations of the model. Using the same image analysis procedure that was applied to the experimental images [125,137], we detected the leading edge of the simulated experiment, and calculated the area enclosed by the leading edge to determine R . Figure 3.4 (e)–(f) show two snapshots from a single realisation of the model with $D = 243 \mu\text{m}^2/\text{hour}$, $q = 0$ and $\lambda = 0/\text{hour}$ at $t = 0$ and $t = 48$ hours. The equivalent circular area is also superimposed on the simulated colony. We observe again that the image analysis software is able to detect the position of the leading edge and that the equivalent radius estimate of the expanding colony is a good approximation of the location of the leading edge. In all cases we repeated equivalent simulations for smaller values of τ while keeping the ratio of P_m/τ constant. This exercise confirmed that our simulations were independent of the temporal discretisation.

To compare the simulation results with our experimental measurements, we assessed the goodness of fit between the experimental measurements and the model simulations using an estimate of the least-squares error, $\text{Error}_{LE}(D, q)$. This allowed us to determine whether there is an optimal choice of D and q in the model which matches the edge detection data. For each set of D and q combinations tested, the least squares error was calculated by comparing the average radius of the experimental expanding cell colony, Er_i , and the average radius of the simulated expanding cell colony, Sr_i given by,

$$\text{Error}_{LE}(D, q) = \frac{\sum_{i=1}^2 (Er_i - Sr_i)^2}{\sum_{i=1}^2 (Er_i)^2}, \quad (3.1)$$

where, i corresponds to the two time points, $t = 24$ and $t = 48$ hours. In all cases, Er_i and Sr_i correspond to the average of three experimental and three simulation replicates.

Results in Figure 3.4 (g)–(h) show the error surface, $\text{Error}_{LE}(D, q)$ for barrier assays initialised with 20,000 and 30,000 cells, respectively. We expect that any optimal choice of D and q would correspond to a unique minimum on the error surface. However, we observe that the low error region, for both initial cell densities, is very wide and there is no such unique minimum. For example, there is little distinction between simulations using combinations of D between 80 and $500 \mu\text{m}^2/\text{hour}$, and for q between 0 and 1, confirming that there is no unique choice of D and q to match our experimental data.

To illustrate this redundancy, we simulated the experiment using three different combinations of D and q . For example, to describe the experiments initialised with 20,000 cells, we performed simulations with $D = 81, 162$ and $810 \mu\text{m}^2/\text{hour}$ and $q = 0, 0.3$ and 0.8 , respectively. In all cases, $\lambda = 0 / \text{hour}$. The simulation results superimposed in Figure 3.4 (c)–(d) show the average radius of the simulated expanding colonies compared to the experimental results. All three combinations of D and q match the experimental data, confirming that there are multiple combinations of D and q which accurately replicate the experimental data. In summary, these results illustrate that calibrating a mathematical model using the position of the leading edge alone is inadequate to uniquely identify the rate of cell motility and strength of cell-to-cell adhesion [137].

Data type 2: Cell density profiles

An alternative approach to estimate the model parameters, which does not solely rely on the location of the leading edge of the expanding cell colony, is to extract detailed information about the location of individual cells throughout the population and to construct a cell density profile throughout the entire expanding colony [113, 125]. This allows us to compare additional information about the distributions of cells in the experiments. For all experiments, a high magnification image of a transect across the center of the colony stained with Propidium Iodide was acquired, as illustrated in Figure 3.5 (a). This allowed us to identify the location of individual cells within the expanding colony [125]. Each transect was partitioned into 98 sections along the transect axis, where each section had length $160 \mu\text{m}$ and width $260 \mu\text{m}$. Figure 3.5 (a) shows a schematic representation of the transect through the centre of the colony. Image analysis was used to count the number of cells in each section of the transect which allowed us to calculate the dimensional cell density, $c^*(r, t)$, and the corresponding non-dimensional cell density profile, $c(r, t)$, [see section 3.3.2 and Appendix B] [125].

To determine an averaged cell density profile for each experiment, we extracted three cell density profiles from three experimental replicates (Appendix B). Each density profile was divided at the centre of the profile so that each half profile described one-half of the entire cell density profile from the centre of the colony ($r = 0$) to the leading edge ($r = R$). The corresponding non-dimensional cell density profiles from all six half profiles were averaged. Figure 3.5 (b)–(c) shows an experimental transect image at $t = 0$ hours and the corresponding averaged cell density profile using three replicates. For both initial cell densities, we observe that the density distribution at $t = 0$ hours is approximately uniform throughout the colony which is consistent with our experimental procedure where we attempted to place the cells inside the barrier as evenly as possible. The experimental transect image and corresponding averaged cell density profile at $t = 48$ hours are shown in Figure 3.5 (d)–(e). Here, we see that the leading edge of the cell colony has expanded as observed previously in the leading edge analysis (Figure 3.4 (c)–(d)).

Simulated cell density profiles were extracted from the mathematical model using the same process applied to the experimental transects. Simulations were performed using the same combinations of D and q as for the analysis of the leading edge data (Figure

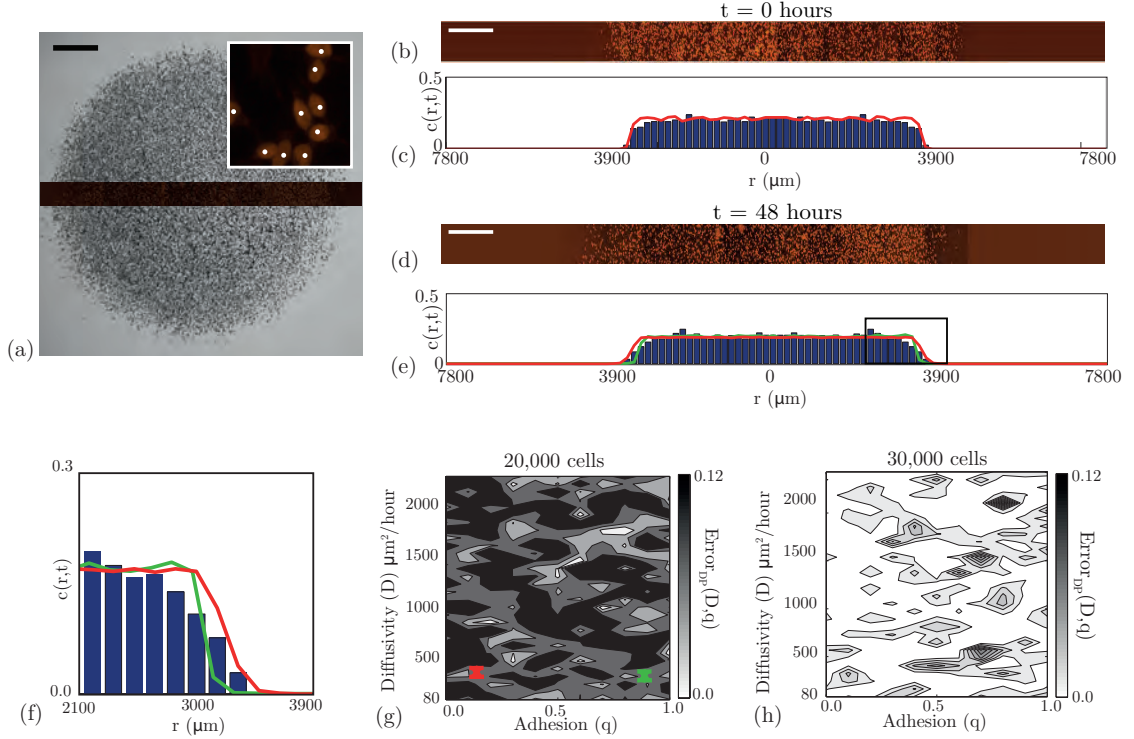


Figure 3.5: Cell density profile data does not allow us to uniquely estimate D and q . All results correspond to experiments where cells were pretreated with Mitomycin-C to prevent cell proliferation. Cell density profiles were extracted from each experiment by partitioning the transect into 98 rectangular regions. The transect is the dark region shown in (a) passing through the entire cell colony. The scale bar corresponds to 1,500 μm . The magnified image inset in (a) shows several cells which have been identified by image analysis software (white dots). Experimental transects at $t = 0$ and $t = 48$ hours are shown in (b) and (d) for experiments initialised with 20,000 cells. The scale bar corresponds to 1,500 μm . Histograms showing the experimental cell density profile along the transect are shown in (c) and (e). Each experimental cell density profile was averaged using three experiments as described in the text. The corresponding model predictions are superimposed at $t = 0$ hours in (c) and at $t = 48$ hours in (e) using five identically-prepared realisations of the model. Both curves correspond to simulations where $D = 243 \mu\text{m}^2/\text{hour}$. The red curve in (e) corresponds to weak cell-to-cell adhesion ($q = 0.1$) and the green curve corresponds to strong cell-to-cell adhesion ($q = 0.9$). The leading edge in (e) is magnified in (f). The error surfaces in (g) and (h) show $\text{Error}_{DP}(D, q)$, given by Equation 3.2, for various values of D and q . Simulation results are averaged over five identically-prepared realisations. The red and green crosses in (g) correspond to the two model solutions superimposed in (e).

3.4 (g)–(h)). The averaged experimental density profile at $t = 0$ hours for each initial cell density was used to initiate the model simulations. One realisation of the simulated density profile is superimposed onto the averaged experimental histogram in Figure 3.5 (c). In all cases, the simulated cell density profiles for each parameter combination were averaged over five identically-prepared realisations of the model. Two averaged simulated cell density profiles for simulations with $D = 81 \mu\text{m}^2/\text{hour}$ at $t = 48$ hours using low cell-to-cell adhesion strength, $q = 0.1$, and strong cell-to-cell adhesion strength, $q = 0.9$, are superimposed onto the corresponding experimental cell density profile in Figure 3.5 (e). A visual comparison of the experimental density profile and the two simulation profiles provides no definite indication of whether a low value of q or high value of q best matches the experimental measurement. This observation is confirmed by examining the magnified image of the leading edge in Figure 3.5 (f) where we again see that it is

not obvious whether the low q or the high q matches the measurements. These results indicate that comparing density profile alone information may not be able to distinguish an optimal parameter combination.

To compare the experimental and simulation density profiles for a broader combination of parameters we used an estimate of the least-squares error, $\text{Error}_{DP}(D, q)$, to determine whether there is an optimal choice of D and q to match the cell density data. The least squares error, Error_{DP} , for each set of D and q parameter sets was calculated by comparing the averaged simulated cell density profile and the corresponding averaged experimental profile using,

$$\text{Error}_{DP}(D, q) = \frac{\sum_{i=1}^2 \left(\sum_{j=1}^{98} (Ed_i^j - Sd_i^j)^2 \right)}{\sum_{i=1}^2 \left(\sum_{j=1}^{98} (Ed_i^j)^2 \right)}. \quad (3.2)$$

Here, Ed_i^j corresponds to the averaged non-dimensional cell density of the j^{th} section of the cell density profile at time i , where i corresponds to the two time points, $t = 24$ and $t = 48$ hours, averaged using three replicate experimental cell density profiles. Similarly, Sd_i^j corresponds to the equivalent density of the simulated cell density profiles, averaged over five realisations. For each combination of D and q , we calculated $\text{Error}_{DP}(D, q)$ and compared the averaged simulated cell density profile with the corresponding averaged experimental profile to produce the error surfaces in Figure 3.5 (g)–(h). The error surfaces confirm that there is no well-defined error, indicating that there is no optimal choice of D and q which indicates that density profiles cannot be used alone to estimate D and q .

Data type 3: Degree of cell clustering

The degree of cell-to-cell clustering within a group of cells is thought to indicate the presence of cell-to-cell adhesion [60, 74]. However, we note that there is no standard, widely accepted measure of cell clustering that has been proposed for this purpose when dealing with experimental data [60, 74, 121, 126].

In this work we propose to measure the degree of cell clustering by identifying isolated cells within the colony. We define an isolated cell to be a cell that appears to lack physical contact with other cells. For each experiment with Mitomycin-C pretreatment, we used image processing software to analyse six regions, containing cells stained with Propidium Iodide, located approximately in the centre of the colony. Each region has a size of $500 \mu\text{m} \times 2000 \mu\text{m}$. The approximate locations of the six regions are illustrated in Figure 3.6 (a). We note that in Figure 3.6 we adopt the convention that red circles correspond to isolated cells while black circles correspond to cells which appear to be connected to other cells within the colony. To determine the proportion of isolated cells in each region, we used image analysis software to count the total number of cells using the same procedure described in the cell density profile analysis. The number of isolated cells was counted using the image analysis software to detect those cells that occupied a circular region,

of radius $18 \mu\text{m}$, that was not occupied any other cells. The inset in Figure 3.6 (a) shows an isolated red cell which occupies a circular region, which has a radius of $18 \mu\text{m}$, that contains no other cells (Appendix B). In all cases, we manually checked the image analysis results to ensure that all isolated cells were identified correctly. Snapshots from the region analysed, shown in Figure 3.6 (b)–(c) at $t = 0$ and $t = 48$ hours, illustrate that the proportion of isolated cells decreases with time which suggests that these cells are more likely to form cell-to-cell contacts as the experiment proceeds. This observation is consistent with the idea that cell-to-cell adhesion plays an important role in the expansion of the MM127 colony. Results comparing the average percentage of isolated cells in the cell colony in each of the six regions are illustrated in Figure 3.6 (g)–(h), confirming that the proportion of isolated cells in the colony decreases over time.

To determine whether there is an optimal choice of D and q that matches our experimental measurements, we simulated the experiments using 11 equally-spaced values of D between 81 and $2430 \mu\text{m}^2/\text{hour}$, and 11 equally-spaced values of q between 0 and 1 . All simulations were performed with $\lambda = 0 / \text{hour}$ since we are dealing with Mitomycin-C pretreated cells. Image analysis software was used to automatically identify isolated cells in the simulations using exactly the same approach applied to the experimental images. Snapshots from the region analysed in each simulation are shown in Figure 3.6 (d) at $t = 0$ hours and in Figure 3.6 (e)–(f) at $t = 48$ hours using a low and high value of q , respectively. We observe that for a low value of q , the proportion of isolated simulated cells does not decrease with time. However, for a high value of q the proportion of isolated simulated cells decreases considerably. We repeated the simulations, averaging our results over twenty identically prepared realisations, for each different value of q , to determine an average estimate of the proportion of isolated simulated cells in the simulated cell colony at each time point.

The average percentage of isolated cells for three different values of q and $D = 243 \mu\text{m}^2/\text{hour}$ are superimposed onto the experimental results in Figure 3.6 (g)–(h). For both initial densities, we observe that the simulation results with $q = 0$ do not match our experimental results. Similarly, results with very high cell-to-cell adhesion strength, $q = 0.9$, also do not match. To determine the optimal value of q , the least squares error, Error_C , was calculated by comparing the average proportion of isolated cells in the experiments to the model simulations. The least squares error is given by,

$$\text{Error}_C(D, q) = \frac{\sum_{i=1}^2 (Ec_i - Sc_i)^2}{\sum_{i=1}^2 (Ec_i)^2}, \quad (3.3)$$

where, Ec_i corresponds to the proportion of cells clustered averaged over six replicates in the experiments, Sc_i corresponds to the proportion of isolated simulated cells in the model simulations, averaged over twenty realisations and i corresponds to the two time points, $t = 24$ and $t = 48$ hours.

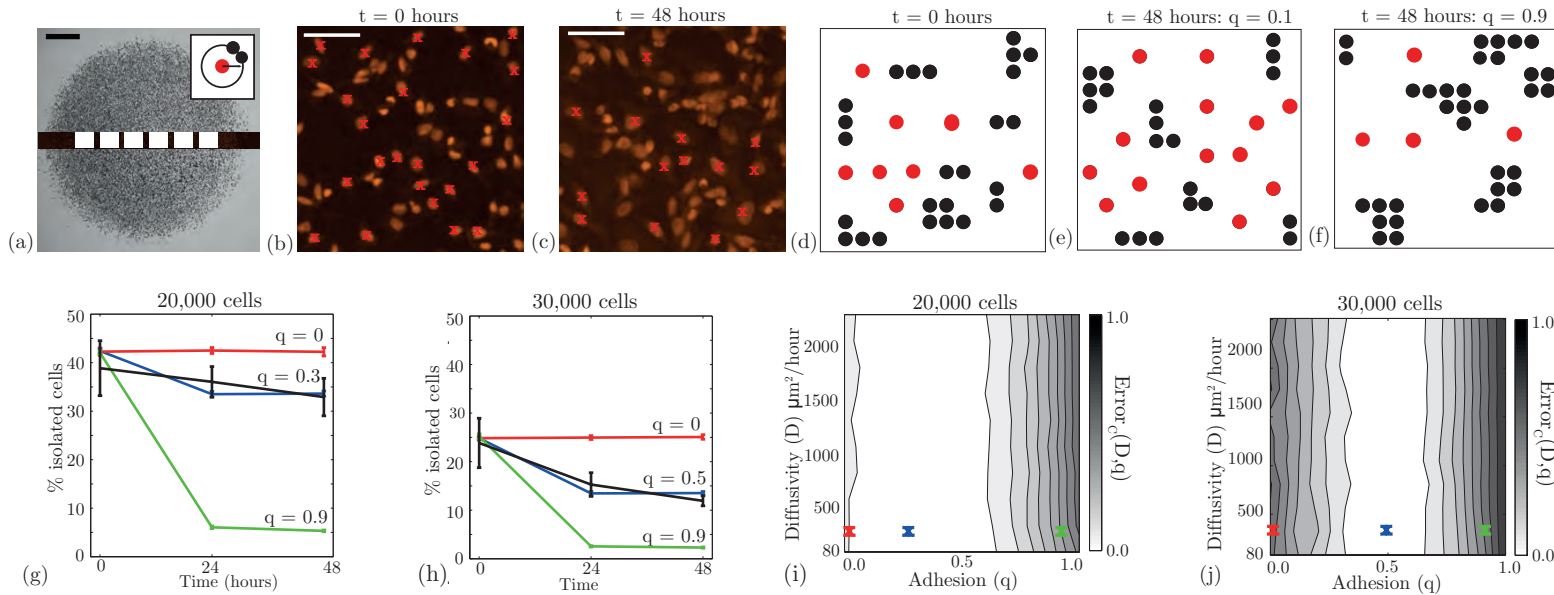


Figure 3.6: The degree of cell clustering allows us to estimate q . All results correspond to experiments where cells were pretreated with Mitomycin-C to prevent cell proliferation. Isolated cells were identified in several regions along the experimental transects, as shown to scale in (a). The scale bar corresponds to $1,500 \mu\text{m}$. The inset in (a) illustrates a schematic representation of our definition of an isolated cell that occupies a circular region of at least radius $18 \mu\text{m}$ that contains no other cells. The inset in (a) is not to scale. Experimental snapshots in (b)–(c) show Propidium Iodide images at $t = 0$ and $t = 48$ hours, respectively, for experiments initialised with 30,000 cells. The scale bar corresponds to $100 \mu\text{m}$. Red crosses indicate cells which were identified as isolated cells by the image analysis software. Snapshots of the model simulations are shown in (d)–(f), at $t = 0$ hours, at $t = 48$ hours with weak cell-to-cell adhesion, $q = 0.1$ and at $t = 48$ hours with strong cell-to-cell adhesion, $q = 0.9$. Simulations were performed using $D = 243 \mu\text{m}^2/\text{hour}$. Red circles correspond to isolated cells, while black circles indicate all other connected cells. Results in (g)–(h), show the time evolution of the average percentage of isolated cells for experiments initialised with 20,000 and 30,000 cells, respectively. The error bars correspond to one standard deviation from the mean (experimental – black, model – red, blue and green) and all simulation results were averaged over twenty realisations. Equivalent simulations of the mathematical model with no cell-to-cell adhesion (red lines) and strong cell-to-cell adhesion are superimposed (green lines). The best match solutions using $q = 0.3$ and $q = 0.5$, respectively, are shown in blue. The error surfaces in (i) and (j) show $\text{Error}_C(D, q)$, given by Equation 3.3, for various values of D and q . Simulation results are averaged over twenty identically-prepared realisations. The red, green and blue crosses in (i) and (j) correspond to the solutions superimposed in (g) and (h), respectively.

The error surfaces for each initial density are shown in Figure 3.6 (i)–(j). In contrast to our previous error surfaces for the leading edge and cell density profile analysis (Figure 3.4 (g)–(h); Figure 3.5 (g)–(h)), our results show that there is a well defined value of q corresponding to a minimum in $\text{Error}_C(D, q)$ for both initial cell densities. This suggests that there is an optimal choice of q to match our observations. We also observe that our results are insensitive to the choice of D since the error surfaces in Figure 3.6 (i)–(j) appear to be independent of the value of D . The error surfaces indicate that for the experiments initialised with 20,000 cells, the optimal choice of q is between $q = 0.1$ and $q = 0.6$ and for experiments initialised with 30,000 cells the optimal range is between $q = 0.3$ and $q = 0.6$. Simulation results using values of q in the middle of these ranges, $q = 0.3$ and $q = 0.5$, for experiments initialised with 20,000 and 30,000 cells, respectively, are superimposed in Figure 3.6 (g)–(h). The correspondence between the experimental measurements and the simulation data suggests that a low-to-moderate cell-to-cell adhesion strength is necessary to describe our measurements in the MM127 melanoma cell colony. Now that we have obtained an estimate of q , we can use this information to determine the associated range of D values using our results from the leading edge analysis (Figure 3.4 (g)–(h)) which we will discuss in section 3.3.5.

3.3.4 Estimating the rate of proliferation

Data type 4: Cell density counts

To quantify the cell proliferation rate we considered experiments performed without Mitomycin–C pretreatment so that cell proliferation is not suppressed. Propidium Iodide stained transect images were used to identify individual cells located approximately at the centre of the colony. For each replicate experiment, the number of cells in four different subregions, each of dimension $230 \mu\text{m} \times 230 \mu\text{m}$, was counted and converted into a measurement of the non-dimensional cell density, $c(t)$, (Appendix B). Here, we report values of $c(t)$, instead of $c(r, t)$, since we are focusing on the centre of each colony away from the leading edge where the cell density is approximately spatially uniform [See section 3.3.2] [125]. The approximate location and size of each subregion is illustrated in Figure 3.7 (a).

Images in Figure 3.7 (d)–(e) show snapshots of cells pretreated with Mitomycin–C indicating that the number of cells does not increase or decrease over time. This confirms that Mitomycin–C pretreatment prevents proliferation and, importantly, did not cause cell death. Snapshots in Figure 3.7 (f)–(g), where the cells are not pretreated with Mitomycin–C, indicates that the number of cells increases dramatically over time. These visual observations are confirmed by examining the evolution of the non-dimensional cell density, $c(t)$, in Figure 3.7 (b)–(c), where we again see that the cell density does not increase or decrease in cell colonies with no proliferation, and increases substantially in cell colonies with proliferation.

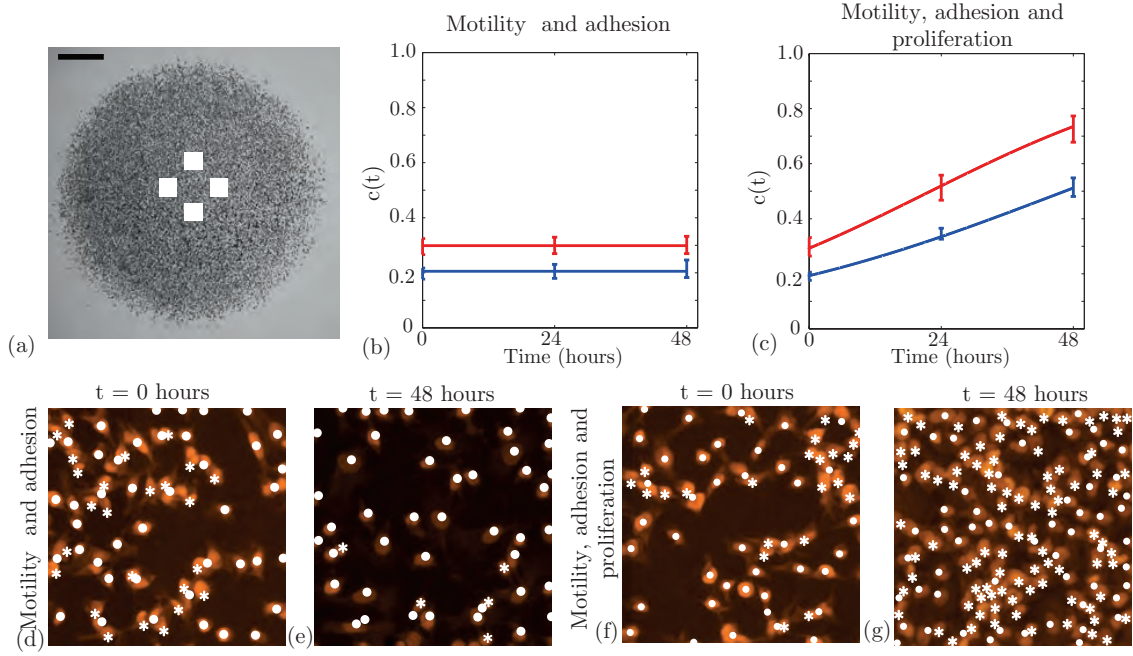


Figure 3.7: Cell density measurements where cell proliferation is not suppressed allows us to estimate λ . The approximate location of the subregions used to measure the cell density are shown in (a), where the scale bar corresponds to $1,500 \mu\text{m}$. Images in (d)–(e) show two subregions of dimensions $230 \mu\text{m} \times 230 \mu\text{m}$ for experiments at $t = 0$ hours and $t = 48$ hours, where 30,000 cells, pretreated with Mitomycin-C, were initially placed inside the barrier. Equivalent images without Mitomycin-C pretreatment are shown in (f)–(g). The Propidium Iodide staining is highlighted in orange. For each subregion, the number of cells was counted; white circles correspond to the cells automatically detected by the image analysis software and white stars indicate cells that were manually counted. The corresponding time evolution of the mean scaled density, $c(t)$, is shown in (b) and (c), where the error bars indicating one standard deviation from the mean. Blue and red data points correspond to the experiments initialised with 20,000 and 30,000 cells, respectively. Our analysis shows that the proliferation rate (λ) and the doubling time ($t_d = \log_2/\lambda$) for the experiments initialised with 20,000 cells is $\lambda = 0.0305 / \text{hour}$ and $t_d = 22.7$ hours, and for experiments initialised with 30,000 cells is $\lambda = 0.0398 / \text{hour}$ and $t_d = 17.42$ hours. The red and blue curves in (b) and (c) show the corresponding solution of the logistic equation, given by Equation 3.5, respectively.

To estimate the proliferation rate, we note that the proliferation mechanism in our mathematical model is related to the logistic equation [121] and is given by

$$\frac{dc(t)}{dt} = \lambda c(t)(1 - c(t)), \quad (3.4)$$

which has the solution

$$c(t) = \frac{c(0) \exp(\lambda t)}{1 + c(0)(\exp(\lambda t) - 1)}, \quad (3.5)$$

where $c(0)$ is the initial non-dimensional cell density. To estimate the cell proliferation rate, we found the value of λ that minimised the least squares error between our experiments and the solution of the logistic equation. Here the least squares error is given by,

$$\text{Error}_P(\lambda) = \frac{\sum_{i=1}^2 (Ep_i - Sp_i)^2}{\sum_{i=1}^2 (Ep_i)^2}, \quad (3.6)$$

where, Ep_i corresponds to the non-dimensional cell density averaged over four experimental replicates, Sp_i is the corresponding non-dimensional cell density from the solution of the logistic equation and i corresponds to the two time points, $t = 24$ and $t = 48$ hours.

For the experiments initialised with 20,000 cells without Mitomycin-C pretreatment, we found that $\lambda = 0.0305$ (0.0278, 0.0329) /hour, here the uncertainty in our estimate is given as a range in parenthesis [125]. For the equivalent experiment with Mitomycin-C pretreatment we have $\lambda = 0.0002$ (0, 0.0015) /hour. For the experiments initialised with 30,000 cells, we found $\lambda = 0.0398$ (0.0338, 0.0444) /hour for the experiments without Mitomycin-C pretreatment. For the experiments initialised with 30,000 cells, we found $\lambda = 0.0001$ (0, 0.0027) /hour for the experiments with Mitomycin-C pretreatment. The relevant logistic growth curves, given by Equation 3.5, are superimposed in Figure 3.7 (b)–(c) and illustrate that the proliferation rate estimates obtained describe the observed changes in the experimental cell density over time. We note that our estimates of λ is associated with a doubling time, $t_d = \log_2/\lambda$, of 22.7 and 17.42 hours for experiments initialised with 20,000 and 30,000 cells, respectively.

3.3.5 Predicting the spatial expansion of a melanoma cell colony

We now test whether our independently-derived estimates of D , q and λ accurately predict the location of the leading edge and the cell density profiles of the expanding melanoma cell colony. Experimental images of the entire cell colony in Figure 3.8 (a)–(c), (e)–(g) compare the distribution of cells at $t = 0$ and $t = 48$ hours, both with and without Mitomycin-C pretreatment. We visually observe that the colonies without proliferation do not appear to expand as fast as the colonies with proliferation. The overall increase in the average radius of the expanding colonies without proliferation after $t = 48$ hours is 2.2%. In contrast, the average radius increase in expanding melanoma cell colonies with proliferation is 9.1%. These results illustrate that proliferation plays a major role in the spatial expansion of melanoma cell colonies.

To compare our model predictions with the experimental measurements we combined our results using all the information obtained from different types of experimental data. For experiments initialised with 20,000 cells we estimated that $q = 0.3$. We obtained an estimate of D from the error surfaces associated with the leading edge data Figure 3.4 (g). For $q = 0.3$, the associated range of D which have the lowest error are between $D = 81$ and $D = 567 \mu\text{m}^2/\text{hour}$. Similarly, for experiments initialised with 30,000 cells, we estimated that $q = 0.5$, giving a corresponding range of D values between $D = 81$ and $D = 729 \mu\text{m}^2/\text{hour}$. For both initial densities, we simulate the experiments with a value of D within the range obtained that gave the minimum error in Figure 3.4 (g)–(h). In summary, for experiments initialised with 20,000 cells, we estimate $D = 162 \mu\text{m}^2/\text{hour}$, $q = 0.3$ and $\lambda = 0.0305 / \text{hour}$ and for experiments initialised with 30,000 cells, we estimate $D = 243 \mu\text{m}^2/\text{hour}$, $q = 0.5$ and $\lambda = 0.0398 / \text{hour}$. We note that our estimates indicate some weak dependence on the initial numbers of cells since the values of the cell diffusivity, strength of cell-to-cell adhesion and proliferation rate all increase slightly as the initial numbers of cells placed inside the barrier increases.

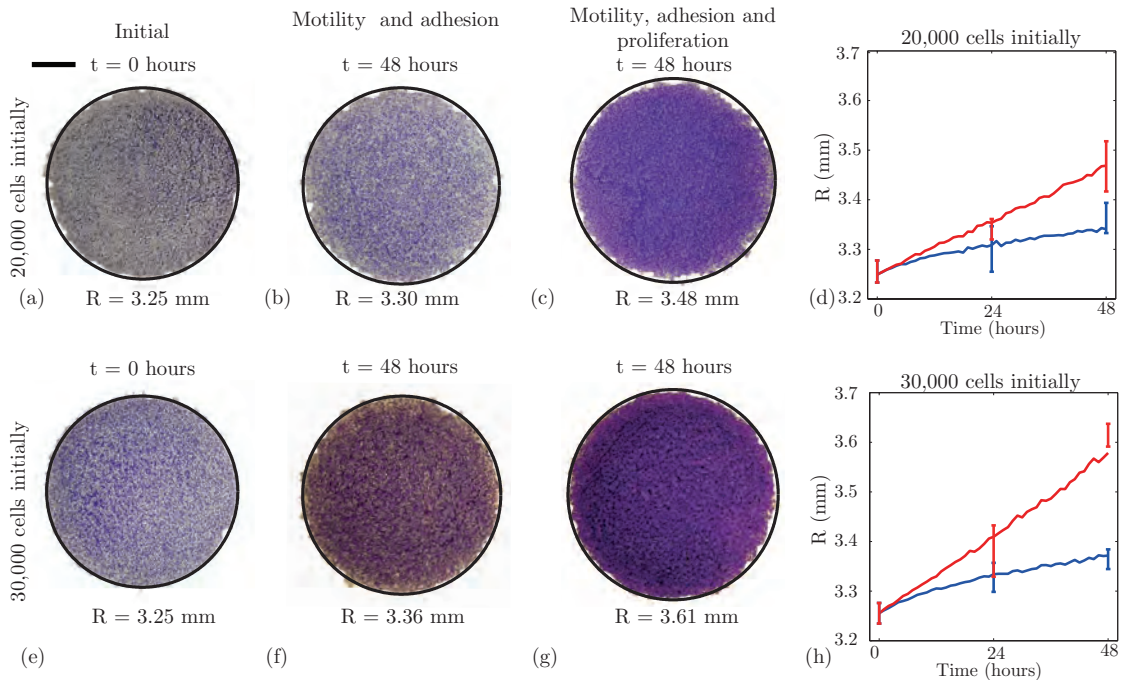


Figure 3.8: Independent estimates of D , q and λ predict the spatial extent of the expanding colony. Experimental measurements of the radius of the expanding colony were compared to predictions from the parameterised mathematical model using the parameter estimates determined previously. Results in (a) and (c), and (e) and (g) compare the position of the leading edge for experiments where 20,000 and 30,000 cells were initially placed inside the barrier, respectively. The scale bar corresponds to 1,500 μm . Images are shown at $t = 0$ hours (a) and (e), at $t = 48$ hours for the experiments with Mitomycin-C pretreatment (b) and (f), and at $t = 48$ hours without Mitomycin-C pretreatment (c) and (g). The solid curves superimposed (black) on each image correspond to the relevant simulation which has been converted into an equivalent circular area. In all cases, simulation results were averaged over three realisations. Results in (d) and (h) show the mean radius calculated from the experimental images at $t = 0$, 24 and 48 hours, with error bars indicating one standard deviation from the mean. The corresponding average radius of the simulated expanding colony is superimposed in (d) and (h). Blue lines correspond to experiments where proliferation was suppressed using Mitomycin-C pretreatment, while red lines correspond to experiments where proliferation was not suppressed. Simulations were averaged over three identically-prepared realisations. Simulations of the experiments initialised with 20,000 cells correspond to $D = 162 \mu\text{m}^2/\text{hour}$, $q = 0.3$ and $\lambda = 0.0305 / \text{hour}$, and simulation of the experiments initialised with 30,000 cells correspond to $D = 243 \mu\text{m}^2/\text{hour}$, $q = 0.5$ and $\lambda = 0.0398 / \text{hour}$.

We performed simulations of experiments using our estimates of D , q and λ to examine whether the parameterised mathematical model predicts the differences observed in the experiments where cell proliferation is suppressed compared with the observations when cell proliferation is allowed (Appendix B). The predictions of the model, in terms of the average circular area enclosing the leading edge of the expanding colony, are superimposed onto the corresponding experimental image in Figure 3.8 (a)–(c), (e)–(g) showing that the parameterised model accurately matches the experimental observations. Analysing all images at $t = 0$, 24 and 48 hours, we produced the data in Figure 3.8 (d) and (h) comparing the radius of the expanding colony measured in the experiments with the predictions of the model. We note that the prediction of the mathematical model at $t = 48$ hours for the experiments without Mitomycin-C pretreatment, initialised with 30,000 cells, slightly underestimated the experimental data. Despite this, overall our comparison indicates that the parameterised model predicts the time evolution of the radius of the expanding

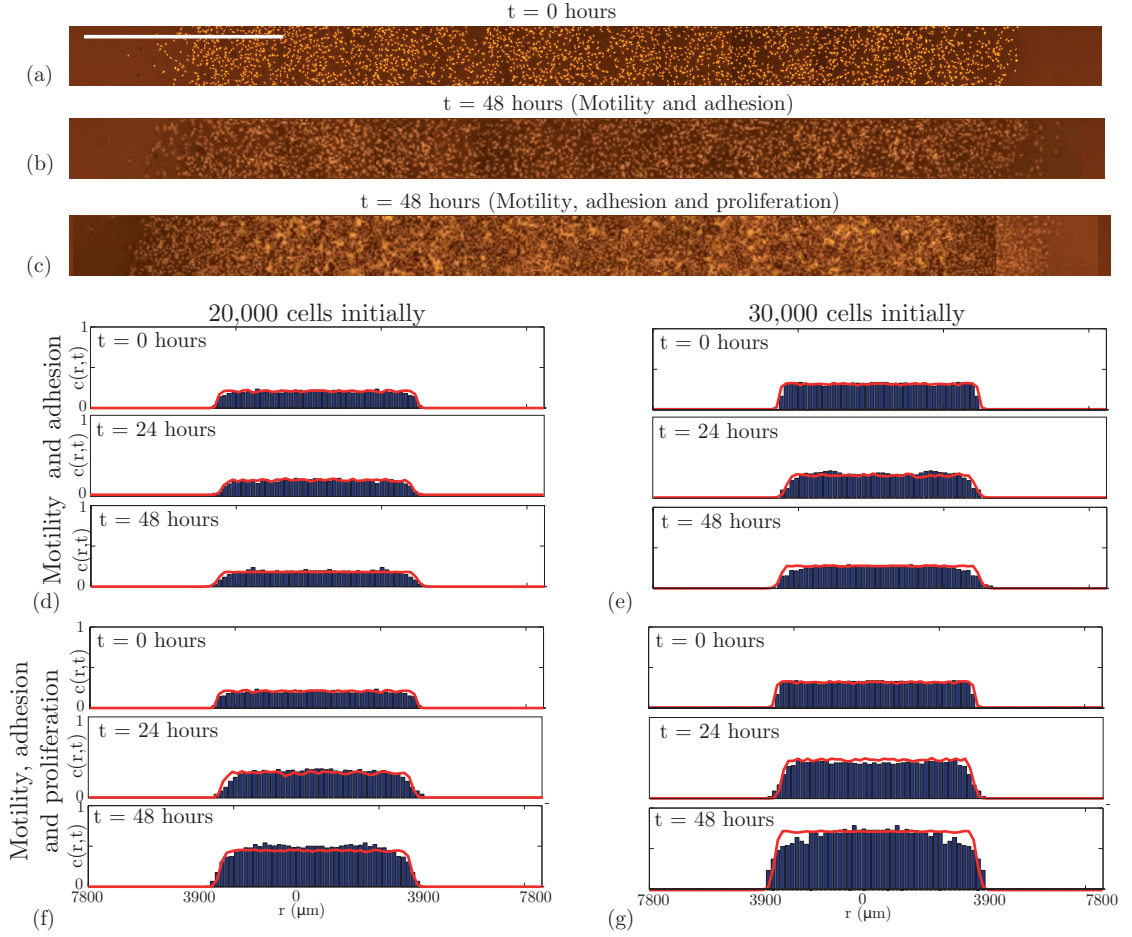


Figure 3.9: Independent estimates of D , q and λ predict the density profiles in the cell colony. Experimental measurements of the cell density profile are compared with the predictions of the mathematical model using the parameter estimates reported previously. Images of the transects for the experiments initialised with 30,000 cells are shown at $t = 0$ hours (a), at $t = 48$ hours where proliferation was suppressed (b), and at $t = 48$ hours where proliferation was not suppressed (c). The scale bar corresponds to 1,500 μm . Experimental histograms and the corresponding simulated cell density profiles for all sets of experiments at $t = 0$, $t = 24$ and $t = 48$ hours, both with and without proliferation, are shown in (d)–(g). Simulations were averaged over five identically-prepared realisations. Model simulations of the experiments initialised with 20,000 cells correspond to $D = 162 \mu\text{m}^2/\text{hour}$, $q = 0.3$ and $\lambda = 0.0305 / \text{hour}$, and for experiments initialised with 30,000 cells, simulations correspond to $D = 243 \mu\text{m}^2/\text{hour}$, $q = 0.5$ and $\lambda = 0.0398 / \text{hour}$.

melanoma cell colony and captures the differences in our experiments where proliferation was either allowed or suppressed.

We now test whether our parameterised model can predict the cell density profile throughout the entire expanding colony for all cases considered in our experimental program. Experimental images in Figure 3.9 (a)–(c) highlight major visual differences between the distribution of cells in the experiments where we suppressed cell proliferation relative to the equivalent experiment where we allowed cell proliferation. The corresponding cell density profiles extracted from the experimental images are shown in Figure 3.9 (d)–(g). Equivalent simulations of these experimental conditions using our parameterised mathematical model are superimposed onto the experimental density profiles and we note that in all cases the match between the model prediction and the experimental measurements

are excellent. This confirms that our parameterised mathematical model accurately predicts both the spatial extent of the expanding cell population and the distribution of individual cells within the expanding melanoma cell colony. Moreover, our approach can predict how differences in individual cell behaviour, such as the cell proliferation rate, affect the emergent properties of the expanding colony.

3.4 Discussion

Despite compelling evidence that cell-to-cell adhesion plays an important role in many expanding cell populations, standard mathematical modelling approaches often neglect to include any such mechanism [85, 97, 113, 116, 125, 132]. This may explain why reported estimates of the cell diffusivity can vary widely since these estimates have often been obtained by calibrating mathematical models which neglect to incorporate cell-to-cell adhesion [85, 121, 125, 132]. To overcome these issues combined experimental and modelling approaches that can separately identify and quantify the roles of cell motility, cell-to-cell adhesion and cell proliferation are required.

In our work, we used a combined experimental and modelling approach to independently quantify the roles of cell motility, cell-to-cell adhesion and cell proliferation in an expanding colony of MM127 melanoma cells. Our experimental approach used a circular barrier assay, while our modelling approach incorporated cell-to-cell adhesion as well as cell motility and cell proliferation mechanisms. In contrast to previous approaches, we extracted multiple types of data from the same barrier assay and used these different kinds of data to attempt to independently quantify the cell motility rate, D , cell-to-cell adhesion strength, q , and proliferation rate, λ . To separate the role of cell proliferation from the roles of cell motility and cell-to-cell adhesion, we first performed a set of experiments where we suppressed proliferation to quantify D and q . We then performed a second set of experiments with proliferation to quantify the cell proliferation rate, λ . All experiments were repeated at two initial cell densities and each experiment was replicated three times.

We extracted three different types of data from experiments where proliferation was suppressed to identify D and q . Our first type of data was to estimate the area enclosed by the leading edge of the expanding colony to determine whether there was a unique choice of D and q that matched the experimental measurements. Our analysis of the leading edge data indicates that this commonly-used measurement is insufficient to uniquely identify D and q suggesting that additional data is required. It is important to recognise the limitations of the leading edge data since this is one of the most commonly-reported types of data [137]. In an attempt to overcome the limitations of the leading edge data, we extracted detailed cell density profiles throughout the entire colony. Our attempts to calibrate the mathematical model to these more detailed measurements also failed to identify a unique choice of D and q to match the measurements.

In an attempt to estimate the strength of cell-to-cell adhesion we then measured the degree of cell clustering in the expanding melanoma cell colony by measuring the proportion of isolated cells within the colony. We found this to be a convenient measure of the degree of cell clustering since isolated cells were easily identifiable using an automated image processing software. Our results indicated that a low to moderate cell-to-cell adhesion strength in the mathematical model provided the best match to the measurements. Once we had estimated q we were then able to identify a range of D from combining our results regarding the degree of cell clustering with our results describing the time evolution of the position of the leading edge of the expanding cell colony.

To estimate the proliferation rate we measured the temporal change in cell density in a set of experiments where cell proliferation was not suppressed. Our estimates of λ indicate that the role of cell proliferation in the experiments is considerable since the doubling time is approximately 20 hours and experiments were performed over a period of 48 hours. We used our estimates of D , q and λ to make predictions about the expansion of the melanoma cell colony which confirmed that our parameterised mathematical model matched the experiments and was able to accurately predict differences between the results when cell proliferation was suppressed compared to experiments when cell proliferation was allowed. In summary, we showed that the spatial expansion of the melanoma cell colony is significantly enhanced by cell proliferation. We also found that our estimates of D , q and λ are weakly dependent on the initial cell density in the experiments. This is an important observation since many experimental and modelling studies do not consider the effect of the initial density in a barrier assay; however, our results illustrate that these effects could be important [125].

One of the advantages of our mathematical modelling approach is that the discrete model explicitly represents cell motility, cell-to-cell adhesion and cell proliferation processes. The model is straightforward to implement and provides us with a relatively straightforward physical interpretation of how different mechanisms acting at the level of an individual cell contributes to the population-level expansion of the cell colony. Most importantly, when combined with appropriate experimental data, our model allows us to separately identify, and quantify, the role of each individual cell-level mechanism in the expanding cell colony.

A schematic illustration of our systematic approach for identifying and quantifying the roles of cell motility, cell proliferation and cell-to-cell adhesion is given in Figure 3.10. Our approach can be summarised in the following way: for a particular cell colony we begin with a hypothesis about which particular mechanisms might be involved in the expansion of that colony. We then attempt to determine whether these putative mechanisms are present in the cell colony using visual inspection of the experimental data or immunofluorescence techniques. If the mechanisms are present, we identify an appropriate modelling method and include model parameters which control that particular mechanism of interest. Next, we attempt to determine what type of experimental data could be used to estimate the relevant model parameters. After we have extracted this

data, we use the mathematical model to simulate the experiment in an attempt to understand if a particular choice of parameter(s) can predict the observed behaviour. If the model predictions give a good agreement with the experimental observations we stop the process. Otherwise, if we find that we do not have enough types of data to completely parameterise the model we should collect more types of different data and repeat the process iteratively. If this approach fails, then the experimental or modelling approach should be reconsidered. In our case, we found that using this approach implied that we had to consider multiple data types to independently identify and quantify the mechanisms controlling the expansion of a melanoma cell colony. We suggest that this general framework could be used to analyse other biological processes.

A clear consequence of our work is that while it is relatively simple to incorporate detailed mechanisms into a mathematical model, it becomes increasingly difficult to independently identify the contributions of each mechanism in the mathematical model using experimental data. However, we anticipate that for every additional mechanism and parameter incorporated into a mathematical model of collective cell behaviour, further additional experimental data types are required so that we can parameterise the mathematical model. This quickly becomes infeasible when multiple mechanisms are considered. For example, in our work, we incorporated three different factors into the mathematical model (cell motility, cell-to-cell adhesion and cell proliferation) and we found that we needed to consider at least four different data types to quantify these mechanisms.

Our work has been aimed at improving our understanding of how 2D *in vitro* colonies of melanoma cells expand. An important limitation of our work is that it cannot be directly applied to three-dimensional (3D) *in vitro* experiments since the techniques used to quantify the cell motility rate, strength of cell-to-cell adhesion and cell proliferation rate in 2D cell colonies do not directly translate to 3D cell colonies. For example, the leading edge of a cell colony in 2D is straightforward to locate using standard imaging software and analysis [137]. In 3D, however, detection of the edge, or surface, of the cell colony is significantly more challenging and requires more sophisticated imaging software and more detailed image analysis algorithms [30, 31, 45, 83]. Similar difficulties are also relevant in terms of locating and counting individual cells within a 3D colony [30, 78].

Our work has been focused on interpreting *in vitro* measurements of cell colony expansion [30]. Extending our approach to *in vivo* colony expansion would involve dealing with many more mechanisms that are not present in the *in vitro* system [30, 78]. These additional mechanisms could include more complicated signalling pathways that regulate morphological and phenotypic cell changes, more complicated interactions between cells and their heterogeneous environment as well as the impact of nutrient deficiency, for example [63, 68]. These additional mechanisms could mean that the amount of data required to independently identify and quantify each mechanism *in vivo* could be impossible to collect. However, despite these difficulties, the fundamental premise of our framework, that we require additional data to uniquely identify additional mechanisms, remains valid.

We would also like to acknowledge and discuss some further difficulties that directly impacted our 2D *in vitro* assays. One of the original aims of this work was to analyse experiments over a period of $t = 72$ hours to determine whether acquiring additional data over a longer period of time would assist in identifying and quantifying the mechanisms driving *in vitro* colony expansion. Unfortunately, during our initial set of experiments we observed that the cell culture medium became discoloured after $t = 72$ hours, indicating that the cells were stressed. Fortunately, no such indication of cell stress was evident before $t = 72$ hours, which is why we have presented data here for $t = 0, 24$ and 48 hours. A preliminary analysis of the data associated with the $t = 72$ hour experiments did not provide us with any additional information about the mechanisms driving colony expansion and this suggests that the difficulties associated with interpreting our data after $t = 0, 24$ and 48 hours can not be alleviated by performing longer experiments. In summary, our approach is limited since we could only perform experiments over a relatively short period of time.

Originally, we also aimed to perform experiments at different initial cell densities. During our preliminary experimental investigations we found that cell colonies initialised with less than 15,000 cells produced extremely diffuse fronts that were impossible to locate and analyse using the image analysis software employed here. We also performed experiments that were initialised with more than 35,000 cells and found that these high density barrier assays tended to form 3D cell aggregates instead of a 2D monolayer. One constraint of our present modelling approach is that it is suitable for describing the expansion of 2D cell colonies and cannot be directly applied to 3D experiments [125]. These difficulties mean that our methods were restricted to a range of initial cell densities. Despite these restrictions, our systematic approach of analysing multiple data sets from the same experiment provided us with practical insights into the role of various mechanisms that drive the expansion of melanoma cell colonies. We anticipate that this approach could be used to quantify the roles of cell motility, cell proliferation and cell-to-cell adhesion in different melanoma cell lines and other cell lines.

In this work, we used a combined experimental and mathematical modelling approach to systematically quantify the cell motility rate, strength of cell-to-cell adhesion and cell proliferation rate in an expanding colony of MM127 melanoma cells. Our work illustrates that the relative contributions of cell motility, cell-to-cell adhesion and cell proliferation are impossible to assess using standard experimental approaches, such as measuring the area enclosed by the leading edge. Our work highlights the importance of using multiple data types to independently identify and quantify the mechanisms involved in the spatial expansion of both melanoma cell colonies and we anticipate that our approach will also be relevant to other cell lines.

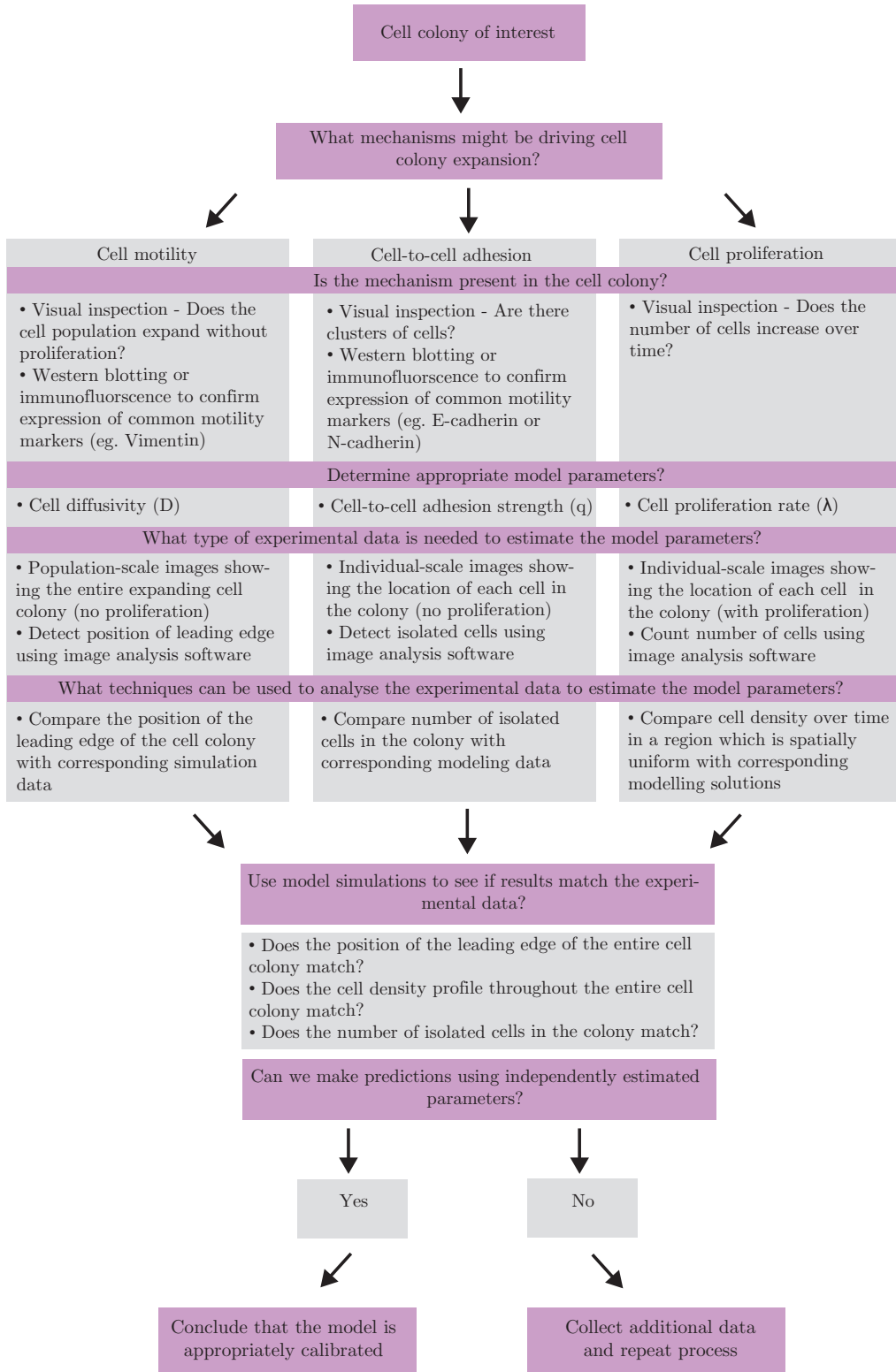


Figure 3.10: Framework illustrating a systematic approach that can be used to independently identify and quantify the mechanisms driving cell colony expansion. The mechanisms thought to be driving the expansion of a selected cell colony are identified and confirmed using visual inspection or other advanced experimental techniques. A mathematical modelling approach is selected and appropriate model parameters defined. Various experimental data is extracted to estimate the model parameters. For each additional mechanism considered, we anticipate that we will require at least one further piece of information from the experiments to quantify the role of that particular mechanism. The experimental data is analysed by extracting simulation data from the mathematical model and testing how well the model predictions match with the experimental data. If the modelling predictions provide a good match to the experimental data we stop the process. Alternatively, if the modelling predictions do not uniquely match the experimental data, we repeat the process iteratively using additional types of data extracted.

CHAPTER 4

Sensitivity of edge detection methods for quantifying cell migration assays

A paper published in *PLoS One*.

Treloar, K.K. & Simpson, M.J. Sensitivity of edge detection methods for quantifying cell migration assays. *PLoS ONE*. **8**, e67389 (2013).

Abstract

Quantitative imaging methods to analyse cell migration assays are not standardised. Here we present a suite of two-dimensional barrier assays describing the collective spreading of an initially-confined population of 3T3 fibroblast cells. To quantify the motility rate we apply two different automatic image detection methods to locate the position of the leading edge of the spreading population after 24, 48 and 72 hours. These results are compared with a manual edge detection method where we systematically vary the detection threshold. Our results indicate that the observed spreading rates are very sensitive to the choice of image analysis tools and we show that a standard measure of cell migration can vary by as much as 25% for the same experimental images depending on the details of the image analysis tools. Our results imply that it is very difficult, if not impossible, to meaningfully compare previously published measures of cell migration since previous results have been obtained using different image analysis techniques and the details of these techniques are not always reported. Using a mathematical model, we provide a physical interpretation of our edge detection results. The physical interpretation is important since edge detection algorithms alone do not specify any physical measure, or physical definition, of the leading edge of the spreading population. Our modelling indicates that variations in the image threshold parameter correspond to a consistent variation in the local cell density. This means that varying the threshold parameter is equivalent to varying the location of the leading edge in the range of approximately 1–5% of the maximum cell density.

4.1 Background

Cell migration plays a key role in development [98,157], repair [85,86,113] and disease [132, 153]. Abnormalities in cell migration are associated with malignant spreading [69,70,153] and slowed wound repair [142]. Potential therapies aimed at treating these abnormalities may seek to manipulate the rate of migration by applying pharmaceutical drugs or topical treatments [69,142,143]. Development and validation of such therapies can be assessed by comparing assays performed under control conditions with an equivalent assay where the treatment has been applied [30]. *In vitro* migration assays can also be used to quantify the role of experimental variations such as the influence of different substrates [85, 86]. Regardless of the purpose for performing an *in vitro* cell migration assay, image detection methods that can be used to quantify the rate of cell migration are an essential element of interpreting and quantifying such assays.

Various types of assays have been used to study cell migration including two-dimensional scratch assays [85, 86] and three-dimensional Transwell assays [35, 121]. More recently, two-dimensional circular barrier assays have become a popular alternative to scratch assays [56] since they do not damage the cell monolayer, or the substrate, and are therefore thought to be more reproducible than scratch assays [69, 145]. Barrier assays are performed by placing a population of cells inside a circular barrier. The barrier is lifted and the subsequent spreading of the population is measured [125]. An essential element of interpreting and quantifying a barrier assay is to locate the position of the leading edge of the spreading population so that the rate at which the cell population spreads across the substrate can be calculated.

A common approach to quantify the cell migration rate in a barrier assay is to report the percentage change in area [7, 56, 94, 145, 161]. This can be expressed as

$$M(t) = \frac{A(t) - A(0)}{A(0)} \times 100, \quad (4.1)$$

where $A(0)$ is the initial area enclosed by the population of cells, $A(t)$ is the area enclosed by the population of cells at time t , and $M(t)$ is the percentage change in area at time t .

Estimates of cell migration rates using Equation (4.1) are often obtained by hand tracing the area enclosing the spreading cell population on an image of the assay [55, 160]. Unfortunately, hand tracing the area enclosed by the leading edge of a spreading cell population is subjective [135]. To overcome this limitation, automated image analysis software, including ImageJ [66] and MATLAB's Image Processing Toolbox [90], have become important alternatives to hand tracing [69, 164]. These software tools use edge detection and segmentation algorithms to determine the location of the leading edge of the spreading cell population. This data can then be used to quantify the cell migration rate in terms of Equation (4.1). In addition to using automatic edge detection algorithms, it is also possible to implement user-defined edge detection options in MATLAB's Image Processing Toolbox [90] so that the user has complete control over the choice of image detection thresholds.

Since there is no standardised method for quantifying the location of the leading edge in a barrier assay, it is often difficult, if not impossible, to meaningfully compare published measures of cell migration in terms of Equation (4.1). This difficulty is exacerbated by the fact that previously published results have been obtained using different image analysis techniques and the details are not always reported [64, 81, 99, 100, 151]. To address this limitation, here we apply three different edge detection techniques to a set of images from a two-dimensional barrier assay describing the collective spreading of a population of 3T3 fibroblast cells. We apply three different edge detection techniques to the same experimental data set and compare results from two commonly used automatic edge detection techniques and one manual edge detection technique. Our results indicate that the location of the leading edge is sensitive to the details of the edge detection procedure and this can lead to significantly different quantitative estimates of cell migration. Using a reasonable range of threshold values we show that estimates of cell migration, given by Equation (4.1), can vary by as much as 25% for the same data set.

To provide further insight into the edge detection techniques, we also interpret our results using a mathematical model to quantitatively describe the temporal cell spreading process associated with the barrier assay. Using previously-determined estimates of the cell diffusivity [125], we show that the location of the leading edge, as defined by the image detection methods, corresponds to contours of cell density in the range of approximately 1–5% of the maximum cell packing density. Comparing the location of the leading edge determined by the image detection methods and the mathematical model of the cell spreading provides us with a simple, but meaningful, physical interpretation of the threshold parameters used in the image detection methods.

4.2 Experimental methods

4.2.1 Cell culture

Murine fibroblast 3T3 cells (ATCC, CCL-92, Manassas, VA, USA) were grown in T175 cm² tissue culture flasks (Nunc, Thermo Scientific, Denmark) using Dulbecco's modified Eagle medium (Invitrogen, Australia) supplemented with 5% fetal calf serum (FCS) (Hyclone, New Zealand), 2mM L-glutamine (Invitrogen) and 1% v/v Penicillin/Streptomycin (Invitrogen) in 5% CO₂ at 37 °C. Prior to confluence, cells were lifted using 0.05 % trypsin (Invitrogen, Australia) and viable cells were counted using a Trypan blue exclusion test and a haemocytometer.

4.2.2 Circular barrier assay

Cell migration experiments were performed using a circular barrier assay. Metal–silicone barriers, 6000 µm in diameter (Aix Scientifics, Germany), were cleaned, sterilised, dried and placed in the center of the wells in a 24-well tissue culture plate with 500 µL of culture medium. The wells in tissue culture plate have a diameter of 15,600 µm. Two different densities of cell suspensions were used: 10,000 and 30,000 cells/µL. Ten µg/mL Mitomycin-C (Sigma Aldrich, Australia) was added to the cell solutions for one hour to inhibit cell proliferation [112]. One µL of cell suspension was carefully inserted in

the barrier to ensure that the cells were approximately evenly distributed. Once seeded, the tissue culture plate was left for one hour in a humidified incubator at 37°C and 5% CO₂ to allow the cells to attach to the surface. After the cells attached to the surface, the barriers were removed and the cell layer was washed with serum free medium (SFM; culture medium without FCS) and replaced with 0.5 mL of culture medium. Plates were incubated at 37°C in 5% CO₂ for four different times, $t = 0, 24, 48$ and 72 hours. Each barrier assay, for each time point, was repeated three times. Images of the spreading cell population were obtained by fixing cells with 10% formalin, followed by 0.01% crystal violet (Sigma-Aldrich, Australia). The stain was rinsed with phosphate-buffered saline (Invitrogen, Australia) and the plates were air-dried. Images were acquired using a stereo microscope with a Nixon digital camera (DXM1200C).

4.2.3 Edge detection methods

Three methods were used to detect the location of the leading edge: (i) a manual detection method written using MATLAB's Image Processing Toolbox (version 7.12) [90], (ii) an automated method using MATLAB's Image Processing Toolbox (version 7.12) [90] and (iii) an automated method using ImageJ (version 1.46r) [66]. All three methods are based on a Sobel edge detection algorithm [1] but differ in the way that the thresholds are chosen. Although different edge detection methods are available, such as the active contour method [95] and the Canny method [49, 50], we choose to focus on MATLAB and ImageJ implementations of the Sobel method since these software tools are widely available.

Manual edge detection using the MATLAB Image Processing Toolbox

Customised image processing software was written using the MATLAB Image Processing Toolbox [90]. The following procedure was used to detect the location of the leading edge of the spreading population. The image was imported (*imread*) and converted from colour to grayscale (*rgbtogray*). The Sobel method was applied to the grayscale image by specifying a sensitivity threshold value S , in which all edges weaker than S are excluded (*edge/grayscale image, 'Sobel', S*). The lines in the resulting image were dilated to show the outlines of detected edges (*strel(7), imdilate*). Remaining empty spaces in the images were filled and all objects disconnected from the leading edge were removed (*imfill, imclearborder*). The image was smoothed and filtered to remove any noise (*imerode, medfilt2*) and the area enclosed by the detected leading edge was estimated (*regionprops*).

Before we analysed the experimental images, we undertook a preliminary step where we applied a wide range of threshold values to our experimental images, $S \in [0.001, 0.5]$. We found that thresholds in the range $S \in [0.01, 0.08]$ produced visually reasonable results.

Automatic edge detection using the MATLAB Image Processing Toolbox

The manual edge detection method described in section 4.2.3 can be implemented in an automated mode by allowing the MATLAB Image Processing toolbox to automatically determine the threshold, S , for each individual image [90]. The following procedure

was used to detect the location of the leading edge. The image was imported (*imread*) and converted from color to grayscale (*rgbtogray*). The Sobel method was applied in the automatic mode (*edge[grayscale image, 'Sobel']*). The lines in the resulting image were dilated (*strel(7)*, *imdilate*). Remaining empty spaces were filled and all objects disconnected from the leading edge were removed (*imfill*, *imclearborder*). The image was smoothed and filtered (*imerode*, *medfilt2*) and the area enclosed by the detected leading edge was estimated (*regionprops*).

Automatic edge detection using ImageJ

ImageJ software [66] was used to automatically detect the position of the leading edge. For all images, the image scale was set (*Analyze–Set scale*) and colour images were converted to grayscale (*Image–Type–32bit*). The Sobel method was used to enhance edges (*Process–Find Edges*). The image was sharpened (*Process–Find Edges*) and an automatically determined threshold was applied (*Image–Adjust–Threshold–B&W–Apply*). After applying the Sobel method again (*Process–Find Edges*), the wand tracing tool, located in the main icons box, was used to select the detected leading edge. The area enclosed by the detected leading edge was calculated (*Analyze–Set Measurements–area*, *Analyze–Measure*).

4.3 Modelling methods

To provide a physical interpretation of our image analysis results, we use a mathematical model to relate the edge detection results to the spatial distribution of the cell density. We model the spreading population of cells using a linear diffusion equation [85, 86, 113], with previously determined values of the cell diffusivity [125] [see Chapter 2]. The effects of cell proliferation are neglected in our mathematical model, and this is consistent with our experimental protocol where cells were pretreated with Mitomycin–C to suppress cell proliferation [112].

To relate our edge detection results to the cell density, we consider the solution of the two-dimensional axisymmetric diffusion equation

$$\frac{\partial c}{\partial t} = D \left(\frac{\partial^2 c}{\partial r^2} + \frac{1}{r} \frac{\partial c}{\partial r} \right), \quad (4.2)$$

where r is radial position, t is time, $c(r, t)$ is the non-dimensional cell density and D is the cell diffusivity, which is a measure of random, undirected, cell motility [121, 125]. The non-dimensional cell density is obtained by scaling the dimensional cell density, $\bar{c}(r, t)$, by the carrying capacity density K . This gives $c(r, t) = \bar{c}(r, t)/K$, with $c(r, t) \in [0, 1]$. The carrying capacity density is estimated by assuming that the maximum packing density of cells corresponds to a square packing density. The average cell diameter is 25 μm , giving $K \approx 1.6 \times 10^{-3}$ cells per μm^2 [125].

We solve Equation (4.2) on the domain $0 \leq r \leq 7,800 \mu\text{m}$. The boundary at $r = 0 \text{ mm}$ corresponds to the centre of the well and we apply a symmetry condition, $\partial c / \partial r = 0$, here [124]. The boundary at $r = 7,800 \mu\text{m}$ corresponds to the outer edge of the well

which is a physical boundary and so we apply a zero flux boundary condition here. The boundary condition at $r = 7,800 \mu\text{m}$ is irrelevant for our barrier assay results since the leading edge of the spreading cell front did not reach this boundary on the time scale of the experiments [125]. The initial condition is given by,

$$c(r, 0) = \begin{cases} c_0, & 0 \leq r < 3,000 \text{ mm}, \\ 0, & 3,000 \leq r \leq 7,800 \text{ mm}, \end{cases} \quad (4.3)$$

where c_0 is the density of cells initially inside the barrier. Assuming that the cells have an average diameter of $25 \mu\text{m}$ [125], we can pack $3000/25$ cells across the radius of the barrier. Hence, we estimate that the maximum number of cells that can be packed in a monolayer in the barrier is $\pi r^2 = \pi(3000/25)^2 = 45,239$. To specify the initial condition using for Equation (5.6), we assume that either 10,000 or 30,000 cells are uniformly distributed within the barrier giving $c_0 = 10,000/45,239 \approx 0.22$ and $c_0 = 30,000/45,239 \approx 0.66$, respectively.

Numerical solutions of Equation (4.2) are obtained using a finite-difference approximation on a grid with a uniform grid spacing of width δr , and implicit Euler stepping with uniform time steps of duration δt [17, 117].

4.4 Results

4.4.1 Locating the leading edge

To demonstrate the sensitivity of different image processing tools, we apply the manual edge detection method, with different threshold values, to images showing the entire spreading populations in several different barrier assays. Images in Figure 4.1 (a) and (g) show the spreading population in a barrier assay with 30,000 cells at $t = 0$ and $t = 72$ hours, respectively. Visually, the leading edge of the cell population at $t = 0$ (Figure 4.1 (a)) appears to be relatively sharp and well-defined. In contrast, the leading edge of the cell population at $t = 72$ hours (Figure 4.1 (g)) is diffuse and less well-defined. This indicates that it is difficult to visually identify the location of the leading edge after the barrier has been lifted and the cell population spreads outwards, away from the initially-confined location.

Our visual interpretation of the images indicate that the precise location of the leading edge is not always straightforward to define. To explore this subjectivity, we use the manual edge detection method (section 4.2.3) by specifying different values of the Sobel threshold, S . Results in Figure 4.1 (b)–(c) show the detected leading edges at $t = 0$ hours using a high threshold ($S = 0.0800$) and a low threshold ($S = 0.0135$), respectively. For both thresholds, the detected leading edges appear to be appropriate representations of the leading edge of the spreading population, and are very similar to each other. Results in Figure 4.1 (h)–(i) show the detected leading edges at $t = 72$ hours for a high threshold ($S = 0.0565$) and a low threshold ($S = 0.0135$), respectively. Both detected edges at $t = 72$ hours appear to be reasonable approximations to the location of the leading edge

of the spreading population, however they are very different to each other which indicates that the results are sensitive to S .

To qualitatively compare the two leading edges detected at $t = 0$ hours (Figure 4.1 (b)–(c)) we superimpose the two detected leading edges in Figure 4.1 (d) and show a magnified portion of these edges in Figure 4.1 (e). The superimposed edges confirm that the choice of S has relatively little influence at $t = 0$ hours. We now compare equivalent results at $t = 72$ hours from Figure 4.1 (h)–(i). Superimposing the two leading edges for high and low S thresholds in Figure 4.1 (j) indicates that there is a distinct difference between them. A magnified portion of the detected leading edges is shown in Figure 4.1 (k) which also supports our initial observation that it is difficult to visually delineate the leading edge of the spreading population when the leading edge is diffuse.

Our edge detection results at $t = 0$ hours and $t = 72$ hours, in Figure 4.1 (a)–(e) and (g)–(k), qualitatively indicate that the threshold value is important in detecting the edge at a later time. To quantitatively compare our edge detection results, we calculate the area enclosed by the detected leading edge and convert this area into an equivalent circle with radius $\sqrt{A/\pi}$. Results in Figure 4.1 (f) show the equivalent circular areas for low and high thresholds at $t = 0$ hours. The area of the low and high thresholds are 32.2 mm^2 and 31.1 mm^2 , respectively, giving a relatively small difference of 1.1 mm^2 . These two circles are almost visually indistinguishable at the scale shown in Figure 4.1 (f), confirming there is very relatively little difference regardless of the threshold. Equivalent circular areas in Figure 4.1 (l) show the low and high threshold areas at $t = 72$ hours superimposed on the initial area. The area of the two outer circles in Figure 4.1 (l) is 52.9 mm^2 and 60.8 mm^2 , giving a relatively large difference of 7.9 mm^2 . If we take the initial area to be $A(0) = 31.1 \text{ mm}^2$ then Equation (4.1) gives us $M(72) = 70.1\%$ for the high threshold leading edge in Figure 4.1 (h) and $M(72) = 95.5\%$ for the low threshold leading edge in Figure 4.1 (i). These results indicate that the increase in area enclosed within the leading edge of the spreading cell population is very sensitive to the choice of threshold and the results can vary by as much as 25%

4.4.2 Comparing edge detection techniques

To explore and quantify the sensitivity in detecting the leading edge for our barrier assays, we now extend our initial investigation and detect the location of the leading edge across all experimental images acquired at different time points. We applied the manual edge detection technique to all images using thresholds within the range $S \in [0.015, 0.8]$. For each threshold value, we calculated the area enclosed by the detected leading edge and we analysed the images from each experimental replicate separately so that we could calculate the mean area enclosed by the leading edge, $\langle A(t) \rangle$. We estimated the variability amongst the experimental replicates by calculating the standard deviation about the mean, σ . Our results are summarised in Table 4.1, where we see that the variability amongst the experimental replicates is small with typical values of $\sigma/\langle A(t) \rangle < 5\%$. From this point onward we will report all our experimental results in terms of the mean area, $\langle A(t) \rangle$, and for convenience we will drop the angle bracket notation.

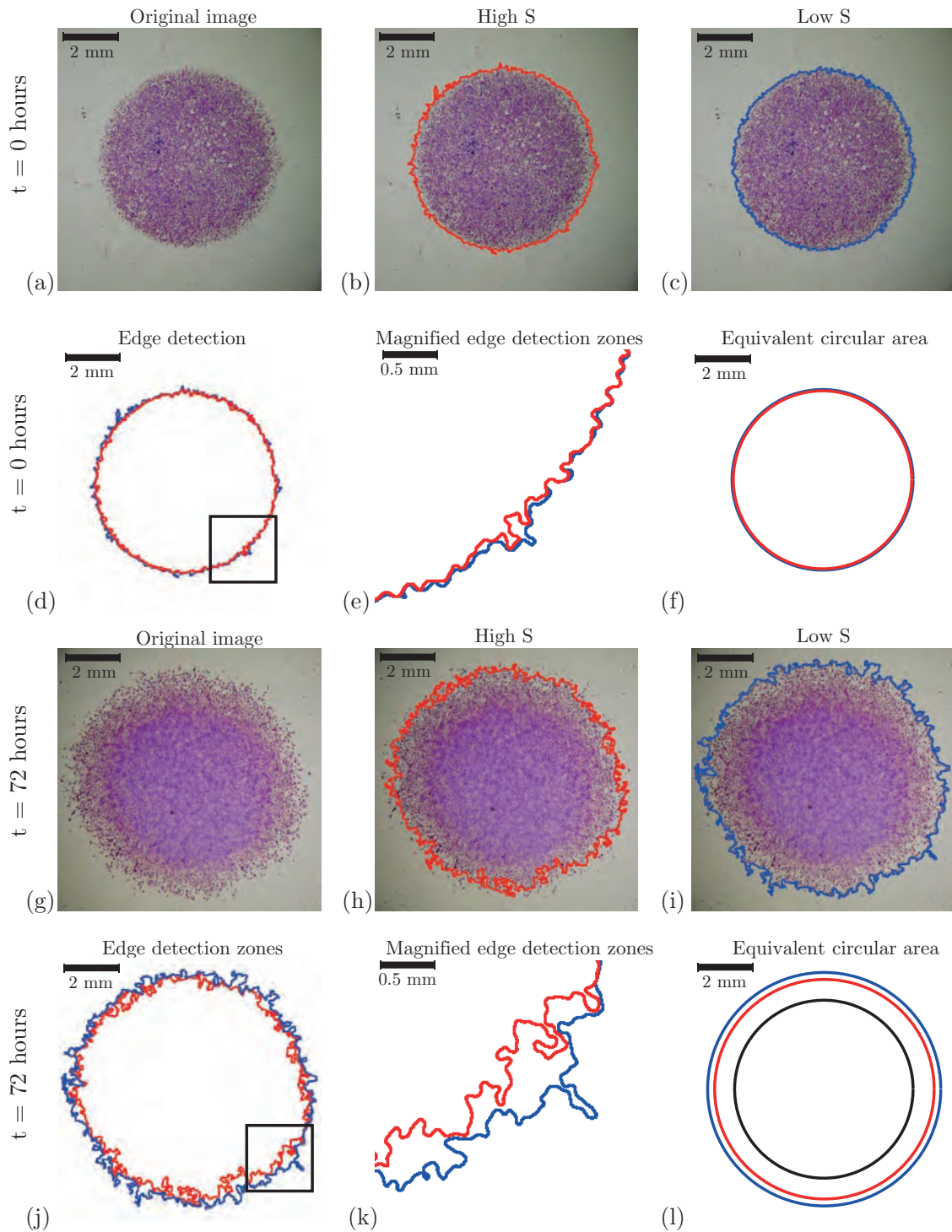


Figure 4.1: Images of barrier assays containing 30,000 cells at $t = 0$ hours (a)–(f) and $t = 72$ hours (g)–(l). (a)–(g): Images from the barrier assay. (b)–(h): Leading edge for a high threshold S in red, superimposed on an image of the spreading population. (c)–(i): Leading edge for a low threshold S in blue, superimposed on the an image of the spreading population. (d)–(j): Comparing high and low S detected edges at $t = 0$ hours. (e)–(k): Detailed comparison of the detected edges in the boxed area in (d) and (j). (f)–(l): Comparing equivalent circular areas. The black line in (l) shows the initial circular area. Scales are given in each subfigure.

Number of cells	Time (hours)	Mean area Manual S High (mm ²)	Standard deviation Manual S High (mm ²)	Mean Area Manual S Low (mm ²)	Standard deviation Manual S Low (mm ²)	Mean area Auto ImageJ (mm ²)	Standard deviation Auto ImageJ (mm ²)	Mean area Auto Matlab (mm ²)	Standard deviation Auto Matlab (mm ²)
10,000	0	27.4	0.67	30.1	1.61	30.3	0.83	29.0	1.64
	24	31.9	0.91	36.0	0.63	35.0	2.26	34.2	0.78
	48	36.2	1.91	43.4	0.68	41.3	1.11	39.1	2.64
	72	39.7	1.98	47.1	0.62	45.8	0.81	44.6	0.81
30,000	0	31.1	0.21	33.5	0.34	33.1	1.40	30.0	1.56
	24	44.8	2.11	50.3	1.08	49.9	1.4	45.0	2.12
	48	50.0	1.52	55.5	1.78	55.2	1.57	51.4	1.47
	72	52.9	2.25	60.8	2.11	55.9	3.01	54.6	3.10

Table 4.1: Edge detection area (mm²) results. Summary of edge detection results comparing the manual edge detection technique (Manual), the MATLAB Image Processing Toolbox automatic technique (Auto MATLAB) and the ImageJ automatic technique (Auto ImageJ). All results show the average area estimated using three identically-prepared and analysed experimental replicates. The variability amongst experimental replicates is estimates using the standard deviation.

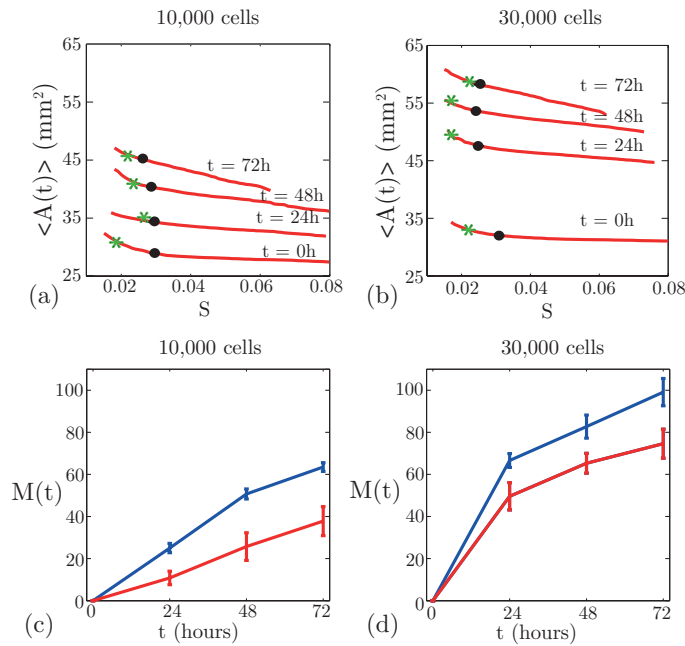


Figure 4.2: Comparing three edge detection techniques for barrier assays with two different cell densities for 10,000 cells in (a) and (c), and 30,000 cells in (b) and (d). (a)–(b): Comparison of the three edge detection techniques showing the mean area enclosed by the leading detected edge at $t = 0, 24, 48$ and 72 hours with time points indicated. Red lines correspond to the the manual edge technique using MATLAB's Image Processing Toolbox for a range of the threshold parameter $S \in [0.015, 0.08]$. Black dots correspond to the automatic MATLAB results and the green asterisks correspond to the automatic ImageJ results. (c)–(d): The migration rate of cells in the barrier assays expressed as $M(t)\%$ using Equation (4.1). Results correspond to the minimum (red) and maximum (blue) average areas detected using the manual MATLAB technique. Error bars correspond to one standard deviation about the mean.

We now compare the sensitivity of our manual edge detection results by analysing the images at using a range of threshold values for several different time points for barrier assays with two different initial cell densities. Results in Figure 4.2 (a)–(b) show the relationship between the average area enclosed by the detected leading edge and the threshold value S for a barrier assay with 10,000 and 30,000 cells, respectively. Initially, for the barrier assay with 10,000 cells, the minimum average area enclosed by the detected leading edge is 27.4 mm² and the maximum area is 30.1 mm². For the barrier assay with 30,000 cells, the minimum and maximum initial average area enclosed by the detected leading edge is 31.1 mm² and 33.5 mm², respectively. For both initial cell densities, the difference between the maximum and minimum detected initial area is relatively small compared to the differences we observe at later times, as we will now demonstrate.

Results in Figure 4.2 (a)–(b) show that the average area enclosed by the detected leading edges increases with time as the cell population spreads outwards from the barrier. We expect that the sensitivity in detecting the location of the leading edge will increase with time as the population spreads and the leading edge becomes increasingly diffuse. For the barrier assays initialised with 10,000 cells, results in Figure 4.2 (a) show that the minimum area detected at $t = 24$ hours is 31.9 mm² and the maximum area detected is 36.0 mm², giving a difference of 4.1 mm². At $t = 48$ hours the minimum area is 36.2 mm² and the maximum area is 43.4 mm², giving a difference of 7.2 mm². At $t = 72$ hours,

the minimum area is 39.7 mm^2 and the maximum area is 47.1 mm^2 , giving a relatively large difference of 7.4 mm^2 . These results indicate that the sensitivity in detecting the leading edge is relatively large and that the results depend on the choice of the threshold, and this sensitivity increases with time as the leading edge of the spreading population becomes increasingly diffuse.

Equivalent manual edge detection results for barrier assays containing 30,000 cells in Figure 4.2 (b) show similar trends to the results previously reported for the barrier assays with 10,000 cells. The minimum detected average areas at 24, 48 and 72 hours are 44.8 mm^2 , 50.0 mm^2 and 52.9 mm^2 , while the maximum detected average areas are 50.3 mm^2 , 55.5 mm^2 and 60.8 mm^2 , respectively. Comparing the minimum and maximum average areas for the barrier assay with 30,000 cells gives differences of 5.5 mm^2 , 5.5 mm^2 and 7.9 mm^2 at $t = 24, 48$ and 72 hours, respectively.

Our results using the manual edge detection method illustrate that there are many plausible approximations of the leading edge of the spreading populations for a range of threshold values. We now compare the manual edge detection algorithm with two automatic edge detection methods. We applied the automatic MATLAB and ImageJ techniques (section 4.2.3 and section 4.2.3), to the same images we previously analysed using the manual edge detection method. For both automatic techniques, the average area enclosed by the detected edge was calculated and compared to the average areas obtained using the manual edge detection method. Results in Figure 4.2 (a)–(b) show the automatic edge detection results relative to the manual results, and estimates of the mean and standard deviation of the area obtained using the automatic techniques are given in Table 4.1. The MATLAB and ImageJ results confirm that both automatic techniques give estimates that are consistent with those obtained using the manual edge detection method. However, the automatic techniques are restricted in the sense that they can only detect one particular location whereas the manual edge detection method can produce many different results, all of which are reasonable estimates of the position of the leading edge of the spreading cell population.

Number of cells	Time (hours)	$M(t)$ Manual S High	$M(t)$ Manual S Low	$M(t)$ Auto ImageJ	$M(t)$ Auto Matlab
10,000	24	10.8	25.0	14.4	17.9
	48	25.7	50.7	35.0	34.8
	72	37.8	63.5	49.7	53.8
30,000	24	49.6	66.6	50.8	50.0
	48	65.6	82.7	66.8	71.3
	72	74.6	99.1	68.9	82.0

Table 4.2: Quantifying the cell migration rate using Equation 4.1. The cell migration rate in terms of $M(t)$ using Equation 4.1 and the average results from Table 4.1. Results are reported for the manual edge detection technique with a high threshold (Manual S high), the manual edge detection technique with a low threshold (Manual S Low), the MATLAB Image Processing Toolbox automatic technique (Auto MATLAB) and the ImageJ automatic technique (Auto ImageJ).

We now use Equation (4.1) to quantify the observed cell migration in our barrier assays. This approach requires that we use an estimate of $A(0)$, the initial average area. Our previous results indicate that the initial average area of the spreading population ranged from 27.4 to 30.1 mm² for the barrier assay with 10,000 cells while the initial average area of the spreading population ranged from 31.1 to 33.5 mm². To estimate $A(0)$ we will take the average of these maximum and minimum estimates so that we have $A(0) = 28.8$ and $A(0) = 32.3$ mm² for the barrier assays with 10,000 and 30,000 cells, respectively. To estimate the sensitivity of our results as a function of the threshold value in the manual edge detection technique, we apply Equation (4.1) using the minimum and maximum detected average areas from our manual edge detection method. The details of the results for all three edge detection techniques are given in Table 4.2. Although we observe that the two automatic methods produce similar results for certain assays at certain times, the differences between the results for the two automatic edge detection methods can be very large with $M(72) = 68.9\%$ for the barrier assay with 30,000 cells according to the ImageJ results whereas $M(72) = 82.0\%$ for the same assay according to the automatic MATLAB method. Profiles in Figure 4.2 (c)–(d) show how $M(t)$ varies with time according to the results obtained from the manual edge detection method applied to the images from the barrier assays initialized with 10,000 and 30,000 cells, respectively. Figure 4.2 (c)–(d) each contain two sets of results corresponding to the average estimate of $M(t)$ calculated using the low S threshold, and the average estimate of $M(t)$ calculated using the high S threshold. The differences between the low and high threshold results in Figure 4.2 (c) is 14.2 %, 25.0 % and 25.7 % for $t = 24, 48$ and 72 hours, respectively. The difference between the low and high threshold results in Figure 4.2 (d) (30,000 cells) is 17.0 %, 17.0 % and 24.5 % for $t = 24, 48$ and 72 hours, respectively. These results indicate that estimates of cell migration using Equation (4.1) are very sensitive to the details of the edge detection technique and that this sensitivity increases with time.

4.4.3 A physical interpretation of the leading edge

Previously, we used three different edge detection techniques to determine the location of the leading edge of spreading cell populations in several barrier assays. Although these techniques produce visually reasonable approximations to the position of the leading edges, the techniques do not give us any physical measure, or definition, of the leading edge. To address this, we now interpret our edge detection results using a mathematical model of the cell spreading process. For each barrier assay experiment, we solve Equation (4.2) using the appropriate boundary and initial conditions (Section 4.3) and previous estimates of the cell diffusivity [125]. The solution profiles in Figure 4.3 (a) and (d), show the predicted cell density near the leading edge of the spreading cell populations in the barrier assay at $t = 24, 48$ and 72 hours. The difference between the two initial cell densities in the barrier assays is shown in these profiles since we have $c_0 = 0.22$ in the centre of the barriers for the assays initialised with 10,000 cells (Figure 4.3 (a)) whereas we have $c_0 = 0.66$ in the centre of the barriers for the assays initialised with 30,000 cells (Figure 4.3 (d)).

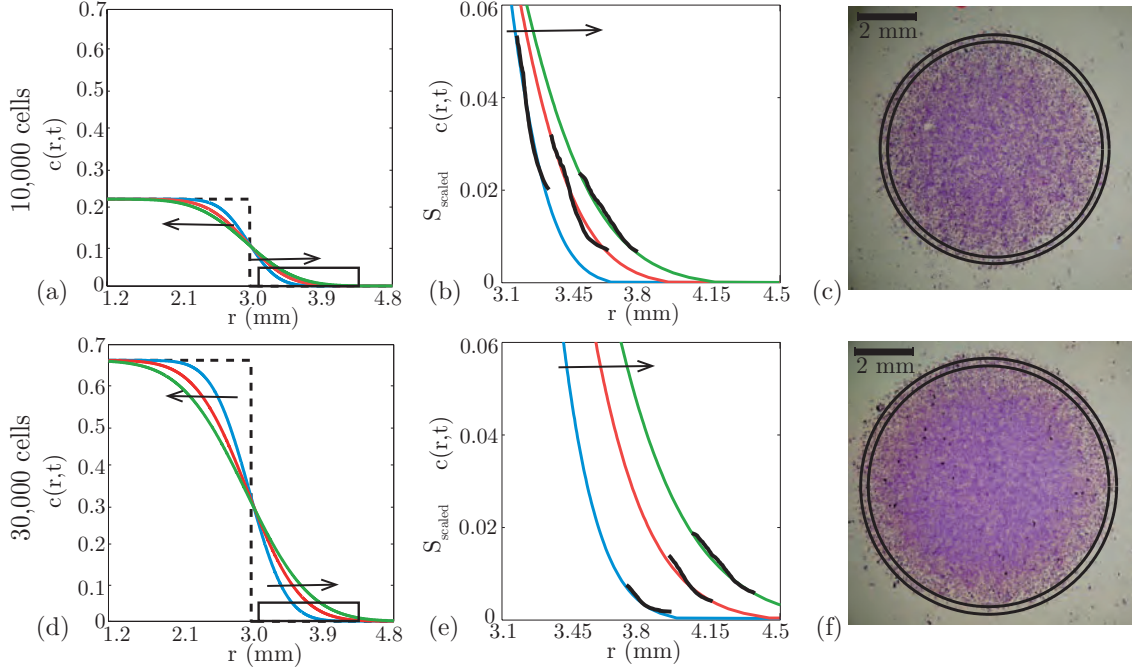


Figure 4.3: (a) and (d): Solutions of Equation (4.2) showing the density profiles near the leading edge at $t = 0$ (dotted black), $t = 24$ (blue), $t = 48$ (red) and $t = 72$ hours (green). Arrows indicate the direction of increasing time. The initial conditions is given by Equation (5.6) with $c_0 = 0.22$ and $c_0 = 0.66$ for barrier assays with 10,000 and 30,000 cells, respectively. Numerical solutions of Equation (4.2) are obtained with $\delta r = 1.0 \mu\text{m}$ and $\delta t = 0.005$ hours, with $D = 1700 \mu\text{m}^2/\text{hour}$ and $D = 2900 \mu\text{m}^2/\text{hour}$ for barrier assays with 10,000 and 30,000 cells, respectively. (b) and (e) The detail of the solutions of Equation (4.2) from the boxed area in (a) and (d) compared with the scaled manual edge detection results (black) from Figure 4.2 (a) and (c). (c) and (f) Images of a barrier assay with 10,000 and 30,000 cells at $t = 72$ hours, respectively. The contours of the solution of Equation (4.2) are superimposed. The values of the contours are $c_{\min} = 0.007$ and $c_{\max} = 0.026$ for the barrier assay with 10,000 cells, and $c_{\min} = 0.008$ and $c_{\max} = 0.020$ for the barrier assay with 30,000 cells.

To determine a physical relationship between the threshold value S and the cell density at the corresponding detected edge, we compare our manual edge detection results to solutions of Equation (4.2). For each set of averaged edge detection results, we scale the threshold values to match the corresponding solution of Equation (4.2). The scaling is given by

$$S_{\text{scaled}} = c_{\min} + (c_{\max} - c_{\min}) \frac{S - S_{\min}}{S_{\max} - S_{\min}}, \quad (4.4)$$

where c_{\min} and c_{\max} are the minimum and maximum contours of the solution of Equation (4.2), $c(r, t)$, which enclose the same average area detected by the manual edge detection method applied with the minimum and maximum thresholds, S_{\min} and S_{\max} , respectively.

Profiles in Figure 4.3 (b) and (e) compare the scaled edge detection results to corresponding solutions of Equation (4.2) at $t = 24, 48$ and 72 hours for barrier assays with 10,000 and 30,000 cells, respectively. For both initial density experiments at all time points, the shape of the $c(r, t)$ density profiles matches the shape of the edge detection results. This match indicates that varying the threshold value S corresponds to a consistent variation in the spatial distribution of cell density in the spreading cell population. Comparing the

edge detection results to the corresponding contours of the cell density, we observe that the manual edge detection technique identifies a range of leading edges corresponding to cell densities of 2–5.5 % at $t = 24$ hours, 0.9–3.2 % at $t = 48$ hours and 0.8–2.5 % at $t = 72$ hours for the barrier assays with 10,000 cells. Equivalent results in Figure 4.3 (e) indicates that the manual edge detection technique identifies a range of leading edges corresponding to cell densities of 0.2–0.8 %, 0.5–1.5 % and 0.8–1.8 %, for $t = 24, 48, 72$ hours for the barrier assay with 30,000 cells. In summary, the manual edge detection technique identifies a range of leading edges corresponding to cell densities of approximately 1–5 % of the maximum packing density.

The images in Figure 4.3 (c) and (f) show snapshots from two barrier assays at $t = 72$ hours with 10,000 and 30,000 cells, respectively. To illustrate the location of the leading edge, defined by contoured solutions of Equation (4.2), we superimpose the c_{\min} and c_{\max} contour of the appropriate solution of Equation (4.2). In both cases we observe that the c_{\min} and c_{\max} contours are reasonable approximations to the location of the position of the leading edge of the spreading populations. In each experiment, the difference between the c_{\min} and c_{\max} contours are relatively large and this recapitulates the sensitivity observed previously in Figure 4.1 (h)–(i).

4.5 Discussion

Cell migration is an essential aspect of development [98, 157], repair [85, 86, 113] and disease [132, 153]. *In vitro* cell migration assays are routinely used to assess the migration potential of different cell types [69, 70] as well as assessing the potential for different types of treatment strategies aimed at regulating cell migration [30, 142, 143, 145]. Currently, many studies report results from cell migration assays without specifying the details of how the assays are measured or interpreted [64, 81, 99, 100, 151]. In an attempt to address this limitation we compare three different image processing techniques to quantify the migration rate of cells in a two-dimensional barrier assay [125]. Our visual interpretation of the images from the barrier assays indicate that the position of the leading edge of the spreading population is relatively sharp and well-defined at the beginning of the assay. However, we observe that the leading edge of the spreading cell population becomes increasingly diffuse and less well-defined at later times as the cell population spreads across the substrate. We quantify the rate of cell migration using a standard measure, given by Equation (4.1), describing how the area enclosed by the leading edge of the spreading population increases with time. To explore how such a standard measure of cell migration depends on the edge detection methods we calculate the location of the leading edge of the spreading population using three different image processing tools. In summary, our results indicate that estimates of the cell migration rate are very sensitive to the details of the image processing tools and we show that our estimates of the cell migration rate can vary by as much as 25% for the same data set. These differences depend on the choice of threshold used in the edge detection technique. Our measurements indicate that the concept of the area enclosed by the leading edge is poorly defined and we suggest that one way to overcome these difficulties is to use a direct measurement of cell

density. For example, a nuclear stain could be used to reveal the locations of individual cells within the spreading population [125].

In addition to comparing estimates of cell migration using different image processing techniques, we also provide a physical interpretation of the results from the manual edge detection technique by using a mathematical model of the cell spreading process. We use a previously-parameterised [125] mathematical model to describe the spatial and temporal variation in cell density associated with the barrier assays and we compare our modelling results with the edge detection results. For all images processed by the manual edge detection technique, we identified a range of Sobel threshold values, from S_{\min} to S_{\max} , that could be used to produce a reasonable estimate of the location of the leading edge of the spreading populations. We scaled these values so that they corresponded with a range of cell density contours, from c_{\min} to c_{\max} , corresponding to the minimum and maximum contours of the relevant solution of Equation (4.2). Our results indicate that varying the threshold S corresponds to a consistent variation in the spatial distribution of cell density in the spreading cell population. In particular, the manual edge detection technique identifies the leading edge of the population within a range of the cell density of approximately 1-5% of the maximum packing density. The close match between the position of the leading edge as a function of the Sobel threshold and the solution of the partial differential equation describing the spreading process suggests that this type of information could be used to estimate the diffusivity of the cells, D . This could be a useful method for estimating the cell diffusivity since it is well known that estimates of cell diffusivity can vary by as much as an order of magnitude and these variations depend on the kind of cell and the substrate being considered [133].

As a result of this study, we recommend that the location of the leading edge of a spreading cell population in a cell migration assay should not be determined using any kind of hand tracing technique. Instead, a computational image processing technique should be used to reduce the impact of the subjectivity of the analyst. Our results demonstrate that the computational edge detection techniques can be very sensitive to the choice of threshold applied to the image. Therefore, we recommend that images of cell migration assays should be analysed using a manual edge detection technique and that the details of the image thresholds should be reported.

We anticipate that our results for the two-dimensional barrier assay will also be relevant to other types of cell migration assays such as scratch assays [85,86], or different types of circular barrier assays that include the outward migration of cells away from an initially-confined circular population [125] as well as barrier assays describing the inward migration of cell populations into an initially-vacant circular region [69,70,145]. We also expect that our results for the two-dimensional barrier assay could be extended by considering other types of experimental conditions. For example, here we chose to present results for cells that were pretreated to prevent cell proliferation [112] so that we could study cell spreading processes driven by cell migration alone in the absence of cell proliferation. Given that the shape of the leading edge of the spreading cell population depends on the relative contribution of cell migration and cell proliferation [125,132], we expect that comparing

different edge detection results for different cell populations with different relative rates of cell proliferation and cell migration will also be of interest [121, 123]. Finally, although we have presented our image analysis techniques in the context of analysing an *in vitro* cell migration assay, these concepts will also be relevant when considering *in vivo* cell spreading, such as in the detection of the leading edge of spreading melanomas [59, 95].

CHAPTER 5

Are *in vitro* estimates of cell diffusivity and cell proliferation rate sensitive to assay geometry?

A paper published in the *Journal of Theoretical Biology*.

Treloar, K.K., Simpson, M.J., McElwain, D.L.S. & Baker, R.E. Are *in vitro* estimates of cell diffusivity and cell proliferation rate sensitive to assay geometry? *J. Theor. Biol.* **356**, 71–84 (2014).

Abstract

Cells respond to various biochemical and physical cues during wound-healing and tumour progression. *In vitro* assays used to study these processes are typically conducted in one particular geometry and it is unclear how the assay geometry affects the capacity of cell populations to spread, or whether the relevant mechanisms, such as cell motility and cell proliferation, are somehow sensitive to the geometry of the assay. In this work we use a circular barrier assay to characterise the spreading of cell populations in two different geometries. Assay 1 describes a tumour-like geometry where a cell population spreads outwards into an open space. Assay 2 describes a wound-like geometry where a cell population spreads inwards to close a void. We use a combination of discrete and continuum mathematical models and automated image processing methods to obtain independent estimates of the effective cell diffusivity, D , and the effective cell proliferation rate, λ . Using our parameterised mathematical model we confirm that our estimates of D and λ accurately predict the time-evolution of the location of the leading edge and the cell density profiles for both assay 1 and assay 2. Our work suggests that the effective cell diffusivity is up to 50% lower for assay 2 compared to assay 1, whereas the effective cell proliferation rate is up to 30% lower for assay 2 compared to assay 1.

5.1 Background

Cell migration and cell proliferation are essential mechanisms that drive wound-healing and tumour progression [26, 51, 89, 153, 158]. During these processes, cells sense and respond to various biochemical and physical cues [7, 18, 77, 84, 149]. Although the role of biochemical cues has been widely explored, it remains relatively unclear how physical cues, such as the local geometry, affect the capacity of cell populations to spread [7, 18, 77, 84, 149].

Wound-healing and tumour progression are often studied in the same context since the mechanisms that drive these processes are thought to be similar [22, 28, 44, 115, 153]. Despite their similarities, these processes have distinct geometries: (i) during wound-healing, cell populations spread inwards to close the wound void, and (ii) during tumour progression, cell populations spread outwards causing the tumour to expand [7, 153].

Cell-based assays are commonly-used to quantify the capacity of cell populations to spread *in vitro* [7, 30, 69, 70, 78, 144]. Several types of assays have been developed to investigate cell population spreading in two and three dimensions including Transwell, scratch, exclusion zone and spheroid assays [7, 30, 78, 144]. While these assays have been used to study the behaviour of various cell lines *in vitro*, most studies neglect to explicitly consider the role of geometry when conducting or interpreting these assays and it is unclear how results obtained for one particular geometry translate into another [7, 30, 78, 144]. Recent work using microfabrication methods focused on creating various-sized channels through which cells could migrate, with the observation that the speed of the leading edge of the cell population depends on the channel width [148]. Therefore, it seems reasonable to assume that assay geometry could play a role in determining the rate at which cell populations spread.

An alternative approach to understand how differences in geometry affect cell population spreading is to conduct a two-dimensional cell spreading assay where the direction of the spreading is intentionally varied. In this work, we will consider two types of assays:

Assay 1. This is a tumour-like assay initialised by placing cells inside a barrier, which is then lifted, allowing the population to spread outwards [7, 78].

Assay 2. This is a wound-like assay initiated by placing cells outside a barrier, which is then lifted, allowing the population to spread inwards [7, 78].

Without analysing any experimental data it is unclear whether a population of otherwise identical cells will exhibit different rates of spreading in the geometry of assay 1 compared to the geometry of assay 2.

A circular barrier assay can be used to study both assay 1 and assay 2 geometries, by initially placing the cells either inside or outside the barrier, which is then lifted to initiate the cell spreading [7, 78, 125, 138, 145]. Barrier assays are thought to be more reproducible than traditional mechanical wounding assays, such as scratch assays, as they do not damage the cell monolayer [56, 145]. In this work, we will consider the spreading

of cell populations in a barrier assay that are driven by combinations of motility and proliferation.

The standard continuum mathematical model used to describe how a population of motile and proliferative cells spread in two dimensions is related to the Fisher–Kolmogorov equation, and is given by

$$\frac{\partial \bar{c}}{\partial t} = D \nabla^2 \bar{c} + \lambda \bar{c} \left(1 - \frac{\bar{c}}{K}\right), \quad (5.1)$$

where $\bar{c}(x, y, t)$ [cells/L²] is the dimensional cell density, D [L²/T] is the cell diffusivity (random motility coefficient), λ [/T] is the cell proliferation rate and K [cells/L²] is the carrying–capacity density [20, 85, 86, 97, 113, 116, 132]. Physical dimensions relevant to *in vitro* cell biology assays are μm and hours for L and T , respectively. Discrete random walk–based models which are related to Equation (5.1) can also be used to study cell population spreading. Discrete models allow us to visualise the biological spreading process in a way that is more closely comparable with experimental results [4, 5, 8, 27, 33, 92, 121, 125, 140, 141]. For example, snapshots from a discrete model showing the location of individual agents in the population can be easily compared to experimental images that show the location of individual cells in the population [125, 138].

Previous studies have used Equation (5.1) to estimate D and λ from experimental observations with the additional implicit assumption that these estimates could be relevant when considering the same cell population spreading in a different geometry. This standard assumption implies that estimates of D and λ obtained by calibrating Equation (5.1) to observations in one particular geometry could be used to accurately predict the spreading of the same cell population, under the same experimental conditions, in a different geometry. However, from a biological point of view, it seems reasonable to anticipate that cell populations could respond differently under different circumstances. This means that our estimates of D and λ in Equation (5.1) might be different when calibrating this model to different experimental conditions. For this reason we will refer to estimates of D as the *effective cell diffusivity* and our estimates of λ as the *effective cell proliferation rate*, thereby making it explicit that we are allowing for the possibility that these estimates could depend on the specific details for the experiment from which they are estimated.

In this work, we use a combined experimental and mathematical modelling approach to investigate how the two-dimensional spreading of a fibroblast cell population is influenced by the assay geometry. In particular, we address the following questions:

- (1) Do estimates of the effective cell diffusivity, D , depend on the geometry of the assay?
- (2) Do estimates of the effective cell proliferation rate, λ , depend on the geometry of the assay?
- (3) Does the geometry of the assay affect the rate at which the leading edge of the cell population moves?
- (4) Are the cell density profiles through the spreading cell population sensitive to changes in the geometry of the assay?

To answer these questions, we conduct several circular barrier experiments using assay 1 and assay 2 geometries. For both assay geometries we independently estimate the effective cell diffusivity, D , using experiments where cell proliferation is suppressed. The effective proliferation rate, λ , is then separately estimated using experiments where proliferation is not suppressed. To ensure that our estimates of D and λ accurately predict the position of the leading edge of the spreading population as well as the cell density profile throughout the spreading cell population we compare predictions of the parameterised mathematical model with experimental measurements. In summary, our results indicate that estimates of D and λ appear to depend on the assay geometry, with D being more sensitive than λ .

5.2 Experimental methods

5.2.1 Circular barrier assay

Figure 5.1 shows a schematic diagram of the two barrier assay geometries considered in this work. To perform these assays metal–silicone barriers (Aix Scientifics, Germany), were cleaned, sterilised, dried and placed in the centre of the wells of a 24-well tissue culture plate. The wells in the tissue culture plate have a diameter of 15,600 μm . The barrier has an approximate radius of 3000 μm on the inside of the silicone tip (located at the end of the barrier) and 4000 μm on the outside of the silicone tip.

Experiments were conducted with fibroblast cells (Appendix C) where, in some cases the spreading was driven by cell motility only, whereas in other cases the spreading was driven by a combination of cell motility and cell proliferation. For those experiments where cell proliferation was suppressed, Mitomycin–C (Sigma Aldrich, Australia) was added to the cell solutions for one hour before the assays were initialised [112]. Experiments using assay 1 and assay 2 geometries were initialised by carefully placing the cells either inside (Figure 5.1 (a)) or outside (Figure 5.1(b)) the barrier, respectively. In all cases great care was taken to ensure that the cells were approximately evenly distributed at the beginning of the experiment. All experiments were repeated using two different initial cell densities: low density ($3.5 \times 10^{-4} \text{ cells}/\mu\text{m}^2$) and high density ($1.1 \times 10^{-3} \text{ cells}/\mu\text{m}^2$). After initially placing the cells in or around the barrier, the tissue culture plate was left for one hour in a humidified incubator at 37°C and 5% CO₂ to allow the cells to attach to the surface, after which the barriers were removed and the cell layer was washed with serum free medium (SFM; culture medium without FCS) and replaced with 0.5 mL of culture medium. Plates were incubated at 37°C in 5% CO₂ for four different durations, $t = 0, 24, 48$ and 72 hours. Each assay, for each time point, for each initial density and for each geometry, was repeated in triplicate ($n = 3$).

5.2.2 Image acquisition and analysis

Two types of images were acquired from each experiment; (i) population-scale images showing the location of the entire spreading population, and (ii) individual-scale images detailing the location of individual cells within the spreading population. Details of the image acquisition and analysis are given in Appendix C.

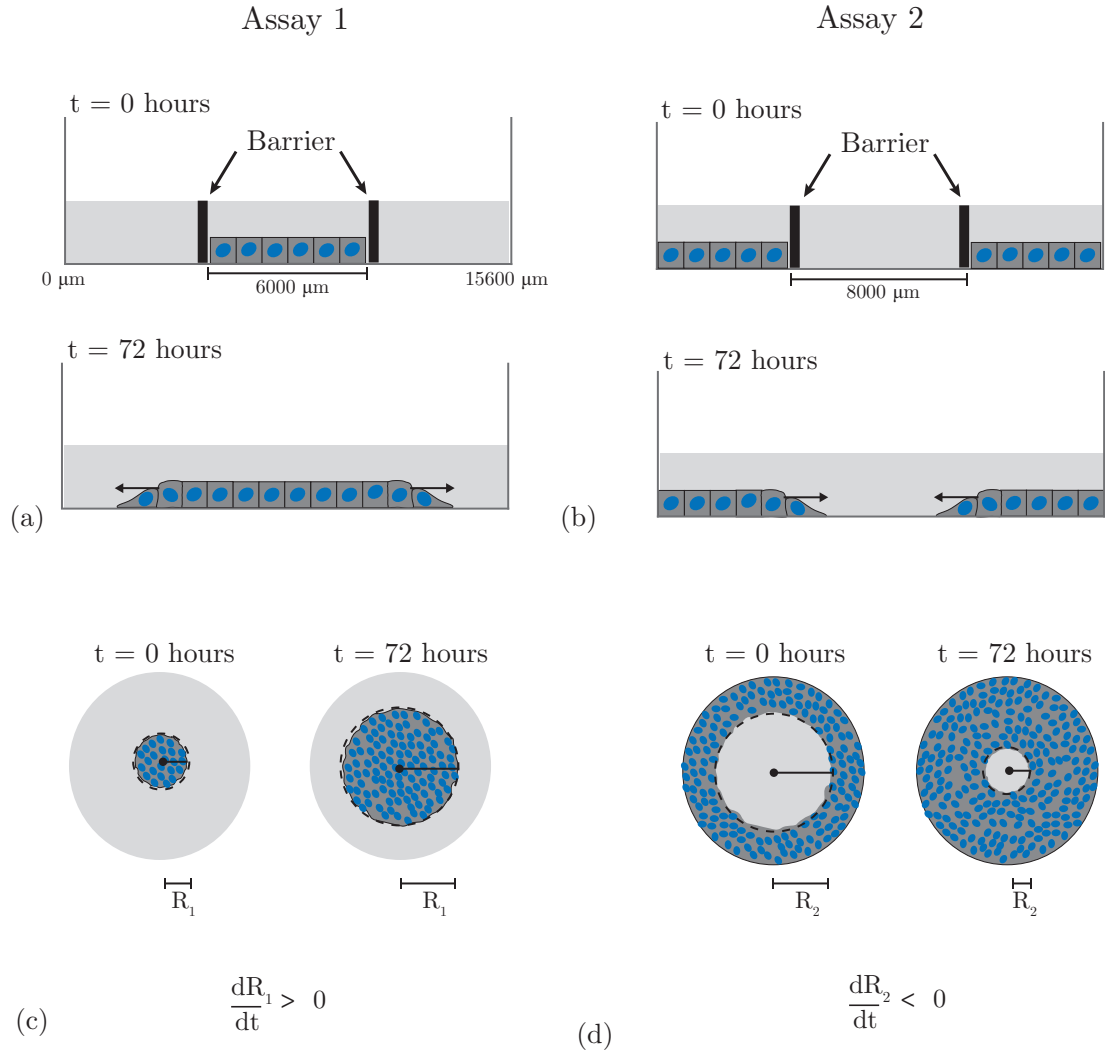


Figure 5.1: Schematic of the circular barrier assay for assay 1 and assay 2 (not to scale). (a) Assay 1: cells are placed inside the barrier allowing the cell population to spread outwards. (b) Assay 2: cells are placed outside the barrier allowing the cell population to spread inwards. The population-scale views for the assay 1 and assay 2 geometries are shown in (c) and (d), respectively, and indicate the radii measurements that were extracted from assay 1 and assay 2. Here, R_1 corresponds to the radius of the circular area enclosed by the spreading cell population for assay 1 ($dR_1/dt > 0$) and R_2 indicates the radius of the circular void area for assay 2 ($dR_2/dt < 0$).

Schematic population-scale images of assay 1 and assay 2 are shown in Figure 5.1 (c) and (d), respectively. We use a standard approach to measure the observed spreading by estimating the radius, R , from the centre of the well to the leading edge of the cell population as shown in Figure 5.1 (c) and (d). Here, R_1 , corresponds to the radius of the spreading cell population in assay 1, and R_2 represents the radius of the void space in assay 2. Estimates of R_1 and R_2 were obtained by locating the position of the leading edge of the spreading cell populations using customised image processing software that was written using the MATLAB image processing toolbox (v7.12) [90] (Appendix C). The same image analysis methods used to detect the location of the experimental leading edge were applied to detect the edges in the snapshots produced by the discrete model described in Section 5.3. For assay 1, the area (*regionprops*) of the spreading population,

A , was estimated and converted into an equivalent circular radius, $R_1 = \sqrt{A/\pi}$. For assay 2, the area of the void region, A , was estimated and converted into an equivalent circular radius, $R_2 = \sqrt{A/\pi}$.

Individual-scale images were used to construct a detailed transect across the spreading populations. Overlapping images were acquired at regular spatial intervals from the leading edge of the cell population to either the centre of the well (assay 1) or the edge of the well (assay 2). Automated image analysis, supplemented with manual counting, was used to count the number of individual cells within various subregions across the transects and these counts were used to construct detailed cell density profiles (Appendix C).

5.3 Modelling methods

To quantify and interpret our experimental observations, we use an interacting random walk model which is related to Equation (5.1). The details of our discrete model have been previously reported in [121].

5.3.1 Discrete model

The discrete model is implemented on a two-dimensional square lattice with spacing Δ , which corresponds to the average diameter of the cells. We estimate Δ by measuring the area of several cells using ImageJ software [66] and convert these estimates into an equivalent circular diameter, giving $\Delta \approx 25 \mu\text{m}$. We assume that the cells form a two-dimensional monolayer, which is reasonable given that our images indicate that individual cells do not pile up onto other cells in the vertical direction. To account for volume exclusion and finite size effects, the model permits only one agent to occupy each lattice site [33, 121]. This exclusion mechanism explicitly accounts for any differences in the availability of free space in assay 1 compared to assay 2. Each site is indexed (i, j) , where $i, j \in \mathbb{Z}^+$, and each site has position $(x, y) = (i\Delta, j\Delta)$. Simulations are initialised by placing agents uniformly, at random, either inside a circle of radius $3000 \mu\text{m}$ located at the centre of the lattice for assay 1 simulations, or outside a circle of radius $4000 \mu\text{m}$ for assay 2 simulations. Here, the initial radii for assay 1 and assay 2 correspond to the physical internal and external radii imposed by the silicone tip of the barrier.

A random sequential update method [24] is used to perform the simulations. If there are $N(t)$ agents at time t , during the next time step of duration τ , $N(t)$ agents are selected at random, one at a time, and given the opportunity to move with probability $P_m \in [0, 1]$. We use an unbiased motility mechanism where an agent at (x, y) attempts to step to $(x \pm \Delta, y)$ or $(x, y \pm \Delta)$ with equal probability of $1/4$. Once the $N(t)$ potential motility events have been assessed, during the same time step another $N(t)$ agents are selected at random, one at a time, and given the opportunity to proliferate with probability $P_p \in [0, 1]$. We model proliferation with an unbiased mechanism whereby a proliferative agent at (x, y) attempts to deposit a daughter agent at $(x \pm \Delta, y)$ or $(x, y \pm \Delta)$, with each target site chosen with equal probability of $1/4$. Potential motility and proliferation events that would place an agent on an occupied site are aborted [33, 121].

5.3.2 Continuum model

To relate the discrete model to Equation (5.1), we note that the average occupancy of site (i, j) , evaluated using \mathcal{R} identically-prepared realisations, is

$$\langle C_{i,j} \rangle = \frac{1}{\mathcal{R}} \sum_{k=1}^{\mathcal{R}} C_{i,j}^k, \quad (5.2)$$

here the superscript denotes the k^{th} identically-prepared realisation of the same stochastic process and the occupancy of site (i, j) is denoted by $C_{i,j}^k$, with $C_{i,j}^k = 1$ for an occupied site, and $C_{i,j}^k = 0$ for a vacant site. The corresponding continuous density, $\bar{c}(x, y, t)$, is governed by Equation (5.1) with carrying capacity, $K = 1$ agents/lattice site [121].

The associated diffusivity and proliferation rate [121] are given by

$$D = \frac{P_m}{4} \lim_{\Delta, \tau \rightarrow 0} \left(\frac{\Delta^2}{\tau} \right), \quad \lambda = \lim_{\tau \rightarrow 0} \left(\frac{P_p}{\tau} \right). \quad (5.3)$$

We note that $\langle C_{i,j} \rangle \in [0, 1]$ is equivalent to $\bar{c}(x, y, t)$ as $\mathcal{R} \rightarrow \infty$, provided that P_p/P_m is sufficiently small [121]. Strictly speaking, the continuum model is valid in the limit that $\Delta \rightarrow 0$ and $\tau \rightarrow 0$ jointly with the ratio Δ^2/τ held constant, implying that $P_p = \mathcal{O}(\tau)$ [121]. As we will show in Section 5.4, the cell populations in all assays maintain an approximately circular geometry for the entire duration of the experiment (Section 5.4.1), hence, we implement Equation (5.1) in an axisymmetric coordinate system,

$$\frac{\partial c}{\partial t} = D \left(\frac{\partial^2 c}{\partial r^2} + \frac{1}{r} \frac{\partial c}{\partial r} \right) + \lambda c(1 - c), \quad (5.4)$$

where the dimensional cell density, $\bar{c}(r, t)$, has been scaled relative to the carrying capacity density, $c(r, t) = \bar{c}(r, t)/K$ so that $c(r, t) \in [0, 1]$. We estimate the carrying capacity density by making the standard assumption that the maximum packing density of cells corresponds to a square packing [125]. Since $\Delta \approx 25 \mu\text{m}$, we have $K = 1/25^2 \approx 1.6 \times 10^{-3}$ cells/ μm^2 [125].

Numerical solutions of Equation (5.4) are obtained using a finite-difference approximation on a grid with a uniform grid spacing δr , and implicit Euler stepping with uniform time steps of duration δt [17, 117]. Picard iteration, with absolute convergence tolerance, ϵ , is used to solve the resulting system of nonlinear equations. For all numerical results presented we tested that the numerical solutions were grid independent. Solutions of Equation (5.4) are obtained on the domain $0 \leq r \leq 7800 \mu\text{m}$, with a symmetry condition, $\partial c / \partial r = 0$, at $r = 0 \mu\text{m}$ and a zero flux boundary condition at $r = 7800 \mu\text{m}$ for both assay 1 and assay 2 geometries. The value $r = 7800 \mu\text{m}$ corresponds to the physical radius of the well ($r = 15600/2$). The initial condition for assay 1 is given by,

$$c(r, 0) = \begin{cases} c_0, & 0 \leq r \leq 3000 \mu\text{m}, \\ 0, & 3000 \leq r \leq 7800 \mu\text{m}, \end{cases} \quad (5.5)$$

where $c_0 \in [0, 1]$ is the initial nondimensional cell density within the barrier. The initial condition for assay 2 is given by

$$c(r, 0) = \begin{cases} 0, & 0 \leq r < 4000 \text{ } \mu\text{m}, \\ c_0, & 4000 \leq r \leq 7800 \text{ } \mu\text{m}. \end{cases} \quad (5.6)$$

The initial nondimensional cell density for low density experiments is $c_0 = 3.5 \times 10^{-4} / 1.6 \times 10^{-3} \approx 0.22$, whereas the initial nondimensional cell density for the high density experiments is $c_0 = 1.1 \times 10^{-3} / 1.6 \times 10^{-3} \approx 0.66$.

5.3.3 Standard measure of spatial spreading

In addition to analysing the data using the mathematical modelling framework described in Sections 5.3.1–5.3.2, we also interpret our results using a standard measure that is often reported in the experimental cell biology literature [7, 56, 94, 137, 145, 161, 162]. This standard measure can be written as

$$M(t) = \frac{R_a(t) - R_a(0)}{R_a(0)} \times 100, \quad (5.7)$$

where $M(t)$ represents the percentage change in the observed radius at time t relative to the initial radius, $a = 1, 2$, represents assay 1 or assay 2, respectively, and $R(t)$ is the detected radius at time t .

5.4 Results

5.4.1 Cell diffusivity estimates

We first investigated whether estimates of D were sensitive to the assay geometry. To identify D we considered experiments where cells were pretreated with Mitomycin-C to suppress cell proliferation. Population-scale images in Figure 5.2 (a) and (b) illustrate the distribution of cells in the assay 1 geometry at $t = 0$ and $t = 72$ hours for an experiment with a high initial cell density inside the barrier. The corresponding images for the assay 2 geometry are shown in Figure 5.2 (c) and (d). For both geometries, the area occupied by the cell population increases with time and the circular geometry is maintained. From these images alone it is difficult to interpret whether the spreading in assay 1 is any different to the spreading in assay 2.

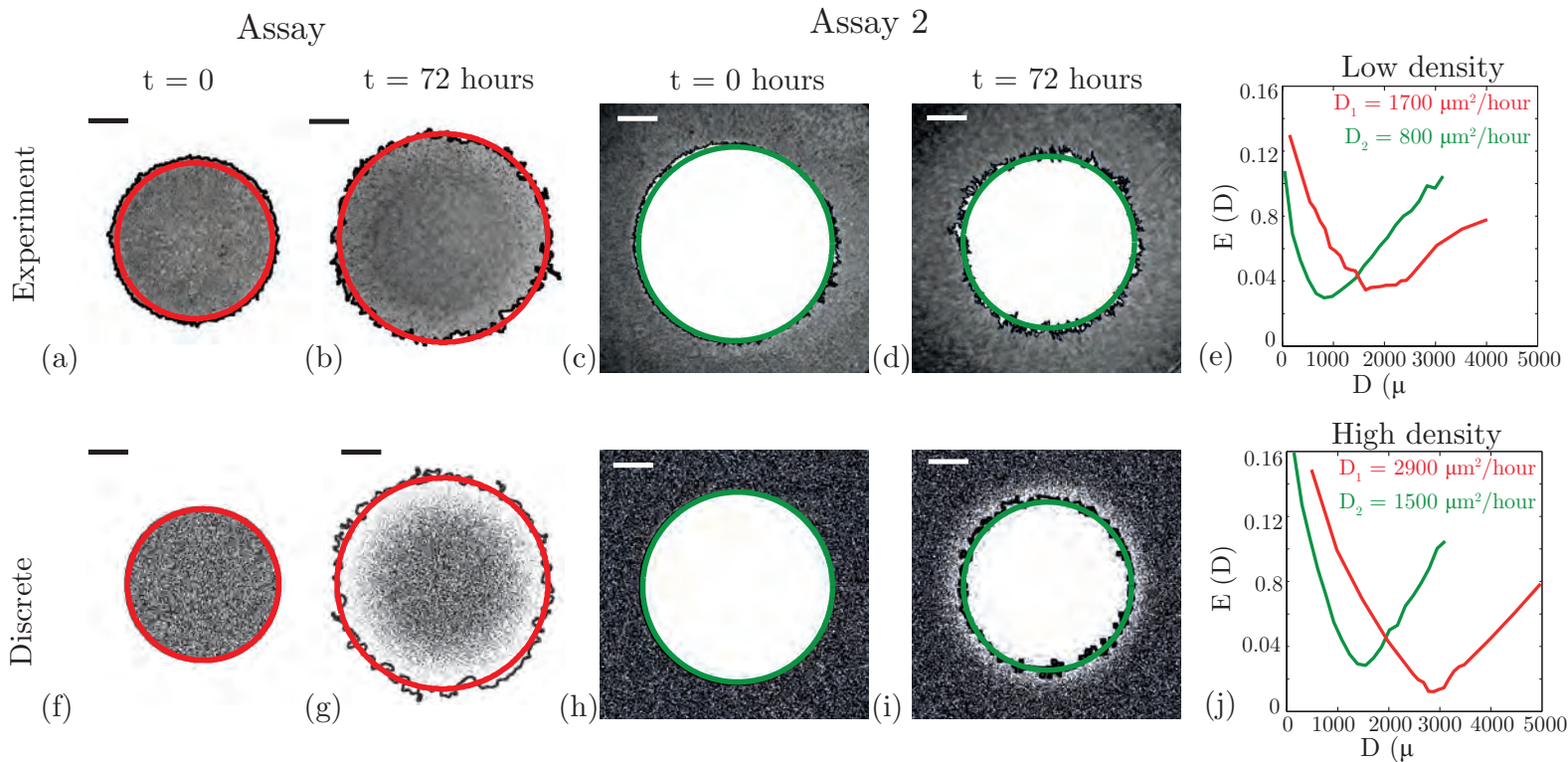


Figure 5.2: Estimates of cell diffusivity. Experimental and modelling images are shown in (a)–(d) and (f)–(i) comparing the position of the leading edge of the spreading cell population for assay 1 and assay 2 geometries at high initial cell density. Experimental images in (a)–(b) show the distribution of cells at $t = 0$ and $t = 72$ hours for a barrier assay where cells are initially placed uniformly inside the barrier after Mitomycin-C pretreatment. Equivalent images using the assay 2 geometry, where cells are initially placed outside the barrier, are shown in (c)–(d). The black solid line indicates the position of the leading edge of the spreading population as detected by the image analysis software. The area enclosed by the spreading cell population was converted to an equivalent circular area. For the assay 1 geometry, the area detected encloses the spreading cell population, while for the assay 2 geometry, the area detected encloses the void. Images in (f)–(i) show the corresponding snapshots of the discrete model on a 624×624 lattice with $\Delta = 25 \mu\text{m}$. Simulations were performed using $P_m = 1$ and $P_p = 0$. Model simulations in (f)–(g) correspond to $\tau = 0.0526$ hours and (h)–(i) correspond to $\tau = 0.1000$ hours. The detected leading edge of the discrete cell population is indicated by the black solid line. The red (assay 1) and green (assay 2) circles which are superimposed onto the experimental and discrete images correspond to the $c(r, t) = 0.019$ contour of the numerical solution of Equation (5.4) with $\lambda = 0$, $D_1 = 2900 \mu\text{m}^2/\text{hour}$ and $D_2 = 1500 \mu\text{m}^2/\text{hour}$. Results in (e) and (j) compare $E(D)$, using Equation (5.8), between the position of the leading edge of the simulated cell population, using various values of D , and the position of the leading edge of the corresponding experimental image for assay 1 (red) and assay 2 (green) at low and high initial cell densities, respectively. The scale bar corresponds to $1500 \mu\text{m}$.

To quantify any differences between the observed spreading in assay 1 and assay 2, we used the image analysis methods (Section 5.2.2) to detect the position of the leading edge of the spreading cell populations in each geometry. The detected leading edges are superimposed onto the images in Figure 5.2 (a)–(d). For assay 1, the area enclosed by the leading edge was converted into an equivalent circular radius, R_1 . Similarly, for assay 2, the area of the void space enclosed by the leading edge was converted into an equivalent circular radius, R_2 . For the assay 1 population-scale images in Figure 5.2, R_1 increases from $3000 \mu\text{m}$ to $4171 \mu\text{m}$, over $t = 72$ hours, giving $M(72) = 39\%$ using Equation (5.7). Similarly, for the population-scale images of assay 2, R_2 decreases from $4000 \mu\text{m}$ to $2950 \mu\text{m}$, giving $M(72) = -26\%$. The corresponding results for the experiments initialised with low cell density give $M(72) = 26\%$ for assay 1 and $M(72) = -14\%$ for assay 2 (Appendix C). Although it is straightforward to compute and compare estimates of $M(t)$ for the different assays, these estimates do not provide us with any quantitative insight into the role of the mechanisms that drive the spreading process.

We estimated D for each geometry by comparing the experimental data with simulation data from the discrete mathematical model. Simulations, as described in Section 5.3, were performed using the discrete model to replicate the initial distribution of cells in both geometries at both initial densities. To estimate D we performed simulations where we systematically varied the duration of the time step, τ , which is equivalent to varying the effective cell diffusivity, $D = P_m \Delta^2 / (4\tau)$, in the continuum model. This procedure enabled us to determine the value of D that produces a prediction that best matches the experimental data. In all cases, we set $P_p = 0$ and $P_m = 1$. We considered 30 equally spaced values of D in the interval $D \in [0, 5000] \mu\text{m}^2/\text{hour}$, and for each value of D we simulated each experiment three times ($n = 3$), over $t = 24, 48$ and 72 hours. The image analysis software was used to locate the position of the leading edge of the simulated cell populations in the same way that the image analysis was used to detect the leading edge in the experimental images. In all cases, the detected leading edge was converted to an equivalent circular radius.

Population-scale images in Figure 5.2 (f) and (g) show the distribution of agents in the discrete model in assay 1 and the corresponding detected position of the leading edge, at $t = 0$ and $t = 72$ hours, for an experiment where a high density cell population was initially placed inside the barrier. The population-scale images in Figure 5.2 (h) and (i) illustrate the equivalent results for assay 2. We note that the distribution of agents in Figure 5.2 (g) and (i) do not appear to be influenced by the underlying lattice structure at this scale since the simulations were initialised at a relatively low density, and the density of agents at the leading edge is, by definition, very low. This qualitative observation is consistent with recent theoretical comparisons between lattice-based and lattice-free descriptions of spreading cell populations which confirmed that there is no difference between a lattice-based and lattice-free model at the leading edge of spreading populations [106].

To determine the value of D for which our model results best match the observed data, we compared the radii estimates from the discrete simulations, at $t = 24, 48$ and 72 hours, to

the corresponding experimental data, using an estimate of the least-squares error given by

$$E(D) = \frac{\sum_{i=1}^3 (ER_a^i - SR_a^i)^2}{\sum_{i=1}^3 (ER_a^i)^2}, \quad (5.8)$$

where i indicates the three time points, $t = 24, 48$ and 72 hours, and a corresponds to the assay geometry, 1 and 2. In all cases, ER and SR are the radii extracted from the experimental cell populations and the corresponding simulated populations, respectively, averaged over ($n = 3$) identically-prepared replicates.

Results in Figure 5.2 (e) and (j) show $E(D)$ for experiments in each geometry for both initial cell densities. For all experiments there is a well-defined minimum which indicates the least-squares estimate of D . We note that the estimate of D is different for each geometry and each initial cell density. Our analysis indicates that for experiments using a low initial cell density we have $D \approx 1700 \mu\text{m}^2/\text{hour}$ for assay 1, while $D \approx 800 \mu\text{m}^2/\text{hour}$ for assay 2. Our results for the experiments using a high initial cell density show a similar trend where $D \approx 2900 \mu\text{m}^2/\text{hour}$ for assay 1, while $D \approx 1500 \mu\text{m}^2/\text{hour}$ for assay 2. For both initial cell densities, our least-squares estimate of D is approximately 50% smaller for assay 2. These differences suggest that the cell motility mechanism is affected by the assay geometry and we note that these differences were not obvious through visual inspection of the experimental images or through the use of the commonly-reported quantity, $M(t)$, given by Equation (5.7).

To confirm that our estimates of D allow us to accurately model the experimental data we compared the numerical solution of Equation (5.4), with $\lambda = 0$, to population-scale images from the experiments and discrete simulations in Figure 5.2 (a)–(d) and (f)–(i). To compare the numerical solution of Equation (5.4) with the experimental images we choose an appropriate contour of the solution, $c(r, t) = 0.019$, which best describes the averaged spreading observed in the experiments (Appendix C). The correspondence between the position of the leading edge in the experimental images and the $c(r, t) = 0.019$ contour of the solution of Equation (5.4) in Figure 5.2 (a)–(d) and (f)–(i) confirms that our estimates of D are appropriate for each geometry and initial cell density.

5.4.2 Cell proliferation estimates

To estimate λ we considered experiments where proliferation was not suppressed. Individual-scale images were used together with the image analysis techniques to count the number of cells, at a fixed position, as a function of time. For each experiment, the number of cells in four different subregions, each of dimension $250 \mu\text{m} \times 250 \mu\text{m}$, was counted. The locations of the subregions were chosen so that the cell density at that location is approximately spatially uniform and locally we have $\bar{c}(r, t) \approx \bar{c}(t)$. The cell counts were converted into a measurement of the nondimensional cell density, $c(t) = \bar{c}(t)/K$. Figure 5.3 (a) and (f) illustrate the approximate location and size of each of the four subregions for assay 1 and assay 2, respectively.

Images in Figure 5.3 (b) and (c), and Figure 5.3 (g) and (h), show snapshots of a subregion analysed for assay 1 and assay 2, respectively. These results correspond to experiments that were initialised with a high cell density. We note that the cell density increases rapidly with time and that there appears to be no visual difference in the cell density behaviour between either geometry. The evolution of $c(t)$ is shown in Figure 5.3 (d) and (i) for both geometries and each initial cell density.

We note that Equation (5.4) can be simplified when the cell density, $c(r, t)$, is spatially uniform so that locally we have $c(r, t) = c(t)$. Hence, Equation (5.4) simplifies to the logistic equation

$$\frac{dc(t)}{dt} = \lambda c(t)(1 - c(t)), \quad (5.9)$$

which has the solution

$$c(t) = \frac{c(0) \exp(\lambda t)}{1 + c(0)(\exp(\lambda t) - 1)}, \quad (5.10)$$

where $c(0)$ is the nondimensional initial cell density.

To estimate λ , we found the value of λ that minimised an estimate of the least-squares error between our experimental measurements and Equation (5.10), given by

$$E(\lambda) = \frac{\sum_{i=1}^3 (EP_a^i - SP_a^i)^2}{\sum_{i=1}^3 (EP_a^i)^2}, \quad (5.11)$$

where i denotes the three time points, $t = 24, 48$ and 72 hours, and a corresponds to the assay geometry, 1 and 2. In all cases, EP corresponds to the nondimensional cell density extracted from the experimental images averaged over ($n = 4$) replicates and SP is the corresponding nondimensional cell density using Equation (5.10).

Results in Figure 5.3 (e) and (j) show $E(\lambda)$ for experiments in both geometries and both initial cell densities. For all cases, our results show that there is a well-defined minimum in $E(\lambda)$. For experiments without Mitomycin-C pretreatment at low density we have $\lambda = 0.056$ /hour for assay 1 and $\lambda = 0.042$ /hour for assay 2. Similarly, for the experiments without Mitomycin-C pretreatment at high density we have $\lambda = 0.059$ /hour for assay 1 and $\lambda = 0.041$ /hour for assay 2. The relevant logistic growth curves, given by Equation (5.10) with our estimates of λ , are superimposed in Figure 5.3 (d) and (i). These growth curves confirm that, on average, our estimates of λ provide a good match to the observed data.

To explore whether our estimates of λ are sensitive to the location of the subregion, we re-estimated λ in two additional subregions located in different positions that were at least $2000\ \mu\text{m}$ behind the leading edge (Appendix C). These additional results show that there is a relatively small variation in λ , confirming that our estimates of λ are relatively insensitive to the choice of the location of the subregions, provided that we are sufficiently far behind the leading edge where $\bar{c}(r, t) \approx \bar{c}(t)$. Therefore, given this insensitivity, we will use the values of λ reported here in Chapter 5.

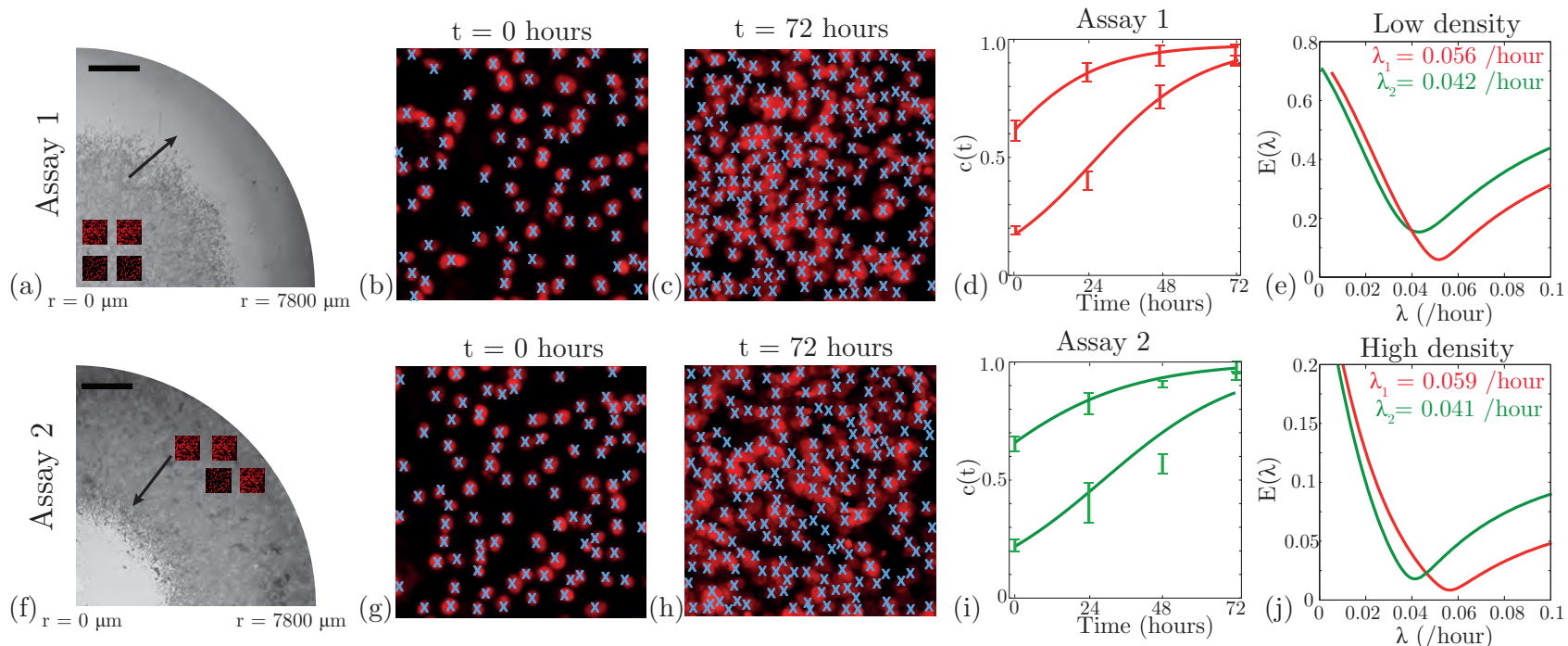


Figure 5.3: Estimates of the cell proliferation rate. Cell proliferation rate estimates were obtained by counting the number of cells in four different subregions in each experimental replicate. The location of subregions were located away from the leading edge so that the cell density in that subregion was approximately spatially uniform giving $c(r, t) = c(t)$. The location and size of the four subregions for assay 1 and assay 2 geometries are shown in (a) and (f), where the scale bar corresponds to $1500 \mu\text{m}$. Images in (b)–(c) and (g)–(h) show snapshots of dimensions $250 \mu\text{m} \times 250 \mu\text{m}$ for experiments with high cell density without Mitomycin-C pretreatment, at $t = 0$ and $t = 72$ hours for assay 1 and assay 2 geometries, respectively. The Propidium Iodide staining highlights the cell nucleus and blue crosses indicate cells that were counted. Results in (d) and (i) compare the mean non-dimensional cell density ($n = 4$) from experiments with an initial low and high cell density for both assay 1 (red) and assay 2 (green) at $t = 0, 24, 48$ and 72 hours, with error bars indicating one standard deviation from the mean. The appropriately parameterised logistic growth curves using the cell proliferation rate estimates from Table 1 are superimposed in (d) and (i). Results in (e) and (j) show $E(\lambda)$, given by Equation (5.11), for various values of λ , for experiments at low and high cell density, respectively.

We also estimated λ for the experiments with Mitomycin–C pretreatment (Appendix C) where cell proliferation was assumed to be suppressed. This gave $\lambda < 0.003$ /hour, indicating that the number of cells did not significantly increase or decrease over the duration of the experiment. This implies that Mitomycin–C pretreatment prevented proliferation and did not induce cell death.

5.4.3 Predicting the behaviour of spreading cell populations in different geometries

A summary of our estimates of D and λ for both geometries and both initial cell densities are given in table 5.1. The variability in our estimates are also reported, and the details of how the variability was determined is given in Appendix C.

We will now consider whether the parameterised mathematical model can accurately predict the position of the leading edge of the spreading cell populations and the details of the cell density profiles throughout the entire spreading cell populations.

Position of the leading edge

Population-scale images in Figure 5.4 and Figure 5.5 compare the position of the leading edge of the cell population for assay 1 and assay 2 with the corresponding predictions from Equation (5.4) using the appropriate parameter values given in Table 5.1. The solution of Equation (5.4) is represented in terms of the $c(r, t) = 0.019$ contour (Appendix C). Overall, the agreement between the experiments and the model predictions indicate that the parameter estimates appear to accurately capture the observed differences between the two geometries, both with and without proliferation, and at all time points considered.

Results in Figure 5.6 compare the time evolution of the observed values of $M(t)$ (Equation (5.7)) with the corresponding predicted values of $M(t)$ using appropriately parameterised solutions of Equation (5.4). We note that the prediction of the mathematical model at $t = 24$ hours for assay 2 appears to systematically underestimates $M(t)$. This small discrepancy could be due to our experimental procedure since the imaging process requires a brief interruption to the incubation conditions when the assay was stopped for imaging. We anticipate that this disruption would have a negligible impact on those experiments conducted for a long period of time whereas the impact could be more important for experiments conducted over a shorter period of time. Despite this discrepancy at one time point in assay 2, our overall comparison between the observations and the modelling

Assay	Initial Density	Diffusivity D ($\mu\text{m}^2/\text{hour}$)	Proliferation rate λ (/ hour)	Doubling time $t_d = \ln(2)/\lambda$ (hours)
1	low	1700 (1000–1900)	0.056 (0.048–0.065)	12.4 (10.6–14.5)
	high	2900 (2400–3200)	0.059 (0.055–0.078)	11.7 (8.8–12.6)
2	low	800 (500–1200)	0.042 (0.037–0.054)	16.5 (12.8–18.7)
	high	1500 (1000–1900)	0.041 (0.035–0.055)	16.9 (12.6–19.8)

Table 5.1: Summary of parameter estimates for assay 1 and assay 2 geometries with the uncertainty given in the parentheses.

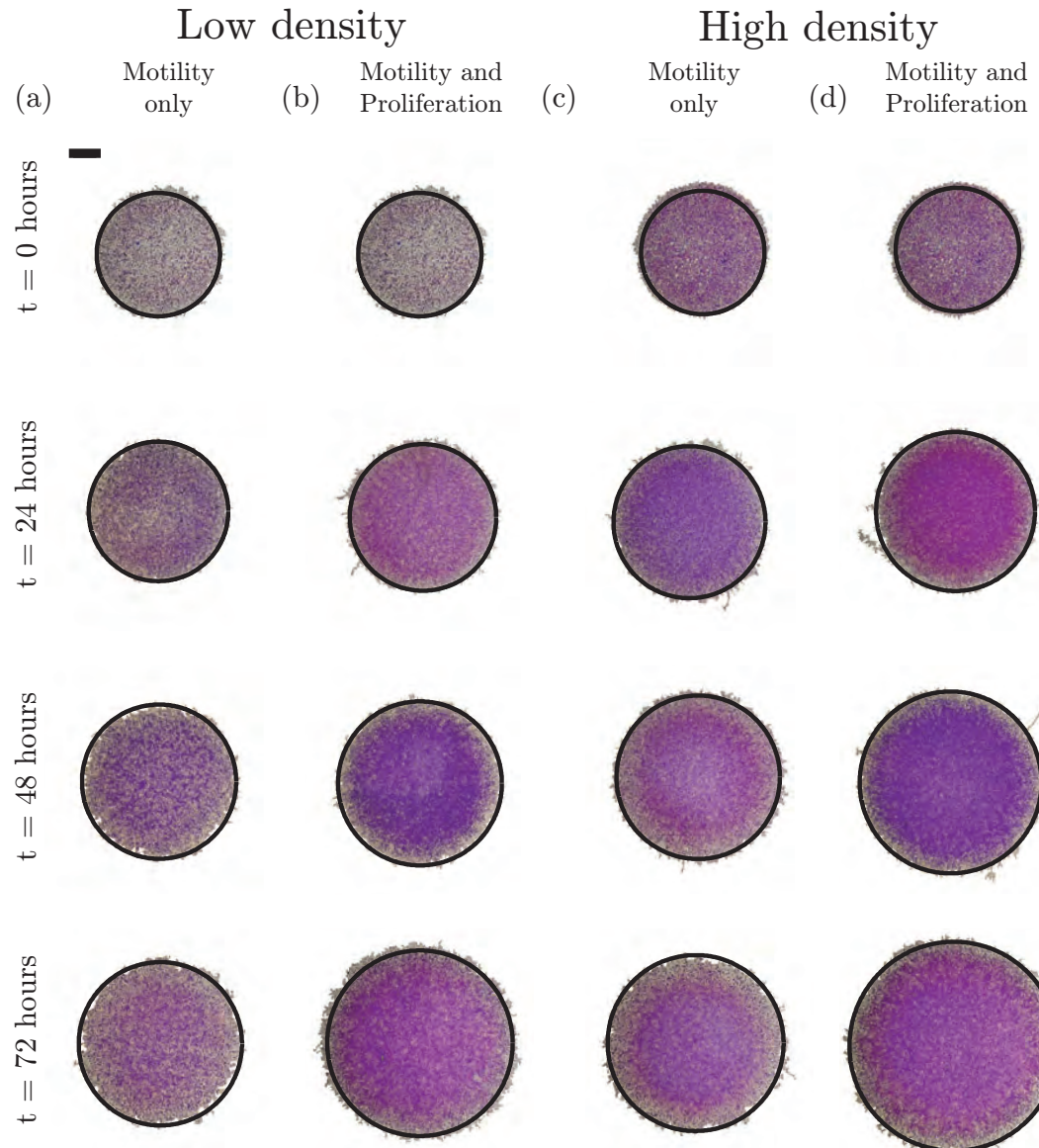


Figure 5.4: Extent of spatial spreading in assay 1 is compared to the corresponding predictions of the mathematical model. The position of the leading edge of the spreading cell population in assay 1 was determined by analysing images from the experiments initialised with low cell density in (a)–(b), and high cell density in (c)–(d). Images in rows 1 to 4 show the spreading cell population at $t = 0, 24, 48$ and 72 hours, respectively. The coloured area corresponds to the spreading cell population. Experiments with Mitomycin-C pretreatment (motility only) are shown in the first and third column, while experiments without Mitomycin-C pretreatment (motility and proliferation) are shown in the second and fourth columns. In each image, we superimpose the $c(r, t) = 0.019$ contour of the relevant solution of Equation (5.4) in black. The scale bar corresponds to $1500 \mu\text{m}$.

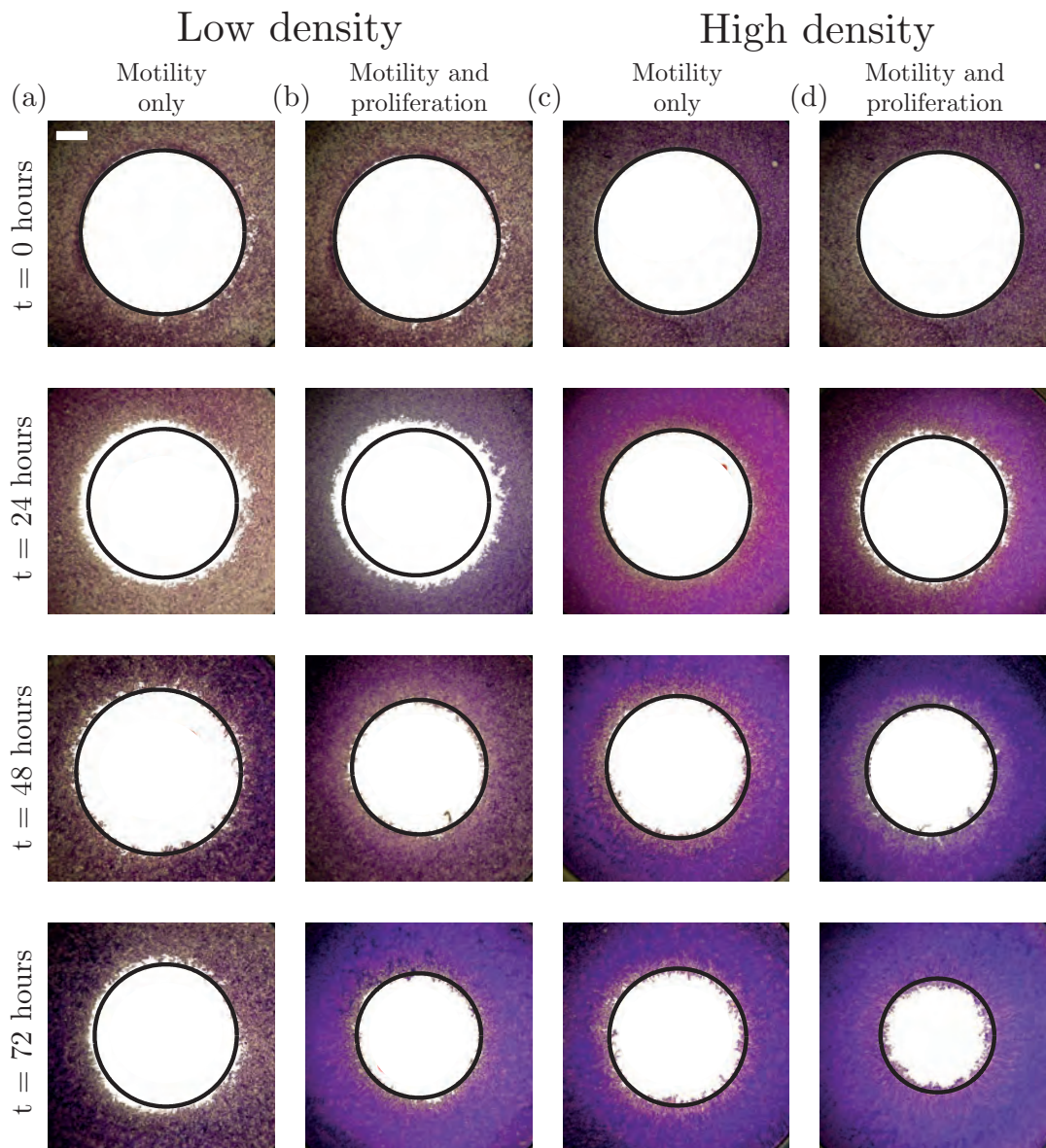


Figure 5.5: Extent of spatial spreading in assay 2 is compared to the corresponding predictions of the mathematical model. The position of the leading edge of spreading cell population in assay 2 was determined by analysing images from the experiments initialised with low cell density in (a)–(b), and high cell density in (c)–(d). Images in rows 1 to 4 show the spreading cell population at $t = 0, 24, 48$ and 72 hours, respectively. The white circular area corresponds to the void region. Experiments with Mitomycin-C pretreatment (motility only) are shown in the first and third column, while experiments without Mitomycin-C pretreatment (motility and proliferation) are shown in the second and fourth columns. In each image, we superimpose the $c(r, t) = 0.019$ contour of the relevant solution of Equation (5.4) in red. The scale bar corresponds to $1500 \mu\text{m}$.

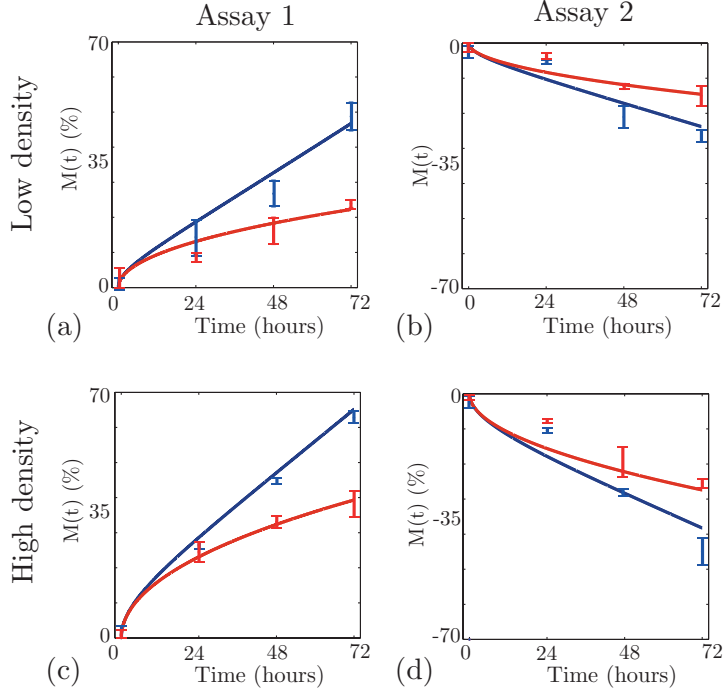


Figure 5.6: Experimental measurements of the position of the leading edge of the spreading population were compared to the corresponding predictions of the mathematical model in terms of $M(t)$. The mean radius estimated from experimental images at $t = 0, 24, 48$ and 72 hours ($n = 3$) were converted into a measurement of $M(t)$ using Equation (5.7). The errors bars indicate one standard deviation from the mean. Results are given for both assay 1 and assay 2 for low (a)–(b) and high (c)–(d) initial cell densities, respectively. Solid curves represent $M(t)$ calculated using the position of the $c(r, t) = 0.019$ contour from the relevant solution of Equation (5.4). Red curves correspond to experiments with Mitomycin–C pretreatment, whereas blue curves correspond to experiments without Mitomycin–C pretreatment.

predictions indicates that the parameterised model accurately predicts the time–evolution of the position of the leading edge and reliably captures the differences in our experiments where cell proliferation was either suppressed or permitted.

Cell density profiles

We now consider comparing the observed cell density profile with the cell density profile predicted by our parameterised mathematical model. Individual–scale images across a transect through the spreading population were used to estimate spatial distribution of the nondimensional cell density. We divided each transect into 20–30 subregions, each of length approximately $150\ \mu\text{m}$, along the transect axis. Figure 5.7 (a) and (f) show the location of the transects relative to the entire population. Snapshots of the images analysed from experiments with a high initial cell density are given in Figure 5.7 (b)–(e) for assay 1, and in Figure 5.7 (g)–(j) for assay 2. Image analysis software was used to count the number of cells in each subregion, and this was converted into an estimate of the nondimensional cell density, $c(t) = \bar{c}(t)/K$, which was used to construct the histograms in Figure 5.8. The appropriately parameterised solutions of Equation (5.4) are superimposed onto these histograms. Comparing the solutions of Equation (5.4) with the experimental measurements confirms that the appropriately parameterised model reliably captures the

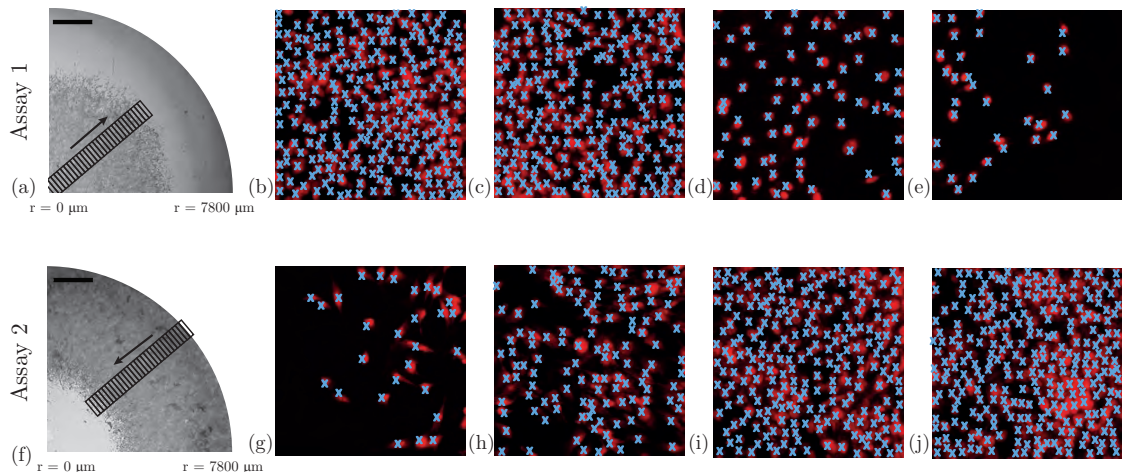


Figure 5.7: Location of the subregions used to construct cell density profiles and individual-scale images showing the locations of cells within these subregions. Experimental cell density profiles were constructed by counting the number of cells in 20–40 subregions along a transect spanning the spreading cell population. The relative size and approximate location of these subregions are illustrated in (a) and (f), where the scale bar corresponds to 1500 μm . Individual-scale images in (b)–(e) and (g)–(j) show snapshots of various subregions of dimensions 250 $\mu\text{m} \times 250 \mu\text{m}$. The subregions in (b)–(e) correspond to assay 1, and the value of the radial coordinate r in each of these subregions increases such that (b) is close to the centre of the well and (e) is located towards the edge of the outward spreading population. The subregions in (g)–(j) correspond to assay 2, and the value of the radial coordinate r in each of these subregions increases such that (g) is located close to the leading edge of the inward spreading population and (j) is located towards the edge of the well. The Propidium Iodide staining highlights the cell nucleus and blue crosses indicate cells that were counted in the analysis.

entire cell density profiles in assay 1 and assay 2, and for both types of experiments where cell proliferation was suppressed or not.

5.4.4 Comparing estimates of D and λ in different geometries

We now compare whether estimates of D and λ obtained by calibrating the model in one particular geometry can be used to predict the extent of spatial spreading in a different geometry. Results in Figure 5.9 compare the population-scale images at $t = 72$ hours with the corresponding predictions of the mathematical model using both the estimates of D and λ obtained from assay 1 and the estimates of D and λ from assay 2. In all cases we see that the prediction of the mathematical model, parameterised with the appropriate estimates of D and λ , provides an excellent match to the observed spreading, as expected. However, we also show that the prediction of the mathematical model, parameterised with the alternative estimates of D and λ , provide a very poor prediction. The difference between the observed position of the leading edge and the prediction of the mathematical model is most evident in the proliferative populations where the discrepancy is as much as 500 μm . These comparisons confirm that estimates of D and λ obtained by focusing on one particular geometry may not be suitable to make predictions in another geometry.

Results in Figure 5.10 present a similar comparison between the observed shape of the cell density profile near the leading edge and the predictions of the mathematical model. Cell density profiles within a distance of 2000 μm of the leading edge were constructed by dividing this region into 9–15 equidistant subregions of length approximately 100 μm .

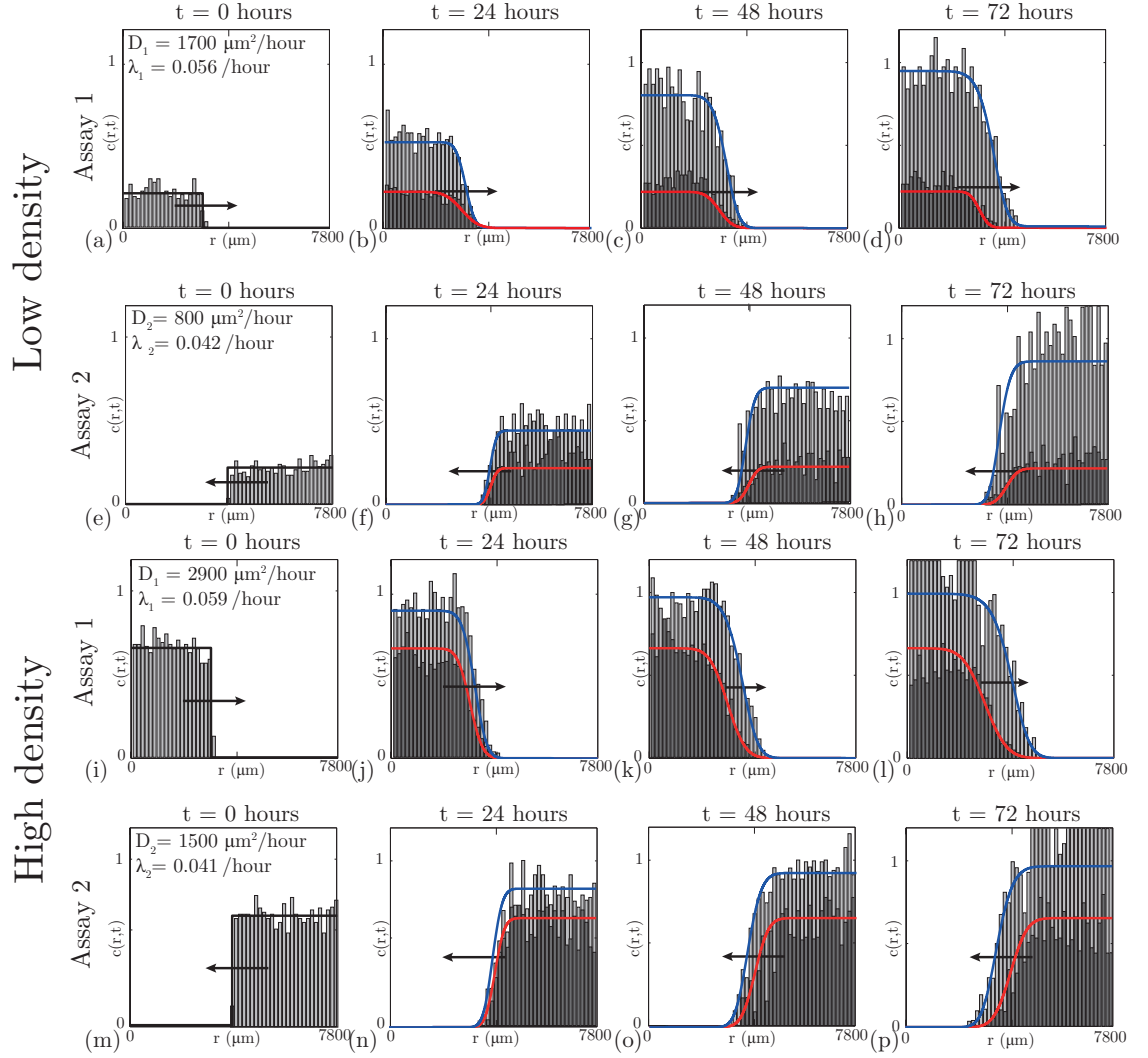


Figure 5.8: Cell density profiles comparing the extracted experimental data and the relevant solution of Equation (5.4) using the parameter estimates in Table 1. Assay 1 results for experiments both with (dark grey) and without Mitomycin-C (light grey) pretreatment, at $t = 0, 24, 48$ and 72 hours, are shown in rows 1 (low initial density) and 3 (high initial density). Equivalent results for assay 2 are shown in rows 2 (low initial density) and 4 (high initial density). Arrows indicate the direction of the spreading cell population. The red (motility only) and blue (motility and proliferation) curves superimposed on all results correspond to the relevant solutions of Equation (5.4).

Image analysis software was used to count the number of cells in each subregion, and this count was converted into a nondimensional cell density, $c(t) = \bar{c}(t)/K$. Again, our results confirm that the predictions of the mathematical model, parameterised with the appropriate estimates of D and λ , provide a good match to the shape and position of the observed density profiles. In contrast, the prediction of the mathematical model, parameterised with the alternative estimates of D and λ , fail to match either the position or shape of the leading edge. Therefore, our results suggest that great care should be taken when estimating D and λ in one situation and then applying the parameterised model to make predictions in another situation.

Our data describing the shape of the cell density profile in Figure 5.10 can also be used to provide a separate estimate of D by matching the solution of Equation (5.4) with

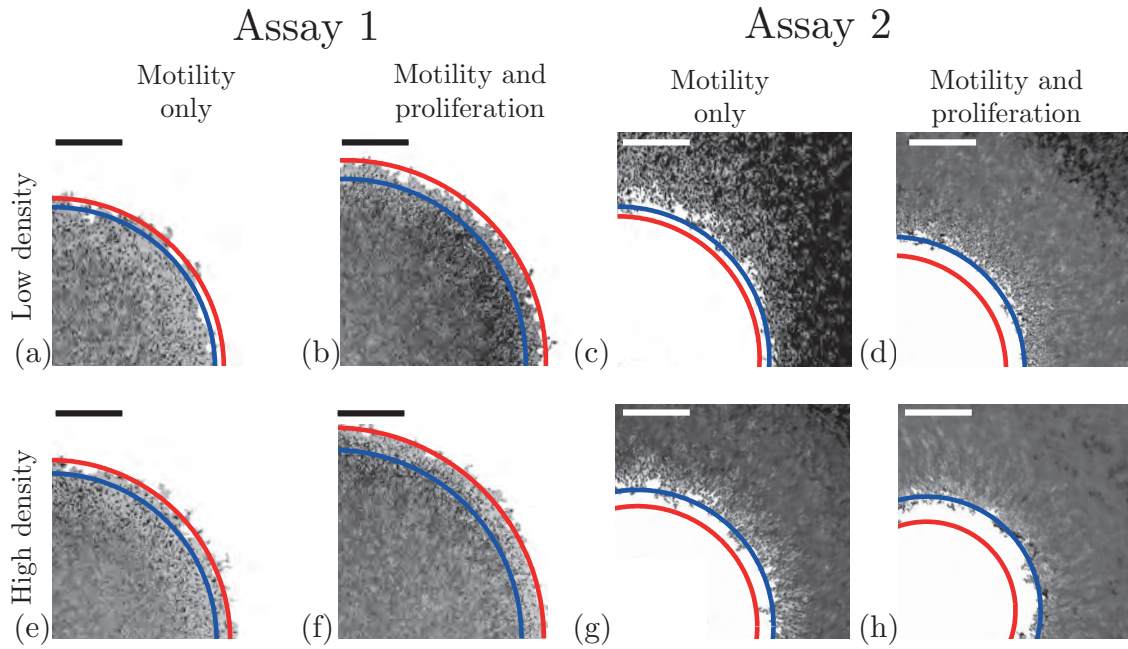


Figure 5.9: Predicting the spread of a cell population using estimates of D and λ from a different geometry: comparing the location of the leading edge. Population-scale images correspond to experiments at $t = 72$ hours are given in (a)–(d) for a low initial cell density, and in (e)–(h) for a high initial cell density. Experiments with Mitomycin-C pretreatment (motility only) are shown in the first and third columns, while experiments without Mitomycin-C pretreatment (motility and proliferation) are shown in the second and fourth columns. In each image we superimpose the $c(r, t) = 0.019$ contour of the relevant solution of Equation (5.4) using the parameter estimates for assay 1 (red) and for assay 2 (blue). The scale bar corresponds to $1500 \mu\text{m}$.

this data for the experiments where proliferation was suppressed. Additional results (Appendix C) confirm that estimates of D obtained using this approach are very similar to our results reported in Section 5.4.1 where we focused on the leading edge data only. Most importantly, when we estimate D using the shape of the cell density profiles we find a very similar discrepancy between our estimates of D when we use the density profiles from assay 1 compared to the density profiles from assay 2. Although we have estimated D using both the density profiles and the leading edge data separately, we chose to focus on the results associated with the leading edge data since this method is simpler to implement since it avoids the need for counting individual cells and constructing cell density profiles.

5.5 Discussion

Various approaches that attempt to investigate how populations of cells spread typically neglect the influence of the assay geometry [37, 77]. In this work, we used a circular barrier assay to analyse the spreading behaviour of a fibroblast cell population in two distinct geometries; (i) assay 1 resembled a tumour-like outward spreading process, and (ii) assay 2 resembled a wound-like inward spreading process. To quantify the differences between these assays we used a combined experimental and a mathematical modelling approach to estimate D from experiments where cell proliferation was suppressed. We then separately estimated λ from experiments where proliferation was not suppressed.

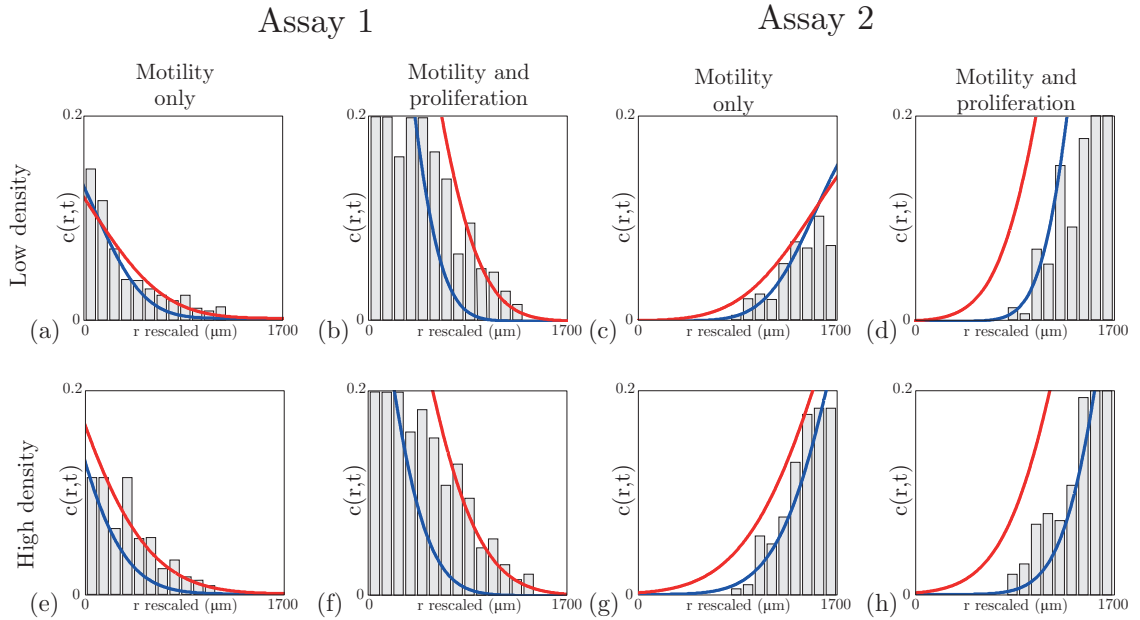


Figure 5.10: Predicting the spread of a cell population using estimates of D and λ from a different geometry: comparing the cell density profile at the leading edge of the spreading population. Cell density profiles correspond to experiments at $t = 72$ hours are given in (a)–(d) for a low initial cell density, and in (e)–(h) for a high initial cell density. Experiments with Mitomycin-C pretreatment (motility only) are shown in the first and third columns, while experiments without Mitomycin-C pretreatment (motility and proliferation) are shown in the second and fourth columns. In each image, we superimpose the solution of Equation (5.4) using the parameter estimates for assay 1 (red) and for assay 2 (blue).

Given our estimates of D and λ , we then independently verified that our parameterised model could predict both the position of the leading edge and the shape of the cell density profiles in both assays for two different initial densities.

Our results suggest that assay geometry can affect the behaviour of spreading cell populations since our estimate of D for assay 2 was up to 50% lower than our estimate of D for assay 1, while our estimate of λ was up to 30% lower for assay 2 compared to assay 1. This observation is important because most experimental and mathematical modelling studies of *in vitro* cell spreading typically focus on one geometry only and make the implicit assumption that observations and measurements in one geometry are relevant for others. Our results, highlighted in Figure 5.9 and Figure 5.10, indicate that this implicit assumption can produce misleading results.

This work highlights the importance of using mathematical modelling tools to quantify the contributions of cell motility and cell proliferation in driving the observed spreading behaviour. For example, standard measures of cell spreading, such as Equation (5.7), do not provide any detailed information regarding how the underlying mechanisms contribute to the observed spreading. Furthermore we have shown that these standard measures cannot be compared between different geometries since comparing estimates of $M(t)$ for assay 1 with estimates of $M(t)$ for assay 2 is not insightful. Our analysis of the data using Equation (5.7) could have been performed in terms of the observed area, $A(t)$, instead of the observed radius, $R(t)$ [7, 94, 137, 161]. However, regardless of whether $M(t)$ is measured in terms of $R(t)$ or $A(t)$ we find the same trends in the data which means that

our conclusions about $M(t)$ are relevant regardless of these details. In contrast, a mathematical modelling approach that explicitly represents the underlying cell motility and cell proliferation mechanisms can overcome this difficulty since we can extract, and quantify, detailed information about both the cell motility and cell proliferation mechanisms separately.

The focus of our work has been to assess quantitative differences between two different assay geometries. It is also worthwhile to discuss some qualitative differences between assay 1 and assay 2. We found that the experimental procedure for assay 1 was more straightforward to implement and analyse for two reasons. First, assay 2 requires the use of a greater number of cells in the experimental procedure which means that discrete simulations are more time consuming to perform. Second, we found that it is more difficult to initialise the cells uniformly outside the barrier compared to inside the barrier. Despite this difficulty, we always ensured that all experiments were initiated as uniformly as possible by performing a large number of experiments and discarding all those results in which the cells were not uniformly initialised.

To illustrate the consequences of our study, we confirmed that estimates of D and λ from one particular geometry could give misleading results by applying the mathematical model parameterised with these estimates to make a prediction of the cell spreading in the other geometry that we considered. These results confirmed that the solution of our mathematical model with estimates of D and λ from assay 1 failed to predict the position of the leading edge and the shape of the density profile in assay 2. Similarly, we confirmed that the solution of the mathematical model with estimates of D and λ from assay 2 failed to predict the position of the leading edge and the shape of the density profile in assay 1.

A key assumption in this work is that the cell spreading always took place in a two-dimensional monolayer for the entire duration of the experiments. Initially, we also performed experiments where cells were placed into and around the barriers at a higher density than we reported here. In these additional experiments we observed that cells did not form a monolayer due to the high initial density. These additional experiments were not analysed here since the two-dimensional model is inappropriate.

One limitation of our study is that we have not resolved the question of why cells appear to behave differently in different geometries. One possible mechanism that could explain our observations is that the total number of cells initially present in assay 2 is always larger than in assay 1. Assuming that each cell consumes nutrients at a particular rate, we might expect that the supply of nutrients in assay 2 would be depleted faster than in assay 1 which is consistent with our observations that D and λ are apparently smaller in assay 2. To test this hypothesis we suggest that additional measurements of the availability of nutrients could be made and that these measurements could be incorporated into an extension of the mathematical model where D and λ explicitly depend on nutrient availability. This suggestion could be important since many mathematical models of collective cell spreading make the implicit assumption that the supply of nutrients is unlimited [20, 85, 86, 113]. Other options for extending this work are to include further

experiments to examine the role of other geometries, such as using barriers with different curvatures. Unfortunately the barriers that we used in this study are fixed in shape and so a different experimental apparatus would be required to study such an extension.

Acknowledgements

We acknowledge the Australian Research Council (DP120100551) and the Royal Society International Exchange Scheme. We appreciate support from Parvathi Haridas, Kerry Manton and David Leavesley, as well as the comments from two anonymous referees.

CHAPTER 6

Assessing the role of spatial correlations in collective cell spreading

A paper published in *Scientific Reports*.

Treloar, K.K., Simpson, M.J., Binder, B.J., McElwain, D.L.S. & Baker, R.E. Assessing the role of spatial correlations during collective cell spreading *Sci. Rep.* 4, 5713 (2014).

Abstract

Spreading cell fronts are essential features of development, repair and disease processes. Many mathematical models used to describe the motion of cell fronts, such as Fisher's equation, invoke a mean-field assumption which implies that there is no spatial structure, such as cell clustering, present. Here, we examine the presence of spatial structure using a combination of *in vitro* circular barrier assays, discrete random walk simulations and pair correlation functions. In particular, we analyse discrete simulation data using pair correlation functions to show that spatial structure can form in a spreading population of cells either through sufficiently strong cell-to-cell adhesion or sufficiently rapid cell proliferation. We analyse images from a circular barrier assay describing the spreading of a population of MM127 melanoma cells using the same pair correlation functions. Our results indicate that the spreading melanoma cell populations remain very close to spatially uniform, suggesting that the strength of cell-to-cell adhesion and the rate of cell proliferation are both sufficiently small so as not to induce any spatial patterning in the spreading populations.

6.1 Background

Moving fronts of cells are frequently observed in embryonic development, tissue repair and cancer progression [20, 44, 85, 89, 116, 152]. *In vitro* experiments, such as scratch or circular barrier assays, play an important role in identifying and quantifying the mechanisms that control the motion of such cell fronts [7, 78, 86, 113, 125, 137–139]. Standard continuum models, such as Fisher’s equation or generalisations thereof, are often used to describe the motion of *in vitro* cell fronts [86, 101, 113, 116, 125, 132, 139]. However, these models invoke a mean–field assumption implying that there is no underlying spatial structure, such as cell clustering, present in the system [80, 127].

It is well known that strong cell–to–cell adhesion or sufficiently rapid cell proliferation can lead an initially uniform population of cells to become clustered over time [2, 127]. Our previous work has compared averaged discrete simulation data with predictions from standard mean–field descriptions of these discrete simulations for systems where either strong adhesion [67] or rapid proliferation is present [12, 126]. These previous comparisons have confirmed that standard mean–field models fail to accurately predict the averaged behaviour of the discrete model which implies that the usual mean–field assumption is inappropriate where either strong cell–to–cell adhesion or rapid proliferation is present [12, 67, 126, 127]. We do not aim to repeat these kinds of comparisons between averaged discrete simulation data and the predictions of a mean–field model in this work. Instead, we analyze a detailed experimental data set with the aim of demonstrating how the presence of spatial structure, such as cell clustering, can be identified and quantified.

Unlike mean–field models, individual–based models explicitly incorporate spatial correlation effects [12, 88, 126] and allow us to visualise the cell spreading process in a way that is directly comparable with experimental images [27, 40, 125, 137]. However, individual–based models are computationally expensive and many realisations are required to obtain reliable statistics, meaning that it is often difficult to simulate realistic biological systems [88]. Mean–field models are more amenable to analytical exploration and hence can be advantageous over individual–based models provided that the mean–field assumption is an accurate representation of the relevant system [88, 127].

It is not always clear which modelling framework is appropriate for a given context without first testing the underlying model assumptions. For example, spreading populations of 3T3 fibroblast cells do not generally exhibit visible cell clustering, whereas populations of MDA MB 231 breast cancer cells appear to be highly clustered [125, 127]. At first glance, it may appear reasonable to use a mean–field model to describe the spreading of a population of 3T3 cells and a discrete model to describe the spreading of a population of MDA MB 231 cells. However, recent work has indicated that the presence or absence of spatial correlations can be difficult to detect visually and so our use of a mean–field model for 3T3 cell population spreading may, in fact, be inappropriate [2]. Consequently, applying diagnostic tools which are capable of identifying spatial structure in a given cell population may provide insights into which modelling frameworks are suitable for exploring a particular system.

Several methods have been developed to assess the degree of spatial correlations in populations including measurements of the coordination number, Ripley's K function and Moran's I statistic [14, 54, 110, 111, 126]. A specific measure of spatial correlations is the pair correlation function, $F(r)$, which describes how the probability of finding two objects at a given distance, r , relates to the probability of finding two objects, separated by the same distance, in a spatially uniform population [2, 14, 127]. Pair correlation functions are a useful tool as they can be used to distinguish between spatial patterns, such as aggregation or segregation, at various length scales [2, 14, 103]. In particular, pair correlation functions have been successfully used to distinguish differences between spatial patterns of benign and malignant cells [91].

In this work, we quantify the extent to which the location of individual MM127 melanoma cells [102, 107, 154] are spatially correlated during an *in vitro* cell spreading assay. We perform several *in vitro* experiments where cells are initially placed in a circular barrier and then the population spreads outwards after the barrier is lifted [125, 137]. In particular, we consider a detailed experimental procedure where all experiments are repeated under two different conditions: first, where cells are treated to prevent proliferation, and second, where cell proliferation is permitted. This is important because MM127 melanoma cells are known to be motile, adhesive and proliferative [137], and our experimental procedure allows us to examine the effects of proliferation separately from adhesion. This therefore allows us to determine whether spatial correlations are present, and, if so, whether the spatial correlations are associated with cell proliferation or cell-to-cell adhesion [125, 137].

To assess the degree of spatial correlations in our experimental cell populations, we calculate the pair correlation function developed by Binder and Simpson [14], which accounts for volume exclusion (crowding) and is relevant when considering biological cells which cannot occupy the same location in space. We also examine the conditions under which spatial structure can form in a spreading cell population using discrete simulations that mimic the spreading melanoma cell population. Using the pair correlation function we confirm that the distribution of cells is initially spatially uniform. Finally, we use the pair correlation function to determine whether any spatial correlations over short length scales emerge during the cell spreading process. All experiments are repeated for two different initial cell densities. Our results confirm that the degree of cell motility, cell proliferation and cell-to-cell adhesion in the spreading melanoma cell populations does not lead to significant spatial correlations.

6.2 Methods

6.2.1 Cell culture

Human malignant melanoma cells (MM127, [102, 107, 154]) were cultured with 10% fetal calf serum (FCS), RPMI-1640, 2mM L-Glutamine, 23mM HEPES (Invitrogen, Australia) and 1% v/v penicillin/streptomycin (Invitrogen, Australia). Prior to confluence, cells were lifted using 0.05% trypsin-EDTA(1×) (Invitrogen, Australia) and viable cells were counted using a Trypan blue exclusion test and a haemocytometer.

6.2.2 Circular barrier assay

The experimental procedure have been reported in detail previously [125, 137]. Metal–silicone barriers (Aix Scientifics, Germany) were cleaned, sterilised, dried and placed in the centre of each well of a 24-well tissue culture plate. Experiments were performed using two different cell densities: 20,000 and 30,000 cells per well. Cell proliferation was suppressed in half of all cell solutions by adding 10 µg/mL Mitomycin–C (Sigma Aldrich, Australia) for one hour at 37°C prior to transfer to the wells [112]. 100 µL of cell suspension was carefully inserted into the barrier to ensure that the cells were approximately evenly distributed. Cells were allowed to settle and attach for four hours in a humidified incubator at 37°C, 5% CO₂ and 95% air. Assays commenced with the removal of the barrier and the cell layer was washed with warm serum free medium (culture medium without FCS) and replaced with 0.5 mL of culture medium. Cultures were incubated at 37°C in 5% CO₂ and 95% air for $t = 0$ and 48 hours. Each assay, for each time point, was repeated three times.

6.2.3 Image acquisition and analysis

The cell nuclei were stained using 1 mg/ml Propidium Iodide (Invitrogen, Australia) in phosphate buffered saline and images were acquired using a Nikon Eclipse Ti inverted microscope fitted with a Nikon digital camera. Overlapping adjacent images were used to reconstruct a transect images detailing the location and size of individual cell nuclei along the spreading cell population. MATLAB’s Image Processing Toolbox [90] was used to convert the images into black and white by thresholding the image (*rgb2gray*, *imadjust*, *im2bw*). Images were discretised onto the pair correlation lattice by rescaling the image so that each square pixel corresponds to a length of $\delta = 1 \mu\text{m}$ (*imresize*). White pixels correspond to unoccupied lattice sites and black pixels indicate occupied lattice sites. Each cell on the pair correlation lattice is composed of several black pixels. In all cases, a visual check was performed to validate that all cells had been correctly identified using the software. For discrete simulations, the simulation lattice was rediscretised onto the pair correlation lattice by scaling the lattice by a factor of 18 such that a simulated cell occupying one lattice site on the simulation lattice instead occupied $18 \times 18 = 324$ lattice sites on the pair correlation lattice and is composed of 324 black pixels.

6.2.4 Pair correlation function

Pair correlation functions were computed by considering pair distances between all black pixels on the pair correlation lattice for both experimental images and discrete simulation data [14]. The pair correlation lattice is a finite square lattice with integer coordinates, each site corresponding to the centre of a pixel and assigned coordinates (r, w) , where $r \in \{1, 2, \dots, R\}$ is a coordinate on an axis aligned in the direction of outward spreading and $w \in \{1, 2, \dots, W\}$ in the direction perpendicular to the direction of outward spreading.

In our calculations we used $R = W$. The occupancy of black pixels on the pair correlation lattice is captured by the indicator function,

$$M(r, w) = \begin{cases} 0 & \text{if site } (r, w) \text{ is vacant,} \\ 1 & \text{if site } (r, w) \text{ is occupied.} \end{cases}$$

The number of black pixels (n) at any given time and the corresponding pair correlation density (ρ) are given by

$$n = \sum_{w=1}^W \sum_{r=1}^R M(r, w), \quad \rho = \frac{n}{RW}.$$

We define the set of paired black pixels as

$$\psi = \{(a, b) | w_a = w_b, r_a \neq r_b, M(r_a, w_a) = M(r_b, w_b) = 1\},$$

where a and b denote generic pixels with coordinates (r_a, w_a) and (r_b, w_b) , respectively. The subset of black pixel pairs at distance i ($1 \leq i \leq R$) is

$$S_i = \{(a, b) | |r_a - r_b| = i, (a, b) \in \psi\}.$$

The number of elements in the subset S_i indicate the counts of pair distances

$$c_r(i) = |S_i| \quad \text{for } i = 1, \dots, R.$$

The normalisation factor is given by

$$\hat{c}_r(i) = W^2(R - i)\rho\hat{\rho},$$

where $\hat{\rho}$ corresponds to the conditional probability of selecting the second black pixel in the black pixel pair given that the probability of selecting the first black pixel is the usual density ρ ,

$$\hat{\rho} = \frac{n - 1}{RW - 1}.$$

The pair correlation function, $F(i)$, is given by

$$F(i) = \frac{c_r(i)}{\hat{c}_r(i)}. \tag{6.1}$$

The pair correlation function is calculated using N subregions giving an average pair correlation function $\bar{F}(r) = \left(\sum_{n=1}^N F_n(r) \right) / N$. If $\bar{F}(r) = 1$, the probability of finding two black pixels at a given distance, r , is equal to the probability of finding two black pixels at the same distance in a spatially uniform distribution of objects [2, 14]. If $\bar{F}(r) < 1$, the probability of finding two black pixels at a given distance, r , is less than the probability of finding two black pixels at the same distance in a spatially uniform distribution of objects [2, 14]. Alternatively, if $\bar{F}(r) > 1$, the probability of finding two black pixels at a

given distance, r , is greater than the probability of finding two black pixels at the same distance in a spatially uniform distribution of objects [2, 14].

6.3 Results

6.3.1 Visual inspection of spreading MM127 melanoma cell populations does not provide insights into possible spatial correlations

Circular barrier assays were conducted to examine the role of spatial correlations in a spreading population of MM127 melanoma cells over a period of $t = 48$ hours [137]. The exact nature of the experiments was described in the methods section. Briefly, cells were initially placed inside a circular barrier and the barrier was then lifted allowing the cell population to spread outwards. To distinguish whether cell proliferation has a significant effect on the presence of spatial correlations in the cell population, we performed experiments with Mitomycin-C pretreatment to suppress cell proliferation [112] and then repeated the experiments without Mitomycin-C pretreatment.

Figure 6.1 shows images of the entire spreading cell populations, as well as the relative location and size of various square subregions, each of dimension $600 \mu\text{m} \times 600 \mu\text{m}$, located both in the centre of the spreading population [Figure 6.1 (a)] and towards the edge of the spreading population [Figure 6.1 (e)]. Our analysis will focus on cell behaviour in these subregions. We also provide images, in Figure 6.1, showing the distribution of individual cells within smaller subregions, of dimensions $300 \mu\text{m} \times 300 \mu\text{m}$, at the centre of the spreading cell population [Figure 6.1 (b-d)] and at the edge of spreading cell population [Figure 6.1 (f-h)]. For the purposes of analysis, R and W denotes the length and width of the subregion, respectively. Here, r corresponds to the radial distance in the direction of outward spreading ($1 \leq r \leq R$) and w corresponds to the direction perpendicular to r ($1 \leq w \leq W$). We expect an even distribution of individual cells at $t = 0$ hours since the experiments were initialised by placing cells as uniformly as possible inside the circular barrier [137]. Examining the snapshots at $t = 0$ hours, the cells appear to be spatially uniform with no visual evidence of clustering. However, without further analysis, it is difficult to conclude whether the cells are clustered or not [2].

If we compare results at $t = 48$ hours in Figure 6.1 (c-d) and (g-h), after cells have had the opportunity to migrate, adhere to other cells, and to proliferate, the cell populations still appear to be relatively uniform. However, it is difficult to conclude whether the cells are clustered or not simply from inspecting these snapshots. Comparing the snapshots where cell proliferation is permitted to those where cell proliferation is absent, it is clear that cell proliferation dramatically increases the density of cells but it is unclear whether there is any major change in the extent of cell clustering. Furthermore, comparing the snapshots of cells within the subregions located at the centre of the population with the subregions located towards the edge indicates that there is very little difference between the distributions of cells in these two different locations. Although there is no clear visual indication of spatial correlations, previous work [2, 14] suggests that further analysis

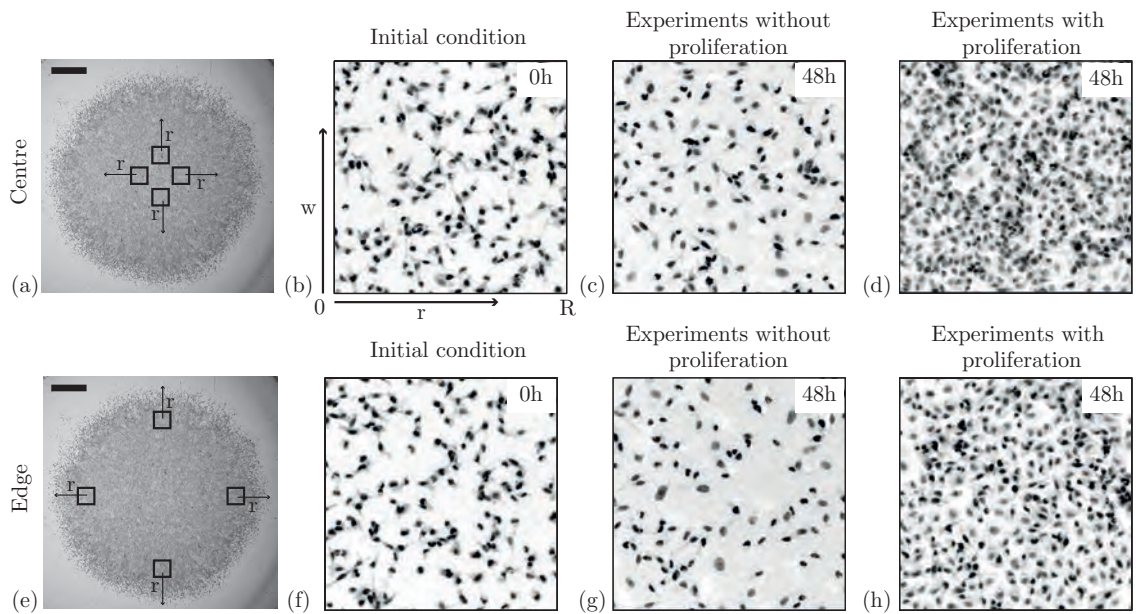


Figure 6.1: Experimental subregions of spreading MM127 melanoma cell populations. The role of spatial correlations in spreading MM127 cell populations was investigated by considering circular barrier assays initiated with 30,000 cells. For each experiment we calculated the pair correlation functions in four subregions, each of dimension $600 \mu\text{m} \times 600 \mu\text{m}$, at the centre of the spreading cell population and in four subregions, each of dimension $600 \mu\text{m} \times 600 \mu\text{m}$, at the edge of the spreading cell population. The relative size and approximate location of these subregions is shown in (a) and (e), where the scale bar corresponds to $1,500 \mu\text{m}$. Subregions showing the location of individual cells are shown at $t = 0$ hours in (b) and (f), at $t = 48$ hours for experiments without cell proliferation in (c) and (g), and at $t = 48$ hours for experiments with cell proliferation in (d) and (h). Note that the subregions in (b–d) and (f–h) are of dimension $300 \mu\text{m} \times 300 \mu\text{m}$. We describe the geometry of each subregion using coordinates (r, w) , such that r indicates the direction of outward spreading and w measures the width of the subregion. The subregions in (a) and (e) correspond to $1 \leq r \leq 600 \mu\text{m}$ and $1 \leq w \leq 600 \mu\text{m}$, while the regions in (b–d) and (f–h) correspond to $1 \leq r \leq 300 \mu\text{m}$ and $1 \leq w \leq 300 \mu\text{m}$.

should be undertaken before we can be certain that there is no underlying spatial structure present in the MM127 cell population.

6.3.2 Discrete simulations of the experimental process provide insight into possible mechanisms inducing spatial correlations

Before we analyse the experimental images to quantify the role of spatial correlations, we first investigate how spatial correlations may emerge in the spreading MM127 melanoma cell populations by simulating the barrier assay using a discrete random walk model that incorporates cell motility, cell-to-cell adhesion and cell proliferation. We consider a two-dimensional model since the MM127 melanoma cell population spreads as a monolayer for the duration of the experiments [137].

In this work, we considered two types of lattices; (i) a simulation lattice, and (ii) a pair correlation lattice. The simulation lattice, with lattice spacing Δ , is used to perform random walk simulations of the barrier assay. This involves modelling the spreading of a population of simulated cells, which mimic real cells in the experiments, undergoing motility events modulated by cell-to-cell adhesion, and proliferation events. Here, Δ is an indication of the average area that each individual cell occupies on the tissue culture

plate. We chose to focus on the area occupied by the nucleus since the total area occupied by the cell fluctuates whereas the area occupied by the nucleus does not. To determine Δ , we measured the area of the nucleus and converted this into an estimate of the diameter of the nucleus ($\Delta \approx 18 \mu\text{m}$, Appendix D).

The pair correlation lattice is used to compute the pair correlation function on a finer lattice, with lattice spacing $\delta = 1 \mu\text{m}$. Both experimental images and discrete simulation images are discretised onto the finer pair correlation lattice by resizing the dimensions of the image such that each pixel is $1 \mu\text{m} \times 1 \mu\text{m}$ (Appendix D). Each pixel on the pair correlation lattice is either vacant (white pixel) or occupied (black pixel). Each black pixel is an object on the pair correlation lattice and corresponds to part of a cell in the experiments or part of a simulated cell in the discrete simulations. The advantage of discretising cells onto a pair correlation lattice using several black pixels ($\delta \ll \Delta$) as opposed to discretising with one cell per lattice site is that we avoid having to select the location of individual cells on the lattice as this is not always an accurate representation of the original location of cells in the experiments [14]. The pair correlation signal is computed for all pair distances on the pair correlation lattice between $1 \mu\text{m}$ and $600 \mu\text{m}$. For specific details of the calculation of the pair correlation function, $F(r)$, we refer the reader to the methods section. When we present our estimates of the pair correlation function, $F(r)$, we focus on pair distances in the interval $1\Delta \leq r \leq 5\Delta$ ($18 \mu\text{m} \leq r \leq 90 \mu\text{m}$) since we are primarily interested assessing spatial correlations over small to intermediate length scales [6,67], but no smaller than the diameter of the nucleus [14].

Random walk simulations are initialised to mimic the experimental procedure where either 20,000 or 30,000 cells are placed, uniformly at random, inside the circular barrier. Each circular barrier, of diameter $6,000 \mu\text{m}$, is placed into the centre of a well on a tissue culture plate. The well has a diameter of $15,600 \mu\text{m}$. To mimic this geometry in the discrete simulations we place either 20,000 or 30,000 simulated cells, uniformly at random, inside a circular region of diameter of $334 \approx 6,000/18$ lattice sites. This circular region is located approximately in the centre of a square lattice of side length $867 \approx 15,600/18$ lattice sites.

A random sequential update algorithm is used to perform the discrete simulations [24]. If there are $S(t)$ simulated cells at time t , during the next time step of duration τ , $S(t)$ simulated cells are selected at random, one at a time, and given the opportunity to move with probability $P_m(1-q)^a$. Here, $0 \leq P_m \leq 1$ is the probability that an isolated simulated cell can move a distance Δ during the time interval τ , $0 \leq q \leq 1$ is a measure of cell-to-cell adhesion strength, and $a = 0, 1, 2, 3$ or 4 is the number of occupied nearest-neighbour lattice sites of that simulated cell. If $q = 0$, there is no cell-to-cell adhesion and nearest neighbour simulated cells do not adhere to each other. As q increases, the strength of cell-to-cell adhesion increases, and the motion of nearest-neighbour simulated cells is reduced as the cells adhere more tightly to each other. A simulated cell at position $(i\Delta, j\Delta)$ steps to $(i\Delta \pm \Delta, j\Delta)$ or $(i\Delta, j\Delta \pm \Delta)$ with each target site chosen with equal probability of $1/4$. Since our model is an exclusion process, which explicitly incorporates crowding effects, any attempted motility event where the target site is occupied will be aborted. Once the $S(t)$ potential motility events have been assessed, another $S(t)$ simulated cells are selected

at random, one at a time, and given the opportunity to proliferate with probability $0 \leq P_p \leq 1$. If the opportunity to proliferate is successful, the proliferative simulated cell attempts to deposit a daughter simulated cell at $(i\Delta \pm \Delta, j\Delta)$ or $(i\Delta, j\Delta \pm \Delta)$ with each target site chosen with equal probability of $1/4$. Again, any attempted proliferation event where the target site is occupied will be aborted. We relate the parameters in the discrete model, P_m and P_p , to standard measures of the cell diffusivity, $D = P_m\Delta^2/(4\tau)$, and the cell doubling time, $t_d = \tau \ln_e(2)/P_p$ [137]. Our previous work, which did not include any measurement of spatial correlation, modelled the spread of MM127 melanoma cell population and indicated that we have $D \approx 248 \mu\text{m}^2/\text{hour}$ [137].

To understand how different mechanisms give rise to different spatial correlations in the discrete model, we simulated the spreading MM127 cell populations with varying degrees of cell motility (D), cell-to-cell adhesion strength (q) and cell proliferation (t_d). Figure 6.2 shows several snapshots from the discrete model after $t = 48$ hours. In each snapshot, the initial distribution of simulated cells is shown as an inset. The corresponding average pair correlation functions, $\bar{F}(r)$, calculated using Equation (6.1) (methods section), are shown in Figure 6.3. In all cases, we analysed four subregions, of dimension $600 \mu\text{m} \times 600 \mu\text{m}$, both at the centre of cell population, as indicated by Figure 6.3 (a), and four subregions at the edge of the cell population, as shown in Figure 6.3 (e). Each spreading experiment was simulated using three identically-prepared realisations of the discrete model, giving a total of $N = 3 \times 4 = 12$ identically prepared subregions. Pair correlation signals, $\bar{F}(r)$, were computed from the discrete simulation data using exactly the same procedure that we apply to the experimental images, as described in the following section. The simulation lattice was resized onto the pair correlation lattice so that each lattice site corresponds to a physical length of $\delta = 1 \mu\text{m}$. This means that each square simulated cell is composed of $18 \times 18 = 324$ black pixels. Additional results indicate that the choice of δ is relatively insensitive provided that $\delta < \Delta$ (Appendix D).

Results in Figure 6.2 (b–c) and (g–h) mimic experiments with Mitomycin–C pretreatment in which cell proliferation is suppressed by setting $P_p = 0$. Here, simulated cells undergo cell motility events modulated by cell-to-cell adhesion, but do not proliferate. Four subregions, each of dimension $600 \mu\text{m} \times 600 \mu\text{m}$, were considered at the centre of the cell population [Figure 6.2 (a)] and at the edge of the cell population [Figure 6.2 (f)]. The discrete snapshot at $t = 0$ hours, shown as an inset in Figure 6.2 (b), appears spatially uniform, and this is confirmed by the corresponding pair correlation signal in Figure 6.3 (b) which shows that $\bar{F}(r) \approx 1$ between $1\Delta \leq r \leq 5\Delta$. If spatial correlations are present, we expect the pair correlation signal to deviate from unity [14].

Discrete snapshots, after $t = 48$ hours, are shown in Figure 6.2 for simulations with weak cell-to-cell adhesion [Figure 6.2 (b) and (g)] and strong cell-to-cell adhesion [Figure 6.2 (c) and (h)]. Visually we see that there is a significant difference in the spatial distribution of individual simulated cells when the strength of cell-to-cell adhesion is high. Here, simulated cells form clusters of around 5–15 individuals. In contrast, if we consider the case with weak cell-to-cell adhesion, the spatial distribution of individual simulated cells appears to be uniform and there are very few clusters. The corresponding

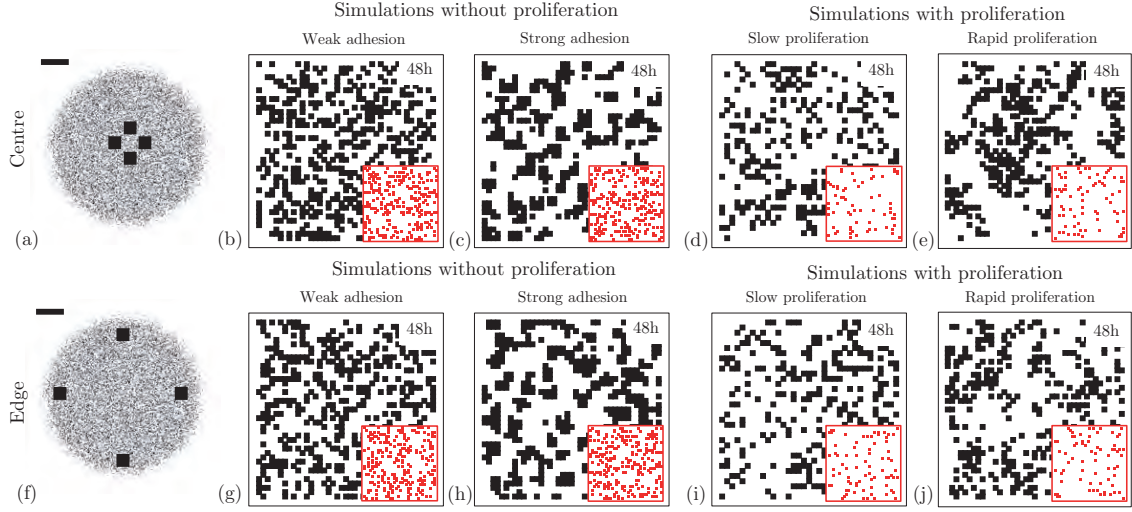


Figure 6.2: Discrete simulation snapshots with different combinations of cell motility, cell-to-cell adhesion and cell proliferation mechanisms. The emergence of spatial correlations in a spreading cell population was examined by simulating the biological process using a discrete random walk model with different combinations of adhesion, motility and proliferation. For each simulation we calculated the pair correlation functions in four subregions, each of dimension $600 \mu\text{m} \times 600 \mu\text{m}$, at the centre of the spreading cell population (a–e) and in four subregions, each of dimension $600 \mu\text{m} \times 600 \mu\text{m}$, at the edge of the spreading cell population (f–j). The relative size and approximate location of these subregions is shown in (a) and (f), where the scale bar corresponds to $1,500 \mu\text{m}$. Simulations are performed on the simulation lattice where the lattice spacing, $\Delta = 18 \mu\text{m}$, corresponds to the average diameter of the nucleus. Results in (b–c) and (g–h) correspond to simulations at $t = 0$ hours where 30% of simulation lattice sites are initially occupied with simulated cells, uniformly at random. While results (d–e) and (i–j) are initially occupied at 5%. The initial distribution of simulated cells, for each simulation, is shown as an inset in red. The size of the inset is approximately $550 \mu\text{m} \times 550 \mu\text{m}$. Simulation snapshots with no proliferation and weak adhesion ($q = 0.3$) are shown in (b) and (g) and snapshots with no proliferation and strong adhesion in (c) and (h). All results with no proliferation include unbiased motility where $D = P_m \Delta^2 / 4\tau = 248 \mu\text{m}^2/\text{hour}$. Snapshots in (d) and (i) illustrate simulations with no adhesion and slow proliferation ($t_d = 23$ hours). While results with no adhesion and rapid proliferation ($t_d = 12$ hours) are shown in (e) and (j). Results with proliferation are simulated using $D = 248 \mu\text{m}^2/\text{hour}$ for $t_d = 23$ hours and $D = 23 \mu\text{m}^2/\text{hour}$ for results with $t_d = 12$ hours. Results in row 1 and 2 correspond to pair correlation signals computed at the centre and at the edge of the cell population, respectively.

pair correlation signals for each case, for subregions located at the centre of the cell population [Figure 6.3 (c)], confirm our visual observations since $\bar{F}(r)$ fluctuates around unity for simulations with weak cell-to-cell adhesion and deviates significantly from unity for simulations with strong cell-to-cell adhesion. The pair correlation signal for strong cell-to-cell adhesion indicates that $\bar{F}(1\Delta) > 1$ meaning that pairs of simulated cells at a distance of 1Δ are more probable than pairs of objects at the same distance in a spatially uniform population. The pair correlation signal at the edge of the population [Figure 6.3 (g)] shows the same trend and illustrates that there is relatively little difference between the spatial distribution of cells at the centre and at the edge of the spreading population.

Similar results can be observed in Figure 6.2 (d–e), (i–j) and Figure 6.3 (d) and (h) where we show the results of simulations that mimic experiments without Mitomycin-C pretreatment and where cell-to-cell adhesion is not present ($q = 0$). Here, simulated cells undergo cell motility and cell proliferation events. In this case, we compare slow and rapid proliferation mechanisms where we observe that rapid cell proliferation leads to clustering. Here, $\bar{F}(1\Delta) > 1$ and $\bar{F}(2\Delta) > 1$, indicating that simulated cells at pair

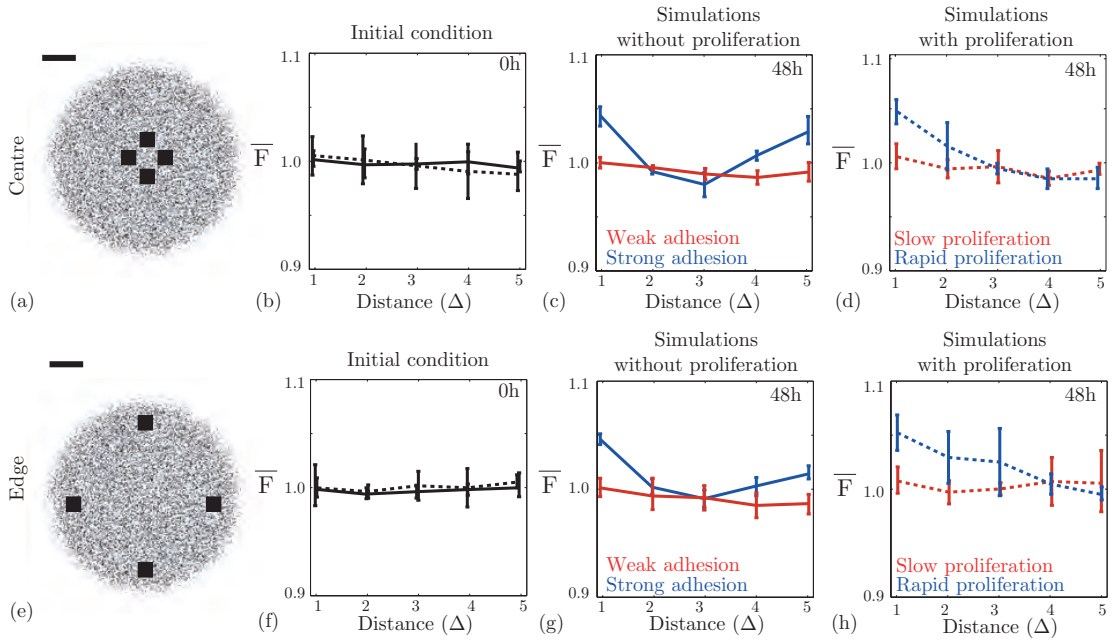


Figure 6.3: Different mechanisms in discrete simulations lead to varying pair correlation signals. Average pair correlation signals were computed from discrete simulations with varying degrees of cell-to-cell adhesion strength and cell proliferation in subregions, of dimension $600 \mu\text{m} \times 600 \mu\text{m}$, located at the centre and at the edge of the spreading simulated populations. The relative size and approximate location these subregions are shown in (a) and (e), respectively, where the scale bar corresponds to $1,500 \mu\text{m}$. Simulations are performed on the simulation lattice where the lattice spacing, $\Delta = 18 \mu\text{m}$, corresponds to the average diameter of the nucleus. Solid lines in (b–d) and (f–h) correspond to simulations without cell proliferation in which 30% of simulation lattice sites are initially occupied with simulated cells, uniformly at random. Dotted lines correspond to simulations with proliferation in which 5% of simulation lattice sites are initially occupied. Average pair correlation signals, constructed using $N = 12$ subregions from three replicate simulations, are shown at $t = 0$ hours in (b) and (f), at $t = 48$ hours for simulations without proliferation in (c) and (g), and at $t = 48$ hours for simulations with proliferation in (d) and (h). Pair correlation signals in (c) and (g) are shown for simulations with no proliferation and weak cell-to-cell adhesion ($q = 0.3$, red) and strong cell-to-cell adhesion ($q = 0.7$, blue). All results without proliferation include unbiased motility where $D = P_m \Delta^2 / 4\tau = 248 \mu\text{m}^2/\text{hour}$. Pair correlation signals for simulations with no adhesion and slow proliferation ($t_d = 23$ hours, red) and rapid proliferation ($t_d = 6$ hours, blue) are shown in (d) and (h). Results with proliferation are simulated using $D = 248 \mu\text{m}^2/\text{hour}$ for $t_d = 23$ hours and $D = 23 \mu\text{m}^2/\text{hour}$ for results with $t_d = 12$ hours. Results in row 1 and 2 correspond to pair correlation signals computed at the centre and at the edge of the cell population, respectively.

distances between $1\Delta \leq r \leq 2\Delta$ are more likely to occur than pairs of objects, separated by the same distance, in a spatially uniform population. To highlight the differences between slow and rapid proliferation, we obtained the results in Figure 6.2 (d–e) and Figure 6.2 (i–j) by initiating the simulations with a smaller number of simulated cells (5,000) than in the experiments. Furthermore, we also reduced the degree of motility in the simulations where we considered rapid proliferation. These differences were required otherwise the lattice becomes fully confluent after $t = 48$ hours with rapid proliferation and we note that a confluent monolayer of simulated cells has, by definition, no spatial structure. Therefore, reducing the initial number of cells and their motility rate allowed us to compare the spatial structure present at $t = 48$ hours before the lattice became confluent. The cell doubling time for MM127 melanoma cells is approximately 23 hours meaning that the total cell number will have approximately tripled over $t = 48$ hours in a

modestly crowded environment. Hence, we expect in our experiments that the cell density, in regions away from the edge of cell population, will be approaching confluence by $t = 48$ hours. This means that any spatial correlations present in experiments with Mitomycin-C pretreatment could be masked by proliferation when it is not suppressed. This observation emphasises the importance of considering different experimental conditions to distinguish between the effects of different mechanisms [125, 137].

Our discrete simulation investigation indicates that cell populations where strong cell-to-cell adhesion or rapid cell proliferation are present are associated with spatial correlations and clustering which implies that the mean-field assumption is inappropriate to describe such systems [2]. The failure of the mean-field assumption to predict the averaged discrete behaviour for systems with either strong adhesion or rapid proliferation has been examined previously [12, 67, 126]. Although we know in advance that cell-to-cell adhesion and cell proliferation plays a role in governing the spreading of MM127 melanoma cell populations [137], without any kind of analysis of the spatial distribution of individual cells within the population it is unclear whether these mechanisms are sufficiently strong to induce significant spatial correlations and clustering [137].

6.3.3 Spatial correlations are not present in spreading MM127 melanoma cell populations

Our experimental snapshots in Figure 6.1 did not provide any conclusive visual evidence about whether spatial correlations may be present in the spreading melanoma cell populations. To quantitatively determine the extent to which the cell populations are spatially correlated, we computed the average pair correlation signals for all experiments using the same procedures applied to the discrete simulations, as discussed in the methods section. For each set of experiments, we analysed four subregions, each of dimension $600 \mu\text{m} \times 600 \mu\text{m}$, at the centre of cell population, as indicated by Figure 6.1 (a), and four subregions, each of dimension $600 \mu\text{m} \times 600 \mu\text{m}$, near the edge of the cell population, as shown in Figure 6.1 (e). Each experiment was repeated three times giving a total of $N = 3 \times 4 = 12$ subregions. We note that each experimental subregion produces a similar pair correlation signal, $F(r)$, over all pair distances considered in this work. Supplementary results in Appendix D illustrate that for each experiment and location considered, there are no obvious differences in the pair correlation signal across replicates or subregions. Hence, we treat each realisation as an identically prepared, independent subregion, and we determine the average pair correlation function, $\bar{F}(r) = \left(\sum_{n=1}^N F_n(r) \right) / N$, where $N = 12$.

Average pair correlation signals for all sets of experiments are shown in Figure 6.4. Given that our experiments were initiated by placing cells as uniformly as possible inside the circular barrier at $t = 0$ hours, we expect that the pair correlation signal will fluctuate around unity ($\bar{F}(r) \approx 1$) for all pair distances. The signals at $t = 0$ hours in Figure 6.4 (b) and (f) confirm that the cells are initially distributed uniformly at random inside the barrier both at the centre of the cell population and at the edge of the cell population. Results after $t = 48$ hours, for subregions located at the centre [Figure 6.4 (c-d)] and at

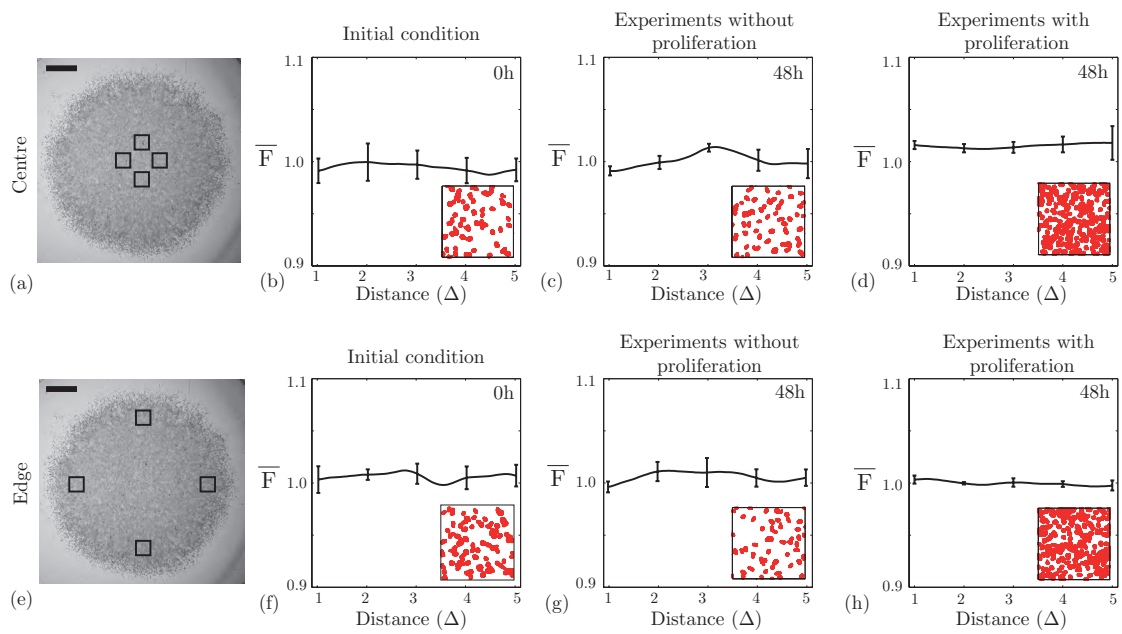


Figure 6.4: Spatial correlations are not present in spreading MM127 melanoma cell populations. Average pair correlation functions were extracted from images showing the location of individual cells in four subregions, each of dimension $600 \mu\text{m} \times 600 \mu\text{m}$, at the centre of the spreading cell population (a) and four subregions, each of dimension $600 \mu\text{m} \times 600 \mu\text{m}$, at the edge of the spreading cell population (e). The relative size and approximate location of these subregions is shown in (a) and (e), respectively, where the scale bar corresponds to $1,500 \mu\text{m}$. Average pair correlation signals are shown at $t = 0$ hours in (b) and (f), at $t = 48$ hours for experiments without cell proliferation in (c) and (g), and at $t = 48$ hours for experiments with cell proliferation in (d) and (h). Results in (b-d) and (f-h) correspond to pair correlation signals computed at the centre and at the edge of the spreading cell population, respectively. The horizontal axis is measured as multiples of the average diameter of the nucleus which is approximately $18 \mu\text{m}$. Snapshots of the experimental subregions after image processing are shown as an inset. The size of the inset is approximately $215 \mu\text{m} \times 215 \mu\text{m}$. Each pair correlation signal was averaged over 12 subregions of dimensions $600 \mu\text{m} \times 600 \mu\text{m}$, using three identically prepared experimental replicates. The error bars correspond to one standard deviation about the mean ($N = 12$). All experiments were conducted by initially placing approximately 30,000 cells inside the barrier assay.

the edge [Figure 6.4 (g-h)] of the cell population, for all experiments with and without cell proliferation, also indicate that the average pair correlation signal, $\bar{F}(r)$, fluctuates around unity for pair distances between $1\Delta \leq r \leq 5\Delta$.

The pair correlation signals in this work were computed using data extracted from experiments where 30,000 cells were placed inside the circular barrier initially. To investigate whether the initial cell density affects the presence of spatial correlations, we repeated the procedure using a different initial cell density where 20,000 cells were placed as uniformly as possible in the barrier and we found similar results (Appendix D). In addition to considering the pair correlation at the centre of the population and at the edge of the population, we also calculated the pair correlation signal at other locations across the spreading cell population. These additional results show that the pair correlation signal does not change significantly across the spreading cell population (Appendix D).

All results presented so far involve computing the pair correlation function, $F(r)$, by considering distances between pairs of pixels in the direction of outward spreading, r .

Alternatively, we could consider distances between pairs of pixels in the direction perpendicular to outward spreading, w , to give $F(w)$. Additional results (Appendix D) compare $F(r)$ and $F(w)$, showing that the average pair correlation function is independent of the direction considered.

6.4 Discussion

In this work, we investigated the presence of spatial correlations in a spreading population of MM127 melanoma cells by computing pair correlation signals at the centre and edge of the spreading cell population. Our results indicate that there is very little underlying spatial structure present in the experimental system. Assessing the presence of spatial correlations using statistical tools, such as the pair correlation function, allows us to quantify the degree to which spatial structure is present in a given cell population. This information may provide insight into which potential modelling frameworks could be used to represent the experimental system. The relative absence of spatial structure in the spreading MM127 melanoma cell populations implies that a mean–field model could be appropriate to represent these experiments, at least over the time scales explored in the experimental data set [80, 127].

Using our experimental data set, we have been able to investigate the relative roles of cell proliferation and cell–to–cell adhesion in terms of how they contribute to the formation of clustering. This is important because many experimental and modelling approaches neglect to consider the roles of adhesion and proliferation separately, meaning that it could be difficult to distinguish between the contributions of each mechanism [125, 137]. We are interested in identifying the potential contribution of each mechanism since the analysis of the resulting spatial patterns from our discrete model indicates that both rapid proliferation and strong cell–to–cell adhesion can lead to significant spatial patterning and clustering. In contrast, our experimental results indicate that there were no major differences between the spatial distribution of cells in a population where cell proliferation was suppressed compared to the spatial distribution in a population where cell proliferation was present.

Acknowledgements

We acknowledge the Australian Research Council (FT130100148) and the Royal Society International Exchange Scheme. We appreciate support from Parvathi Haridas, Mitchell Stark and the suggestions from two anonymous referees.

CHAPTER 7

Conclusions

In this chapter we summarise the results and novel contributions of this work, and discuss potential avenues of further investigation.

7.1 Summary

This study utilised combined mathematical modelling tools and experimental investigation to identify and quantify several key features of collective cell spreading. The tandem use of experimental investigations to inform and parameterise mathematical models for collective cell spreading has been a key focus of this work.

The principal aims of this thesis were to

- Apply multiscale models of collective cell spreading to new experimental data with the aim of independently quantifying the rate of cell motility and rate of cell proliferation in a spreading cell population,
- Identify multiple types of data to distinguish between the roles of cell motility, cell proliferation and cell-to-cell adhesion in spreading melanoma cell populations,
- Quantify the variability in detecting the leading edge of cell migration assays using image analysis techniques, and in turn use mathematical modelling to provide a physical interpretation of the leading edge,
- Investigate the affect of *in vitro* assay geometry on estimates of the rate of cell motility and rate of cell proliferation, and
- Use modelling tools to diagnose the presence of spatial correlations in spreading melanoma cell populations.

We began this study in Chapter 2, by describing a set of experiments which investigated the roles of cell motility and cell proliferation in driving an initially confined fibroblast cell population. To distinguish between cell motility and cell proliferation, experiments were performed by suppressing cell proliferation in the first instance, and then repeating the experiments with cell proliferation. The experimental data was analysed using two mathematical models; a lattice-based discrete random walk model and a related continuum partial differential equation model. Using our approach, we were able to obtain independent estimates of the cell diffusivity and cell proliferation rate, and confirm that

these estimates led to accurate modelling predictions of the temporal and spatial evolution of the position of the leading edge and the cell density profile of the spreading cell populations.

Previous experimental and modelling studies have focused on measuring the speed of the leading edge of the spreading cell population [85, 86]. However, according to the Fisher–Komogorov equation there are multiple combinations of D and λ that give rise to the same prediction of the leading edge speed [85, 86]. One way to overcome this is to fit the solution of the model to cell density observations [113, 114, 116]. However, this does not necessarily ensure that the process of model calibration can be separated from the process of model prediction. Our work provided a method to overcome these limitations by intentionally altering the details of the experiments so that we were able to isolate and separately quantify the roles of cell motility and cell proliferation. In turn, we were able to confirm previous suggestions that the relative combinations of cell motility and cell proliferation control the shape of the leading edge; in which steep fronts are characterised by a high λ/D ratio and shallow diffuse fronts by a low λ/D ratio. Our results illustrated that continuum models, based on the Fisher–Kolmogorov equation, are appropriate to interpret and predict the spread of the spreading fibroblast cell populations.

In Chapter 3, we applied the experimental and modelling techniques discussed in Chapter 2 to quantify the mechanisms driving the spread of melanoma cell populations. Cell-to-cell adhesion is thought to be important in melanoma cell population spreading and we accounted for this by incorporating cell motility, cell proliferation and cell-to-cell adhesion mechanisms into our discrete mathematical framework. To identify the cell diffusivity, strength of cell-to-cell adhesion and cell proliferation rate of the spreading melanoma cell populations, we undertook a systematic approach which integrated several types of experimental data. Our approach illustrated that standard types of data, such as the area enclosed by the leading edge of the spreading cell population and more detailed cell density profiles throughout the spreading cell population does not provide sufficient information to uniquely identify the cell diffusivity and cell proliferation rate. Instead, we found that additional data relating to the degree of cell clustering was required to provide independent estimates of the strength of cell-to-cell adhesion, and in turn the cell diffusivity. We also illustrated that the same techniques applied in Chapter 2 to estimate the cell proliferation rate could be used to independently estimate the proliferation rate of the melanoma cell populations.

One of the consequences of this work is that while it is relatively simple to incorporate detailed mechanisms into a mathematical model, it becomes increasingly difficult to independently identify the contributions of each mechanism in the mathematical model using experimental data. However, where possible, the systematic identification and extraction of multiple types of data may provide important insights into the contributions of individual mechanisms to the spread of a cell population. For example, standard mathematical models for collective cell spreading typically neglect cell-to-cell adhesion and many estimates of the cell diffusivity vary widely [85, 113, 132]. Separating the role of cell-to-cell adhesion from the role of cell motility, as was undertaken in this work, may provide one

tool to investigate this variation. Additionally, there is currently no standard method to quantify the degree of cell-to-cell adhesion present in a spreading cell population and our work addressed this by providing a method to assess the strength of cell-to-cell adhesion by extracting information about the location of isolated cells in the population.

Throughout Chapter 2 and Chapter 3, we used information about the position of the leading edge of the spreading cell populations to estimate the cell diffusivity. For each study, image analysis tools were used to detect the position of the leading edge. In Chapter 4, we investigated how the details of these tools, such as the edge detection threshold, affected the position of the detected leading edge of the spreading population. Our results indicated that the observed spreading rates are very sensitive to the choice of image analysis tools and that a standard measure of cell migration can vary by as much as 25% for the same experimental images depending on the details of the image analysis tools. Our results implied that it is very difficult, if not impossible, to meaningfully compare previously published measures of cell migration since previous results have been obtained using different image analysis techniques and the details of these techniques are not always reported.

One limitation of edge detection algorithms is that they do not specify any physical measure, or physical definition, of the leading edge of the spreading population. We addressed this here by providing a physical interpretation of our edge detection results using a mathematical model. Our modelling indicated that variations in the image threshold parameter correspond to a consistent variation in the local cell density. This means that varying the threshold parameter is equivalent to varying the location of the leading edge in the range of approximately 1–5% of the maximum cell density.

The research presented in Chapters 2 to 4 considered the spread of fibroblast and melanoma cell population in one particular geometry. Chapter 5 investigated whether the geometry of the *in vitro* assay affects estimates of the cell diffusivity and cell proliferation rate of spreading fibroblast cell populations. To address this question, we performed experiments in two distinct geometries: (i) a tumour-like geometry where a cell population spreads outwards into an open space and (ii) a wound-like geometry where a cell population spreads inwards to close a void. Applying the same experimental and modelling techniques presented in Chapter 2, we obtained estimates of the cell diffusivity and cell proliferation rate for each different assay geometry. Using the obtained estimates, we were able to accurately predict the time-evolution of the location of the leading edge and the cell density profiles throughout the spreading cell populations for both geometries considered. Our work showed that estimates of the cell diffusivity and cell proliferation rate were different depending on the geometry considered, with estimates of the cell diffusivity varying by up to 50% and estimates of the cell proliferation rate varying by up to 30%. An important consequence of our work is that estimates obtained in one geometry can not necessarily be used to predict the spreading of the same cell population in a different geometry.

Throughout Chapters 2 to 5, we applied a mathematical modelling framework in which we implicitly assumed that there was no spatial structure, such as cell clustering, present in any of the cell populations considered. This allowed us to use a mean-field approach to predict the spatial and temporal evolution of the fibroblast cell populations, as well as quantify the rate of cell proliferation in both the fibroblast and melanoma cell populations. However, without first testing whether spatial correlations are present in the cell population, it is unclear whether the modelling approaches applied in Chapters 2 to 5, were in fact appropriate. Chapter 6 assessed the validity of this assumption by using tools to diagnose spatial structure in the spreading melanoma cell populations considered in Chapter 3. In particular, we analysed discrete simulation data using pair correlation functions to show that spatial structure can form in a spreading population of cells either through sufficiently strong cell-to-cell adhesion or sufficiently rapid cell proliferation.

Analysing the experimental data using the same methods applied to the discrete simulation data, indicated that the spreading melanoma cell populations remain very close to spatially uniform. This suggested that the strength of cell-to-cell adhesion and the rate of cell proliferation are both sufficiently small so as not to induce any spatial patterning in the spreading populations. Hence, a mean-field model may be appropriate to describe the collective spreading of this particular cell line. Overall, our work highlighted the importance of testing the underlying assumptions of a given mathematical model and provided one method to diagnose spatial structure in a spreading cell population.

7.2 Future work

There are multiple avenues of future investigation that have arisen from the research in this thesis and we consider some of these below.

- **Quantifying cell motility, cell proliferation and cell-to-cell adhesion mechanisms driving three-dimensional (3D) spreading cell populations**

Our work has been solely focused on understanding the mechanisms driving the spread of cell populations in two-dimensions (2D). However, development, tissue repair and disease progression are three-dimensional environments and the mechanisms underlying the spread of cell populations may be very different in 3D as opposed to those in 2D [7, 30, 78]. Hence, it is unsurprising that several 3D *in vitro* assays have been developed to investigate collective cell spreading in 3D environments [30, 78]. For example, spheroid assays allow us to mimic the spatial expansion of clusters in 3D which would not be possible using a 2D assay [78]. A natural extension of our work, is to consider how the mechanisms driving collective cell spreading can be identified and quantified in 3D. It is relatively straightforward to adapt and apply the mathematical models in 3D, however, conducting and extracting complementary experimental data may be relatively more complicated in 3D. Advances in various microscopy techniques, such as confocal imaging, enables us to observe intricate details about 3D cell populations [30, 78]. For example, we may be able to track the location of several points on the surface of an expanding spheroid over time and consequently use this type of experimental data to calculate

model parameters or compare model predictions. We note that the edge detection algorithms required to locate the surface of a 3D spheroid cell population would require more sophisticated strategies than those applied to the 2D cell populations in this work. A preliminary investigation into these aspects may highlight whether it is feasible to extend the concepts in this work from 2D into 3D.

- **Investigating methods to extract model parameters from experimental data**

In this work, we estimated the cell diffusivity by considering the change in the position of the leading edge of the spreading cell populations over time. Similarly, we estimated the cell proliferation rate by extracting experimental data relating to the temporal change in cell density, in the middle of the cell population. One advantage of the methods used in this work, is that they are relatively easy to extract and analyse from both a experimental and modelling viewpoint. With recent advances in imaging and image analysis technologies, there is the potential to extract more detailed information about the spreading cell populations [7, 30, 78]. For example, time-lapse imaging allows us to capture trajectories of individual cells within the population [78]. Measurements of the cell diffusivity could be obtained from trajectory data using methods such as the relationship between diffusivity and the mean square displacement [127]. Consequently, it would be interesting to consider whether measurements of the cell diffusivity, obtained from many individual cells are any different to estimates obtained from population-scale level such as the location of the leading edge.

- **Exploring the role of drug therapies on the cell diffusivity and cell proliferation rate**

Cell motility and cell proliferation can be significantly affected by the addition of drugs into the system [7, 78]. For example, in this work we applied the drug Mitomycin-C to suppress cell proliferation in our experiments, observing that the overall spread of the cell populations were greatly reduced by the presence of this drug [112]. One extension of our work is to apply the methods developed in this work to understand how different concentrations of drugs affect the rate of cell motility and cell proliferation in a spreading cell population. The methods applied in this work could be used to extract estimates of these parameters and as a result we may be able to quantify whether the cell diffusivity, D , or cell proliferation rate, λ , is a function of the concentration of drug in the system.

- **Distinguishing between the contributions of cell motility and cell proliferation in multiple species cell populations**

Collective cell spreading often involves multiple species [119]. For example, one element of wound-healing is the interaction between fibroblast and keratinocyte cell populations [89]. Consequently, it could be insightful to quantify the spread of multi-species cell populations and identify methods to isolate the exact contributions of each population to the overall spread of entire population. In turn, this

may allow us to understand how cell populations may influence other cell populations. One possible procedure that could be used to understand this interaction is by systematically repeating the circular barrier assays conducted in this work. In particular, estimates of the cell diffusivity and cell proliferation rate could be obtained separately for each cell population, and then from experiments where the two cell populations are combined. From a modelling viewpoint, it is relatively straightforward to model multi-species populations and a model similar to the approach used in this work has been described in detail by Simpson *et al.* [119]. We note that several additional considerations may be required. For example, cells may form a cell monolayer in single-species cell populations, however, this may not be the case in multi-species cell populations and hence, the mathematical model may require adaptation to account for these potential differences.

- **Understanding the role of nutrient supply in collective cell spreading**

In Chapter 5 we observed that the cell diffusivity and cell proliferation rate varied significantly depending on the geometry of the *in vitro* assay. One possible reason is that the number of cells is always larger in the assay 1 geometry as opposed to the assay 2 geometry. Assuming that each cell consumes nutrients at a particular rate, we might expect that the supply of nutrients in assay 2 would be depleted faster than that in assay 1. We could test this hypothesis, by obtaining measurements from experiments where either the nutrient supply is monitored or maintained throughout. These measurements could then be incorporated into the mathematical model where the cell diffusivity and cell proliferation rate depend explicitly on the nutrients available. This could also help to address whether the assumption of unlimited nutrients in many mathematical models for collective cell spreading is reasonable.

- **Providing user-friendly access to image analysis software**

Throughout this thesis, we applied image analysis techniques to detect various features of the spreading 3T3 fibroblast and MM127 melanoma cell populations. These techniques used software platforms such as Matlab's Image Processing Toolbox [90] and ImageJ [66]. We also illustrated in Chapter 4 how varying the details of the image analysis can lead to different physical measurements, which in turn can alter modelling predictions. This poses an important question about providing accessibility to the image analysis software techniques used in research. Although the techniques used in this work are relatively simple and are already heavily documented in the manuals for Matlab's Image Processing toolbox and ImageJ, it is relatively easy to see how more advanced image analysis work could be distributed by providing original codes or written tutorials.

- **Addressing issues, practicalities and usefulness of mathematical models for collective cell spreading**

Collective cell spreading is inherently variable [24, 125, 132]. It is therefore unsurprising that mathematical models cannot possibly account for all of this variability and there will always be active debate regarding appropriate techniques to model

collective cell spreading [24, 125, 132]. Furthermore, there are many questions surrounding the issue of how we account for the high degree of uncertainty in modelling approaches. Other issues relevant to modelling collective cell spreading include:

- Simple versus complex models [3, 27, 125].
- Discrete models versus continuous models [4, 27, 113, 114, 125].
- Sufficient use of experimental platforms to provide insights [20, 30, 85, 86, 88, 125].
- Linear versus non-linear diffusion models [20, 85, 86, 113, 116, 125, 155].
- Lattice versus lattice-free approaches [105, 106].
- Incorporating simple or complex features in the model e.g. varying the mechanisms in the model [13, 24, 119].

An important consequence of this debate is that we need to continually reassess the appropriateness of our modelling choices depending on the aims of future investigations. For example, the experimental observations in this thesis indicated that there is a consistent density-dependent mechanism involved in the spread of both the 3T3 fibroblast and MM127 melanoma cell populations. Although our current experimental platform was not designed to resolve these details, our results illustrated the importance of repeating barrier assays with different initial numbers of cells so that these effects can be observed and quantified. In this context, our choice of modelling and experimental platforms were appropriate given our initial aims. However, in different circumstances our choice of modelling tools may not be appropriate given that we do not always have access to sufficient experimental data nor is it practical to repeat experiments for every single initial condition. Balancing aims, model complexity and the availability of experimental data is essential for continued insights into collective cell spreading.

7.3 Final remarks

Mathematical modelling in conjunction with experimental investigation has the potential to provide crucial insights into the mechanisms driving collective cell spreading. In this study, we investigated how experimental and modelling frameworks can be used to identify several key features underlying collective cell spreading. In particular, we were able to independently quantify the roles of cell motility and cell proliferation in a spreading cell population, and investigate how these roles are influenced by factors such as the initial cell density, type of cell population and the assay geometry. Efforts to explore how quantitative tools, such as mathematical modelling, can be effectively combined with experimental investigation while recognising and testing the limitations of such tools, are important for continued insights into collective cell spreading.

APPENDIX A

Supplementary material for Chapter 2: ‘Quantifying the role of cell motility and cell proliferation in a circular barrier assay’

A.1 Estimates of the cell diameter

Images of 3T3 cells were analysed using a Leica AF6000 wide field microscope (Figure A.1). Leica software was used to measure the cell diameter.

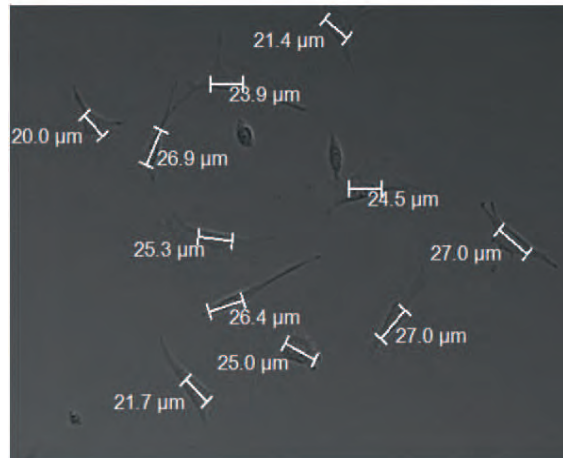


Figure A.1: Cell diameter measurements. Low cell density images, under high magnification, were used to record the diameter measurements of many individual 3T3 cells. Images were acquired using a Leica AF6000 wide field microscope and Leica software was used to measure the diameter of each cell.

The cell diameter data, reported in Table A.1, indicates that the mean cell diameter is 25 μm .

Cell diameter (μm)	29.44	23.90	31.86	20.14	24.06	28.05	17.51	22.80
	27.05	23.95	26.68	18.53	26.89	19.05	33.68	29.44
	23.70	23.40	20.40	23.60	31.90	22.60	29.60	26.60
Mean (μm)	25.08							
s.d. (μm)	4.66							

Table A.1: Cell diameter measurements from 24 3T3 cells show the average cell diameter is approximately $25 \pm 5 \mu\text{m}$

A.2 Image analysis using the MATLAB image processing toolbox

Customised image processing software was written using MATLAB's image processing toolbox. Figure A.2 illustrates the key steps used to detect the leading edge of the spreading populations. Each image was imported (`imread`), and displayed (`imshow`) (Figure A.2 (a)). The colour image was converted to greyscale (`rgb2gray`) (Figure A.2 (b)), and a binary gradient mask containing the segmented cell population was obtained by applying the Sobel operator (`edge(Original Image, Sobel)`, `edge(I,'sobel',threshold*0.5)`) to enhance lines of high contrast (Figure A.2 (c)). The lines in the binary gradient mask were dilated (`strel`, `imdilate`) to show the outline of the object (Figure A.2 (d)). Any remaining holes in the images were filled (`imfill`) and objects disconnected from the edge were removed (`imclearborder`). The image was smoothed and filtered to remove small objects (noise) detected in the previous steps (`imerode`, `medfilt2`). The resulting image contains both a large object (corresponding to the spreading cell population) and smaller objects (noise). The smaller objects were removed (`regionprops`, `bwareopen`) to leave the edge of the cell population (Figure A.2 (e)). An outline of the detected edge was superimposed back onto the original image (`bwperim`) (Figure A.2 (f)) to verify the accuracy of the procedure. The area (`regionprops`) of the detected object was estimated and converted into an equivalent circular diameter.

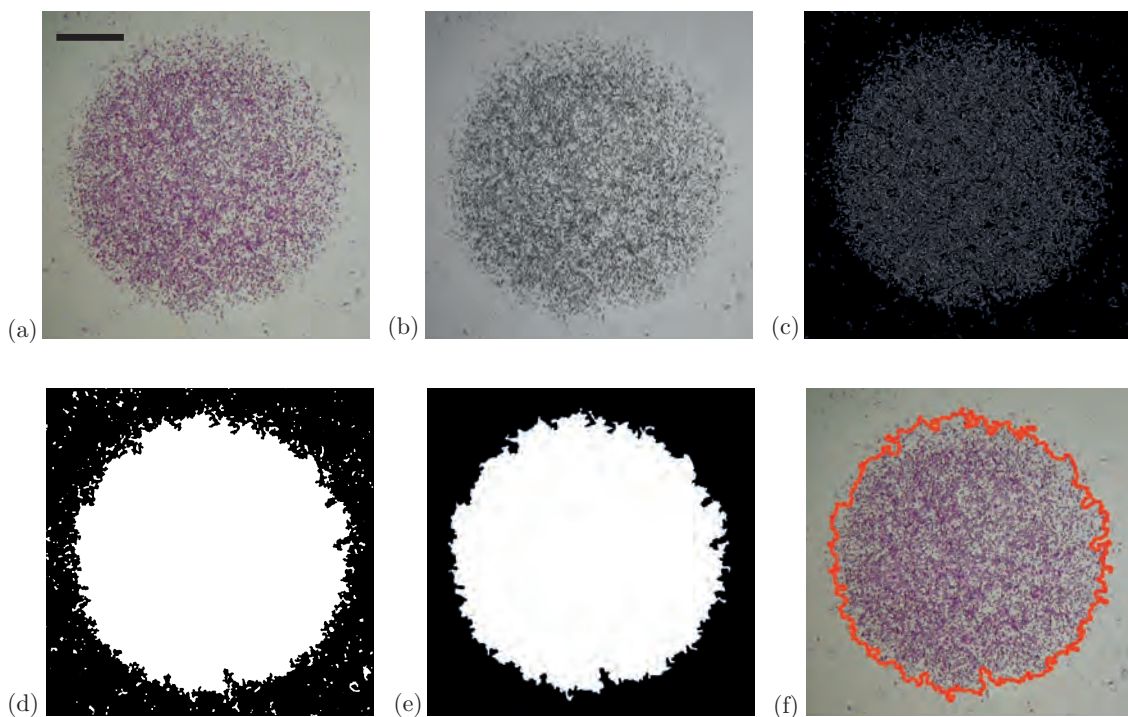


Figure A.2: (a)-(f) Customised image processing software (written using the MATLAB image processing toolbox) is used to detect the leading edge of a crystal violet stained experimental image with initially 5000 cells, at $t = 24$ hours, without Mitomycin-C. Scale bar corresponds to 1.5 mm.

To count the number of cells in the various subregions, we used a combination of customised image processing software, written using the MATLAB image processing toolbox, and manual counting where necessary. Images in Figure A.3 illustrate the key steps in the cell counting procedure. The subregion shown corresponds to an experiment where 5,000 cells were initially placed in the barrier without Mitomycin-C pretreatment. The image shows the density of P-stained cells after 24 hours. To count the cells we imported (imread) and displayed (imshow) the original image (Figure A.2 (a)). The colour image was converted to greyscale (rgb2gray) (Figure A.2 (b)) which was enhanced (imadjust) to provide sufficient contrast between each cell and the background of the image (Figure (c)). The image was converted to black and white based on a threshold (graythresh, im2bw). Objects less than 30 pixels were removed (bwareaopen) to reduce noise. Similar to the image processing for the leading edge detection, remaining holes in the image were filled (strel, imfill, Bwboundaries) (Figure A.2 (d)). The centre of each detected region (which we assume to be an individual cell) was identified (regionprops(image,Centroid)) and superimposed back on the original image to test the accuracy of the detection method (Figure A.2 (e)). The number of cells detected by the automated software was recorded, and any undetected cell was manually included in the total cell count (Figure A.2 (f)).

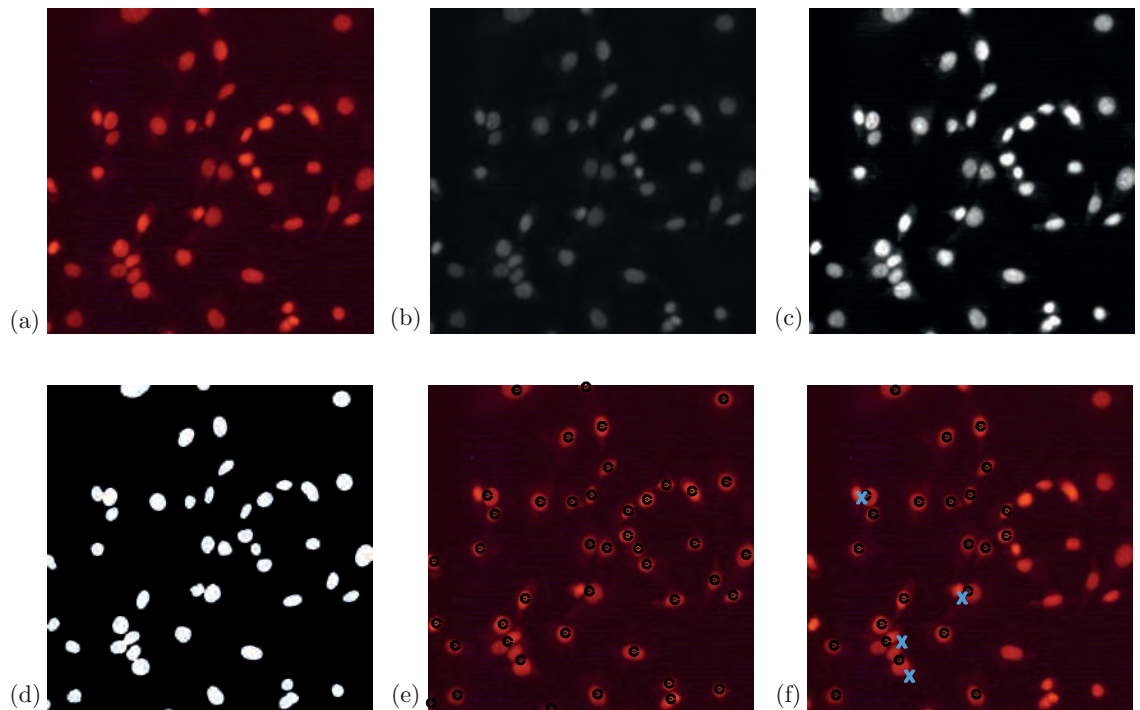


Figure A.3: (a)-(f) The number of cells in a small area is detected and counted using a combination of automated software (written using MATLAB) and manual counting. Each region is approximately $300 \mu\text{m} \times 300 \mu\text{m}$. Crosses in (f) indicate the location of manually-detected cells.

A.3 Experimental edge detection of the population–scale images (crystal violet stained images)

Table A.2 summarises the diameter of the spreading populations estimated from the experimental images.

Cell density	Time (hours)	Motility only		Motility and proliferation	
		Diameter		Diameter	
		mean (μm)	s.d. (μm)	mean (μm)	s.d. (μm)
5,000 cells	0	5981	129	3040	129
	24	6273	129	6277	152
	48	6966	119	7242	57
	72	7295	34	8179	117
10,000 cells	0	6079	172	6073	46
	24	6601	75	6953	304
	48	7062	238	7708	232
	72	7535	69	9042	251
30,000 cells	0	6178	161	6348	152
	24	7569	179	7590	69
	48	8091	116	8643	50
	72	8342	237	9766	96

Table A.2: Mean diameter estimates extracted from the population–scale images. Image processing was used to detect the location of the leading edge of the spreading cell populations from the experiments both with (motility only) and without Mitomycin–C (motility and proliferation) pretreatment, at $t = 0$, 24, 48 and 72 hours, with low and high initial cell densities. The area enclosed by the detected leading edge was converted into an equivalent circular radius to give a mean radius and standard deviation (s.d.) ($n = 3$).

A.4 Numerical solutions of the partial differential equation models

The numerical solution of Equation (2.2) (Chapter 2) was obtained using a finite difference approximation with uniform grid spacing, δr , and implicit Euler stepping with constant time steps, δt . Picard iteration, with absolute convergence tolerance ϵ was used to solve the resulting system of nonlinear equations.

A.5 Estimating the random motility coefficient

To estimate the diffusivity in the discrete random walk model we compared the experimental and simulated estimates of the diameter of the spreading populations by evaluating the least-squares error, which can be written as

$$E^2 = \frac{\sum_{i=1}^3 (d_s^i - d_e^i)^2}{\sum_{i=1}^3 (d_e^i)^2} \quad (\text{A.1})$$

where E is the least-squares error, d_s^i is the average simulated diameter at the three different time points, $i = 1, 2, 3$, and d_e^i is the average experimental diameter. The time points $i = 1, 2, 3$ correspond to $t = 24, 48$ and 72 hours, respectively.

We performed discrete simulations of cell spreading with Mitomycin-C pretreatment (no proliferation) for many different values of the diffusivity, D , which is equivalent to considering discrete simulations with different values of the time step, τ . For various values of diffusivity, we simulated each experiment until $t = 24, 48$ and 72 hours. The image analysis software was used to calculate the area enclosed by the leading edge, and the area was converted into an equivalent circular diameter. This process was repeated three times to mimic the experimental replicates and an average diameter for each experiment at each time point was obtained. Equation (A.1) was used to give the least-squares error between the experimental observations and the simulation data. Plots of the least-squares error for different values of the diffusivity are given in Figure A.4 which shows that we observe a well defined minimum for each experiment.

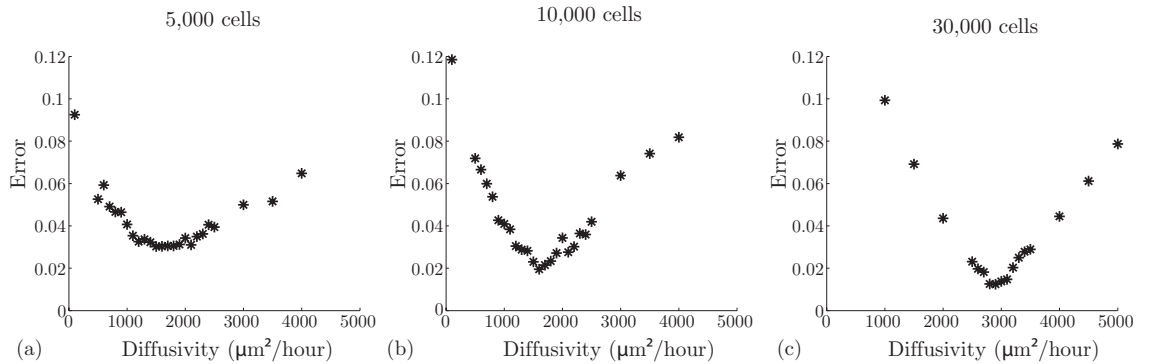


Figure A.4: Least-squares error versus diffusivity for the experiments with (a) 5,000, (b) 10,000 and (c) 30,000 initial number of cells placed into the barrier after Mitomycin-C pretreatment.

A summary of the least-squares estimates of the diffusivity (or equivalently the time step, τ) are given in Table A.3.

Initial number of cells	Time duration τ hours	Diffusivity $D \mu\text{m}^2/\text{hour}$	Error E
5,000	0.1042	1500	0.0302
10,000	0.0919	1700	0.0215
30,000	0.0539	2900	0.0165

Table A.3: Summary of the parameter estimation results with the optimal value of time duration τ and the corresponding value of diffusivity (D) for all three initial densities. The associated error as calculated using Equation (A.1) is also given.

The variability in our estimates of the diffusivity was estimated by repeating the calibration process using the experimental data without averaging. For our four different time points ($t = 0, 24, 48$ and 72 hours) we have three replicates of each experiment, giving us a total of 12 experimental images for each initial density. To conservatively estimate the variability in the diffusivity, we calibrated our random walk model for combinations of these 12 images that corresponded to the smallest observed spreading and the largest observed spreading. This approach gave us estimates of 1500 ($1500 - 2100$), 1700 ($1000 - 1900$) and 2900 ($2400 - 3200$) $\mu\text{m}^2/\text{hour}$ for the experiments with $5,000$, $10,000$ and $30,000$ initial number of cells, respectively. Here, the variability is given in the parenthesis.

A.6 Position of the leading edge with Mitomycin–C pretreatment

The location of the leading edge of the spreading populations for all experiments with Mitomycin–C pretreatment was determined using the image analysis software. The area enclosed by the leading edge was converted into an equivalent circular diameter. Results are summarised in Table A.4.

Initial number of cells	Average exp. d (μm)	Average discrete d (μm)	Average exp. d (μm)	Average discrete d (μm)	Average exp. d (μm)	Average discrete d (μm)
	$t = 24$ hours	$t = 24$ hours	$t = 48$ hours	$t = 48$ hours	$t = 72$ hours	$t = 72$ hours
5,000	6273	6536	6966	6774	7295	6926
10,000	6601	6822	7062	7123	7535	7451
30,000	7567	7458	8091	8084	8341	8466

Table A.4: The diameter, d , estimates (with Mitomycin–C pretreatment) of the experimental images were compared with the corresponding diameter estimates of the discrete snapshots using the calculated diffusivities at $t = 24, 48$ and 72 hours for all three initial densities. Results show good comparison between experimental and discrete estimates.

The images associated with the diameter estimates in Table A.4 for the experiment with $10,000$ cells initially placed in the barrier initially are reported in Figure 2.1 (Chapter 2). The remaining images associated with the estimates in Table A.4 are given in Figure A.5.

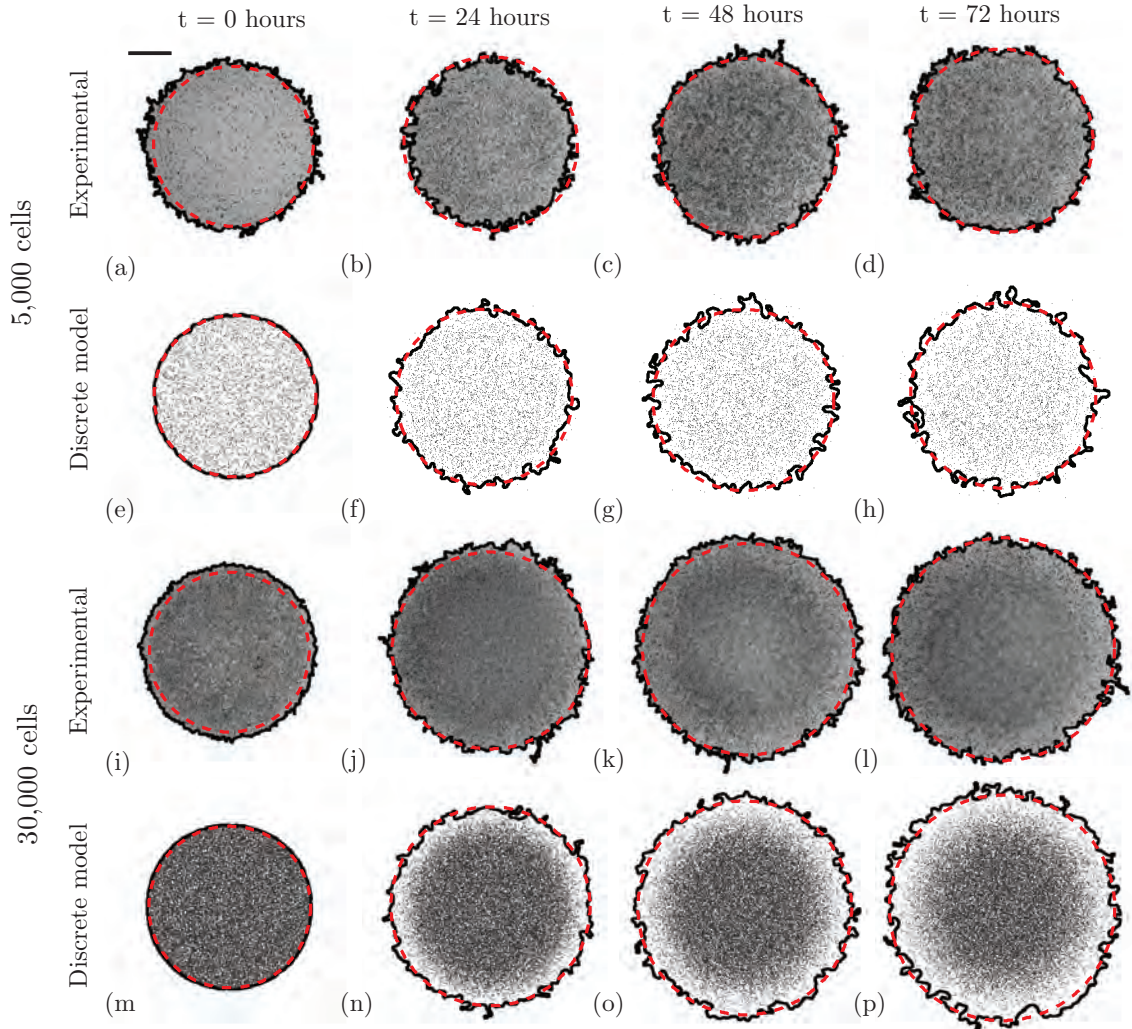


Figure A.5: Images for the experiments where 5,000 and 30,000 cells were placed in the barrier initially (corresponding to Figure 2.1 in the Chapter 2). Experimental images in (a)–(d) and (i)–(l) show barrier assays where 5,000 cells and 30,000 cells were placed initially into the barrier after pretreatment with Mitomycin-C, respectively. Images in (e)–(h) and (m)–(p) are snapshots from the discrete random walk model. Simulations were performed by placing either 5,000 or 30,000 agents uniformly inside a circular region of diameter $d = 6.0$ mm, and the system evolved with $P_m = 1$, $P_p = 0$ and $\tau = 0.1042$ (5,000 cells) or $\tau = 0.1042$ (30,000 cells). In all images (a)–(p), the black (stochastic) line indicates the position of the leading edge of the population as detected by the image analysis software. The red (smooth) curves in (a)–(p) are numerical solutions of Equation (5.1) (Chapter 2) with $\lambda = 0$ and $D = 1,500 \mu\text{m}^2/\text{hour}$ (5,000 initial cells) and $D = 2,900 \mu\text{m}^2/\text{hour}$ (30,000 initial cells). The $c^* = c(r, t) = 0.0017$ contour of the numerical solution is presented. The numerical solution of Equation (5.1) was obtained numerically with $\delta r = 1 \mu\text{m}$ and $\delta t = 0.005$ hours and absolute convergence tolerance $\epsilon = 1 \times 10^{-6}$. The scale bar corresponds to 1.5 mm.

A.7 Proliferation rate estimates

To quantify the proliferation rate we counted the number of cells in four different subregions located away from the leading edge of the spreading population for each experiment at each time point. These cell numbers were converted into a scaled cell density. Results are summarised in Table A.5.

Motility only (with Mitomycin-C)							
Initial number of cells	Time (hours)	c(t) (cells/ μm^2)			Mean	Standard deviation	
5,000 cells	0	0.1108	0.1440	0.1219	0.1662	0.1357	0.0250
	24	0.1234	0.1382	0.1481	0.0938	0.1259	0.0237
	48	0.1224	0.1275	0.1530	0.1632	0.1415	0.0197
	72	0.1420	0.1616	0.1224	0.1665	0.1481	0.0202
10,000 cells	0	0.2635	0.2572	0.2604	0.2309	0.2530	0.0150
	24	0.2234	0.2201	0.2170	0.2201	0.2201	0.0026
	48	0.2799	0.2170	0.2893	0.2704	0.2641	0.0324
	72	0.2728	0.2892	0.2673	0.2892	0.2796	0.0112
30,000 cells	0	0.5529	0.5161	0.6758	0.5867	0.5867	0.0691
	24	0.5543	0.6102	0.5912	0.5596	0.5788	0.0265
	48	0.6344	0.6598	0.6344	0.6090	0.6344	0.0207
	72	0.6220	0.5619	0.6110	0.5945	0.5974	0.0264
Motility and proliferation (without Mitomycin-C)							
Initial number of cells	Time (hours)	c(t) (cells/ μm^2)			Mean	Standard deviation	
5,000 cells	0	0.1335	0.1230	0.1440	0.1230	0.1492	0.0116
	24	0.2093	0.2486	0.2067	0.2486	0.1259	0.0234
	48	0.5861	0.5312	0.6646	0.6620	0.1415	0.0645
	72	0.9394	0.7484	0.7641	0.8530	0.8262	0.0884
10,000 cells	0	0.2234	0.2075	0.2233	0.1950	0.2123	0.0137
	24	0.4748	0.4025	0.4151	0.3962	0.4222	0.0359
	48	0.8459	0.7484	0.7794	0.7390	0.7782	0.0483
	72	0.8967	0.8748	0.9002	0.8302	0.8758	0.0032
30,000 cells	0	0.5845	0.6495	0.6387	0.6820	0.6387	0.0410
	24	0.8731	0.8421	0.9248	0.9041	0.8860	0.0362
	48	0.9929	0.9824	0.9459	0.9041	0.9563	0.0402
	72	1.0366	1.0584	1.1834	1.2002	1.1197	0.0841

Table A.5: Scaled density data for cell counts in the middle of the PI-stained transects for all initial densities at $t = 0, 24, 48$ and 72 hours, for experiments both with and without Mitomycin-C pretreatment at each time point.

To estimate the proliferation rate, λ , we used the experimental cell density estimates (Table A.5) and the solution of the logistic equation (Equation (2.4) in the Chapter 2) to estimate the least-squares error, which can be written as

$$E^2 = \frac{\sum_{i=1}^3 (c_l^i - c_e^i)^2}{\sum_{i=1}^3 (c_e^i)} \quad (\text{A.2})$$

where E is the least-squares error, c_l^i is the scaled cell density at the three different time points, $i = 1, 2, 3$, given by the solution of the logistic equation. c_e^i is the scaled cell density estimates obtained from the experimental images. The time points $i = 1, 2, 3$ correspond to 24, 48 and 72 hours, respectively. Plots of the least-squares error for different values of

the proliferation rate are given in Figure A.6 which shows that we observe a well-defined minimum for each experiment.

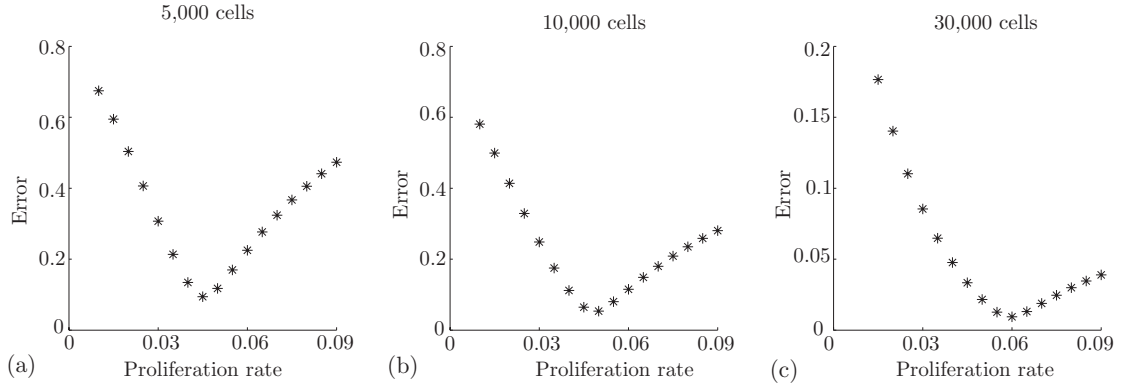


Figure A.6: Least-squares error versus proliferation rate λ for the experiments with (a) 5,000, (b) 10,000 and (c) 30,000 initial number of cells placed into the barrier without Mitomycin-C pretreatment.

A summary of the proliferation rate, λ , for each experimental condition is given in Table A.6.

Initial number of cells	Motility only	Error	Motility and Proliferation	Error
	λ /hour	E	λ /hour	E
5,000	0.0016	0.0758	0.0561	0.120
10,000	0.0021	0.0981	0.0552	0.0814
30,000	0.0026	0.0362	0.0594	0.0760
Average	0.0021	—	0.0569	—

Table A.6: Estimates of λ for the experiments with initially 5,000, 10,000 and 30,000 cells with and without Mitomycin-C pretreatment, and the associated least-squares error, given by Equation (A.2).

The variability in our estimates of the proliferation rate was estimated by repeating the calibration process using the experimental data without averaging. For our four different time points ($t = 0, 24, 48$ and 72 hours) we have four replicates of each experiment, giving us a total of 16 experimental images for each initial density. To conservatively estimate the variability in the proliferation rate, we calibrated the logistic model for combinations of these 16 images corresponding to the slowest observed growth and the fastest observed growth. This approach gave us estimates of 0.0561 (0.0443 – 0.0720), 0.0552 (0.0476 – 0.0645) and 0.0594 (0.0551 – 0.0784) /hour for the experiments with 5,000, 10,000 and 30,000 initial number of cells. Here, the variability is given in the parenthesis.

A.8 Locating the leading edge using the solution of a partial differential equation

Snapshots in Figure 2.2 (a)(d) (Chapter 2) show the leading edge of the spreading population as determined by the image analysis software. To determine the position of the leading edge using solutions of Equation (2.2) (Chapter 2), we determined a value of c^* , which is a contour of the solution of Equation (2.2) (Chapter 2) so that the area enclosed by the contour, $c^* = c(r, t)$, matches on average, the area enclosed by the leading edge of the spreading population determined by the image analysis software. To find c^* , we solved Equation (2.2) (Chapter 2) numerically for the appropriate initial conditions to model the spreading shown in Figure 2.2 (Chapter 2). Given the experimental estimates of the diameter at $t = 24, 48$ and 72 hours, we used the solution of Equation (2.2) (Chapter 2) to predict the diameter of the spreading population and compared these results with the experimental estimates of the diameter. Details are shown in Figure A.7 for this particular experiment where 10,000 cells were placed into the barrier initially. The profiles in Figure A.7 show how the diameter of the spreading population varies with the threshold contour value of the solution of Equation (2.2) (Chapter 2). We choose the relevant contour value that corresponds to the average experimental diameter. A summary of results for the same procedure applied to all three initial densities of cells is given in Table A.7, which, on average, indicates that $c^* = 0.0170$.

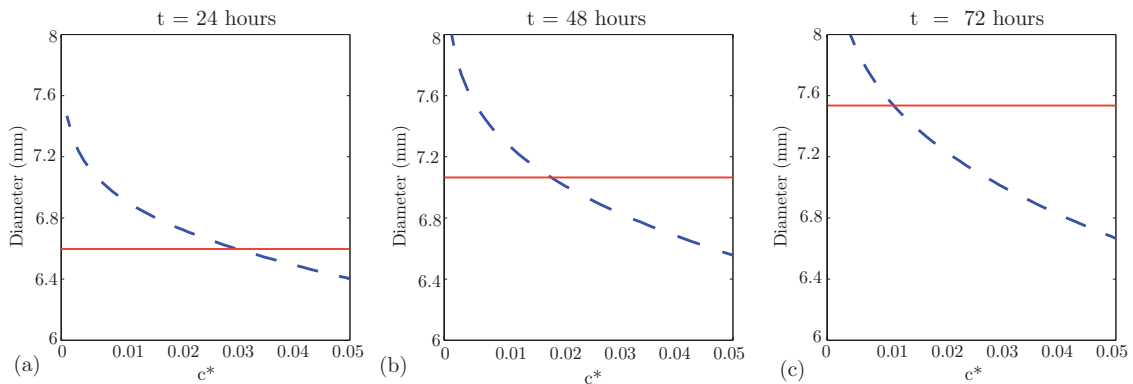


Figure A.7: Diameter estimates for the experiment where 10,000 cells were initially placed in the barrier after Mitomycin-C pretreatment in red (solid) at $t = 24$ (a), $t = 48$ (b), $t = 72$ (c) hours. The corresponding solution of Equation (2.2) (Chapter 2) is given in blue (dashed) for a range of contour values, $0.001 < c^* < 0.05$. The intersection of the curves gives the appropriate contour value for that time point. For this experiment we have $c^* = 0.030, 0.019$ and 0.012 for results at 24, 28 and 72 hours, respectively.

A.9 Leading edge position after 24 and 48 hours

Figure 2.3 (Chapter 2) show images of the spreading populations after 72 hours for all three initial densities of cells. Additional results are given in Figure A.8 to illustrate the observed spreading after $t = 0, 24$ and 48 hours for all experimental conditions.

Initial number of cells	c^* ($t=24$ hours)	c^* ($t=48$ hours)	c^* ($t=72$ hours)	Average
5,000	0.032	0.010	0.008	0.0167
10,000	0.030	0.019	0.012	0.0203
30,000	0.010	0.013	0.019	0.0140
Average	0.0240	0.0140	0.0130	0.0170

Table A.7: Contour values c^* giving the best match to the experimental diameter estimates with Mitomycin-C pretreatment for $t = 24, 48$ and 72 hours.

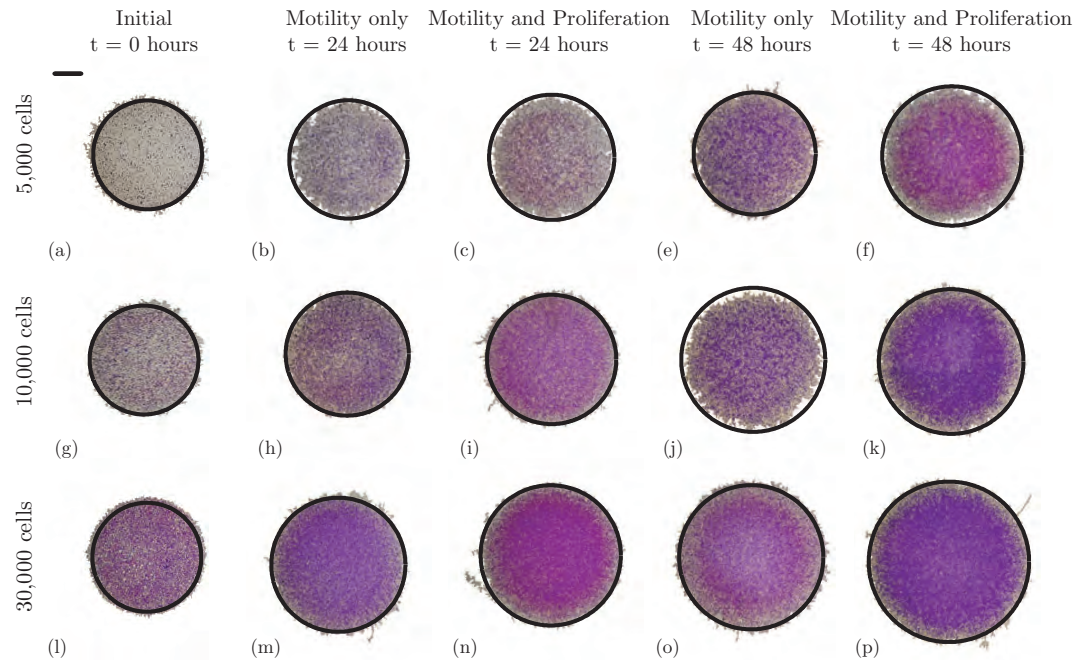


Figure A.8: The position of the leading edge was determined by analysing experimental images for the experiments where 5,000 (a)–(f), 10,000 (g)–(k), and 30,000 (l)–(p) cells were placed initially into the barrier. Images are shown at $t = 0$ (first column); at $t = 24$ hours both with and without Mitomycin-C pretreatment (second and third columns respectively); and at $t = 48$ hours both with and without Mitomycin-C pretreatment (fourth and fifth columns respectively). In each image, we superimpose the $c(r,t) = 0.017$ contour of the relevant solution of Equation (2.2) (Chapter 2) in black. The numerical solution of Equation (2.2) (Chapter 2) is obtained numerically with $\Delta r = 1 \mu\text{m}$ and $\Delta t = 0.005$ hours and absolute convergence tolerance $\epsilon = 1 \times 10^{-6}$. The scale bar corresponds to 1.5 mm.

APPENDIX B

Supplementary material for Chapter 3: ‘Multiple types of data are required to identify the mechanisms influencing the spatial expansion of melanoma cell colonies’

B.1 Estimating the diameter of the cell nucleus

High magnification images of MM127 cells were used to obtain an estimate of the mean diameter of the cell nucleus. To account for this variation, we estimate the diameter of the cell nucleus since the fluctuations in the size of the nucleus appear to be much smaller than the fluctuations in the size of the entire cell and therefore provides us with a more reliable estimate of the average area occupied by each cell. Images were acquired using a Nikon TI Eclipse microscope fitted with a Nikon digital camera. ImageJ was used to measure the diameter of the cell nucleus in the images (Figure B.1). These measurements are reported in Table B.1, and indicate that the mean diameter of the MM127 cell nucleus is approximately $18 \mu\text{m}$.

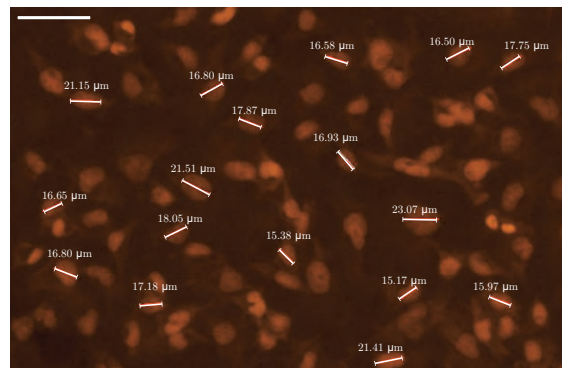


Figure B.1: High magnification images of MM127 cells. Images were acquired using a Nikon Ti Eclipse microscope fitted with a Nikon digital camera and the diameter of each cell nucleus was measured using ImageJ software. The scale bar corresponds to $50 \mu\text{m}$

Diameter of cell nucleus (μm)	18.94 18.78 21.98 17.34 23.50 17.00 16.00 16.74 16.42 15.03 16.49 18.95 17.00 21.52 16.15 16.86 16.11 14.17 19.32 21.15 16.80 17.87 16.58 16.50 17.75 16.93 16.65 16.80 21.51 18.05 17.18 15.38 23.07 15.17 15.97 21.41 22.48 17.58 16.50 18.00
Mean (μm)	17.94
Standard deviation (μm)	2.37

Table B.1: Cell diameter measurements of 40 MM127 cells indicate that the mean diameter of the cell nucleus is $17.94 \pm 2.37 \mu\text{m}$

B.2 Data type 1: Location of the leading edge

Image analysis software was used to detect the location of the leading edge of the expanding MM127 cell colonies. All measurements of the location of the leading edge were converted to an equivalent circular radius R . Table B.2 summarises the leading edge data for all experiments performed. All measurements reported are averaged over three experimental replicates.

Initial number of cells	Time (hours)	R (Motility and adhesion)		R (Motility, adhesion and proliferation)	
		Mean (mm)	Standard deviation (mm)	Mean (mm)	Standard deviation (mm)
20,000	0	3.2476	0.0223	3.2476	0.0223
	24	3.3007	0.0250	3.3407	0.0206
	48	3.3633	0.0305	3.4672	0.0506
30,000	0	3.2583	0.0208	3.2583	0.0208
	24	3.3277	0.0292	3.3807	0.0517
	48	3.3644	0.0198	3.6143	0.0229

Table B.2: Experimental radius measurements of the entire expanding cell colonies for all experiments performed. Image processing was used to determine the area of the expanding colony for each experiment with and without Mitomycin–C pretreatment at $t = 0$, $t = 24$ and $t = 48$ hours for both initial densities. The area of the expanding colony was converted into an equivalent circle from which we estimated the radius $R = \sqrt{A/\pi}$. Each data point was replicated three times to give the mean radius and standard deviation.

B.3 Data type 2: Cell density profiles

Cell density profiles were extracted from Propidium Iodide stained images which show the location of the nucleus of individual cells throughout the entire colony. Cell density profiles for each experiment were averaged over three experimental replicates as described in Chapter 3. Figure B.2 compares the cell density profiles extracted from three replicate experiments with the final averaged cell density profile for experiments initialised with 20,000 and 30,000 cells both with and without Mitomycin–C pretreatment. For all experiments, the averaged cell density profile appears to be an appropriate approximation given that the variation between the three replicate cell density profiles is minimal.

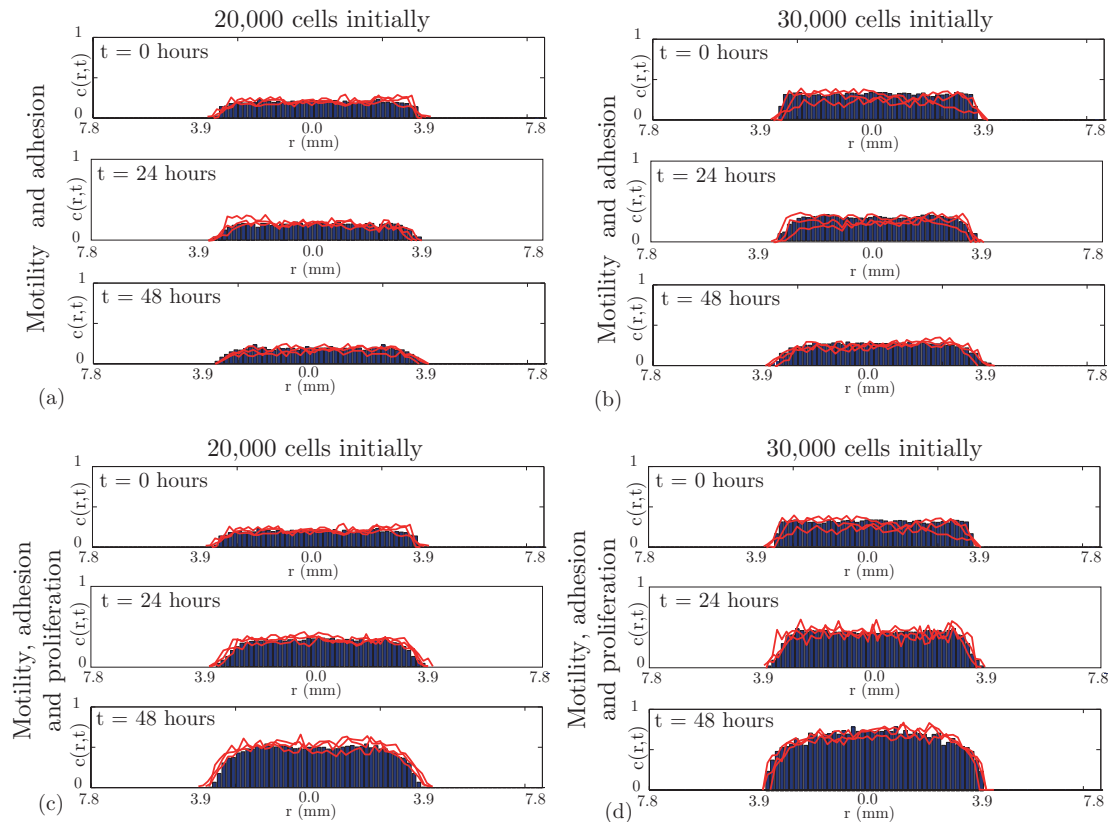


Figure B.2: Extracted cell density profiles (red lines) are compared with the averaged cell density profile (blue histograms) for experiments initialised with 20,000 cells and 30,000 cells, with and without Mitomycin–C pretreatment at $t = 0$, $t = 24$ and $t = 48$ hours. Cell density profiles were averaged as described in Chapter 3. Results in (a)–(b) correspond to experiments with Mitomycin–C pretreatment, while results in (c)–(d) correspond to experiments without Mitomycin–C pretreatment. For each experiment, the red lines correspond to the cell density profile extracted from each replicate experiment.

B.4 Data type 3: Degree of cell clustering

The degree of cell clustering in the MM127 cell colonies was measured by counting the number of isolated cells in Propidium Iodide images showing the location of the nucleus of individual cells throughout the entire colony. Table B.3 summarises the proportion of isolated cells compared to total number of cells in six subregions in the middle of the colony as described in Chapter 3.

Initial number of cells	Time	% Isolated cells in the colony	Mean	Standard deviation
20,000	0	34.14 36.01 45.25 33.68 36.50 47.19	38.80	5.88
	24	36.01 34.14 37.65 34.25 41.58 32.25	35.98	3.30
	48	29.82 37.17 33.68 31.81 28.58 36.71	32.96	3.54
30,000	0	15.69 13.83 11.25 15.23 16.98 18.25	22.58	5.01
	24	15.69 13.83 11.25 15.23 16.98 18.25	15.21	2.46
	48	11.96 12.58 9.94 11.9 10.88 12.58	11.64	1.04

Table B.3: Proportion of isolated cells in the MM127 cell colonies with Mitomycin–C pretreatment. Image processing was used to identify the number of isolated cells and the total number of cells in the expanding colony for each experiment with Mitomycin–C pretreatment at $t = 0$, $t = 24$ and $t = 48$ hours. The proportion of isolated cells in the expanding colony was converted into a percentage. Each data point was replicated six times to give the mean and standard deviation.

B.5 Data type 4: Cell density counts

The rate of cell proliferation in the cell population was quantified by counting the number of cells in four subregions located in the centre of the cell colonies for each experiment and at each time point. Results in Table B.4 summarise the nondimensional cell density measurements. The proliferation rate, λ , was estimated by comparing the time evolution of the experimental non-dimensional cell density measurements with the corresponding solutions of the logistic equation for various values of λ as described in Chapter 3. An estimate of the least squares error was used to determine the optimal value of λ for each experiment. Results in Figure B.3 illustrate the corresponding error, $\text{Error}_P(\lambda)$ for different values of λ for experiments without Mitomycin-C pretreatment. For each initial cell density, we observe a well-defined minimum, indicating that the proliferation rate is $\lambda = 0.0305$ /hours for experiments initialised with 20,000 cells and $\lambda = 0.0398$ /hours for experiments initialised with 30,000 cells.

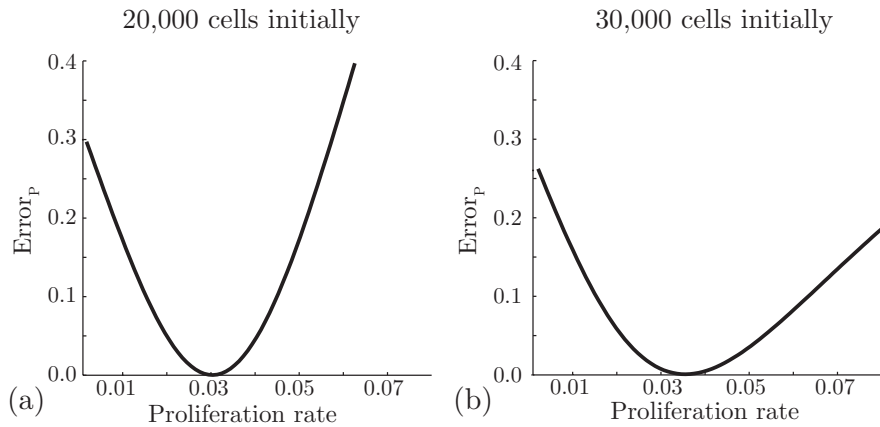


Figure B.3: An estimate of the least squares error was used to determine the proliferation rate in the MM127 melanoma cell colony. (a)–(b) indicates the error, $\text{Error}_P(\lambda)$ produced for various values of λ between 0.001 and 0.08 for experiments initialised with 20,000 and 30,000 cells, respectively.

Initial number of cells	Time (hours)	Motility and adhesion (with Mitomycin-C)				Motility, adhesion and proliferation (without Mitomycin-C)			
		c(t) (cells / μm^2)	Mean	Standard Deviation	c(t) (cells / μm^2)	Mean	Standard Deviation		
20,000	0	0.2015 0.2058 0.1958 0.2158	0.2047	0.0084	0.1757 0.1909 0.2100 0.1871	0.1909	0.0149		
	24	0.1985 0.2150 0.2048 0.2008	0.2048	0.0073	0.3399 0.3322 0.3513 0.3590	0.3456	0.0119		
	48	0.1985 0.2058 0.2150 0.2058	0.2063	0.0084	0.5227 0.4769 0.4616 0.5303	0.4979	0.0338		
30,000	0	0.2750 0.2993 0.3150 0.3447	0.3085	0.0292	0.2688 0.3421 0.2750 0.3054	0.2979	0.0336		
	24	0.2627 0.323 0.3090 0.3269	0.3056	0.0300	0.5993 0.5814 0.5695 0.6706	0.6052	0.0453		
	48	0.2627 0.3055 0.2912 0.3387	0.2995	0.0316	0.7251 0.7213 0.6869 0.6220	0.6888	0.0477		

Table B.4: Experimental measurements of the non-dimensional cell density, $c(t)$. Image processing was used to count the total number of cells in four subregions located in the centre of the cell colonies for each set of experiments, with and without Mitomycin-C pretreatment. The number of cells was converted into a non-dimensional cell density. Each data point was replicated four times to give the mean non-dimensional cell density and standard deviation.

B.6 Predicting the spatial expansion of a MM127 melanoma cell colony

Table B.5 summarises the estimates of the cell diffusivity, D , cell-to-cell adhesion strength, q , and cell proliferation rate, λ , obtained from the analysis described in Chapter 3.

Experimental images of the entire expanding cell colony and the corresponding simulated cell colonies using the estimates of D , q and λ are shown in Figure B.4. The location of the leading edge and the radius of the expanding cell colonies are superimposed on both experimental and model images of the colony. In all cases, the estimates obtained using the analysis described in Chapter 3 visually appear to predict the location of the leading edge of the MM127 cell colonies.

Initial number of cells	Cell diffusivity (D)	Cell-to-cell adhesion strength (q)	Proliferation rate (λ)
20,000	162 μm^2 /hour	0.3	0.0305 /hour
30,000	243 μm^2 /hour	0.5	0.0398 /hour

Table B.5: Estimates of the cell diffusivity, D , cell-to-cell adhesion strength, q and cell proliferation rate λ obtained from the analysis described in Chapter 3.



Figure B.4: (a)–(d) Experimental images of the entire expanding cell colony for each different set of experiments and corresponding model simulations using the parameter estimates obtained in Chapter 3. In all images, the detected location of the leading edge is outlined in black while the equivalent mean radius of the expanding colony is shown in red. Model simulations of the experiments initialised with 20,000 cells were performed using $D = 162 \mu\text{m}^2/\text{hour}$, $q = 0.3$ and $\lambda = 0.0305 \text{ /hour}$, and for experiments initialised with 30,000 cells, simulations were performed using $D = 243 \mu\text{m}^2/\text{hour}$, $q = 0.5$ and $\lambda = 0.0398 \text{ /hour}$.

B.7 Image acquisition and analysis

Detecting the location of the leading edge of the cell colony

Customised image processing software was written in MATLAB's image processing toolbox. The same software was used to detect the location of the leading edge in both the experimental cell colonies and the simulated cell colonies. Each colour image was imported (*imread*) and converted to greyscale (*rgbtogray*). A binary gradient mask containing the segmented cell colony was obtained by applying the Sobel operator (*edge(Original Image, 'Sobel')*, *edge(I, 'sobel', threshold)*) to enhance lines of high contrast. To show the outline of the object, the lines in the binary gradient mask were dilated (*strel*, *imdilate*). Remaining holes in the images were filled (*imfill*) and objects disconnected from the edge were removed (*imclearborder*). The image was smoothed and filtered to remove small objects detected in the previous steps (*imerode*, *medfilt2*). The resulting image contains both a large object (corresponding to the expanding cell colony) and smaller objects. The smaller objects were removed (*regionprops*, *bwareopen*) to leave the edge of the cell colony. An outline of the detected edge was superimposed back onto the original image (*buperim*) to verify the accuracy of the procedure. The area (*regionprops*) of the detected object was estimated and converted into an equivalent circular radius.

Detecting individual cells in the cell colony

To count the number of cells in the various subregions, we used a combination of customised image processing software, written using the MATLAB image processing toolbox, and manual counting where necessary. Each colour image was imported (*imread*), converted to greyscale (*rgbtogray*) and enhanced (*imadjust*) to provide sufficient contrast between each cell and the background of the image. The image was converted to black and white based on a threshold (*graythresh*, *im2bw*). To reduce noise, objects less than 30 pixels were removed (*bwareopen*). Remaining holes in the image were filled (*strel*, *imfill*, *Bwboundaries*), using a similar method as in the leading edge software. The centre of each detected region (which we assume to be an individual cell) was identified (*regionprops(image, 'Centroid')*) and superimposed back on the original image to test the accuracy of the detection method. The number of cells detected by the automated software was recorded. All remaining cells not automatically identified were manually included in the total cell count.

Identifying isolated cells in the cell colony

In addition to counting individual cells, we identified isolated cells that did not share a circular region, of radius 18 μm , with other cells. To do this, we repeated the same image processing procedure to identify the total number of cells in the colony. For each identified region corresponding to a cell, we recorded the physical location of each identified cell using (*regionprops*). Each identified cell was checked to determine whether the cell was isolated by comparing the location of the identified cell with the locations of all other cells. For example, to check if cell A, located at (x_1, y_1) , and cell B, located at (x_2, x_2) share the same circular region of radius 18 μm , we calculated the physical distance between the two

cells using $W = \sqrt{(x_2 - x_1)^2 + (y_2 - y_1)^2}$. If $W > 18 \mu\text{m}$, this indicates that cell B does not share the same circular region of radius $18 \mu\text{m}$ around cell A and vice versa. This was repeated systematically for all cells to identify which cells were completely isolated in the cell colony. To test the accuracy of the detection method, we superimposed the locations of each isolated cell back onto the original image and overlaid a square grid of size $18 \mu\text{m}$. The image was visually checked to make sure all identified isolated cells were correctly detected and that the image processing had identified all isolated cells. In some cases, a small number of identified cells were incorrectly identified and were deleted. Similarly, a small number of isolated cells were not identified and had to be manually added.

APPENDIX C

Supplementary material for Chapter 5: ‘Are *in vitro* estimates of cell diffusivity and cell proliferation rate sensitive to assay geometry?’

C.1 Cell culture

Murine fibroblast 3T3 cells (ATCC, CCL-92, Manassas, VA, USA) were maintained in Dulbecco’s modified Eagle medium (Invitrogen, Australia) supplemented with 5% fetal calf serum (FCS) (Hyclone, New Zealand), 2mM L-glutamine (Invitrogen) and 1% v/v Penicillin/Streptomycin (Invitrogen). The cells were grown in 5% CO₂ at 37°C. Cells were lifted using 0.05 % Trypsin (Invitrogen, Australia) and viable cells were counted using a Trypan blue exclusion test and a haemocytometer.

C.2 Measurements of the cell diameter

Images of 3T3 cells were acquired using a Leica AF6000 wide-field microscope (Figure C.1). ImageJ software was used to manually trace the outline of individual 3T3 cells. The area, A , enclosed by the outline of the cell was converted into a cell diameter estimate by assuming that, on average, the morphology of the cell is circular ($2\sqrt{A/\pi}$). Figure C.1 shows the outline of several 3T3 cells and the associated measurement of the cell diameter. Table C.1 summarises measurements for $n = 24$ cells.

Cell diameter (μm)	29.44	23.90	31.86	20.14	24.06	28.05	17.51	22.80
	27.05	23.95	26.68	18.53	26.89	19.05	33.68	29.44
	23.70	23.40	20.40	23.60	31.90	22.60	29.60	26.60
Mean (μm)	25.08							
s.d. (μm)	4.66							

Table C.1: The cell diameter data, including the mean and standard deviation (s.d.)

C.3 Image acquisition and analysis

C.3.1 Population-scale image acquisition and analysis

Images of the entire spreading population were obtained by fixing the cells with 10% formalin, followed by 0.01% crystal violet (Sigma–Aldrich, Australia). The stain was

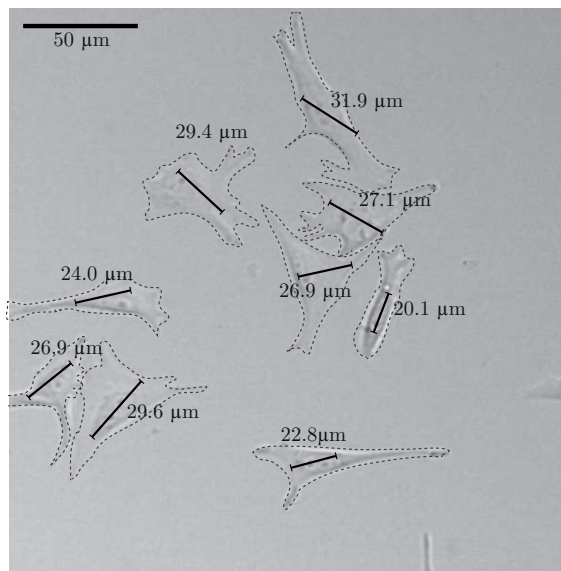


Figure C.1: Measurements of the cell diameter. Low cell density images, under high magnification, were used to measure the diameter of many individual 3T3 cells. Images were acquired using a Leica AF6000 wide-field microscope and ImageJ software was used to measure the diameter of each cell. The scale bar corresponds to 50 μm .

rinsed with phosphate-buffered saline (Invitrogen, Australia) and the plates were air-dried. Images were acquired using a stereo microscope with a Nikon digital camera (DXM1200C). Customised image processing software was written using MATLAB's image processing toolbox (v7.12).

To detect the leading edge the colour image was imported (*imread*) and converted to greyscale (*rgbtogray*). A binary gradient mask containing the segmented image was obtained by applying the Sobel operator ($I = \text{edge}(\text{Original Image}, \text{'sobel'})$, $\text{edge}(I, \text{'sobel'}, \text{threshold})$) to enhance lines of high contrast. To show the outline of the object, the lines in the binary gradient mask were dilated (*strel*, *imdilate*). Remaining holes in the images were filled (*imfill*) and objects disconnected from the edge were removed (*imclearborder*). The image was smoothed and filtered to remove small objects detected in the previous steps (*imerode*, *medfilt2*). The resulting image contains both a large object (corresponding to the expanding cell colony) and smaller objects. The smaller objects were removed (*regionprops*, *bwareopen*) to leave the edge of the cell colony. An outline of the detected edge was superimposed back onto the original image (*buperim*) to verify the accuracy of the procedure. The area (*regionprops*) of the detected object, A , was estimated and converted into an equivalent circular radius, $R_1 = \sqrt{A/\pi}$.

The same procedure was repeated to detect the location of the leading edge in images of assay 2 except that we further enhanced the edges in the image by thresholding the greyscale image (*im2bw*) before applying the Sobel operator. All other steps in the procedure were the same. The thresholds applied to each image were manually chosen for each image. This process allowed us to estimate the area of the void region, A , which was converted into an equivalent circular radius, $R_2 = \sqrt{A/\pi}$.

In all cases, we ensured that the image analysis methods applied to assay 1 and assay 2 produced quantitatively equivalent results by performing preliminary edge detection using ImageJ software. For all images, the scale was set (Analyse–Set scale) and colour images were converted to greyscale (Image–Type–32bit). The Sobel method was used to enhance edges (Process–Find Edges). The image was sharpened (Process–Find Edges) and an automatically determined threshold was applied (Image–Adjust–Threshold–B&W–Apply). After applying the Sobel method again (Process–Find Edges), the wand tracing tool, located in the main icons box, was used to select the detected leading edge. The area enclosed by the detected leading edge was calculated (Analyze–Set Measurements–area, Analyze–Measure). We observed in all cases, that the edge detected by the ImageJ software was similar to the edge detected by the MATLAB software.

The same image analysis methods used to detect the location of the leading edge in the experimental images was also applied to detect the leading edges in the images produced by the discrete model.

C.3.2 Individual-scale image acquisition and analysis

Images detailing the location of individual cells within the population were obtained by fixing the cells with 10% formalin, then made permeable using ice–cold 70% ethanol and the nuclei stained with Propidium Iodide (PI), 1 mg/ml (Invitrogen, Australia). Images were acquired using a Laborlux fluorescence microscope fitted with a Nikon digital camera (DXM1200C) at 100x magnification. Overlapping images were acquired to reconstruct a transect image which shows the location of individual cells across the entire spreading cell population.

To count the number of cells in various subregions of the individual–scale images, we used a combination of customised image processing software, written using the MATLAB image processing toolbox, and manual counting. Each colour image was imported (*imread*), converted to greyscale (*rgbtogray*) and enhanced (*imadjust*) to provide sufficient contrast between each cell and the background of the image. The image was converted to black and white based on a threshold (*graythresh*, *im2bw*). To reduce noise, objects less than 30 pixels were removed (*bwareaopen*). Remaining holes in the image were filled (*strel*, *imfill*, *Bwboundaries*), using a similar method as in the leading edge software. The centre of each detected region (which we assume to be an individual cell) was identified (*regionprops(image, 'Centroid')*) and superimposed back on the original image to test the accuracy of the detection method. The number of cells detected by the automated software was recorded. All remaining cells not automatically identified were manually included in the total cell count.

C.4 Leading edge data

Table C.2 summarises the leading edge results obtained by analysing the population–scale images. Image analysis was used to detect the position of the leading edge of the spreading cell populations and the area enclosed by the leading edge was converted into an equivalent circular area, $R = \sqrt{A/\pi}$. For assay 1, R corresponds to the radius of the

area enclosed by the spreading cell populations and for assay 2, the estimates represent the radius of the void area. For all experiments, Table C.2 summarises the mean and standard deviation ($n = 3$) of R .

	Cell density	Time (hours)	Motility only		Motility and proliferation	
			R		R	
			mean (μm)	s.d. (μm)	mean (μm)	s.d. (μm)
Assay 1	low	0	3040	86	3040	86
		24	3301	38	3476	152
		48	3531	119	3854	116
		72	3768	34	4521	126
	high	0	3089	80	3089	80
		24	3784	89	3795	35
		48	4046	58	4322	25
		72	4171	118	4883	48
	Assay 2	0	4062	21	4062	21
		24	3909	34	3845	16
		48	3560	35	3208	133
		72	3453	117	2988	74
	high	0	3956	53	3956	53
		24	3644	23	3544	34
		48	3155	170	2861	40
		72	2950	51	2181	158

Table C.2: Mean R estimates extracted from the population-scale images. Image processing was used to detect the location of the leading edge of the spreading cell populations from assay 1 and assay 2 experiments both with (motility only) and without Mitomycin-C (motility and proliferation) pretreatment, at $t = 0, 24, 48$ and 72 hours, with low and high initial cell densities. The area enclosed by the detected leading edge was converted into an equivalent circular radius to give a mean radius and standard deviation (s.d.) ($n = 3$).

C.5 Effective cell diffusivity estimates

Estimates of D were obtained in the Chapter 5 by comparing the position of the leading edge in the experimental images with the equivalent measurements applied to snapshots produced by the discrete mathematical model. To confirm our estimates of D , we also compared the shape of the cell density profiles near the leading edge, shown in Figure 5.10 (Chapter 5), to corresponding solutions of Equation (5.4).

The same least-squares procedure described in Chapter 5 was used to obtain estimates of D with the cell density information. Briefly, we compared numerical solutions of Equation (5.4) (Chapter 5) to the experimental cell density profiles, at $t = 72$ hours, for 30 equally-spaced values of D in the interval $D \in [0, 3000] \mu\text{m}^2/\text{hour}$. Since we are focussing on experimental data where the cells were pretreated with Mitomycin-C we set

$\lambda = 0$ in our numerical calculations. We used an estimate of the least-squares error to determine D . The least-squares estimate is given by

$$E(D) = \frac{\sum_{j=1}^N (EC^j - SC^j)^2}{\sum_{j=1}^N (EC^j)^2}, \quad (\text{C.1})$$

where EC^j is the non-dimensional cell density of the j^{th} subsection of the cell density profile at time $t = 72$ hours, SC^j is the non-dimensional cell density at the corresponding location predicted by Equation (5.4) (Chapter 5) at $t = 72$ hours and N is to the total number of sections considered.

Table C.3 summarises our estimates of D using both the leading edge data and the cell density profiles. In all cases considered, we observed a well-defined minimum in $E(D)$, and our estimates of D obtained using the cell density profiles are very similar to those obtained using the leading edge data.

Assay	Initial Density	Leading edge data D ($\mu\text{m}^2/\text{hour}$)	Cell density profiles D ($\mu\text{m}^2/\text{hour}$)
1	low	1700	1500
	high	2900	2700
2	low	800	1000
	high	1500	1700

Table C.3: Estimates of D for assay 1 and assay 2. Estimates obtained by considering leading edge data are compared to estimates obtained by comparing the shape of the cell density profile with the solution of Equation (5.4) (Chapter 5).

C.6 Cell proliferation rate data

Estimates of λ from assay 1 and assay 2 geometries were obtained by counting the number of cells in certain subregions ($n = 4$) located far behind the leading edge so that the cell density within the subregion was approximately spatially uniform, $c(r, t) = c(t)$. The cell counts were converted into an estimate of the non-dimensional cell density, $c(t) = \bar{c}(t)/K$, where $K = 1/25^2 \approx 1.6 \times 10^{-3}$ cells/ μm^2 . Results showing the mean non-dimensional cell density and standard deviation are summarised in Table C.4

C.7 Alternative effective cell proliferation rate estimates

Estimates of λ in Chapter 5 were obtained by considering a subregion located at least 2000 μm behind the leading edge of the spreading cell populations. To confirm that our estimates of λ do not depend on the location of the subregion, we re-estimated λ in two additional subregions that were also located behind the leading edge. These additional

	Cell density	Time (hours)	Motility only		Motility and proliferation	
			$c(t)$		$c(t)$	
			mean	s.d.	mean	s.d.
Assay 1	low	0	0.2530	0.0150	0.2123	0.0137
		24	0.2201	0.0375	0.4222	0.0359
		48	0.2641	0.0324	0.7782	0.0483
		72	0.2796	0.0112	0.8758	0.0032
	high	0	0.5867	0.0691	0.6387	0.0410
		24	0.5788	0.0265	0.8860	0.0362
		48	0.6344	0.0207	0.9563	0.0402
		72	0.5974	0.0262	1.1197	0.0841
Assay 2	low	0	0.2102	0.0241	0.2206	0.0248
		24	0.1902	0.0280	0.4054	0.0878
		48	0.1805	0.0458	0.5703	0.0445
		72	0.1958	0.0158	1.0212	0.0875
	high	0	0.6350	0.0634	0.6424	0.0389
		24	0.6482	0.0358	0.8265	0.0412
		48	0.6258	0.0458	0.9094	0.0010
		72	0.6242	0.0958	1.0200	0.0798

Table C.4: Non-dimensional density data from cell counts in four subregions located away from the leading edge for assay 1 and assay 2 geometries. Density data are shown for assay 1 and assay 2 experiments both with (motility only) and without Mitomycin–C pretreatment (motility and proliferation), at $t = 0, 24, 48$ and 72 hours, with low and high initial cell densities. All results were averaged over ($n = 4$) replicates to give the mean and standard deviation (s.d.).

estimates of λ were obtained using the same procedure as the previous estimates except that the location of the subregions considered was changed.

The locations of the two additional subregions for assay 1 and assay 2 are shown in Figure C.2 (a) and (c), respectively, and are approximately $300\text{ }\mu\text{m} \times 300\text{ }\mu\text{m}$ in size. Figure C.2 (b)–(c) and (e)–(f) show the corresponding time–evolution of the non-dimensional cell density in each of the two subregions for experiments without Mitomycin–C pretreatment in assay 1 and assay 2, respectively. Results are shown at both initial cell densities and the relevant logistic growth curves, given by Equation (5.4) (Chapter 5) are superimposed.

Estimates of λ were obtained using data from the additional two subregions for both assays, and the results are summarised in Table C.5. We note that there is a relatively small variation between the estimates of λ obtained in each additional subregion indicating that our estimates of λ are not sensitive to the location of the subregion provided that it is located sufficiently far away from the leading edge that we can assume that the density is spatially constant within that subregion.

	Cell density	R1 λ (/hour)	R2 λ (/hour)	mean	s.d.
Assay 1	low	0.056	0.040	0.048	0.011
	high	0.059	0.053	0.056	0.004
Assay 2	low	0.042	0.044	0.043	0.001
	high	0.041	0.043	0.042	0.001

Table C.5: Summary of effective cell proliferation rates from assay 1 and assay 2 using two additional subregions that are located at least 2000 μm behind the leading edge. Results are shown for experiments without Mitomycin-C (motility and proliferation) pretreatment with low and high initial cell densities and are obtained using $n = 4$ replicates.

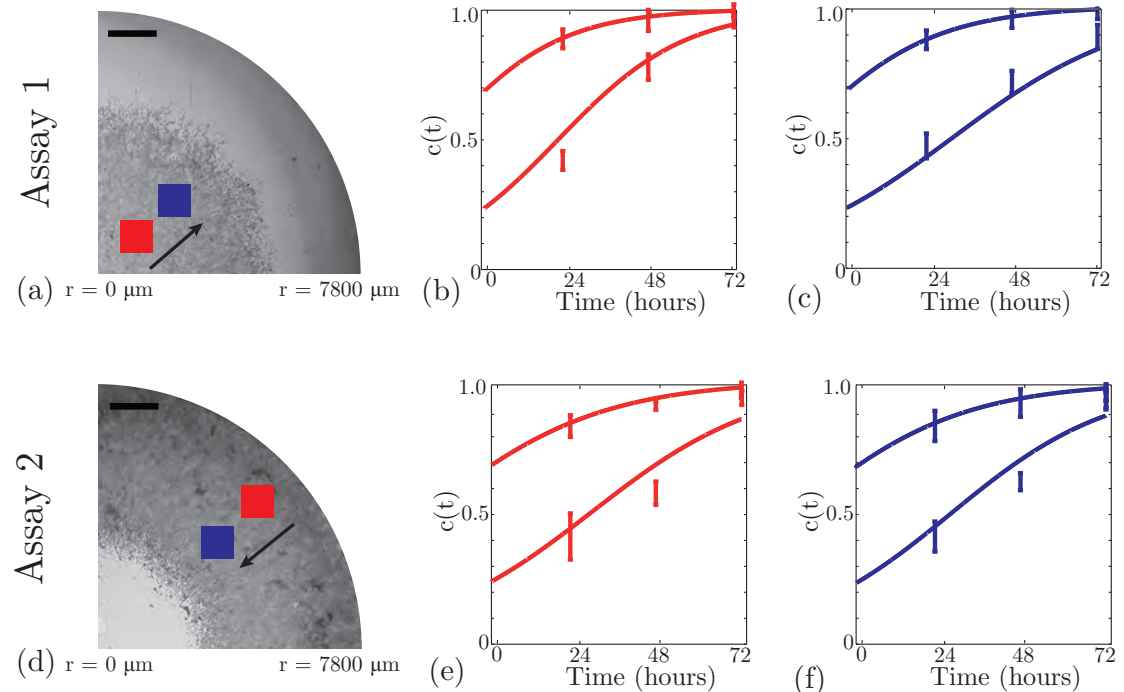


Figure C.2: Estimates of the effective cell proliferation rate are similar across the spreading cell population. Cell proliferation rate estimates were obtained by counting the number of cells in two different subregions located at least 2000 μm behind the leading edge of the spreading cell populations. The locations of the subregions are indicated in (a) and (d), where the scale bar corresponds to 1500 μm . Results in (b)–(c) and (e)–(f) compare the mean non-dimensional cell density ($n = 4$) from experiments with an initial low and high cell density for both assay 1 (red) and assay 2 (green) at $t = 0, 24, 48$ and 72 hours, with error bars indicating one standard deviation from the mean. The appropriately parameterized logistic growth curves using the cell proliferation rate estimates from Table C.5 are superimposed. In each case, the colours correspond to the results obtained from the subregion highlighted in (a) and (d).

C.8 Effective cell proliferation rate estimates with Mitomycin–C pretreatment

Chapter 5 presents analysis for experiments without Mitomycin–C pretreatment (motility and proliferation) in Figure C.3. Here we present the corresponding analysis for experiments with Mitomycin–C pretreatment (motility only), in addition to summarising the results presented in Chapter 5. Table C.6 summarises the estimates of λ from all experiments in both assay 1 and assay 2 geometries.

		Motility only	Motility and proliferation
	Cell density	λ (/hour)	λ (/hour)
Assay 1	low	0.003	0.056
	high	0.002	0.059
Assay 2	low	0.001	0.042
	high	0.001	0.041

Table C.6: Summary of proliferation rates from assay 1 and assay 2 experiments both with (motility) and without Mitomycin–C (motility and proliferation) pretreatment, at $t = 0, 24, 48$ and 72 hours, with low and high initial cell densities.

Figure C.3 shows the time–evolution of the non–dimensional cell density for experiments with Mitomycin–C pretreatment in assay 1 and assay 2. The relevant logistic growth curves, given by Equation (5.4) (Chapter 5) are superimposed. Our results illustrate that the estimates of the effective proliferation rate describe the observed time–evolution of the experimental cell density in both geometries. They confirm that the number of cells did not significantly increase or decrease over time and, importantly, that Mitomycin–C pretreatment prevents proliferation and did not cause cell death.

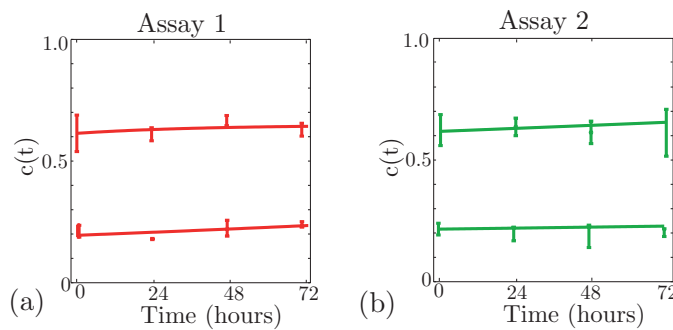


Figure C.3: Estimates of λ for experiments with Mitomycin–C pretreatment. Estimates of λ were obtained by counting the number of cells in four different subregions in each experimental replicate. Results in (a) and (b) compare the mean non–dimensional cell density ($n = 3$) for assay 1 (red) and assay 2 (green) from experiments with Mitomycin–C pretreatment, at $t = 0, 24, 48$ and 72 hours, with low and high initial cell densities. Error bars indicate one standard deviation from the mean. The appropriately parameterized logistic growth curves are superimposed.

C.9 Locating the leading edge using the solution of a partial differential equation

To compare solutions of Equation (5.4) (Chapter 5) with the experimental images we determined a value of c^* , which is a contour of the solution of Equation (5.4) (Chapter 5) so that the area enclosed by the contour $c^* = c(r, t)$, matches, on average, the area enclosed by the detected leading edge determined by the image analysis software. To determine c^* we solved Eq. (5.4) (Chapter 5) numerically for the appropriate initial conditions to model the spreading shown in Figure 5.2 (Chapter 5). Given the experimental estimates of the radius, as shown in Table C.2, we used the solution of Equation (5.4) (Chapter 5) to predict the radius of the spreading population (assay 1) or radius of the void area (assay 2) and compared these estimates to the corresponding experimental estimates at $t = 24$, 48 and 72 hours for experiments with Mitomycin–C pretreatment. In each case, we chose the value of c^* so that the area defined by the contour $c^* = c(r, t)$ corresponded to the average area obtained by applying the leading edge detection methods to the experimental images. A summary of results for the assay 1 and assay 2 geometries for each initial cell density is given in Table C.7. These data indicate that, on average, choosing $c^* = 0.019$ provides the best overall match. We use this value of c^* to compare the experimental results to the solution of Equation (5.4) (Chapter 5).

	Cell density	$c^* (t = 24 \text{ hours})$	$c^* (t = 48 \text{ hours})$	$c^* (t = 72 \text{ hours})$	Mean
Assay 1	low	0.030	0.010	0.008	0.016
	high	0.010	0.013	0.019	0.014
Assay 2	low	0.054	0.010	0.010	0.025
	high	0.049	0.007	0.008	0.021
Mean		0.036	0.010	0.011	0.019

Table C.7: Summary of the contour values, c^* , determined for the assay 1 and assay 2 geometries, with Mitomycin–C pretreatment, at $t = 0, 24, 48$ and 72 hours, with low and high initial cell densities. For both geometries, the values of c^* are similar and indicate that, on average, $c^* = 0.019$.

C.10 Calculating the variation in the parameter estimates

The variability in our estimates of D and λ was estimated by repeating the calibration process using each piece of the experimental data separately, without averaging the data. To determine the variability in our estimate of D we have three replicates of measurements for R in each experiment at each of the four time points ($t = 0, 24, 48$ and 72 hours), giving a total of 12 experimental images for each initial density and each assay geometry. To conservatively estimate the variability in D , we calibrated the discrete model for each combination of these 12 images. The combination of measurements that corresponded to the smallest observed spreading was used to specify the lowest possible value of D and the combination of measurements corresponding to the largest observed spreading was used to specify the highest possible value of D . The upper and lower estimates of D are given Table 5.1 (Chapter 5). A similar procedure was used to estimate the variability

in λ using four replicates at each time point and repeating the calibration procedure using all combinations of the experimental measurements and the solution of the logistic equation (Equation (5.4), Chapter 5). Table 5.1 (Chapter 5) indicates the upper and lower estimates of λ .

APPENDIX D

Supplementary material for Chapter 6: ‘Assessing the role of spatial correlations during collective cell spreading’

D.1 Estimating the total area occupied by individual MM127 melanoma cells

In our work, we require an estimate of Δ , which approximates the diameter of the area occupied by a cell. During our experiments we observe that the shape of the cells constantly fluctuate with time. To account for this variation, we estimate the diameter of the cell nucleus since the fluctuations in the size of the nucleus appear to be much smaller than the fluctuations in the size of the entire cell and therefore provides us with a more reliable estimate of the average area occupied by each cell. Images of the cell nuclei were acquired using a Nikon TI Eclipse microscope fitted with a Nikon digital camera. Images were thresholded using MATLAB’s image processing toolbox and discretised on a lattice by resizing the dimensions such that each pixel is $1 \mu\text{m} \times 1 \mu\text{m}$. Each pixel on the lattice is either vacant (white pixel) or occupied (black pixel) and a cell is composed of several black pixels. The process used is the same process used to discretise experimental images onto the pair correlation lattice in Chapter 6.

Estimates of Δ were obtained by counting the number of black pixels per cell and converting this measurement into an area, A . We assume that, on average, the morphology of each cell is circular and we convert A into a diameter estimate using $2\sqrt{A/\pi}$. Figure D.1 (a) shows an image of MM127 cell nuclei and the corresponding discretisation onto a lattice Figure D.1 (b). Table D.1 summarises measurements for $n = 40$ cells and indicates that, on average, $\Delta \approx 18 \mu\text{m}$.

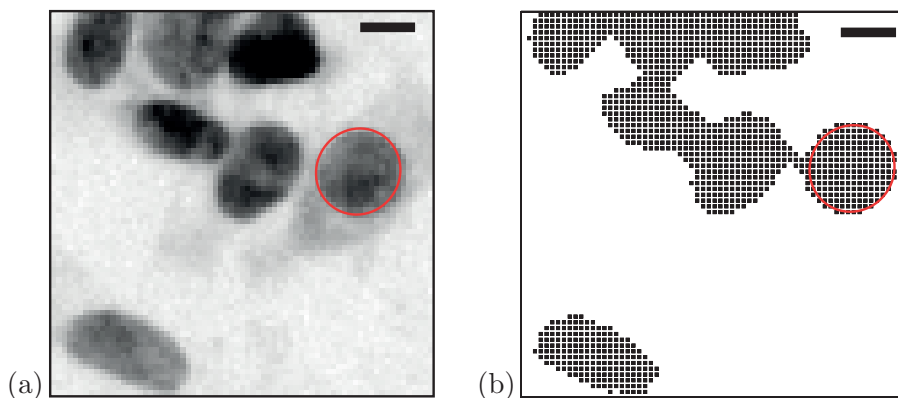


Figure D.1: Cell diameter measurements. High magnification images of MM127 cells are shown in (a). Images were acquired using a Nikon Ti Eclipse microscope fitted with a Nikon digital camera. The scale bar corresponds to $10 \mu\text{m}$. The nucleus diameter (b) of cells was determined by counting the number of black pixels of each cell in a discretised image, where each pixel corresponds to $1 \mu\text{m} \times 1 \mu\text{m}$ and converting this into a circular measurement.

Diameter of cell nucleus (μm)	18.94 18.78 21.98 17.34 23.50 17.00 16.00 16.74 16.42 15.03 16.49 18.95 17.00 21.52 16.15 16.86 16.11 14.17 19.32 21.15 16.80 17.87 16.58 16.50 17.75 16.93 16.65 16.80 21.51 18.05 17.18 15.38 23.07 15.17 15.97 21.41 22.48 17.58 16.50 18.00
Mean (μm)	17.94
Standard deviation (μm)	2.37

Table D.1: Cell nucleus diameter measurements of 40 MM127 cells indicate that the mean nucleus diameter of the cell, Δ , is $17.94 \pm 2.37 \mu\text{m}$

D.2 Computing average pair correlation functions

In Chapter 6, we present average pair correlation functions, $\bar{F}(r)$, for all experimental results. Here, we demonstrate that there are no obvious differences in the pair correlation signal between each subregion in an individual experiment. Furthermore, we also demonstrate that the averaging approach taken in Chapter 6 is reasonable. Figure D.2 presents results for subregions located at the centre of the cell population for experiments without cell proliferation and with cell proliferation. Pair correlation signals shown in Figure D.2 (b) and (f) illustrate the signal extracted from four subregions, of dimension $600 \mu\text{m} \times 600 \mu\text{m}$, using one experimental replicate. The approximate locations of these subregions are illustrated in Figure D.2 (a) and (e), respectively. We observe that each signal fluctuates around unity for all pair distances between $1\Delta \leq r \leq 5\Delta$. We note that there is some variability between the pair correlation signals. However, there does not seem to be obvious differences or trends in the data. Results in Figure D.2 (c) and (g) illustrate the average pair correlation signal, $\bar{F}(r)$, from three experimental replicates of the same experiment using four subregions in each replicate. Again the pair correlation signals fluctuate around unity for all pair distances without any obvious trends in the data. In addition our results illustrate that the pair correlation signal for each different replicate of the same experiment is similar. The final average pair correlation signals, averaged using 12 subregions from three experimental replicates of the same experiment, is shown in Figure D.2 (d) and (h). Our results confirm that there are no obvious differences in the pair correlation signal across experimental subregions or replicates indicating that our averaging approach used in Chapter 6 is appropriate.

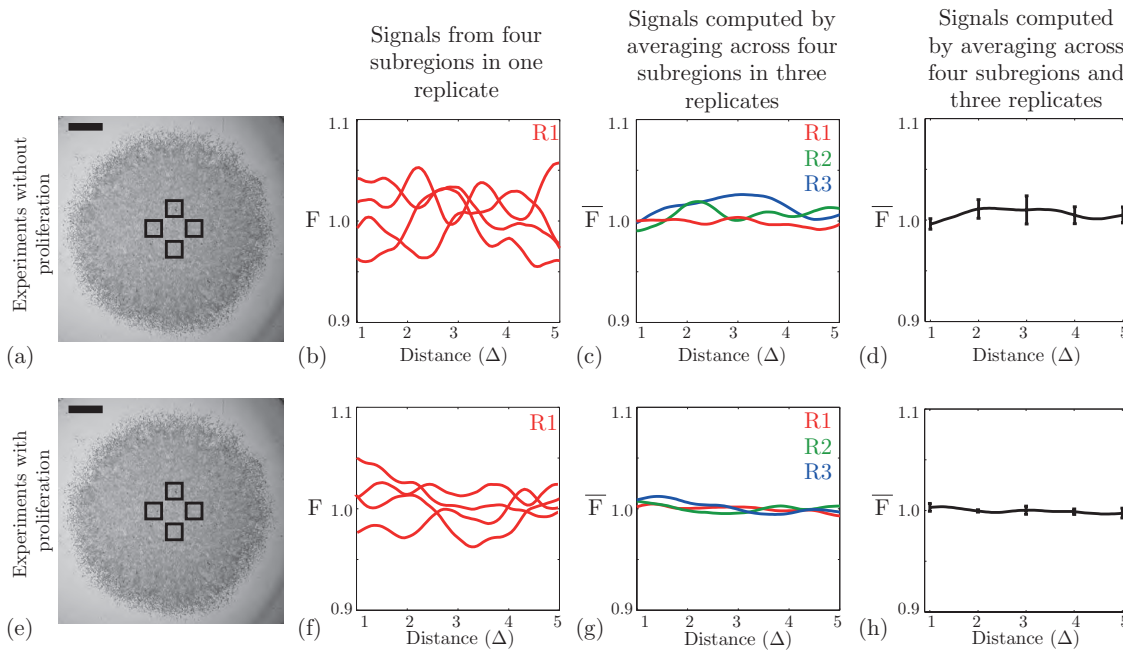


Figure D.2: Average pair correlation functions. The role of spatial correlations in spreading MM127 cell populations was investigated by calculating pair correlation functions in four subregions, each of dimension $600 \mu\text{m} \times 600 \mu\text{m}$, at the centre of the spreading cell population and at the edge of the spreading cell population (e)–(h). The relative size and approximate location of these subregions is shown in (a) and (e), where the scale bar corresponds to $1,500 \mu\text{m}$. Pair correlation functions were computed for experiments with Mitomycin-C pretreatment to suppress cell proliferation (b)–(d) and without Mitomycin-C pretreatment (f)–(h). Pair correlation signals were computed from four subregions of dimensions $600 \mu\text{m} \times 600 \mu\text{m}$ and each individual realisation from replicate 1, $R1$, is shown in (b) and (f). The horizontal axis is measured as multiples of the average diameter of the nucleus. Averaging the pair correlation signals across four subregions for three experimental replicates is shown in (c) and (g), where, $R1$, $R2$ and $R3$ correspond to replicates 1, 2 and 3, respectively. Results in (d) and (h) illustrate the final pair correlation signal which is averaged across all 12 subregions from the three experimental replicates. The error bars correspond to one standard deviation about the mean ($N = 12$). All experiments were conducted by initially placing approximately 30,000 cells inside the barrier assay.

D.3 Average pair correlation signals for experiments with different initial cell densities

Chapter 6 presents average pair correlation signals from all sets of experiments in which 30,000 cells were initially placed inside the circular barrier. To investigate whether the initial cell density affects the presence of spatial correlations in the spreading cell populations, we repeated the procedure using a different initial cell density where 20,000 cells were placed as uniformly as possible in the barrier and we found similar results. Results in Figure D.3 at $t = 0$ hours and after $t = 48$ hours, for subregions located at the centre and at the edge of the cell population, for all experiments with and without cell proliferation, indicate that the average pair correlation signal, $\bar{F}(r)$, fluctuates around unity for pair distances between $1\Delta \leq r \leq 5\Delta$. These results suggest that there is very little spatial structure and clustering present in the spreading MM127 melanoma cell populations.

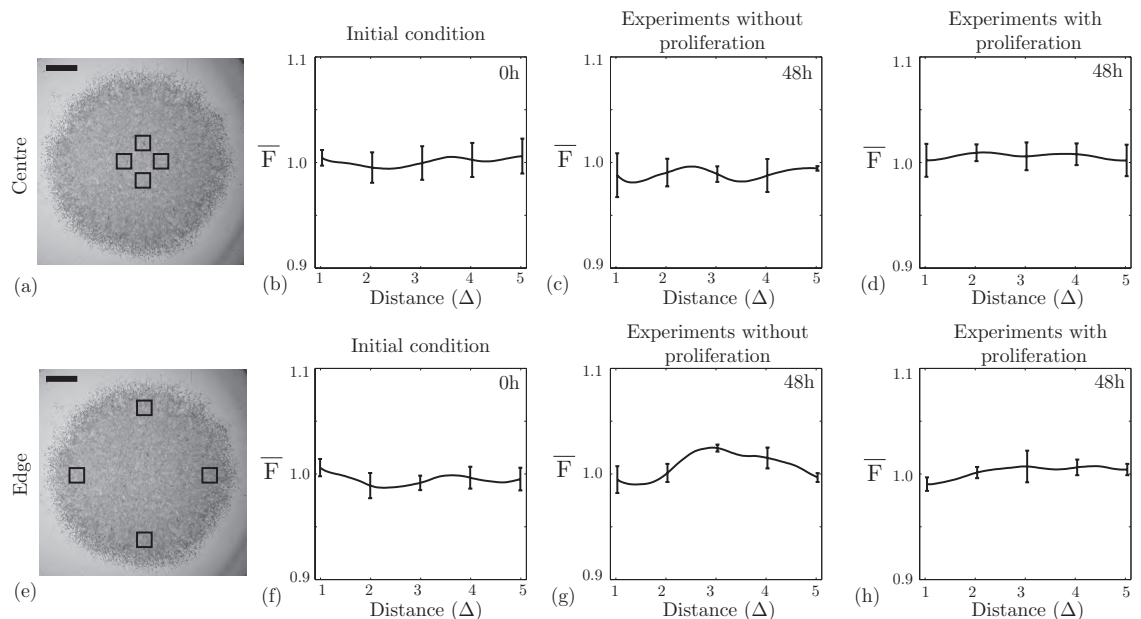


Figure D.3: Spatial correlations are not present in spreading MM127 melanoma cell populations. Average pair correlation functions were extracted from images showing the location of individual cells in four subregions, each of dimension $600 \mu\text{m} \times 600 \mu\text{m}$, at the centre of the spreading cell population (a) and four subregions at the edge of the spreading cell population (e). The relative size and approximate location of these subregions is shown in (a) and (e), respectively, where the scale bar corresponds to $1,500 \mu\text{m}$. Average pair correlation signals are shown at $t = 0$ hours in (b) and (f), at $t = 48$ hours for experiments without cell proliferation in (c) and (g), and at $t = 48$ hours for experiments with cell proliferation in (d) and (h). Results in (a)–(d) and (e)–(h) correspond to pair correlation signals computed at the centre and at the edge of the spreading cell population, respectively. The horizontal axis is measured as multiples of the average diameter of the nucleus. Each pair correlation signal was averaged over 12 subregions of dimensions $600 \mu\text{m} \times 600 \mu\text{m}$, using three identically prepared experimental replicates. The error bars correspond to one standard deviation about the mean ($N = 12$). All experiments were conducted by initially placing approximately 20,000 cells inside the barrier assay.

D.4 Pair correlation signals in subregions located across the spreading cell population

We compute the pair correlation signal, in Chapter 6, in subregions located at the centre and at the edge of the spreading cell populations. Our results show that there are no obvious differences in the pair correlation signal at these locations. To confirm that the pair correlation signal does not change significantly depending on the location of the subregion, we computed the pair correlation signal in five different subregions, each of dimension $800 \mu\text{m} \times 800 \mu\text{m}$, equally spaced between the centre and the edge of the cell population. The relative size and location of each of these subregions is illustrated in Figure D.4 (a)–(e). The corresponding pair correlation signal, using one experimental replicate, is shown in Figure D.4 (g)–(k), where we observe that the pair correlation signals, $F(r)$, fluctuates around unity for pair distances between $1\Delta \leq r \leq 5\Delta$ in each subregion. Our results illustrate that the pair correlation signals in subregions located across the spreading cell population are similar and we do not observe any obvious differences that depend on the location of the subregion. Hence, it seems reasonable that the pair correlation signals at each of these five subregions could be averaged to determine $\bar{F}(r)$. Results shown in Figure D.4 (f) and (l) illustrate the average pair correlation signal determined from the five subregions. The average pair correlation signal illustrates that $\bar{F}(r)$, fluctuates around unity for pair distances between $1\Delta \leq r \leq 5\Delta$ and that the standard deviation, shown by the error bars, is small confirming that the pair correlation signals extracted in subregions located across the spreading cell population are similar.

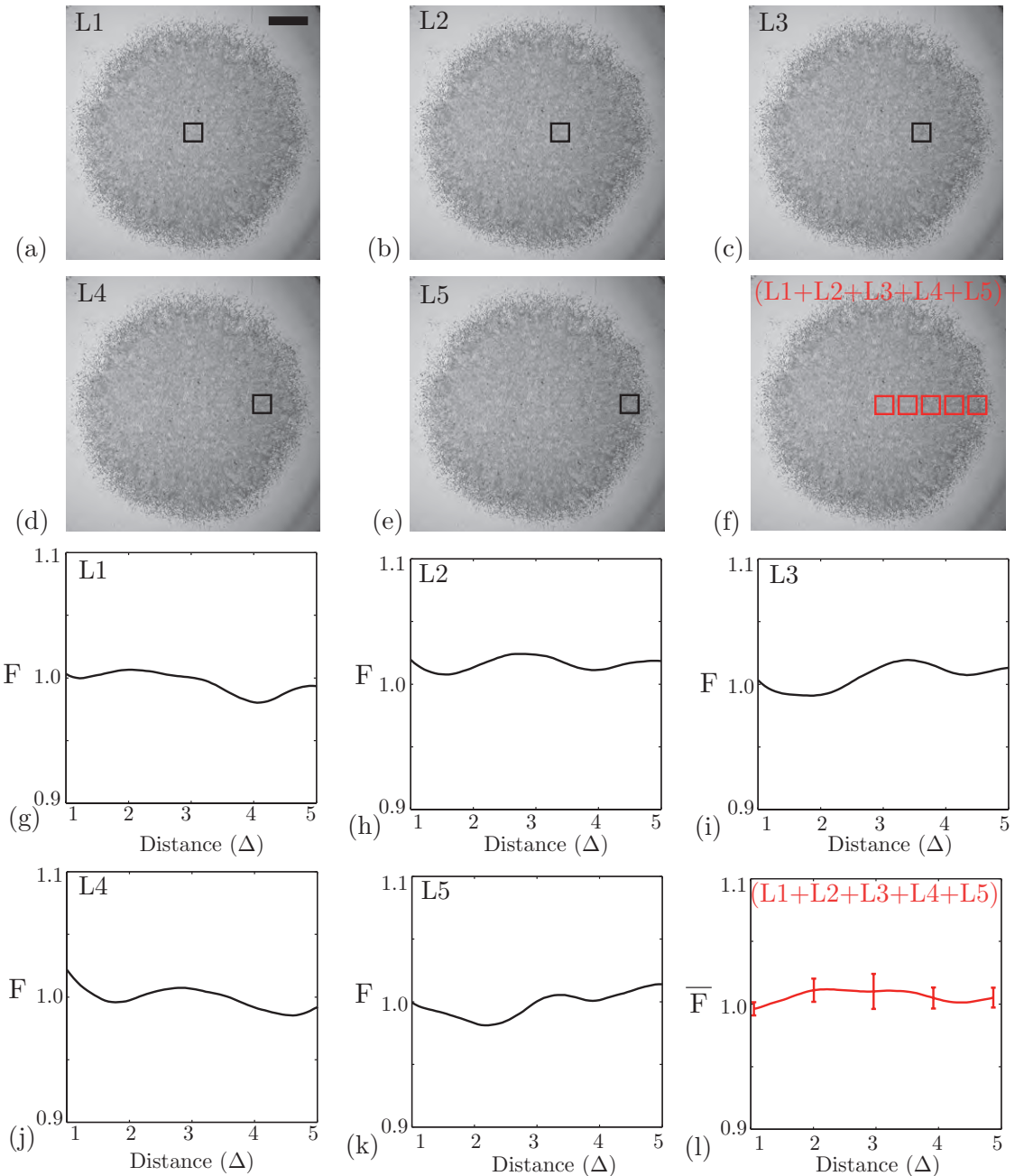


Figure D.4: Pair correlation signals are similar across the entire spreading cell population. Pair correlation functions were extracted from images showing the location of individual cells in five subregions of dimensions, $800 \mu\text{m} \times 800 \mu\text{m}$ located across the spreading cell population. The location of the subregion considered is shown in (a–e), where the scale bar corresponds to $1,500 \mu\text{m}$. The corresponding pair correlation signal for each location is shown in (g)–(k). The horizontal axis is measured as multiples of the average diameter of the nucleus. The average pair correlation signal, calculated using $N = 5$ subregions across the spreading cell population as illustrated in (f), is shown in (l). The error bars correspond to one standard deviation about the mean ($N = 12$). All experiments were conducted by initially placing approximately 30,000 cells inside the barrier assay.

D.5 Insensitivity of pair correlation signal to δ

In Chapter 6, we discretise experimental and discrete simulation images onto a finer pair correlation lattice by resizing the dimensions of the image such that each pixel is $1 \mu\text{m} \times 1 \mu\text{m}$. Here, the lattice spacing is $\delta = 1 \mu\text{m}$. To test whether the pair correlation signal is sensitive to δ , we repeated the process by discretising the images onto the pair correlation lattice using various values of δ between $0.1 \mu\text{m} \leq \delta \leq 3 \mu\text{m}$ for the experimental images and $0.1 \mu\text{m} \leq \delta \leq 18 \mu\text{m}$ for the discrete simulation images. For the experimental images, we do not consider any values of $\delta > 3 \mu\text{m}$ since we wish to avoid specifying or disrupting the physical location of the cells on the lattice. Results in Figure D.5 show two examples of the experimental and discrete images, shown inset in each subfigure, where $\overline{F}(r)$ has been computed for various values of δ . We observe that the δ values examined produce similar pair correlation signals.

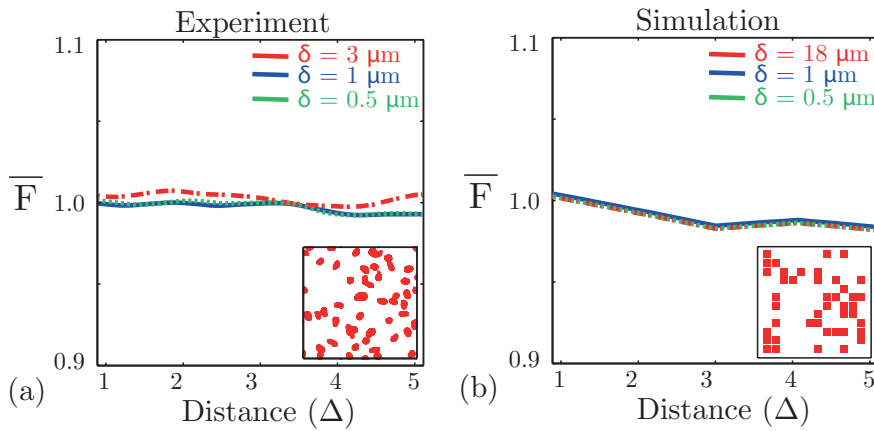


Figure D.5: Size of pair correlation lattice spacing, δ does not affect the pair correlation signal. Experimental and discrete simulation images were discretised onto a pair correlation lattice with various values of δ . Average pair correlation signals were extracted from four subregions, each of dimension $600 \mu\text{m} \times 600 \mu\text{m}$, at the centre of the population at $t = 48$ hours from (a) experiments with Mitomycin-C pretreatment and (b) simulations with cell motility ($D = P_m \Delta^2 / 4\tau = 248 \mu\text{m}^2/\text{hour}$), weak adhesion ($q = 0.3$) and no proliferation. Snapshots of the entire subregion analysed are shown as an inset. The physical size of the inset is approximately $215 \mu\text{m} \times 215 \mu\text{m}$. All experiments and simulations were initialised with approximately 30,000 cells or simulated cells, respectively. The green dotted lines correspond to average pair correlation signals computed on a pair correlation lattice with $\delta = 0.5 \mu\text{m}$. Summarily, blue solid lines indicate $\delta = 1 \mu\text{m}$ and red dashed lines illustrate results with $\delta = 3 \mu\text{m}$ for the experimental images and $\delta = 18 \mu\text{m}$ for the discrete simulation images. The horizontal axis is measured as multiples of the average diameter of the nucleus.

D.6 Average pair correlation function in the w direction

In Chapter 6, spatial correlations in the spreading MM127 melanoma cell populations were assessed by considering distances between pairs of pixels in the direction of outward spreading, r , to give an estimate of the pair correlation signal, $F(r)$. For completeness, we now consider whether the pair correlation signals are sensitive to direction by repeating the analysis by considering distances between pairs of pixels in the direction perpendicular to the direction of outward spreading, w , to give an estimate of the pair correlation signal, $F(w)$. Results in Figure D.6 compare the corresponding average pair correlations signals, $\overline{F}(r)$ and $\overline{F}(w)$, confirming that the pair correlation signals in the intervals $1\Delta \leq r \leq 5\Delta$ and $1\Delta \leq w \leq 5\Delta$ are similar regardless of whether we analyse the r or w direction.

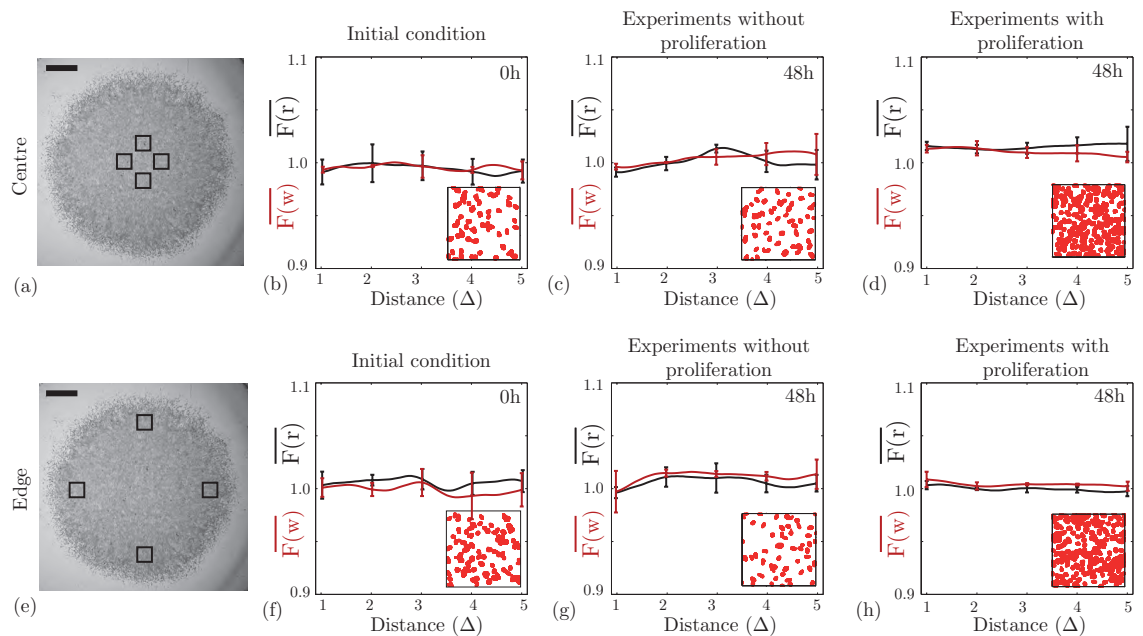


Figure D.6: Comparing the average pair correlation function in the w direction with the average pair correlation function in the r direction. Average pair correlation functions were extracted from images showing the location of individual cells in four subregions, each of dimension $600 \mu\text{m} \times 600 \mu\text{m}$, at the centre of the spreading cell population (a) and four subregions, each of dimension $600 \mu\text{m} \times 600 \mu\text{m}$, at the edge of the spreading cell population (e). The relative size and approximate location of these subregions is shown in (a) and (e), respectively, where the scale bar corresponds to $1,500 \mu\text{m}$. Pair correlation signals were computed by considering the pair distances of pixels in both the r direction (black, $F(r)$) and in the w direction (red, $F(w)$). Average pair correlation signals are shown at $t = 0$ hours in (b) and (f), at $t = 48$ hours for experiments without cell proliferation in (c) and (g), and at $t = 48$ hours for experiments with cell proliferation in (d) and (h). Results in (b)–(d) and (f)–(h) correspond to pair correlation signals computed at the centre and at the edge of the spreading cell population, respectively. The horizontal axis is measured as multiples of the average diameter of the nucleus. Snapshots of the experimental subregions after image processing are shown as an inset. The size of the inset is approximately $215 \mu\text{m} \times 215 \mu\text{m}$. Each pair correlation signal was averaged over 12 subregions of dimensions $600 \mu\text{m} \times 600 \mu\text{m}$, using three identically prepared experimental replicates. The error bars correspond to one standard deviation about the mean ($N = 12$). All experiments were conducted by initially placing approximately 30,000 cells inside the barrier assay.

Bibliography

- [1] Abdou, I.E. & Pratt, W.K. Quantitative design and evaluation of enhancement/thresholding edge detectors. *Proc. IEEE.* **67**, 753–763 (1979).
- [2] Agnew, D.J.G., Green, J.E.F., Brown, T.M., Simpson, M.J. & Binder, B.J. Distinguishing between mechanisms of cell aggregation using pair-correlation functions. *J. Theor. Biol.* **352**, 16–23 (2014).
- [3] Alber, M., Kiskowski, M., Glazier, J. & Jiang, Y. On cellular automaton approaches to modeling biological cells. *IMA. V. Math.* **134**, 1–39 (2003).
- [4] Anderson, A.R.A. & Chaplain, M.A.J. Continuous and discrete mathematical models of tumor-induced angiogenesis. *Bull. Math. Biol.* **4**, 576–594 (1998).
- [5] Anderson, A., Chaplain, M. & Rejniak, K. Single-cell-based models in biology and medicine. *Springer.* (2007).
- [6] Ascoli, G., Badoual, M. & Deroulers, C. Exclusion processes: short-range correlations induced by adhesion and contact interactions. *Phys. Rev. E.* **87**, 012702 (2013).
- [7] Ashby, W.J. & Zijlstra, A. Established and novel methods of interrogating two-dimensional cell migration. *Intergr. Biol.* **4**, 1338–1350 (2012).
- [8] Aubert, M., Fereol, S., Christov, C. & Grammaticos, B. A cellular automation model for the migration of glioma cells. *Phys. Biol.* **3**, 93–100 (2006).
- [9] Aubert, M., Badoual, M. & Grammaticos, B. A model for short- and long-range interactions of migrating tumour cells. *Acta. Biotheor.* **56**, 297–314 (2008).
- [10] Australian Institute of Health and Welfare and Australasian Associate of Cancer Registries. Cancer in Australia: an overview. (74, CAN 70, Canberra) Accessed: August 2013, [<http://www.aihw.gov.au/WorkArea/DownloadAsset.aspx?id=60129542353>] (2012).
- [11] Balch, C., Gershenwald, J., Soong, S., Thompson, J., Atkins, M., Byrd, D., Buzaid, A., Cochran, A., Coit, D., Ding, S., Eggermont, A., Flaherty, K., Gimotty, P., Kirkwood, J., McMasters, K., Mihm, M., Morton, D., Sober A. & Sondak, V. Final version of 2009 AJCC melanoma staging and classification. *J. Clin. Oncol.* **20**, 6199–6206 (2009).
- [12] Baker, R.E. & Simpson, M.J. Correcting mean-field approximations for birth-death-movement processes. *Phys. Rev. E.* **82**, 041905 (2010).
- [13] Baker, R.E. & Simpson, M.J. Models of collective cell motion for cell populations with different aspect ratio: diffusion, proliferation and travelling waves. *Physica A.* **391**, 3729–3750 (2012).
- [14] Binder, B.J. & Simpson, M.J. Quantifying spatial structure in experimental observations and agent-based simulations using pair-correlation functions. *Phys. Rev. E.* **88**, 022705 (2013).
- [15] Block, M., Schöll, E. & Drasdo, D. Classifying the expansion kinetics and critical surface dynamics of growing cell populations. *Phys. Rev. Lett.* **99**, 248101 (2007).
- [16] Bonaventure, J., Domingues, M. & Larue, L. Cellular and molecular mechanisms controlling the migration of melanocytes and melanoma cells. *Nat. Genet.* **26**, 316–325 (2013).

- [17] Bradie, B. A friendly introduction to numerical analysis. Pearson Prentice Hall. United States of America (2006).
- [18] Brock, A., Chang, E., Ho, C., LeDuc, P., Jiang, X., Whitesides, G. & Ingber, D. Geometric determinants of directional cell motility revealed using microcontact printing. *Langmuir*. **19**, 1611–1617 (2003).
- [19] Bruna, M. & Chapman, S.J. Excluded-volume effects in the diffusion of hard spheres. *Phys. Rev. E*. **85**, 011103 (2012).
- [20] Cai, A.Q., Landman, K.A. & Hughes, B.D. Multi-scale modeling of a wound-healing cell migration assay. *J. Theor. Biol.* **245**, 576–594 (2007).
- [21] Callaghan, T., Khain, E., Sander, L.M. & Ziff, R.M. A stochastic model for wound healing. *J. Stat. Phys.* **122**, 909–924 (2006).
- [22] Chang, H., Sneddon, J., Alizadeh, A., Sood, R., West, R., Montogomery, K., Chi, J., van de Rijn, M., Botstein, D. & Brown, P. Gene expression signature of fibroblast serum response predicts human cancer progression: similarities between tumors and wounds. *PLoS Biology*. **2**, 0206–0214 (2004).
- [23] Chatelain, C., Ciarletta, P. & Ben Amar, M. Morphological changes in early melanoma development: influence of nutrients, growth inhibitors and cell-adhesion mechanisms. *J. Theor. Biol.* **290**, 46–59 (2011).
- [24] Chowdhury, D., Schadschneider, A. & Nishinari, K. Physics of transport and traffic phenomena in biology: from molecular motors and cells to organisms. *Phys. Life Rev.* **2**, 318–652 (2005).
- [25] Ciarletta, P., Foret, L. & Ben Amar, M. The radial growth phase of malignant melanoma: multi-phase modelling, numerical simulations and linear stability analysis. *J. R. Soc. Interface*. **8**, 345–368 (2011).
- [26] Clark, R. The molecular and cellular biology of wound repair, Plenum. New York. (1996).
- [27] Codling, E. A., Plank, M. J. & Benhamou, S. Random walks in biology. *J. Roy. Soc. B*. **5**, 813–834 (2008).
- [28] Coussens, L. & Werb, Z. Inflammation and cancer. *Nature*. **420**, 860–867 (2002).
- [29] Danen, E., de Vries, T., Morandini, R., Ghanem, G., Ruiter, D. & van Muijen, G. E-cadherin expression in human melanoma. *Melanoma Res.* **6**, 127–131 (1996).
- [30] Decaestecker, C., Debeir, O., Van Ham, P. & Kiss, R. Can anti-migratory drugs be screened in vitro? A Review of 2D and 3D assays for the quantitative analysis of cell migration. *Med. Res. Rev.* **27**, 149–176 (2006).
- [31] Deisboeck, T., Berens, M., Kansal, A., Torquato, S., Stemmer-Rachamimov, A. & Chiocca, E. Pattern of self-organization in tumour systems: complex growth dynamics in a novel brain tumour spheroid model. *Cell Prolif.* **34**, 115–134 (2001).
- [32] Deisboeck, T., Wang, Z. & Macklin, P. Multiscale cancer modeling. *Annu. Rev. Biomed. Eng.* **13**, 127–155 (2011).
- [33] Deroulers, C., Aubert, M., Badoual, M. & Grammaticos, B. Modeling tumor cell migration: from microscopic to macroscopic models. *Phys. Rev. E*. **79**, 031917 (2009).
- [34] Derycke, L. & Bracke, M. N-cadherin in the spotlight of cell-cell adhesion, differentiation, embryogenesis, invasion and signalling. *Int. J. Dev. Biol.* **48**, 463–476 (2004).

- [35] Dixit, V.D., Weeraratna, A.T., Yang, H.Y., Bertak, D., Cooper-Jenkins, A., Riggins, G.J., Eberhart, C.G. & Taub, D.D. Ghrelin and the growth hormone secretagogue receptor constitute a novel autocrine pathway in astrocytoma motility. *J. Biol. Chem.* **281**, 16681–16690 (2006).
- [36] Druckenbrod, N.R. & Epstein, M.L. Behavior of enteric neural crest-derived cells varies with respect to the migratory wavefront. *Dev. Dynam.* **237**, 84–92 (2007).
- [37] Doxzen, K., Vedula, S., Leong, M., Hirata, H., Gov, N., Kabla, A., Ladoux, B. & Lim, C. Guidance of collective cell migration by substrate geometry. *Integr. Biol.* **5**, 1026–1035 (2013).
- [38] Drasdo, D. & Höhme, S. A single-cell-based model of tumor growth *in vitro*: monolayers and spheroids. *Phys. Biol.* **2**, 133–147 (2005).
- [39] Eikenberry, S., Thalhauser, C. & Kuang, Y. Tumor-immune interaction, surgical treatment, and cancer recurrence in a mathematical model of melanoma. *PLoS Comput. Biol.* **5**, e1000362 (2009).
- [40] Enderling, H., Alexander, N.R., Clark, E.S., Branch, K.M., Estrada, L., Crooke, C., Jourquin, J., Lobdell, N., Zaman, M.H., Guelcher, S.A., Anderson, A.R.A. & Weaver, A.M. Dependence of invadopodia function on collagen fiber spacing and cross-linking: computational modeling and experimental evidence. *Biophys. J.* **95**, 2203–2218 (2008).
- [41] Enderling, H., Anderson, A., Chaplain, M., Beheshti, A., Hlatky, L. & Hahnfeldt, P. Paradoxical dependencies of tumor dormancy and progression on basic cell kinetics. *Cancer Res.* **69**, 8814–8821 (2009).
- [42] Fisher, R.A. The wave of advance of advantageous genes. *Ann. Eugenics.* **7**, 353–369 (1937).
- [43] Frieboes, H., Edgerton, M., Fruehauf, J., Rose, F., Worrall, L., Gatenby, R., Ferrari, M. & Cristini, V. Prediction of drug response in breast cancer using integrative experimental/computational modeling. *Cancer Res.* **69**, 4484–4492 (2009).
- [44] Friedl, P. & Gilmour, D. Collective cell migration in morphogenesis, regeneration and cancer. *Nat. Rev. Mol. Cell. Bio.* **10** (2009), 445–457.
- [45] Friedrich, J., Seidel, C., Ebner, R. & Kunz-Schughart, L. Spheroid-based drug screen: considerations and practical approach. *Nat. Protoc.* **4**, 309–324 (2009).
- [46] Frixen, U., Behrens, J., Sachs, M., Eberle, G., Voss, B., Warda, A., Löchner, D. & Birchmeier, W. E-cadherin-mediated cell-cell adhesion prevents invasiveness of human carcinoma cells. *J. Cell Biol.* **113**, 173–85 (1991).
- [47] Gallaher, J. & Anderson, A.R.A. Evolution of intertumoral phenotypic heterogeneity: the role of trait inheritance. *Interface Focus.* **3**, (2013)
- [48] Garbe, C., Peris, K., Hauschild, A., Saiag, P., Middleton, M., Spatz, A., Grob, J., Malvehy, J., Newton-Bishop, J., Stratigos, A., Pehamberger, H. & Eggermont, A. Diagnosis and treatment of melanoma. European consensus-based interdisciplinary guideline – Update 2012. *Eur. J. Cancer.* **48**, 2375–239 (2012).
- [49] Gebäck, T. & Koumoutsakos, P. Edge detection in microscopy images using curvelets. *BMC Bioinformatics* **10**, 75 (2009).
- [50] Gebäck, T., Schulz, M.M.P., Koumoutsakos, P. & Detmar, M. TScratch: a novel and simple software tool for automated analysis of monolayer wound healing assays. *Biotechniques.* **46**, 265–274 (2009).
- [51] Geho, D., Bandle, R., Clair, T. & Liotta, L. Physiological mechanisms of tumor cell invasion and migration. *Physiology (Bethesda).* **20**, 194–200 (2005).

- [52] Gerlee, P. & Anderson, A. Evolution of cell motility in an individual-based model of tumour growth. *J. Theor. Biol.* **259**, 67–83 (2009).
- [53] Gerlee, P. & Nelander, S. The impact of phenotypic switching on glioblastoma growth and invasion. *PLoS Comp Biol.* **8**, e1002556 (2012).
- [54] Getis, A. & Ord, J.K. The analysis of spatial association by use of distance statistics. *Geogr. Anal.* **24**, 189–206 (2010).
- [55] Goetsch, K.P. & Nielser, C.U. Optimization of the scratch assay for *in vitro* skeletal muscle wound healing analysis. *Anal. Biochem.* **411**, 158–160 (2011).
- [56] Gough, W., Hulkower, K.I., Lynch, R., McGlynn, P., Uhlik, M., Yan, L. & Lee, J.A. A quantitative, facile, and high-throughput image-based cell migration methods is a robust alternative to the scratch assay. *J. Biomol. Screen.* **16**, 155–163 (2011).
- [57] Graner, F. & Glazier, J. Simulation of biological cell sorting using a two-dimensional extended potts model. *Phys. Rev. Lett.* **69**, 2013–2017 (1992).
- [58] Gray-Schopfer, V., Wellbrock, C. & Marais, R. Melanoma biology and new targeted therapy. *Nature.* **445**, 851–857 (2007).
- [59] Guitera, P. & Menzies, S.W. State of the art of diagnostic technology for early-stage melanoma. *Expert. Rev. Anticanc.* **11**, 715–723 (2011).
- [60] Hackett-Jones, E., Landman, K., Newgreen, D. & Zhang, D. On the role of differential adhesion in gangliogenesis in the enteric nervous system. *J. Theor. Biol.* **287**, 148–159 (2011).
- [61] Hallatschek, O. & Korolev, K.S. Fisher waves in the strong noise limit. *Phys. Rev. Lett.* **103**, 108103 (2009).
- [62] Hallatschek, O. The noisy edge of traveling waves. *PNAS.* **108**, 1783–1787 (2011).
- [63] Hanahan, D. & Weinberg, R. Hallmarks of cancer: the next generation. *Cell.* **144**, 646–674 (2011).
- [64] Hidalgo-Grass, C., Mishalian, I., Dan-Goor, M., Beloterkovsky, I., Eran, Y., Nizet, V., Peled, A. & Hanski, E. A streptococcal protease that degrades CXC chemokines and impairs bacterial clearance from infected tissues. *EMBO J.* **25**, 4628–4637 (2006).
- [65] Hsu, M., Meier, F., Nesbit, M., Hsu, J., Van Belle, P., Elder, D. & Herlyn, M. E-Cadherin expression in melanoma cells restores keratinocyte-mediated growth control and down-regulates expression of invasion-related adhesion receptors. *Am. J. Pathol.* **156**, 1515–1525 (2000).
- [66] Research Services Branch, National Institute of Health, ImageJ user guide. Accessed: January 2013, [<http://rsbweb.nih.gov/ij/docs/guide/146-29.html>] (2012).
- [67] Johnston, S.T., Simpson, M.J. & Baker, R.E. Mean-field descriptions of collective migration with strong adhesion. *Phys. Rev. E.* **85**, 051922 (2012).
- [68] Kalluri, R. & Weinberg, R. The basics of epithelial–mesenchymal transition. *J. Clin. Invest.* **119**, 1420–1428 (2009).
- [69] Kam, Y., Guess, C., Estrada, L., Weidow, B. & Quaranta, V. A novel circular invasion assay mimics *in vivo* invasive behavior of cancer cell lines and distinguishes single-cell motility *in vitro*. *BMC Cancer.* **8**, 198 (2008).
- [70] Kam, Y., Karperien, A., Weidow, B., Estrada, L., Anderson, A.R.A. & Quaranta, V. Nest expansion assay: a cancer systems biology approach to *in vitro* invasion measurements. *BMC Cancer.* **9**, 130–139 (2009).

- [71] Kennedy, J. & Mendes, R. Population structure and particle swarm performance. *Evol. Comput.* **2**, 1671–1676 (2002).
- [72] Khain, E., Sander, L. & Scheider-Mizell, C. The role of cell-cell adhesion in wound healing. *J. Stat. Phys.* **128**, 209–218 (2007).
- [73] Khain, E. & Sander, L. Generalized Cahn–Hilliard equation for biological applications. *Phys. Rev. E* **77**, 051129 (2008).
- [74] Khain, E., Schneider-Mizell, C., Nowicki, M., Chiocca, A., Lawler, S. & Sander, L. Pattern formation of glioma cells: effects of adhesion. *Europhys. Lett.* **88**, 28006 (2009).
- [75] Khain, E., Katakowski, M., Charteris, N., Jiang, F. & Chopp, M. Migration of adhesive glioma cells: front propagation and fingering. *Phys. Rev. E* **88**, 28006 (2012).
- [76] Khain, E., Katakowski, M., Hopkins, S., Szalad, A., Zheng, X., Jiang, F. & Chopp, M. Collective behavior of brain tumor cells: the role of hypoxia. *Phys. Rev. E* **83**, 031920 (2012).
- [77] Kilian, K., Bugarija, B., Lahn, B. & Mrksich, M. Geometric cues for directing the differentiation of mesenchymal stem cells. *PNAS* **107**, 4872–4877 (2010).
- [78] Kramer, N., Walzi, A., Unger, C., Rosner, M., Krupitza, G., Hengstschläger, M. & Dolsnig, H. *In vitro* cell migration and invasion assays. *Mutat. Res-Rev. Mutat.* **752**, 10–20 (2013).
- [79] Kreiseder, B., Orel, L., Bujnow, C., Buschek, S., Pflueger, M., Schuett, W., Hundsberger, H., de Martin, H. & Wiesner, C. α -Catulin downregulates E-cadherin and promotes melanoma progression and invasion. *Int. J. Cancer* **132**, 521–530 (2013).
- [80] Law, R. & Dieckman, U. A dynamical system for neighbourhoods in plant communities. *Ecology* **81**, 2137–2148 (2000).
- [81] Lee, J., Wang, Y.L., Ren, F. & Lele, T.P. Stamp wound assay for studying couple cell migration and cell debris clearance. *Langmuir* **26**, 16672–16676 (2010).
- [82] Li, G., Satyamoorthy, K. & Herlyn, M. N-cadherin-mediated intercellular interactions promote survival and migration of melanoma cells. *Cancer Res.* **61**, 3819–3825 (2001).
- [83] Lorensen, W. & Cline, H. Marching cubes: a high resolution 3D surface construction algorithm. *Comp. Graph.* **752**, 163–169 (1987).
- [84] Lutolf, M. & Hubbell, J. Synthetic biomaterials as instructive extracellular microenvironments for morphogenesis in tissue engineering. *Nat. Biotechnol.* **23**, 47–55 (2005).
- [85] Maini, P.K., McElwain, D.L.S. & Leavesley, D.I. Traveling wave model to interpret a wound-healing cell migration assay for human peritoneal mesothelial cells. *Tissue Eng.* **10**, 475–482 (2004).
- [86] Maini, P.K., McElwain, D.L.S. & Leavesley, D.I. Travelling waves in a wound healing assay. *Appl. Math. Lett.* **17**, 575–580 (2004).
- [87] Maret, D., Gruzlin, E., Sadr, M., Siu, V., Shan, W., Koch, A., Seidah, N., Del Maestro, R. & Colman, D. Surface expression of precursor N-cadherin promotes tumor cell invasion. *Neoplasia* **12**, 1066–1080 (2010).
- [88] Markham, D.C., Simpson, M.J., Maini, P.K., Gaffney, E.A. & Baker, R.E. Comparing methods for modelling spreading cell fronts. *J. Theor. Biol.* **353**, 95–103 (2014).
- [89] Martin, P. Wound healing—aiming for perfect skin regeneration. *Science* **276**, 75–81 (1997).
- [90] Image Acqusition Toolbox User Guide R2012 b: Mathworks. Accessed: April 2014, [<http://www.mathworks.com.au/products/image/>] (2014).

- [91] Mattfeldt, T., Frey, H. & Rose, C. Second-order stereology of benign and malignant alterations of the human mammary gland. *J. Microsc.* **171**, 143–151 (1993).
- [92] McDougall, S.R., Watson, M.G., Devlin, A.H., Mitchell, C.A. & Chaplain, M.A.J. A hybrid discrete–continuum mathematical model of pattern prediction in the developing retinal vasculature. *Bull. Math. Biol.* **74**, 2272–2314 (2012).
- [93] McGary, E., Lev, D. & Bar-Eli, M. Cellular adhesion pathways and metastasis potential of human melanoma. *Cancer Biol. Ther.* **1**, 459–465 (2002).
- [94] McKenzie, A.J., Campbell, S.L. & Howe, A.K. Protein Kinase A activity and anchoring are required for ovarian cancer cell migration and invasion. *PLoS One.* **6**, e26552 (2011).
- [95] Mete, M. & Sirakov, N.M. Lesion detection in demoscopy images with novel density-based and active contour approaches. *BMC Bioinformatics.* **11** (Suppl 6) S23 (2010).
- [96] Moghaddasi, F.L., Bezak, E. & Marcu, L. *In silico* modelling of tumour margin diffusion and infiltration: review of current status. *Comput. Math. Method M.* **2012**, 672895 (2012).
- [97] Murray, J.D. *Mathematical Biology 1: An Introduction*. Springer-Verlag, Berlin (2002).
- [98] Nishiyama, C., Uesaka, T., Manabe, T., Yonekura, Y., Nagasawa, T., Newgreen, D.F., Young, H.M. & Enomoto, H. Trans-mesenteric neural crest cells are the principal source of the colonic enteric nervous system. *Nat. Neurosci.* **15**, 1211–1219 (2012).
- [99] Nizet, V., Ohtake, T., Lauth, X., Trowbridge, J., Rudisill, J., Dorschner, R.A., Pestonjamsap, V., Piraino, J., Huttner, K. & Gallo, R.L. Innate antimicrobial peptide protects the skin from invasive bacterial infection. *Nature.* **414**, 454–457 (2001).
- [100] Okumara, C.Y.M., Hollands, A., Tran, D.N., Olson, J., Dahesh, S., von Kockritz-Blickwede, M., Thienphrapa, W., Corle, C., Nam Jeung, S., Kotsakis, A., Shalwitz, R.A., Johnson, R.S. & Nizet, V. A new pharmacological agent (AKB-4924) stabilizes hypoxia inducible factor (HIF-1) and increases skin innate defenses against bacterial infection. *J. Mol. Med.* **90**, 1079–1089 (2012).
- [101] Painter, K.J. & Hillen, T. Mathematical modelling of glioma growth: the use of diffusion tensor imaging (DTI) data to predict the anisotropic pathways of cancer invasion. *J. Theor. Biol.* **323**, 25–39 (2013).
- [102] Pavey, S., Johansson, P., Packer, L., Taylor, J., Stark, M., Pollock, P., Walker, G., Boyle, G., Harper, U., Cozzi, S., Hansen, K., Yudt, L., Schmidt, C., Hersey, P., Ellem, K., O'Rourke, M., Parsons, P., Meltzer, P., Ringnér, M. & Hayward, N. Microarray expression profiling in melanoma reveals a BRAF mutation signature. *Oncogene.* **23**, 4060–4067 (2004).
- [103] Pecky, D.B., Baudoin, J., Eder, M., Werner, U. & de Jonge, N. Epidermal growth factor receptor subunit locations determined in hydrated cells with environmental scanning electron microscopy. *Sci. Rep.* **3**, 2626 (2013).
- [104] Perumpanani, A.J., Sherratt, J.A., Norbury, J. & Byrne, H.M. A two parameter family of travelling waves with a singular barrier arising from the modelling of extracellular matrix mediated cellular invasion. *Physica D.* **126**, 145–159 (1999).
- [105] Plank, M.J. & Simpson, M.J. Models of collective cell behaviour with crowding effects: comparing lattice-based and lattice-free approaches. *J. R. Soc. Interface.* **9**, 2983–2996 (2012).
- [106] Plank, M.J. & Simpson, M.J. Lattice-free models of cell invasion: discrete simulations and travelling waves. *Bull. Math. Biol.* **75**, 2150–2166 (2013).
- [107] Pope, J., Morrison, L., Moss, D., Parsons, P. & Mary, SR. Human malignant melanoma cell lines. *Pathology.* **11**, 191–195 (1979).

- [108] Poser, I., Dominquez, D., de Herreros, A., Varnai, A., Buettner, R. & Bosserhoff, A. Loss of E-cadherin expression in melanoma cells involves up-regulation of the transcriptional repressor Snail. *J. Biol. Chem.* **276**, 24661–24666 (2001).
- [109] Rejniak, K. & Anderson, A.R.A. Hybrid models of tumor growth. *Wiley Interdiscip. Rev. Syst. Biol. Med.* **3**, 115–125 (2010).
- [110] Ripley, B.D. Modelling spatial patterns. *J. Roy. Stat. Soc. B.* **39**, 172–212 (1977).
- [111] Ripley, B.D. Spatial statistics. Wiley, New York (1990).
- [112] Sadeghi, M., Seitz, B., Hayashi, S., LaBree, L. & McDonnell, P. *In vitro* effects of mitomycin-c on human keratocytes. *J. Refract. Surg.* **14**, 534–540 (1998).
- [113] Sengers, B.J., Please, C.P. & Oreffo, R.O.C. Experimental characterization and computational modelling of two-dimensional cell spreading for skeletal regeneration. *J. R. Soc. Interface.* **4**, 107–1117 (2007).
- [114] Sengers, B.G., Please, C.P., Taylor, M. & Oreffo, R.O.C. Experimental-computational evaluation of human bone marrow stromal cell spreading on trabecular bone structures. *Ann. Biomed. Eng.* **37**, 1165–1176 (2009).
- [115] Schafer, M. & Werner, S. Cancer as an overhealing wound: an old hypothesis revisited. *Nat. Rev. Mol. Cell Bio.* **10**, 445–457 (2008).
- [116] Sherratt, J.A. & Murray, J.D. Models of epidermal wound healing. *Proc. R. Soc. Lond. B.* **241**, 29–36 (1990).
- [117] Simpson, M.J., Landman, K.A. & Clement, T.P. Assessment of a non-traditional operator split algorithm for simulation of reactive transport. *Math Comput Simulat.* **70**, 44–60 (2005).
- [118] Simpson, M.J., Zhang, D.C., Mariani, M., Landman, K.A. & Newgreen, D.F. (2007). Cell proliferation drives neural crest cell invasion of the intestine. *Dev Biol.* **302**, 553–568.
- [119] Simpson, M.J., Landman, K.A. & Hughes, B.D. Multi-species simple exclusion processes. *Physica A.* **388**, 399–406 (2009).
- [120] Simpson, M.J., Landman, K.A. & Hughes, B.D. Cell invasion with proliferation mechanisms motivated by time-lapse data. *Physica A.* **389**, 3779–3790 (2010).
- [121] Simpson, M.J., Towne, C., McElwain, D.L.S. & Upton, Z. Migration of breast cancer cells: understanding the roles of volume exclusion and cell-to-cell adhesion. *Phys. Rev. E.* **82**, 041901 (2010).
- [122] Simpson, M.J. & Baker, R.E. Corrected mean-field models for spatially dependent advection-diffusion-reaction phenomena. *Phys. Rev. E.* **83**, 051922 (2011).
- [123] Simpson, M.J., Baker, R.E. & McCue, S.W. Models of collective cell spreading with variable cell aspect ratio: a motivation for degenerate diffusion models. *Phys. Rev. E.* **83**, 021901 (2011).
- [124] Simpson, M.J. & Ellery, A.J. An analytical solution for diffusion and nonlinear uptake of oxygen in a spherical cell. *Appl. Math. Model.* **36**, 3329–3334 (2012).
- [125] Simpson, M.J., Treloar, K.K., Binder, B.J., Haridas, P., Manton, K.J., Leavesley, D.I., McElwain, D.L.S. & Baker, R.E. Quantifying the roles of cell motility and cell proliferation in a circular barrier assay. *J. R. Soc. Interface.* **10**, 2013007 (2013).
- [126] Simpson, M.J., Sharp, J.A. & Baker, R.E. Distinguishing between mean-field, moment dynamics and stochastic descriptions of birth-death-movement processes. *Physica A.* **395**, 236–246 (2014).

- [127] Simpson, M.J., Binder, B.J., Haridas, P., Wood, B.K., Treloar, K.K., McElwain, D.L.S. & Baker, R.E. Experimental and modelling investigations of monolayer development with clustering. *Bull. Math. Biol.* **75**, 871–889 (2013).
- [128] Søndergaard, J., Nazarian, R., Wang, Q., Guo, D., Hsueh, T., Mok, S., Sazegar, H., MacConaill, L., Barretina, J., Kehoe, S., Attar, N., von Euw, E., Zuckerman, J., Chmielowski, B., Comin-Anduix, B., Koya, R., Mischel, P., Lo, R. & Ribas, A. Research Differential sensitivity of melanoma cell lines with BRAFV600E mutation to the specific Raf inhibitor PLX4032. *J. Transl. Med.* **8**, 1479–5876 (2010).
- [129] Soong, S., Shaw, H., Balch, C., McCarthy, W., Urist, M. & Lee, J. Predicting survival and recurrence in localised melanoma: a multivariate approach. *World J. Surg.* **290**, 46–59 (1992).
- [130] Sottoriva, A., Verhoeff, J., Borovski, T., McWeeney, S., Naumov, L., Medema, J., Sloot, P. & Vermeulen, L. Cancer stem cell tumor model reveals invasive morphology and increased phenotypical heterogeneity. *Cancer Res.* **70**, 46–56 (2010).
- [131] Su, D., Zhang, Q., Wang, X., He, P., Zhu, Y., Zhao, J., Rennert, O. & Ya, S. Two types of human malignant melanoma cell lines revealed by expression patterns of mitochondrial and survival-apoptosis genes: implications for malignant melanoma therapy. *Mol. Cancer Ther.* **8**, 1292–1304 (2009).
- [132] Swanson, K.R., Bridge, C., Murray, J.D. & Alvord, E.C. Jr. Virtual and real brain tumours: using mathematical modeling to quantify glioma growth and invasion. *J. Neurol. Sci.* **216**, 1–10 (2003).
- [133] Swanson, K.R. Quantifying glioma cell growth and invasion *in vitro*. *Math. Comput. Model.* **47**, 638–648 (2008).
- [134] Swanson, K.R., Harpold, H.L.P., Peacock, D.L., Rockne, R., Pennington, C., Kilbride, L., Grantly, R., Wardlaw, J.M. & Alvord, Jr. E.C. Velocity of radial expansion of contrast-enhancing gliomas and the effectiveness of radiotherapy in individual patients: a proof of principle. *Clin. Oncol.* **20**, 301–308 (2008).
- [135] Topman, G., Sharabani-Yosef, O. & Gefen, A. A standardized objective method for continuously measuring the kinematics of cultures covering a mechanically damaged site. *Med. Eng. Phys.* **34**, 225–232 (2012).
- [136] Treloar, K.K., Simpson, M.J. & McCue, S.W. Velocity-jump models with crowding effects. *Phys. Rev. E.* **84**, 061920–1 (2011).
- [137] Treloar, K.K. & Simpson, M.J. Sensitivity of edge detection methods for quantifying cell migration assays. *PLoS ONE*, **8**, e67389 (2013).
- [138] Treloar, K.K., Simpson, M.J., Haridas, P., Manton, K.J., Leavesley, D.I., McElwain, D.L.S. & Baker, R.E. Multiple types of data are required to identify the mechanisms influencing the spatial expansion of melanoma cell colonies. *BMC Syst. Biol.* **7**, 137 (2013).
- [139] Treloar, K.K., Simpson, M.J., D.L.S & Baker, R.E. Are *in vitro* estimates of cell diffusivity and cell proliferation rate sensitive to assay geometry? *J. Theor. Biol.* **356**, 71–84 (2014).
- [140] Turner, S & Sherratt, J.A. Intracellular adhesion and cancer invasion: a discrete simulation using the extended potts model. *J. Theor. Biol.* **216**, 85–100 (2002).
- [141] Turner, S, Sherratt, J.A., Painter, K.A. & Savill, N.J. From a discrete to a continuous model of biological cell movement. *Phys. Rev. E.* **69**, 021910 (2004).
- [142] Upton, Z., Cuttle, L., Noble, A., Kempf, M., Topping, G., Malda, J., Xie, Y., Mill, J., Harkin, D.G., Kravchuk, O., Leavesley, D.I. & Kimble, R.M. Vitronectin: growth factor complexes hold potential as a wound therapy approach. *J. Invest. Dermatol.* **128**, 1535–1544 (2008).

- [143] Upton, Z., Wallace, H.J., Shooter, G.K., van Lonkhuyzen, D.R., Yeoh–Ellerton, S., Rayment, E.A., Fleming, J.M., Broszczak, D., Queen, D., Sibbald, R.G., Leavesley, D.I. & Stacey, M.C. Human pilot studies reveal the potential of a vitronectin: growth factor complex as a treatment for chronic wounds. *International Wound Journal.* **8**, 522–532 (2011).
- [144] Valster, A., Tran, N., Nakada, M., Berens, M., Chan, A. & Symons, M. Cell migration and invasion assays. *Methods.* **37**, 208–215 (2005).
- [145] Van Horssen, R. & Ten Hagen, T.L.M. Crossing Barriers: The new dimension of 2D cell migration assays. *J. Cell Physiol.* **226**, 288–290 (2010).
- [146] Van Leeuwen, I., Mirams, G., Walter, A., Fletcher, A., Murray, P., Osborne, J., Varma, S., Young, S., Cooper, J., Doyle, B., Pitt–Francis, J., Momtahan, L., Pathmanathan, P., Whiteley, J., Chapman, S., Gavaghan, D., Jensen, O., King, J., Maini, P., Waters, S. & Byrne, H. An integrative computational model for intestinal tissue removal. *Cell Prolif.* **42**, 617–636 (2009).
- [147] Veatch, S.L., Machta, B.B., Shelby, S. A., Chiang, E.N., Holowka, D.A. & Baird, B.A. Correlation functions quantify super–resolution images and estimate apparent clustering due to over–counting. *PLoS One.* **7**, e31457 (2012).
- [148] Vedula, S.R.K., Leong, M.C., Lai, T.L., Hersen, P., Kabla, A.J., Lim, C.T. & Ladoux, B. Emerging modes of collective cell migration induced by geometrical constraints. *PNAS.* **109**, 12974–12979 (2012).
- [149] Vogel, V. & Sheetz, M. Local force and geometry sensing regulate cell functions. *Nat. Rev. Mol. Cell Bio.* **7**, 265–275 (2006).
- [150] Walker, D. & Southgate, J. The virtual cell – a candidate coordinator for ‘middle–out’ modelling of biological systems. *Brief. Bioinforma.* **10**, 450–461 (2009).
- [151] Wang, X., Cui, M., Wang, L., Chen, X. & Xin, P. Inhibition of neurotrophin receptor p75 intramembran proteolysis by gamma-secretase inhibitor reduces medulloblastoma spinal metastasis. *Biochem. Biophys. Res. Co.* **403**, 264–269 (2010).
- [152] Weijer, C.J. Collective cell migration in development. *J. Cell Sci.* **122**, 3215–3223 (2009).
- [153] Weinberg, R.A. *The biology of cancer*. Garland Science. New York (2006).
- [154] Whitehead, R. & Little, J. Tissue culture studies on human malignant melanoma. *Pigment. Cell.* **1**, 382–389 (1973).
- [155] Witelski, T.P. An asymptotic solution for traveling waves of a nonlinear-diffusion fisher’s equation. *J Math Biol.* **33**, 1–16 (1994).
- [156] Witelski, T.P., Ono, K. & Kaper, T.J. On axisymmetric traveling waves and radial solutions of semi-linear elliptic equations. *Nat. Resour. Model.* **13**, 339–388 (2010).
- [157] Wolpert, L. Principles of development. Oxford University Press. Oxford (2011).
- [158] Woodhouse, E., Chuaqui, R. & Liotta, L. General mechanisms of metastasis. *Cancer.* **80**, 1529–1537 (1997).
- [159] Young, H.M., Bergner, A.J., Anderson, R.B., Enomoto, H., Milbrandt, J., Newgreen, D.F. & Whitington, P.M. Dynamics of neural crest–derived cell migration in the embryonic mouse gut. *Dev Biol.* **270**, 455–473 (2004).
- [160] Yue, P.Y.K., Leung, E.P.Y., Make, N.K. & Wong, R.N.S. A simplified method for quantifying cell migration/wound healing in 96-well plates. *J. Biomol. Screen.* **4**, 427–433 (2010).

- [161] Zaritsky, A., Natan, S., Horev, J., Hecht, I., Wolf, L., Ben-Jacob, E. & Tsarfaty, I. Cell motility dynamics: a novel segmentation algorithm to quantify multi-cellular bright field microscopy images. *PLoS One.* **6**: e27593 (2011).
- [162] Zaritsky, A., Manor, N., Wolf, L., Ben-Jacob, E. & Tsarfaty, I. Benchmark for multi-cellular segmentation of bright field microscopy images. *BMC Bioinformatics.* **14**, 319–324 (2013).
- [163] Zeisberg, M. & Neilson, E. Biomarkers for epithelial–mesenchymal transitions. *J. Clin. Invest.* **119**, 1429–1437 (2009).
- [164] Zordan, M.D., Mill, C.P., Riese, D.J. & Leary, J.F. A high throughput, interactive imaging, bright-field wound healing assay. *Cytom. Part A.* **79**, 227–232 (2011).